Universidade de Aveiro
2018

Departamento de Física

Seyed Ali Salehizadeh

Encapsulamento de nanopartículas à base de óxido de ferro com sílica para aplicações biomédicas

Encapsulation of iron oxide-based nanoparticles in silica for biomedical applications

Universidade de Aveiro
2018

Departamento de Física

Seyed Ali Salehizadeh

Encapsulamento de nanopartículas à base de óxido de ferro com sílica para aplicações biomédicas

Encapsulation of iron oxide-based nanoparticles in silica for biomedical applications

Dissertação apresentada à Universidade de Aveiro para cumprimento dos requisitos necessários à obtenção do grau de Doutor em Engenharia Física, realizada sob a orientação científica do Professor Doutor Manuel Pedro Fernandes Graça, Investigador Principal do Departamento de Física da Universidade de Aveiro, e coorientação do Professor Doutor Manuel Almeida Valente, Professor Associado do Departamento de Física da Universidade de Aveiro.

To my parents

O júri

Presidente

Profª. Doutora Ana Isabel Couto Neto da Silva Miranda,
Professora Catedrática, Universidade de Aveiro;

Vogais/Members:

Prof. Doutor Pablo Hernandez-Gomez,
Professor Catedrático, Universidad de Valladolid;

Prof. Doutor Henrique Leonel Gomes,
Professor Associado Com Agregação, Universidade do Algarve;

Profª. Doutora Florinda Mendes da Costa,
Professora Associada, Universidade de Aveiro;

Profª. Doutora Maria Benilde Faria de Oliveira e Costa,
Professora Auxiliar Com Agregação, Universidade de Coimbra;

Prof. Doutor Manuel Pedro Fernandes Graça (Orientador)
Professor Equiparado a Investigador Principal, Universidade de Aveiro

Agradecimentos
Acknowledgments

First of all, I would like to thank Prof. Dr. Manuel Pedro Fernandes Graça and Prof. Dr. Manuel Almeida Valente for providing an opportunity to accomplish my Ph.D. study, generous support of my research and their valuable guidance and patience with me.

It was a great honor and valuable experience for me to work under their supervision. I also appreciate their valuable time especially during the correction of this dissertation and their insightful comments.

I would like to thank Dr. Nuno Ferriera for his assistance in the preparation of glass fibers by LFZ technique. Also, I would like to express my sincere appreciation to Prof. Dr. Florinda Mendes Costa for her generous support, kind attention and fruitful comments on the study of the LFZ glass fibers. Many thanks to my dear friend and colleague Dr. Suresh Kumar Jakka for his endless help on Raman measurements of my samples, great collaboration, and helpful comments. Many thanks to Dr. Rosario Soares for the great help on XRD measurements and very kind attention. Many thanks to Dr. Maxim Ivanov, from the University of Coimbra, for AFM/MFM measurement which excelled a lot my research. Many thanks to Dr. Janez Zavasnik, from Max Planck Institute for Iron Research GmbH, Dusseldorf, Germany, for his excellent assistance in TEM analysis.

I also acknowledge Mr. Francisco Reis, Mr. Antnio José Silva Fernandes, Mr. Ivo and Mr. Rocha for their great help in resolving the technical issues that I faced during my P.h.D study.

And at last, but for sure the most, my sincere and countless gratitude to my mother, my father, my sister and my brothers, for great love, support, and encouragement throughout my life and during the Ph.D. study.

Ali Salehizadeh

keywords iron oxide; nanoparticles; silica coating; laser floating zone; sol-gel; magnetic properties, impedance spectroscopy

Abstract

Over last decades, a great attention has been devoted to iron oxide-based nanoparticles coated by dielectric organic or inorganic materials for the potential contributions in biomedical applications and microwave absorbers industry.

The present Ph.D. study focuses on the fabrication of iron-based oxide nanoparticles and coating the particles within the silica matrix in the form of a core-shell structure exhibiting interesting magnetic and electrical properties for application in the biomedical and microwave technology areas. The combined study of electrical and magnetic properties of the silica-iron oxide composites allowed us to examine the requisites for application in a new generation of the high-efficient microwave absorbents and also for the possibility of hyperthermia and drug delivery agents.

In this context, four synthesis methods: sol-gel route, laser floating zone (LFZ), auto-combustion, and Pechini method were employed to prepare the iron oxide-based/silica composites.

Several studies, namely, structural, morphological, electrical and magnetic characterizations, were performed on the prepared samples. The utilization

Abstract (cont.)

of several experimental characterizing techniques not only provide us a comprehensive knowledge of the physical properties of these materials but also look over the future employment of the prepared composites in the biomedical application and the microwave absorbing materials.

It was prepared a series of glasses with the composition, xFe_2O_3-$(100-x)SiO_2$ (x=1, 2, 10, 20 in mol%) by the sol-gel route. The effect of the heat treatment conditions and the Fe/Si ratio on the morphology, electrical and magnetic properties of the glass ceramics were investigated.

Fibers with the composition of $10Fe_2O_3$-$90SiO_2$ were processed by LFZ technique. Their morphology, structure, magnetic properties and redox state were studied in function of the pulling rate. An exhautive study on the Raman spectroscopy and the local magnetic microstructure of the fibers were performed to support for a deeper understanding of the magnetic properties of the fibers.

A series of manganese ferrite-silica nanocomposites with the composition $xMnFe_2O_4$-$(100-x)SiO_2$ (x=100, 20, 15 and 10 in mol%) were prepared by the auto combustion method. The physical parameters obtained from this study showed the great potential of the silica-manganese ferrite nanocomposites for the proposed applications as well other suggested future works.

In addition, a preliminary study on the synthesis by the Pechini method and characterization of iron oxide was carried out. The structure, the magnetic properties and the electric conduction mechanism of the prepared iron oxide polycrystallites were investigated leaving open other possible applications industries.

Palavras-chave Nanopartículas; óxido de ferro; revestimento de sílica; fusão de zona flutuante com laser; sol-gel; propriedades magnéticas; espectroscopia de impedância

Resumo

Nas últimas décadas grande atenção tem sido dedicada ao estudo de nanopartículas à base de óxido de ferro revestidas por materiais dielétricos orgânicos ou inorgânicos com potencial para aplicações biomédicas e na indústria de absorventes de microondas.

O presente trabalho de doutoramento centra-se na fabricação de nanopartículas de óxido de ferro e no seu revestimento com sílica na forma de uma estrutura núcleo-casca com o objectivo de obter propriedades magnéticas e elétricas interessantes para aplicações práticas na área biomédica e na indústria de microondas. O estudo combinado das propriedades elétricas e magnéticas dos compósitos de óxido de ferro-sílica permitiu estudar as características para aplicações em nova geração de absorventes de micro-ondas de alta eficiência e também agentes com possíveis utilizações em hipertermia e libertação de drogas.

Neste contexto foram utilizados, quatro métodos de síntese: método de sol-gel, técnica fusão de zona flutuante com laser (LFZ), autocombustão e método de Pechini na preparação dos compósitos à base de óxido de ferro / sílica.

Vários estudos como caracterização estrutural, morfológica, elétrica e magnética, foram realizados nas amostras preparadas. A utilização de várias técnicas de caracterização experimental fornece um conhecimento abrangente das propriedades físicas destes materiais e permite perspectivar o possível emprego destes compósitos para aplicações biomédicas e como materiais absorventes de micro-ondas no futuro.

Foi preparada a série de vidros xFe_2O_3- (100-x) SiO_2 (x = 1, 2, 10, 20 em mol%) pelo método de rota sol-gel. O efeito das condições de tratamento

térmico e da relação Fe / Si na morfologia, propriedades elétricas e magnéticas das cerâmicas vítreas foi investigado.

Fibras com a composição $10Fe_2O_3$-$90SiO_2$ foram processadas pela técnica de LFZ. A sua morfologia, estrutura, propriedades magnéticas e estado de redução foram estudadas em função da taxa de extração da preparação das amostras. Foi realizada uma análise exaustiva dos resultados da espectroscopia de Raman e uma pesquisa da microestrutura magnética local para melhor interpretar as características magnéticas das fibras.

Uma série de nanocompósitos de silício-ferrite de manganês com a composição $xMnFe_2O_4$- (100-x) SiO_2 (x = 100, 20, 15 e 10 em % molar) foi preparada pelo método de auto-combustão. Foi realizada investigação das propriedades estruturais, morfológicas, elétricas e magnéticas destas amostras. Os parâmetros físicos obtidos a partir desse estudo mostraram o grande potencial dos nanocompósitos de silício-ferrita de manganês para as aplicações propostas assim como para o trabalho futuro sugerido.

Além disso, também foi realizado um estudo preliminar sobre a síntese e caracterização do óxido de ferro pelo método de Pechini.A estrutura, as propriedades magnéticas, o mecanismo de condução elétrica das policristalitas de óxido de ferro preparados foram realizadas deixando em aberto outras possíveis aplicações industriais.

Index

PREFACE

The present Ph.D. thesis aims to synthesize new iron oxide-based/silica composites and characterize the structural, morphological, electrical and magnetic properties overlooking potential applications in the area of biomedical devices and microwave absorptive materials.

In this framework, the thesis is divided into eight chapters as follows:

Chapter 1 contextualizes the primary motivations and goals of the thesis. An overall skim of the materials and the characterization techniques used in this work is also given.

In chapter 2, firstly, state of the art and the conceptual review of the experimental synthesis methods are presented. The chapter is followed by a thorough description of the synthesized materials and their challenges and complexities through a bibliographic investigation.

Chapter 3 describes extensively the experimental characterization techniques employed in this study with the respective theoretical background and the mathematical formalism. More emphasis is dedicated to the electrical and magnetic fundamental aspects.

Chapter 4 deals with the investigation of the physical characteristics of xFe_2O_3-$(100-x)SiO_2$ glass ceramics prepared using the sol-gel method.

In chapter 5 we investigate the influence of the pulling rate on the physical properties and the redox state of the $10Fe_2O_3$-$90SiO_2$ fibers processed by LFZ technique. The Raman analysis, the local magnetic structure and the magnetic properties of the LFZ fibers are highlighted.

Chapter 6 presents to the description of the structural, morphological, electrical and magnetic characteristics of the $xMnFe_2O_4$-$(100-x)SiO_2$ nanocomposites derived from a one-pot auto combustion method.

Chapter 7 describes the preliminary physical properties of the polycrystalline iron oxide particles prepared by the Pechini technique.

Finally, in chapter 8 a general overview of the work, the main conclusions of each chapter, and also future perspectives are presented.

LIST OF ACRONYMS AND SYMBOLS

Acronym	**Definition**
AC	Alternating current
AFM	Atomic force microscopy
BSEs	Backscattered electrons
BET	Brunauer-Emmett-Teller
BF	Bright field
BZc	Center of brillouin zone
CA	Citric acid
CBT	Correlated Barrier Hopping
CCD	Charge-coupled device
CPE	Constant phase element
CTAB	Cetyltrimethyl ammonium bromide
DC	Direct current
DF	Dark-field
DTA	Differential thermal analysis
EDS	Energy dispersive X-ray spectroscopy
E-S	Efros- Shklovskii
e.m.f	Electromagnetic force
FTIR	Fourier-transform infrared
FWHM	Full-width half maximum
GPIB	General Purpose Interface Bus

Acronym	**Definition**
HR-TEM	High resolution Transmission electron microscopy
ICCD	International Centre for Diffraction Data
IS	Impedance Spectroscopy
KWW	Kohlrausch-Williams-Watts
LFZ	Laser floating zone
LO	Logitudinal optical
MLCIs	Multilayer chip inductors
MFM	Magnetic force Microscopy
MNPs	Magnetic nanoparticles
MnFe NPs	Manganese ferrite nanoparticles
MRI	Magnetic resonance imaging
NNH	Nearest-neighbor-hopping
OLPT	Overlapping large polaron tunneling
PAA	Poly(acrylic acid)
PC	Personal computer
PEG	Poly(ethylene glycol)
PEVA	Poly(ethylene-co-vinyl acetate)
PLGA	Poly(lactic-co-glycolic acid)
PVP	Poly(vinyl pyrrolidone)
QTM	Quantum Tunneling Mechanism
SAED	Selected area electron diffraction
SE	Solid electrolyte
SEs	Secondary electrons

Acronym	**Definition**
SEM	Scanning electron microscopy
SMD	Single-magnetic-domain
SP	Superparamagnetic
SQ	Squarence
TA	Thermal analysis
TEM	Transmission electron microscopy
TEOS	Tetraethyl orthosilicate
TO	Transverse optical
UDR	Universal dynamic response
VRH	Variable-range-hopping
VSM	Vibrating sample magnetometer
W-H	Williamson–Hall
XRD	X-ray diffraction
XANES	X-ray absorption near edge structure

Symbol	**Definition**
ΔE	Activation energy
ω	Angular frequency
T_b	Blocking temperature
k_B	Boltzmann constant
σ	Conductivity
B_C	Coercivity
ρ_{fib}	Density of fiber
N_D	Dislocation Density
n_f	Free charge carriers
n_t	Trapped charge carrers
ε´and ε´´	Imaginary and real parts of Dielectric constant
T_{irr}	Irreversible temperature
tan δ	Loss tangent
G	Temperature gradient
C_g	Grain capacitance
C_{gb}	Grain boundary capacitance
M^*	Complex modulus
ρ	Density
R2	Transverse relaxation
R1	Logitudinal relaxation
R_g	Grain resistance
R_{gb}	Grain boundary resistance

Symbol	**Definition**
S	Specific surface area
T_C	Curie temperature
m_p	Magnetic momnet per particle
μ_B	Bohr magneton
μ	Magnetic moment
T_M	Morin temperature
T_N	Neel temperature
M_r/M_S	Squarence
M_S	Saturation magnetization
τ	Relaxation time
T_V	Verwey temperature
M_r	Remanence
χ	Susceptibility
Z´ and Z´´	Real and imaginary part of impedence

LIST OF FIGURES

LIST OF TABLES

Chapter 1 - Introduction

1.1) Motivation

The application of iron-based nanoparticles encapsulated by organic or inorganic shells has been investigated extensively for both medical implementation and electromagnetic absorber materials [1-4].

The potential benefits of superparamagnetic (SP) iron-based nanoparticles, i.e., particles that present magnetization only in the presence of an external magnetic field, with appropriate surface chemistries, are the inoffensive toxicity profile and a reactive surface which make them biocompatible and biofunctionalized [1-3]. This flexibility has led to use in numerous in-vivo applications such as contrast enhancement in magnetic resonance imaging, tissue repair, detoxification of biological fluids, hyperthermia, drug delivery, stem cell tracking and cell separation [1,2].

The capability of magnetic nanoparticles of absorbing the energy of microwave radiation has been already exploited as:

i) therapeutic agent in anticancer hyperthermia treatments;

ii) microwave-assisted protein digestion;

iii) transducers for the remote and selective activation of specific cellular functions [3].

For this purpose, a combination of the electrical properties of conductive polymers or inorganic encaging shell and the magnetic properties of small magnetic particles can be useful to obtain enhanced absorption of electromagnetic waves [4].

For the above applications, the particles must have combined properties of high magnetic saturation, biocompatibility and interactive functions at the surface. The surfaces of these particles can be modified through the creation of few atomic layers of organic polymer or oxide surfaces (e.g., silica), suitable for further functionalization by the attachment of various bioactive molecules [5].

The wet chemical routes for materials preparation, like sol-gel method, are exciting techniques to prepare core/shell structures because it is typically performed at low temperatures and can be used to synthesize pure, stoichiometric, monodisperse with relatively narrow size distribution on a large scale [6].

Besides the wet chemical synthesis methods, solid-state reaction method and other high-temperature methods such as the melt-quenching and the laser floating zone (LFZ) methods can be employed to disperse magnetic nanocrystalline particles into a matrix, which can have an amorphous nature or not. Also, it is already known that the LFZ method is a powerful processing tool for studying crystallization and vitrification mechanisms in silicate-based glasses. Moreover, it can tune the states of the redox-active iron cations [7].

Extensive developments in the preparation and also tuning of the electrical and magnetic characteristics of hybrid nanocomposites based on organic and inorganic materials and magnetic particles have been made recently because of and widespread usage in electromagnetic shielding and microwave wave industry and many other fields such as biomedical applications data storage and environmental remediation separation [8].

However, in spite of the extensive research devoted to nanomagnetic particles and their biomedical applications, there is very few information available on the magnetic and impedance spectroscopic characterizations of such particles embedded in organic or inorganic matrices. Such studies are essential to help us finding ideal nanostructured materials served potentially the two desired applications.

1.2) Objectives

In this thesis, we are focusing on the synthesis of silica coated core iron oxide-based nanoparticles on obtaining two simultaneously essential characteristics stating, below:

- Improved magnetization, high saturation magnetization and anisotropy constant with narrow size distribution applicable in various biomedical and bioengineering applications.
- Enhanced resistivity with an excellent match between magnetic and dielectric features and operating in the high-frequency region.

To achieve these primary objectives, the process followed was:

i. Preparation of iron oxide nanoparticles embedded in a silica matrix, using sol-gel and laser floating zone methods.

ii. Preparation of Fe_2O_3 and $MnFe_2O_4$-SiO_2 nanocomposites using auto-combustion and Pechini sol-gel routes.

iii. The structural and morphological characterizations were carried out using X-ray diffraction (XRD), differential thermal analysis (DTA), Fourier-transform infrared (FTIR), atomic force microscope (AFM) including magnetic force microscopy (MFM) mode, Raman spectroscopy, transmission electron microscopy (TEM), scanning electron microscopy (SEM) and energy-dispersive X-ray spectroscopy (EDS) techniques.

iv. DC and AC electrical conductivity and dielectric properties were exploited as a function of frequency in the temperature range 100 K and 400 K.

v. Vibrating Sample Magnetometer (VSM) were used to analyze the magnetic behavior of the samples.

The novel magnetic nanoparticles encapsulated in silica shell will be synthesized with the enhanced functionality in the high-frequency region for biomedical application. Therefore, as a high-efficient microwave absorbent, both large magnetic permeability and dielectric constant are indispensable factors. So the proper impedance matching through the efficient complementarities between complex permeability and complex permittivity should be considered.

1.3) Materials preparation

Preparation of Fe_2O_3-SiO_2 compositions was made using sol-gel method due to the advantage of this method for formation of small grains and low processing temperatures. SiO_2 is used as the coater due to its significant properties as easily synthesis in large-scale, regular crystalline structure, bioactivity, biocompatibility and non-biodegradable. The three following parameters: Fe/Si ratio, heat-treatment (HT) temperature, and atmosphere (oxidizing or reducing) which influence in the crystallization of iron oxide core and silica host and the redox state of Fe, respectively, is controlled to reach to the optimized composition based on the plan goals.

LFZ is a well-known method to produce a wide range of oxides crystals in fiber form with highest homogeneity and purity [7, 9] was employed to produce iron oxide-SiO_2 nanofibers. The growth rate variation impact on the crystallization, the morphology and structure of nano-

sized iron oxide clusters and their effect on the magnetic anisotropy of the formed iron oxide particles was studied.

The Fe_2O_3, Fe_3O_4, and $MnFe_2O_4$ particles, with sizes below 200 nm with high permittivity and permeability, as well as $MnFe_2O_4$-SiO_2 nanocomposite, were prepared using Pechini and auto-combustion methods which can compromise the conditions for single domain non-interacting magnetic particles with higher saturation magnetization and high effective anisotropy constant.

1.4) Materials Characterization

Structure, crystallite size, lattice parameters of the prepared nanosize particles and composites, by recording their X-ray Diffraction profiles, can be analyzed using analytical methods such as the Debye-Scherrer (D-Sch) and the Williamson–Hall (WH) [12]. Samples morphology were examined by transmission electron microscopy (TEM) and scanning electron microscopy (SEM). The topology and surface magnetic properties were measured using the atomic-force microscope (AFM) including magnetic force microscopy (MFM) mode.

For a generation of MFM images, we utilized two-pass method: at the first pass the surface topology, AFM, was obtained (in semicontact mode); at the second pass the needle was lifted up and followed the trajectory obtained at the first pass, MFM topography [13]. The structural modification and the chemical bindings are investigated by FTIR and Raman spectroscopies [14,15]. Thermal analysis (TA) as a suitable technique to study the structural transformation, like glass transition, crystallization [6] and other exo/endothermic phenomena occurred during chemical reactions is used.

The study of electrical and dielectric properties in wide frequency (100 Hz - 1 MHz) and temperature (100 K - 400 K) ranges were used as an effective tool to investigate the conduction mechanism, normally owned by polaronic hopping between cationic sites in ferrites. Direct current (DC) measurements were also analyzed.

The influence of interparticle dipolar interactions in the core-shell structure will be evaluated by VSM in the temperature range of 2 K – 300 K applying an external field that can be up to 10 T.

The obtained results will be taken into account as a criterion to determine the optimal core/shell structures and electromagnetic parameters for application in remotely controlled biological nanomachine in the microwave region.

1.5) References

[1] H. Maleki, Simchi, M. Imani, B.F.O. Costa, **Journal of Magnetism and Magnetic Materials**, 324, 23, 2012, 3997–4005.

[2] J. R. McCarthy, and R. Weissleder, **Advanced Drug Delivery Reviews**, 2008, 60, 11, 1241-1251.

[3] G. Bellizzi, O.M. Bucci, and A. Capozzoli, **Journal of Magnetism and Magnetic Materials**, 2010, 322, 3004-3013.

[4] J. Hongxia, L. Qiaoling, Y. Yun, G. Zhiwu, and Y. Xiaofeng, **Journal of Magnetism and Magnetic Materials**, 2013, 332, 10-14.

[5] C. C. Berry, and A. S. G. Curtis, **Journal of Physics D: Applied Physics**, 2003, 36, R198-R206.

[6] I. Sharifi, H. Shokrollahi and, S. Amiri, **Journal of Magnetism and Magnetic Materials**, 2012,324, 6, 903–915.

[7] N. M. Ferreira, A.V. Kovalevsky, J.C. Waerenborgh, M. Quevedo-Reyes, A.A. Timopheev, F.M. Costa and, J.R. Frade, **Journal of Alloys and Compounds**, 2014, 611, 57–64.

[8] V. Kumar S. Kalia, H. C. Swart, **Conducting Polymers Hybrids: Magnetic Nanoparticles-Based Conducting Polymer Nanocomposites**, 2017, Springer.

[9] N.M. Ferreira, A.V. Kovalevsky, M.A. Valente, N.A. Sobolev, J.C. Waerenborgh, F.M. Costa and J.R. Frade, **Ceramics International**, 2016, 42, 2, Part A, 2016, 2693–2698.

[10] O. Yalçın, H. Bayrakdar, S. Özüm, **Journal of Magnetism and Magnetic Materials**, 2013, 343, 157-162.

[11] I. Sharifi, H. Shokrollahi, S. Amiri, **Journal of Magnetism and Magnetic Materials**, 2012,324, 6, 903–915.

[12] R. Zamiri, H. M. Chenari, H. F. Moafi, M. Shabani, S. A. Salehizadeh, A. Rebelo, J. S. Kumar, M. P. F. Graça, M. J. Soares, J. M. F. Ferreira, **Ceramics International**, 2016, Volume 42, Issue 11, 12860-12867.

[13] C. S. Neves, P. Quaresma, P. V. Baptista, P. A. Carvalho, J. P. Araújo, **Nanotechnology**, 2010, 21(30), 305706.

[14] S. A. Salehizadeh, M. P. F. Graça, M. A. Valente, **Physica Status Solidi (c)**, 2014, 11(9), 1455-1458.

[15] S. A. Salehizadeh, B. M. G. Melo, F. N. A. Freire, M.A. Valente and M.P.F. Graça, **Journal of Non-Crystalline Solids**, 2016, 443, 65–74.

This page intestinally was left blank

Chapter 2 - State of the art, challenges, and concepts

2.1) Introductory remarks

A brief introduction to the role of synthesis route and composition with particular attention to the magnetic and electrical characteristics of bare iron oxide-based nanosize particles and also their encapsulation in organic-inorganic hosts is given in this chapter.

The chapter will present the description of relevant processes, the related limitations and possible ways to overcome in iron-based oxide nanocomposite production. It will also introduce the approaches, on the structural, electrical and magnetic properties of iron oxide-based materials, from a fundamental point of view.

Recently, research in nanomagnetic actuation has focused on activating mechanosensitive ion channels, on cell surfaces, which are selectively bounded to magnetic nanoparticles (MNPs) [1]. In this approach, MNPs have been proposed as transducers for the remote and selective activation of specific cellular functions, when driven by applied microwave radiation.

To have ideal electromagnetic absorbers, materials with high permeability in microwave frequency region, low dielectric and magnetic losses, suitable frequency dependence of permeability and favorable match between dielectric and magnetic properties must be found [2].

It is already known that magnetic and electrical properties of iron-based compounds can be understood regarding grain size, grain structure, porosity and metal cation distribution in the sublattices, mainly the tetrahedral and octahedral sites [3].

In this chapter, the chemical compositions based on iron which are more common to use for the preparation of magnetic nanosize particles are introduced. It should be noticed that chemical composition is one of the determinant factor in the magnetic properties of such particles. Despite the high saturation magnetization for pure iron, and since the pure iron is extremely sensitive to oxidation and consequently highly toxic, it is not a proper material for employ in biomedical applications [4]. Magnetic alloys containing iron, such as Nd-Fe-B, need to be affected by a large external field. Also, they show a very high corrosion rate [5, 6]. Therefore, due to this disadvantage, they are rarely used for our proposed goals [5]. In this

work, among the different types of ceramics, we dedicate more attention to the following two types:

i) Iron oxides (α-Fe_2O_3, γ-Fe_2O_3 and Fe_3O_4);

ii) Manganese ferrite ($MnFe_2O_4$).

2.2) Experimental Methods for Synthesis Magnetic Nanoparticles

Several synthesis methods have been employed to prepare magnetic nanosize composites including chemical methods and physical methods. In this section, it will be outlined the various techniques, which have been studied and used extensively in this research work.

2.2.1) Sol-gel method (metallic alkoxides and Pechini routes)

The sol-gel technique has been used to produce nanosize magnetic particle and also for coatings of them into diverse kinds of matrices which allows the obtaining [7-10]:

i) homogenous multi-component systems;

ii) low-temperature material process;

iii) the formation of fibers, coatings or composites because of rheological properties of sols or gels.

Various studies have been based on the fabrication of nonmetallic sieving matrices with nanoscale pores through a step of hydrolysis and condensation of commercial precursors in a water/ethanol mixture [11-13]. This method makes possible to control the thickness of the embedding layer on the surface of the magnetic nanoparticle [14]. In this method, the early formation of a gel provides a high chemical homogeneity and reduces the atomic diffusion during the thermal treatment [15].

Sol-gel chemistry is defined as the preparation of inorganic polymers or ceramics from solution via a transformation from liquid precursors to sol and finally to a network structure called a ‘gel’ [16]. Normally, a sol is formed through hydrolysis and condensation of metal alkoxide precursors. However, Kakihana in 1996 [17] present a more precise classification of different gel types, used for the preparation of inorganic solids. The five key types of gel featuring in ‘sol-gel’ chemistry are outlined in table 2.1 [18].

Table 2.1) Types of gels that are relevant in sol-gel synthesis of materials [18].

Type of Gel	Bonding	Source	Gel Schematic
Colloidal	Particles connected by Van der Waals or Hydrogen bonding	Metal oxides or hydroxide sols	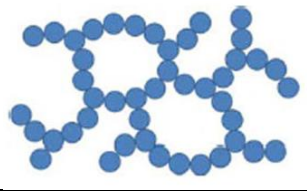
Metal-oxane polymer	Inorganic polymers interconnected via covalent or intermolecular bonding	Hydrolysis and condensation of metal oxides, e.g., SiO_2 from tetraethyl orthosilicate	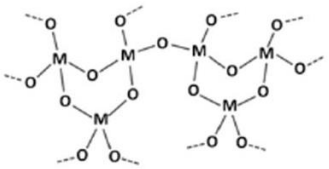
Metal complex	Weakly interconnected complexes	Concentrated metal complex solution, e.g. aqueous metal citrate or ethanoic metal urea often form resins or glassy solids rather than gels	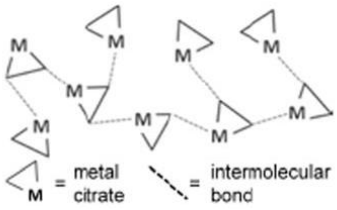
Polymer complex I In situ polymerizable complex (Pechini route)	Organic polymers interconnected by covalent and coordinate bonding	Polyesterification between polyhydroxy alcohol (e.g., ethylene glycol) and carboxylic acid with metal complex (e.g., metal citrate)	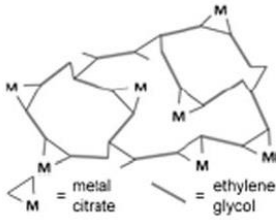
Polymer complex II Coordinating and crosslinking polymers	Organic polymers interconnected by intermolecular and coordinate bonding	Coordinating polymers and metal salt solution	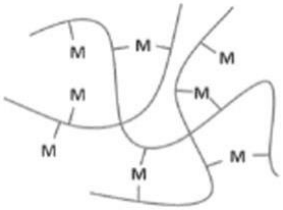

After precursor preparation, the sol-gel process can be summarized in the following key steps:
(i) Synthesis of the colloidal solution (sol) from hydroxylation of the alkoxides within the precursors.
(ii) A polycondensation process follows the hydroxylation reaction leading to form metal–oxo–metal or metal–hydroxy–metal bonds.
(iii) Gel aging step, where condensation continues within the gel network, increasing the cohesion, strength, and stiffness of the solid network. Often the network will shrink resulting in the expulsion of solvent (linear shrink can be up to 50%).
(iv) Drying the gel either to form a dense xerogel via the collapse of the porous network or an aerogel for example through supercritical drying.
(v) Densification of the gel through heat-treatments at temperatures higher than 800 ºC (if required).

2.2.1.a) Metallic alkoxide route

Although Sol-gel chemistry initially formed with the hydrolysis and condensation of metal alkoxides, it can also happen between hydrated metal species including transition group metals (e.g., Fe) or early p-block elements (e.g., Al, Si) [18, 19, 20]. However, there are many other examples of elemental alkoxides [19]. The main factors which impact the suitability of the various alkoxides and outcome the reactions for sol-gel chemistry are including [18]:
i) how electronegativity differences between the oxygen and metal affect the ionic character of the M–O bond;
ii) the electron donating/withdrawing ability of the alkyl ($R=C_2H_5$)/ aryl (C_6H_5) chain on the stability of the alkoxy groups;
iii) volatility and viscosity.
The knowledge of the hydrolysis and condensation reactions is the crucial key to understand the sol-gel chemistry of alkoxides. These reactions are strongly affected by process parameters such as the nature of the R-group (e.g., inductive effects), the ratio of water to alkoxide and the presence and concentration of catalysts [18]. The sol-gel chemistry of silica is typically driven by either acid or base catalysts as the neutral reaction is prolonged. The structure of the resulting gel significantly depends on the catalyst as well as the relative rates of the hydrolysis

and condensation reactions. Hydrolysis occurs when an alkoxy group replaces with a hydroxyl having a pentacoordinate transition state in both the acid (Fig. 2.1) and base (Fig. 2.2) catalyzed systems [18].

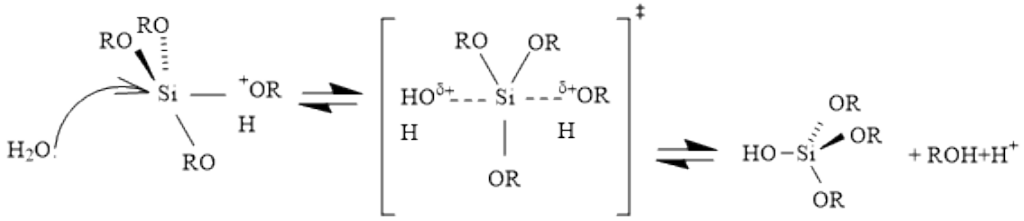

Fig. 2.1) Acid-catalyzed hydrolysis of silicon alkoxides [18].

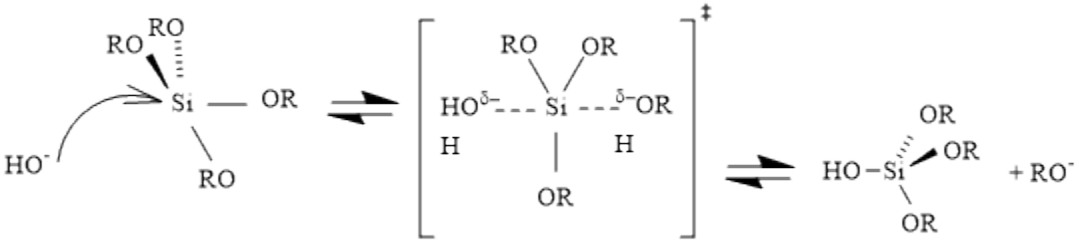

Fig. 2.2) Base-catalyzed hydrolysis of silicon alkoxides [18].

Depending on the Si/H_2O ratio, more than one alkoxy group may be hydrolyzed (eq (2.1)).

$$Si(OR)_4 + nH_2O \longrightarrow Si(OR)_{4-n}(OH)_n + nROH \qquad (2.1)$$

The stability of the transition state resulted from the relative electron withdrawing or donating power of –OH versus –OR groups, will determine the rate of each hydrolysis step. As a result, continuous hydrolysis steps get progressively slower and faster under acidic and basic conditions, respectively [18].

Condensation is in the same manner; being catalyzed by either acid (Fig. 2.3) or base (Fig. 2.4) and resulting in the formation of siloxane bonds (or metaloxane bonds for other metals). The condensation progression is related to the degree of hydrolysis. This take place when a silanol group is needed on at least one silicon center. In basic conditions where the product $(OH)_3Si–O–Si(OH)_3$ consists of six sites for subsequent condensation steps, hydrolysis is completed before the first condensation step occurs. So hydrolysis gets progressively faster. While in

acidic conditions, where the first hydrolysis step is the fastest, condensation begins before hydrolysis is complete. In this case, condensation occurs in the terminal silanols, and network like gel is formed [18].

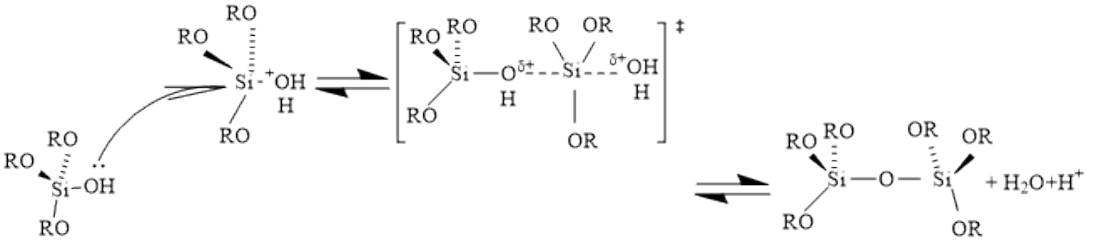

Fig. 2.3) Acid-catalyzed condensation of silicon alkoxides [18].

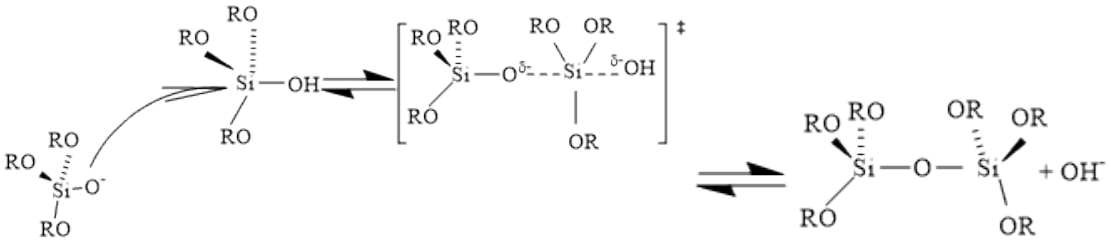

Fig. 2.4) Base-catalyzed condensation of silicon alkoxides [18].

The presence of solvents and the water-alkoxide ratio are significantly effective to tune the hydrolysis rate [18]. Similar reactions and pathways can be followed to describe other metal alkoxides reactions in sol-gel chemistry. However, most other metal alkoxides are based on elements with substantially lower electronegativity than silicon, the most important being the transition metals [19].

2.2.1.b) Pechini route

Pechini's route has based in the fact that a hydrocarboxylic acid such as citric, tartaric and glycolic acids can form polybasic acid chelates with different metal cations in aqueous solutions [21]. When compared with the majority of the acids, citric acid is more widely used in Pechini's processing because of its high stability [18]. The transesterification between citrate and ethylene glycol is the key reaction used in Pechini synthesis [22]. The typical metal complexes can stably link with citric ligands because of the strong coordination of the citric

ion to the metal cation involving two carboxyl groups and one hydroxyl group, which lead to form a polymeric resin, as shown in Fig. 2.5 [18]. In such rigid organic polymer networks, metal complexes are immobilized leading to reduce the segregation of particular metal ions. So the compositional homogeneity achieves [18]. Ultimately, a pure phase multicomponent metal oxides are produced, followed by calcination of the polymeric resin at a moderate temperature (500-1000 °C) [21].

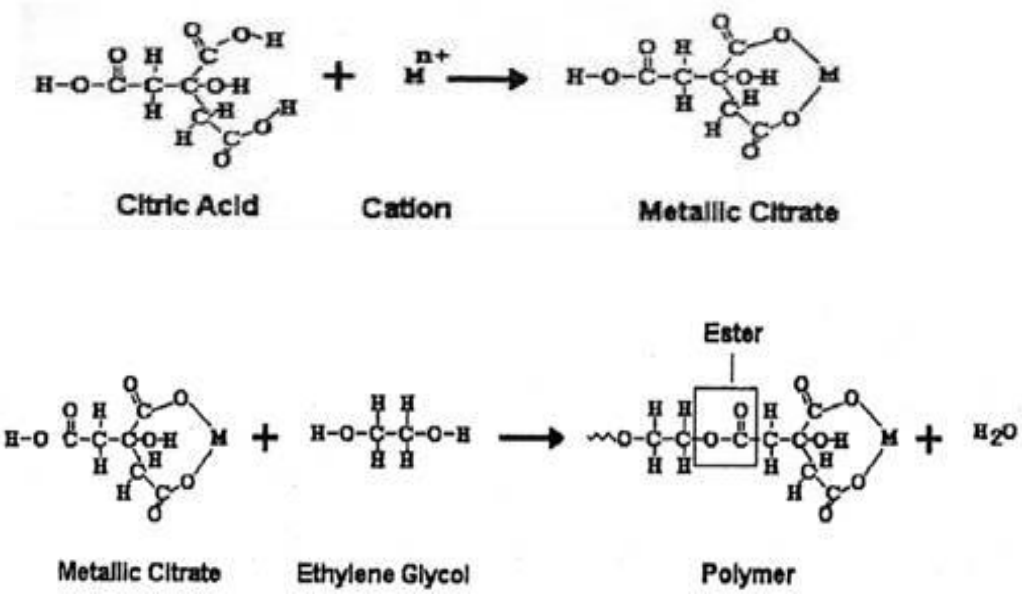

Fig. 2.5) Schematic illustration showing the solution chemistry and reactions involved in the Pechini process [18].

2.2.2) Auto-combustion method

In recent years, auto-combustion synthesis method has attracted considerable attention in fabricating homogeneous, un-agglomerated multi-component ferrites fine crystallines [23-25]. The auto combustion is associated to an exothermic and self-sustaining thermally-induced anionic redox reaction of xerogel, which is obtained from an aqueous solution containing desired metal salts, usually nitrates, (oxidant) and organic complexant (reductant or organic fuel) [26]. The nitrate salts are favorable precursors because they act like a water-soluble low temperature NO^{3-} oxidant source for synthesis [27]. The auto-combustion method has several interesting advantages including [27-29]:

i) highly chemical homogeneity;

ii) high product purity and crystallinity;

iii) fine particle size and narrow particle size distribution;

iv) controllable stoichiometry;

v) facile introduction of the dopants into the final product;

vi) low-cost and rapid process;

vii) low external energy consumption (process initiates at low temperatures) and multiple steps are not involved.

The macroscopic result of the auto-combustion reaction of one of our reactant mixtures is shown in Fig. 2.6, as an example.

The particle size, morphology and physical characteristics of the final product obtained by auto-combustion synthesis are depending on several parameters such as the type of organic fuel, complexant to oxidant ratio (Oxygen balance), the pH and ambient atmosphere [26]. For example, in the high value of pH (> 6) in the precursor solution resulted in oxide products with a more open and porous network structure resulting in 'sponge-like' products due to the large volume of gases evolved during the reaction of nitrate with the organic component. While for pH= 2 and 3, gels exhibited dense microstructures having only a few pores in the gel structure [18, 26].

During self-ignition, the xerogel transforms directly to the crystalline phase due to the high thermal energy generated by the exothermic reaction. The flame temperature during combustion is in the range of 600 °C to 1350 °C [30].

Fig. 2.6) Photograph of powder $15MnFe_2O_4$-$85SiO_2$ obtained by auto-combustion.

2.2.3) Laser Floating Zone (LFZ) method

The Laser Floating Zone (LFZ) method shows good prospects for studying the crystallization mechanisms in a silica-based glasses with additions of redox-active cations, by providing flexibility in tuning their oxidation state and crystalline/amorphous conditions. Moreover, being a unique technique to obtain high-quality single crystals, eutectic structures, and highly oriented polycrystalline materials, LFZ method allows us to deeply study phase transformation kinetics, diffusion phenomena and how to control the crystallization/amorphization degree in the sample's crystallization path [31]. Moreover, as a crucible-free, LFZ process allows the production of high purity composite fibers, avoiding mechanical stress and contamination during the solidification process due to the crucible material [32].

The LFZ technique is similar to the floating-zone-like method where the heating element is substituted by a focused laser ring to generate the small molten zone instead of being completely melted inside of a crucible [33]. The pulling process starts with basically four steps inside the growth chamber, as follows [34]:

i) The alignment of the seed and the pedestal (feed-rod) mechanically, both centralized in the optical axis of the laser beam.

ii) Creation of a small molten zone on top of the pedestal, by turning on the laser and slowly increasing the laser power.

iii) The seed is introduced into the liquid, and a molten zone is formed.

iv) The motors start the fiber pulling and rotation.

All these four steps are indicated in Fig. 2.7 [34].

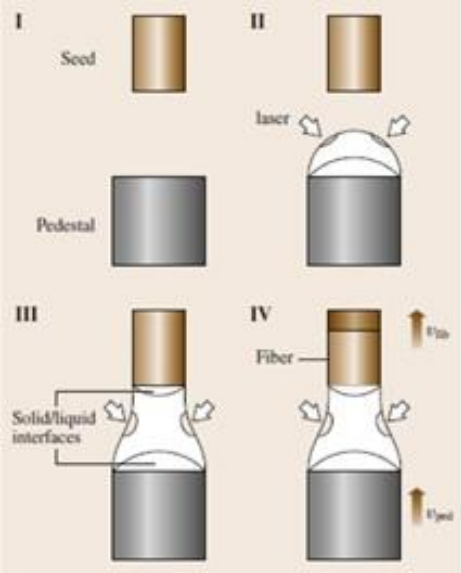

Fig. 2.7) Schematic drawing of the four steps performed in the LFZ technique: (I) mechanical alignment of the seed and the pedestal and (II) creation of a small molten zone on the top of the pedestal. (III) The seed is then introduced in the liquid phase, and there is the creation of a molten zone. (IV) The motors started, and the fiber-pulling process begins [34].

In the LFZ technique, there are several parameters necessary to grow crystals which should be taken into account in the pulling process. These aspects are going to be discussed in the following sub-sections.

2.2.3.a) Conservation of Mass

Based on the conversation of mass relation, we can simply correlate the pedestal and fiber cross-section areas with their respective pulling rates, yielding [35]

$$\rho_{fib} r_{fib}^{2} \upsilon_{fib} = \rho_{ped} r_{ped}^{2} \upsilon_{ped} \quad \text{if} \quad \rho_{fib} = \rho_{ped} \Rightarrow r_{fib} = r_{ped} \sqrt{\frac{\upsilon_{ped}}{\upsilon_{fib}}} \tag{2.2}$$

where ρ_{fib}, r_{ib}, υ_{fib}, and ρ_{ped}, r_{ped}, υ_{ped} are the density, fiber radius, and pulling rates of the fiber and pedestal, respectively.

In LFZ growth, during the growth process, the laser power and pulling rates can be modified. It is obvious that the fiber diameter will be constant if all the physical parameters remain unchanged. However, if small imperfections in the pedestals occur, it is essential to change one of the growth parameters to keep the fiber diameter constant.

2.2.3.b) Heat Transfer Balance

A schematic representation of the most important heat fluxes during fiber pulling is illustrated in Fig. 2.8. The energy of laser beam to keep the molten zone active is consumed in four different ways [34]:

i) main energy is conducted through the fiber and pedestal;

ii) lost to the growth chamber by irradiation, because of the black-body emission;

iii) convected to the fluid inside, when present;

iv) the latent heat of solidification and melting is generated at the fiber-liquid and pedestal–melt interfaces.

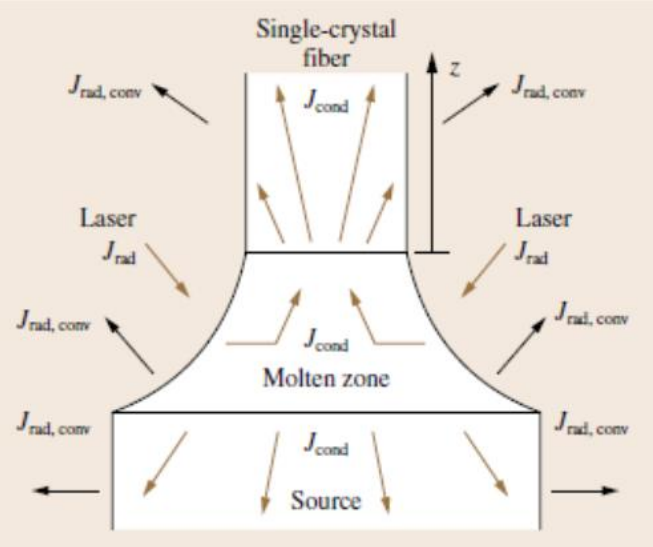

Fig. 2.8) Schematic drawing of the heat fluxes acting during the fiber growth process [34].

In LFZ technique thermal gradients at the growing interface are much higher than any other crystal growth method (ranging from 10^3–10^4 °C/cm) which assists to grow at the high pulling rate. The high axial temperature gradient also can inhibit constitutional supercooling [34]. The condition for constitutional supercooling can be written as [34]:

$$\frac{G}{\upsilon} \leq \frac{mC_S}{D_1}\left(\frac{1-k_0}{k_0}\right) \tag{2.3}$$

where G is the absolute value of the temperature gradient at the solid-liquid interface, υ is the pulling rate, m is the absolute value of the liquidus slope, C_S is the concentration in the solid phase, D_l is the diffusion coefficient of the solute in the liquid and k_0 is the equilibrium distribution coefficient. A sharper temperature gradient can lead to a concave solid/liquid interface towards the melt, while a reduction in the temperature gradient can give a convex interface [36].

Unfavorably, the same axial temperature can induce a high level of stress in the grown fiber and consequently various crystallographic defects are formed [34, 37]. According to Prokofiev et al. [37], the dislocation density (N_d) regarding the axial temperature gradient can be expressed as:

$$N_d = \frac{\alpha}{b}\frac{dT}{dz} - \frac{2\varepsilon_b}{ba} \tag{2.4}$$

where b is the Burger's vector, α linear expansion coefficient, ε_b breaking strain and dT/dz is the axial temperature gradient at the crystallization interface.

2.2.3.c) Congruent Melting Fibers: search for stoichiometry

Congruently melting materials are the easiest type of compounds to pull successfully and form a fiber. However, nonstoichiometric melting compositions can give rise to unwanted effects such as thermodynamic instabilities, precipitates, intrinsic impurities, and deviations of the distribution coefficient [35]. Besides the composition variation of metal elements along the fiber, those compounds also may suffer from oxygen deficiency. The congruency originates from the defect structure, thereby, the oxygen vacancy also plays a vital role in the growth of highly homogeneous fibers. In other words, metal oxides having different oxygen stoichiometry will possess different congruent compositions [38].

2.2.3.d) Incongruent Melting Fibers

Another important feature of the LFZ technique is the possibility of growing incongruently melting and evaporating materials. The growth of incongruently melting bulk oxide is usually achieved by high-temperature solution growth, which is a slow and complicated technique. The source material in this technique must be rich in one or more elements to compensate for the incongruent melting [39].

Controlling conveniently the pulling and feeding ratio, it is possible to regulate the melt evaporation that can lead, in the worst cases, to incongruent evaporation of some elements of the "feed". This again is only possible because of the high-temperature gradients at the growth interface, allowing the growth velocities to be higher than in the conventional floating zone technique, and that a small amount of material stays at a high temperature for a short period, minimizing the metal oxide evaporation [40].

2.3) Iron oxides based core materials

Usually, iron oxide can be found in the form of hematite (α-Fe_2O_3), maghemite (γ-Fe_2O_3) and magnetite (Fe_3O_4). They have various technological advantages over the metallic form of Fe including high chemical stability, easy preparation, less oxidation, reactive surface, non-toxicity, and multi-functionality that is why they are interesting for biomedical purposes and also microwave absorbers [41-44]. Among these three well-known iron oxides, due to better magnetic features including high saturation magnetization and high anisotropy constant, magnetite, with cubic spinel ferrite structure, has gained greater attention in biomedical fields, such as targeted drug delivery, therapeutic agents, biomolecules separation [45-47]. Another example from cubic spinel ferrites is $MnFe_2O_4$ which has shown much attraction to investigate as a very promising candidate for both electromagnetic applications and biomedicine employment [48]. Owing to a great biocompatibility [49] and a strong T2 phase contrast for magnetic resonance imaging (MRI) [50], $MnFe_2O_4$ nanoparticles favors for the multifunctional biomedical applications like MRI, hyperthermia and targeted drug delivery [51, 52]. Also, because of excellent electrical and dielectric characteristics of $MnFe_2O_4$ nanoparticles, there are many potential benefits to utilize them as new types of microwave absorptive materials [53]. The brief description of the characteristics which are essential for us is given in the next subsections.

2.3.1) Hematite (α-Fe_2O_3)

Being isostructural with corundum, hematite has a hexagonal unit cell (a= 5.034 nm, c=1.375 nm) [54]. The structure of hematite is formed by a hexagonal closed packed (hcp) oxygen array with Fe^{3+} in two-thirds of octahedral sites. Each octahedron, $Fe(O)_6$, shares edges with three neighboring octahedral in the same plane and one face with an octahedron in an adjacent plane. This edge sharing distorts cation sublattice. The face sharing Fe atoms in the octahedral are repelled along the direction normal to the [001]. Hence the cations shift towards to the unshared faces. Consequently, the O-O distances along the shared face of an octahedron are shorter (0.269 nm) than the distances along the shared edge (0.3035 nm) and the octahedron is trigonally distorted as depicted in Fig. 2.9 [54-57]. The O and Fe arrangement around a shared face impacts the magnetic properties of the oxide [55].

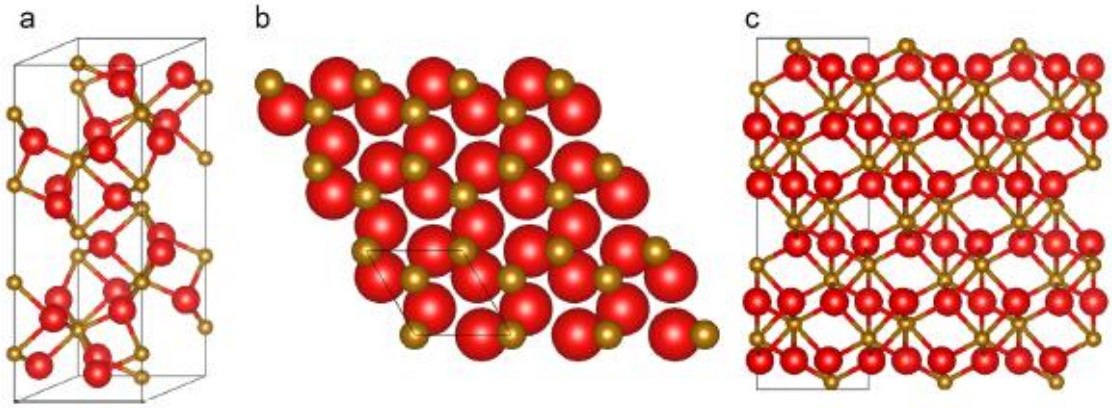

Fig. 2.9) a) A ball and stick model of α-Fe_2O_3 containing 6 hexagonal unit cells. O^{2-} anions are the red balls, Fe_{oct}^{3+} cations are in brown; b) The demonstration of the distribution of Fe ions over a given oxygen layer and the hexagonal arrangement of octahedral (drawn in space filling style with unit cell indicated); c) Side view of the α-Fe_2O_3 structure that shows how the Fe_{oct}^{3+} cations are not coplanar [54].

Hematite at room temperature is weakly ferromagnetic and at 260 K (the Morin temperature, T_M) it undergoes to a phase transition and becomes an antiferromagnetic material [58]. Superparamagnetic state for nano-sized hematite was observed when the average size of crystalline is below 20 nm [59]. Hematite is paramagnetic above T_C =956 K. (T_C, the Currie temperature where a ferri/ferromagnetic material is converted to a paramagnetic material) [54-58].

The Morin transition can be explained in the following way: in basal plane of hematite, perpendicular to the hexagonal c-axis, there are two magnetic sublattices with the equal moment. Above the Morin transition temperature (T_M), the spins are not perfectly anti-parallel, and a slight canting (with canting angle <0.1°) leads to a weak, "parasitic" ferromagnetism. At $T = T_M$, magnetocrystalline anisotropy changes sign, the easy axis of magnetization shifts, and the spins rotate from the basal plane into alignment with the c-axis at $T < T_M$. In this state, the sublattice spins are perfectly anti-parallel, and hematite is antiferromagnetic [60, 61]

Several studies showed the dependence of hematite magnetic behavior on crystallinity, particle size, the preparation procedure, and cation substitution [59-61]. Both T_M and T_C values reduce as the average nanocrystal size decreases. Moreover, the T_M is suppressed by poor crystallinity and also cation alteration.

A compound is defined as a semiconductor when the separation between the valence band of orbitals and the conduction band within the material is less than 5 eV. It is proposed that electrical conductivity in hematite is due to an O^{2-} -Fe^{3+} charge transfer transition with an energy of 2.0 eV. So the semiconducting condition is met for hematite. Pure Stoichiometric hematite is a poor n-type semiconductor with very low hole mobility at room temperature (10^{-2} $cm^2V^{-1}s^{-1}$), a very high electrical resistivity, sluggish surface kinetics, and rapid electron-hole recombination rate [55, 62]. However, the improvement in conductivity can be accomplished by tuning various factors such as the type of preparation method, the size of crystalline, the heat treatment temperature and ambient, the addition of dopant and so on [63].

2.3.2) Spinel ferrites (Fe_3O_4 and $MnFe_2O_4$)

The spinel ferrite structure with a general formula of MFe_2O_4, where M refers to a divalent metal ion with an ionic radius ranged from 0.06 to 0.1 nm, can be described as a cubic close-packed arrangement of oxygen atoms. M can be Zn^{2+}, Mg^{2+}, Mn^{2+}, Fe^{2+}, Co^{2+}, Ni^{2+}, Cu^{2+}, ($0.5Li^{+}$+ 0.5 Fe^{3+}), etc. and the ion Fe^{3+} is at two different crystallographic sites [64]. Here our attentions were attracted to two examples of this group: Fe_3O_4 and $MnFe_2O_4$. The spinel structure contains two cation sites for metal cation occupancy. There are 8 A-sites in which the metal cations are tetrahedrally coordinated with oxygen and 16 B-sites which possess octahedral coordination. According to the distribution of cations (Fig. 2.10), there are the following types of ferrospinels:

i) Normal spinel structure, where all M^{2+} ions occupy A-sites; the structural formula of such ferrites is $M^{2+}[Fe_2^{3+}]O_4^{2-}$. This type of structure is represented in zinc ferrites $Zn^{2+}[Fe^{2+}Fe^{3+}]O_4^{2-}$.

ii) Inversed spinel structure, where all M^{2+} are in B-positions and Fe^{3+} ions are equally distributed between A and B-sites: the structural formula of these ferrites are $Fe^{3+}[M^{2+}Fe^{3+}]O_4^{2-}$. Magnetite Fe_3O_4, ferrites $NiFe_2O_4$ and $CoFe_2O_4$ have inversed spinel structure.

iii) Mixed spinel structure, when cations M^{2+} and Fe^{3+} occupy both A and B-positions; the structural formula of this ferrite is $M_{1-\delta}^{2+}Fe_{\delta}^{3+}[M_{\delta}^{2+}Fe_{2-\delta}^{3+}]O_4^{2-}$, where δ is the degree of

inversion. This kind of distribution takes place in $MnFe_2O_4$ with an inversion degree of δ=0.2. Thus, its structural formula is $Mn_{0.8}^{2+}Fe_{0.2}^{3+}[Mn_{0.2}^{2+}Fe_{1.8}^{3+}]O_4^{2-}$.

Another example from this category is Mn–Zn ferrites (Zn^{2+} prefers to occupy A-sites) $Zn_x^{2+}Mn_y^{2+}Fe_{1-x-y}^{3+}[Mn_{1-x-y}^{2+}Fe_{1+x+y}^{3+}]O_4^{2-}$, where $\delta = 1 - x - y$ [56, 64].

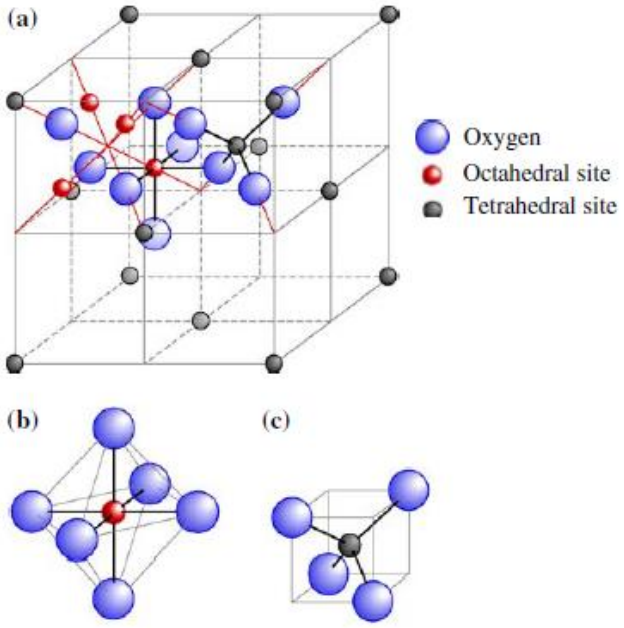

Fig. 2.10) a) Spinel unit cell structure; b) octahedral interstice (B site: 32 atoms per unit cell, 16 occupied); c) tetrahedral interstice (A site: 64 atoms per unit cell, eight occupied) [56].

The magnetic properties of the ferrimagnetic spinel depend on how the ions on the tetrahedral (A) and octahedral (B) sites interact with each other [65]. Therefore, the ion distribution on these sites is of vital importance. Magnetite is ferromagnetic at room temperature with a Curie temperature T_C of 850 K. Below T_C, the spins on the A and B sites are antiparallel, and the magnitudes of the two types of spins are unequal causing ferrimagnetism. The main type of interaction is antiferromagnetic coupling via the 127° Fe_A-O-Fe_B linkage, and this is stronger than coupling than one on the octahedral sites. The electrons are thermally delocalized over the Fe^{2+} and Fe^{3+} on the octahedral sites. Below, 120 K, the Verwey temperature, T_V, a metal-insulator transition occurs explained by the onset of charge localization at the respective individual iron ions. This peculiar electronic transition occurs at or close to a first-order structural phase transition from a cubic to a monoclinic structure [57]. For magnetite each unit cell consistants of 8 formula unit.

For manganese ferrite, considering the magnetic moments of the Mn^{2+} and Fe^{3+} are both 5 μ_B and each unit cell contains 8 formula units, a magnetic moment of 8×5 μ_B per unit cell is accepted [54, 58, 66, 67]. Although, it was experimentally found the $MnFe_2O_4$ has an 8×4.6 μ_B magnetic moment per unit cell arising from the simultaneous occurrence of Mn^{3+} and Fe^{2+} both with 5 μ_B [66, 67]. If we suppose the crystal field stabilization energy is the only factor to determine the site occupation, the ions Mn^{2+} and Fe^{3+} have no preference for either octahedral or tetrahedral site.

Koop has shown that the conduction process in magnetite ferrite is attributed to the electron interchange between the Fe^{2+} and Fe^{3+} ions located close together on the octahedral sites [55]. In the other spinel ferrites, for example, $MnFe_2O_4$, the conduction process is mainly governed by choice of the cations along with Fe^{2+}, Fe^{3+} ions and their distribution between tetrahedral (A) and octahedral (B) sites of the spinel lattice. So the presence of Mn favors the following reaction [66, 67]: $Mn^{3+}+Fe^{2+} \leftrightarrow Mn^{2+}+Fe^{3+}$.

2.3.3) Maghemite

Maghemite is a cubic spinel with a=0.834 nm where all or most Fe is in the trivalent state. Cation vacancies compensate for the oxidation of Fe^{2+}. The unit cell formed by 32 O^{2-} ions, 21 1/3 Fe^{3+} ions, and 21/3 vacancies. Tetrahedral sites are occupied by eight cations, and the remaining cations are randomly distributed over the octahedral sites. Maghemite can be obtained through oxidation of magnetite [68]. A schematic representation of the chemical steps in this transformation is given which explains the formation of vacancies in octahedral positions (□) as a result of the oxidation of the Fe^{2+} to Fe^{3+} ($3Fe^{2+}$ $2Fe^{3+}+□$.) [54, 55, 57]:

$$Fe^{3+}\,[Fe^{2+}\,Fe^{3+}]\,O_4\ (\text{magnetite}) \xrightarrow{\times 8} {Fe^{3+}}_8\,[{Fe^{2+}}_8\,{Fe^{3+}}_8]\,O_{32}\ (\text{unit cell}) \xrightarrow{\text{oxidation}} {Fe^{3+}}_8\,[{Fe^{3+}}_{5.3}\square_{2.7}\,{Fe^{3+}}_8]\,O_{32}\ (\text{maghemite}) \xrightarrow{\times 3} {Fe^{3+}}_{24}\,[{Fe^{3+}}_{16}\square_8\,{Fe^{3+}}_{24}]\,O_{96}\ (\text{unit cell}) \quad (2.5)$$

Similar to magnetite is ferrimagnetic at room temperature with a net magnetic moment of 2.5 μ_B per formula unit. The Curie temperature of 985 K is estimated for maghemite. However it is difficult to measure T_C of maghemite because maghemite transforms to hematite at

temperatures above 800 K. In maghemite, the atomic moments within the A and B sublattices are antiparallel giving rise a ferromagnetism nature. Maghemite is a semiconductor [55, 57].

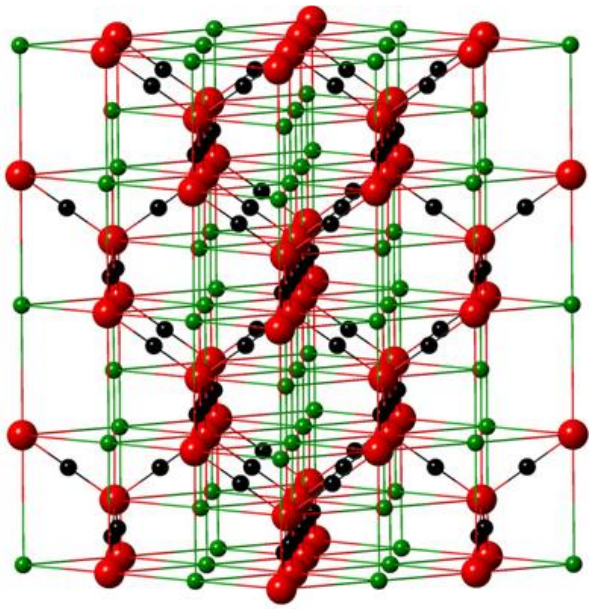

Fig. 2.11) Crystal structure of maghemite. The black ball is a vacancy, the green ball is $Fe^{3+,}$ and the red ball is O^{2-} [68].

2.3.4) Wüstite, $Fe_{1-x}O$

Wüstite, $Fe_{1-x}O$, (with l-x ranging from 0.83 to 0.95) takes the cubic NaCl structure. The cubic unit cell contains four formula units and, depending on the vacancy content, a ranges from 0.428-0.431 nm [55]. Wüstite has a defective structure. In this structure, the defects, the Fe^{3+} cations placed on tetrahedral sites, are linked to four Fe_{oct} vacancies. The unit will be agglomerated into clusters of four Fe_{tet} interstitials linked to 13 Fe_{oct} vacancies [54]. This phase disproportionate to Fe metal and Fe_3O_4 were cooled slowly to temperatures lower than 567 ^oC. If $Fe_{1-x}O$ is rapidly quenched from the equilibrium region, the nonstoichiometric form can be obtained as a metastable phase at room temperature [55]. $Fe_{1-x}O$ exhibits antiferromagnetic behavior below the Néel temperature of 200 K, with the Fe^{2+} magnetic moments aligned parallel to the close-packed (111) planes, but in opposite directions from one plane to the next. The Fe defect clusters discussed above are thought to affect the magnetic properties [55, 58]. In resemblance to above-mentioned iron oxide-based materials, Wüstite is a semiconducting substance [55].

The main structural, physical, electrical and magnetic properties of the iron oxide-based structures which are essential (and or unlikely detected) in this research work summarized in tables 2.2 and 2.3 (part 1 and 2) (the data collected from the literatures [54-77]).

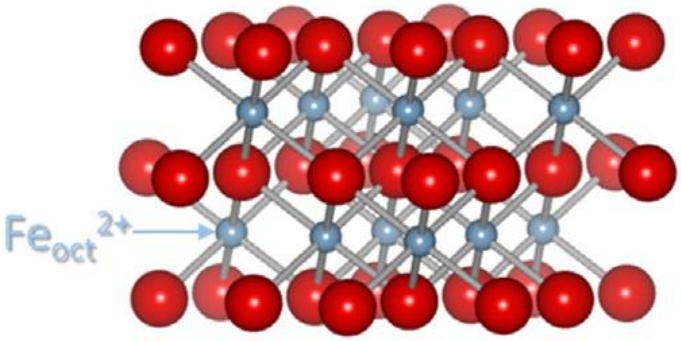

Fig. 2.12) Wüstite structure based on a close-packed O^{2-} anion lattice with metal cations in octahedral and tetrahedral coordinated interstitial sites [54].

Table 2. 2-part I) Physical and crystallographic properties of the iron oxide-based materials [54-59].

Substance Name	**Magnetite**	**Manganese ferrite**	**Hematite**
Formula	Fe_3O_4	$MnFe_2O_4$	α-Fe_2O_3
Cation	Fe^{3+}, Fe^{2+}	$Mn^{3,2+}$, $F^{3,2+}$	Fe^{3+}
Structure type	Inverse spinel	Mixed spinel	Corundum
Crystallographic system	Cubic	Cubic	Hexagonal
Space group	Fd3m	Fd3m	$P4_332$
Anion Stacking	FCC (111)	FCC (111)	HCP (001)
Formula units/unit cell	8	8	6
Lattice parameter (Å)	a=8.396	a=8.513	a=5.0436 c=13.7489
Color	Black	Black-brown	Red
Density ($g.cm^{-3}$)	5.18	4.75	5.26
Melting point (ºC)	1583–1597	> 1300	1350
Boiling point (ºC)	2623	-	-

Table 2.2 - part II) Physical and crystallographic properties of the iron oxide-based materials [54-59].

Substance Name	**Maghemite**	**Wüstite**	**Fayalite**
Formula	γ-Fe_2O_3	$Fe_{1-x}O$	Fe_2SiO_4
Cation	Fe^{3+}	Fe^{2+}	Fe^{2+}
Structure type	Defect spinel	Defect NaCl	Dipyramidal
Crystallographic system	Cubic/Tetragonal	Cubic	Orthorhombic
Space group	$R\bar{3}c$	Fm3m	Pbnm
Anion Stacking	FCC (111)	FCC (111)	FCC (100)
Formula units/unit cell	8	4	4
Lattice parameter (Å)	a=8.3474	a=4.302–4.275	a = 4.79, b = 10.39, c = 6.06
Color	Reddish brown	Black	Yellow-brown
Density ($g.cm^{-3}$)	4.87	5.9	4.66
Melting point (ºC)	-	1377	1200
Boiling point (ºC)	-	2512	-

Table 2. 3- part 1) Magnetic and electrical characteristics of the iron oxide-based bulk materials (*Antiferromagnetically ordered below RT; † Measured at a frequency > 1 GHz; •• nanoscale size) [54-77].

Substance Name	**Magnetite**	**Manganese ferrite**	**Hematite**
Formula	Fe_3O_4	$MnFe_2O_4$	α-Fe_2O_3
Magnetic Order	Ferrimagnetic	Ferrimagnetic	Canted antiferromagnetic (weak ferromagnetic)
Magnetic transition	T_V=120 K, T_C=860 K	T_C=575 K	T_M= 260 K, T_N=960 K
Saturation magnetization (Am^2/kg) @ 300 K	90-92	77	0.4
magnetic moment per unit cell (m(μ_B))	4	4.6	4.9
Anisotropy constant (K_{eff}) (Jm^{-3})	13×10^3	3×10^3	9×10^3
Conductivity (1/Ωm) @ 300 K	10^{-1}	10^5 (~5†)	$>10^{-3}$
Dielectric constant @ 300 K	100	57.2†	20.6
Dielectric tan(δ) @ 300 K	2	10•• (0.42†)	1.5••
Permeability	5	2.31†	1.05

Table 2.3 - part 2) Magnetic and electrical characteristics of the iron oxide-based bulk materials. (*Antiferromagnetically ordered below RT; † Measured at a frequency > 1 GHz; •• nanoscale size) [54-77].

Substance Name	**Maghemite**	**Wüstite**	**Fayalite**
Formula	γ-Fe_2O_3	$Fe_{1-x}O$	Fe_2SiO_4
Magnetic Order	Ferrimagnetic	Antiferromagnetic*	Antiferromagnetic*
Magnetic transition	T_C=985 K	T_N=200 K	T_N=65 K
Saturation magnetization (Am^2/kg) @ 300 K	~80	-	-
magnetic moment per unit cell ($m(\mu_B)$) @ 0 K	3.3	3.3	4.4
Anisotropy constant (k_{eff}) (Jm^{-3})	5×10^3	-	-
Conductivity (1/Ωm) @ 300 K	~1	$\sim10^{-1}$	$<10^{-8}$
Dielectric constant @ 300 K	~120••	~100	9‡
Dielectric tan(δ) @ 300 K	2••	-	0.0006
Permeability	-	-	-

2.4) Coating materials

Coating materials can be mainly divided into 3 groups: 1) polymers; 2) metal oxides; and 3) inorganic metallic materials, carbon nanotubes and graphene. Among them, we describe briefly silica and polymeric coating materials. However, in this thesis, we could only concentrate on the silica coating as will be seen in the next chapters. Silica coating is a popular choice to make MNPs stable and multifunctional. By simply hydrolyzing silica precursors (e.g., tetraethyl orthosilicate (TEOS)) under the basic solution, a uniform and thickness-controllable silica shell can be obtained. Silica formed through this approach (Sol-gel approach) is usually amorphous and has strong affinity to MNPs [4]. Moreover, previous studies have demonstrated that the LFZ method is a powerful processing tool for studying crystallization and vitrification mechanisms in silica-based glasses and tuning the states of the redox-active cations [78]. Polymeric coating materials are categorized into two groups: synthetic and natural. Synthetic polymeric systems are based on poly(ethylene-co-vinyl acetate) (PEVA), poly(vinyl pyrrolidone) (PVP), poly(lactic-co-glycolic acid) (PLGA), poly(ethylene glycol) (PEG), and poly(vinyl alcohol) (PVA). Gelatin dextran, chitosan, and

pullulan are in natural polymer systems group [79]. Several key elements like: the nature of the chemical structure of the polymer, the length or molecular weight of the polymer, the chemical bonding type (electrostatic or covalent bonding), the conformation of the polymer, and the degree of particle surface coverage and the molecular weight and geometric orientation of the polymer on the surface of the particles should be taken into account regarding effective polymeric coatings and the performance of magnetic nano core/shell structures [80-84]. Based on these factors, the polymers can be classified in [44, 80, 85]:

i) End-grafted polymers;

ii) Surface adsorption polymers;

iii) Phospholipids;

iv) Copolymers.

In the following table, some used coating materials for biomedical applications and microwave devices are explained in detail (Table 2.4).

Table 2.4) Mostly used coating materials for biomedical application and microwave absorbing materials.

Coating Materials	Biomedical and Electromagnetic characteristics
SiO_2	Easily synthesis in large scale, constant crystalline structure, reduce the specific surface area, high surface energy, and dipolar attraction, effective on the interparticle interactions and magnetic anisotropy of the particles, Bioactivity, Biocompatibility and Non-Biodegradable [86-90].
CetylTrimethylAmmonium Bromide (CTAB)	Non-toxic, Flexibility, ductility and processibility, excellent dielectric properties [91, 92].
PolyAniline (PAni)	Controllable dielectric loss, to ease and inexpensive preparation method, low specific mass, good thermal and chemical stability, unique doping mechanism, ease of protonic acid doping and high conductivity at microwave frequencies [93, 94].
PVA	Hydrophlic and biocompatible polymer to obtain size controllable, nonagglomerated and monodisperse magnetic particles [95].

2.5) Exigencies and challenges

This section has the purpose of highlight the recent scientific and technological findings on synthesis, electrical and magnetic characteristics of ferrite nanocomposites. To pursue the demands associated with the applications, various physical and chemical features of MNPs (with or without surface modification) should also be considered.

2.5.1) Oxidation, corrosion and chemical stability

Iron oxides are less sensitive to oxidation than the metallic iron. However, due to the existence of vulnerable Fe^{2+} in Fe_3O_4, under high-temperature heat-treatment, it would be oxidized and converted to α-Fe_2O_3 [96]. Prevention from oxidation and corrosion requires controllable calcination temperature [96], non-oxidative atmosphere [97] and protective coatings [98]. Edström investigated the oxidation of magnetite pellets in both air and oxygen at a single temperature of 1230 °C. After reaction, the material possesses both oxidized and nonreacted sections [96]. A transformation from hematite to magnetite can be procedure by a thermal treatment under atmosphere consisting of 20% H_2 and 80% N_2 at 375 ^oC [97]. According to Hong et al. Fe_3O_4/SiO_2 core-shell MNPs have shown better oxidation resistance compared with bare Fe_3O_4 nanoparticles [98].

Mechanical stability and adhesion to cores are crucial factors for coating of materials. Also, colloidal stability can change with pH medium. Chemical bonding between matrix and MNPs, for example, Van der walls and hydroxyl groups for organic coatings and covalent bonds for inorganic plays an important role [99].

2.5.2) Crystallinity, homogeneity, size distribution and coating thickness

Characterization of size distribution, homogeneity, and thickness of matrix are very important to evaluate the efficiency of MNPs in the application. Several parameters like synthesis method, heat treatment in different atmospheric and thermal conditions, the thickness of the coating, and narrow size distribution should be taken account [100-103]. For instance, in high crystalline MFe_2O_4 (M=Mn, Fe, Co) ferrite spinel nanoparticles synthesized by the solvothermal reaction the average grain size was found to be in the range of 10 to 23 nm. The

prepared iron oxide spinel nanoparticles demonstrated a weak interparticle interaction [104]. Moreover, as shown in another study [105] highly crystalline and monodisperse manganese ferrite nanocrystals was processed via a combination of the thermal decomposition of metal-surfactant complexes and mild oxidation using trimethylamine N-oxide. In the prepared nanocrystals the uniformity of the nanocrystals causes the typical magnetic behavior with the characteristic narrow energy barrier distributions of magnetic anisotropy. In seeking for the coating thickness effect, an exclusive investigation on bare $CoFe_2O_4$ nanoparticles and also embedded ones in an amorphous silica matrix with the particle size of about 16 nm, prepared by the hydrothermal method was carried on [106]. A similar magnetic behavior was observed for both cases resulted from their identical particle sizes and also the negligible matrix effect on the coupled-moment carriers in embedded ferrite nanoparticles [106]. Also, a uniform and thickness-controllable silica amorphous shell with strong affinity to MNPs could be obtained through the Sol-gel approach [107]. Although, in particular, case, with an increase in the thickness silica coating the saturation magnetization reduces [108]. Also, for monocrystalline superparamagnetic iron oxide nanoparticles coated with polyethylene glycol (PEG) when coating thickness increases the transverse relaxation rate, R2, sharply decreases. Inversely, the thicker coat is accompanied by a smooth increase in the longitudinal relaxation rate, R1 [109].

2.5.3) One-pot and post-coating synthesis

Intensive efforts have been devoted to developing techniques for the synthesis of core-shell nanocomposites including in situ coating (carried out during synthesis) and post-coating [44]. A time-saving microwave driven iron oxide nanoparticle successfully was coated with an amphoteric Poly(acrylic acid) via both past synthesis and in-situ (simultaneously with the nanoparticle formation) method. However, the one-pot synthetic route gave better results. The stable hybrid organic-inorganic nanocomposites with homogenous shape and narrow size distribution showed the capacity to behave as MRI contrast agents [110].

Diverse wet chemistry routes have been employed to polymerize nano particles such as: microwave irradiation; electrochemical synthesis; anodic oxidation; seeding polymerization; interfacial polymerization; and electro-spinning; etc. However, limited approaches have been used to develop a simple, and efficient route to tune the properties of multicomponent

ferrite/polymeric nanocomposites [111]. A magnetically separable $MnFe_2O_4$ decorated with graphene [112] and also conjugation of silica and CTAB [113], prepared using a one-step hydrothermal method, showed high photocatalytic activity, although $MnFe_2O_4$ alone is photocatalytically inactive [112].

2.5.4) Electrical and magnetic characteristics

Based on the Maxwell–Wagner theory of interfacial, activation energy for dielectric relaxation of semiconducting iron oxide-based composites can be evaluated. These studies for nanosized $MnFe_2O_4$ prepared by co-precipitation technique suggested the overlapping large polaron tunneling (OLPT) conduction mechanism with the privilege of the enhanced dielectric properties compared with its bulk counterpart [114]. While the substitution of Na^+ and Li^+ ions with Mn^{2+} ions makes manganese ferrite more suitable for multilayer chip inductors (MLCIs) operable in the radio frequency range and even in high-frequency devices and components [115]. By the same token, Core−shell nanocomposites composed of $Mn_{0.5}Zn_{0.5}Fe_2O_4$ ferrite nanocrystals as core and conjugated polymer polyaniline as shell synthesized by in situ emulsion polymerization exhibited strong microwave absorption properties in the X-band frequency range of 31.2 dB at 12 GHz with a minimal reflection loss of 4.8 dB. So these materials were found to be promising as new types of microwave absorptive materials functional in a wide range of frequencies with strong absorption [116]. According to S. Sen et al. study to their experimental results, amine functionalized $MnFe_2O_4$ nanoparticles are found to inhibit the formation of fibrils more effectively than bare ones, while carboxylated nanoparticles do not have a significant effect on fibrillation [117].

Beside that the hydroxyl radical oxidation reaction in the polymers favors the efficient separation of photo-generated carriers in the $MnFe_2O_4$ and inorganic shell coupling system [47, 48]. Due to the coexistence of its biocompatibility, ligand-induced intrinsic multiple fluorescence, and also the unprecedented photocatalytic activity, the functionalized material might open up new opportunities to their prospective use in bioimaging, drug delivery as well the degradation of a model water contaminant.

The diversity of magnetic compounds for preparation single domain nanoparticles and also different coating materials which possess characteristics for both biomedical and

electromagnetic devices operating in high-frequency range make us able to reach to optimized core/shell structures for the proposed aims. Mentioning and comparison of these results enlighten our path to achieve the optimized nanocomposites with superior magnetic and electrical properties.

2.6) References

[1] G. Bellizzi, O.M. Bucci, and A. Capozzoli, **Journal of Magnetism and Magnetic Materials**, 2010, 322, 3004-3013.

[2] T. I. Yang, R. N. C. Brown, L. C. Kempel and P. Kofinas, **Journal of Nanoparticle Research**, 2010, 12, 2967-2978.

[3] M. Jnaneshwara, D. N. Avadhani, B. D. Prasad, B. M. Nagabhushana, H. Nagabhushana, S. C. Sharma, C. Shivakumara, J. L. Rao, N.O. Gopal, S. C. Ke and R. P. S. Chakradhar, **Journal of Magnetism and Magnetic Materials**, 2013, 339, 40-45.

[4] M. Moravej, A. Purnama, A. Fiset, J. Couet, D. Mantovani, **Acta Biometrialia**, 2010, 6, 5, 1843-1851.

[5] I. Gurrapa, **Journal of Alloys and Compounds**, 2002, 339, 1-2, 241, 247.

[6] S. Sundad, K. Majima, Y. Akasofu and Y. Kaneko, **Journal of Alloys and Compounds**, 2006, 408-412, 9, 1373-1376.

[7] F. Perez-Robles, F. J. Garica-Rodriguez, S. Jimenez-Sandoval and J. Gonzalez-Hernandez, **Journal of Raman Spectroscopy**, 1999, 39, 1099-1104

[8] J. Xu, H. Yang, , W. Fu, K. Du, Y. Sui, J. Chen, Y. Zeng, M. Li, G. Zou, **Journal of Magnetism and Magnetic Materials**, 2007, 309, 2, 307-311 29

[9] B. J. Clapsaddle, A. E. Gash, J. H. Satcher, R. L. Simpson, **Journal of Non-Crystalline Solids**, 2003, 331, 190-201

[10] V. S. Nagineni, S. Zhao, A. Potluri, Y. Liang, U. Siriwardane, N. V. Seetala , J. Fang, J. Palmer and D. Kuila, **Industrial & Engineering Chemistry Research**, 2005, 44 (15), 5602-5607

[11] J. Xu, S. Thompson, E. O'Keefe, and C. C. Perry, **Materials Letters**, 2004, 58, 1696-1700

[12] M. P. F. Graça, M. G. Ferreira da Silva, and M. A. Valente, **Journal of Non-Crystalline Solids**, 2005, 351, 2951–2957

[13] D. Sunil, J. Dong and H. D. Gafney, **Journal of American Chemical Society**, 2009, 131, 14768-14777

[14] R. Zhang, J. Huang, J. Zhao, Z. Sun and Yang Wang, **Energy & Fuels**, 2007, 21, 2682-2687.

[15] M. Zayat, D. Levy, **Chemistry of Materials**, 2000, 12(9), 2763-2769.

[16] C. J. Brinker and G. W. Scherer, **Sol-gel Science: The physics and chemistry of sol-gel processing**, 1990, Academic Press, London.

[17] M. Kakihana, **Journal of Sol-Gel Science and Technology**, 1996, 6, 7–55.

[18] A. E. Danks, S. R. Hall and Z. Schnepp, **Materials Horizons**, 2016, 3, 91-112.

[19] M. Guglielmi, G. Carturan, **Journal of Non-Crystalline Solids**, 1988, 100, 16-30.

[20] S. Sakka, **Handbook of Sol–Gel Science and Technology: Processing, Characterization and Applications**, 2005, Springer-Verlag, USA

[21] A. M. Hulizar-Felix, T. Hernandez, S. de la Parra, J. Ibarra, B. Kharisov, **Powder Technology**, 2012, 229, 290-293.

[22] J. Lin, M. Yu, C. Lin, and X. Liu, **Journal of Physical Chemistry C**, 2007, 11, 5835-5845.

[23] S. A. Seyyed Ebrahimi, S. M. Masoudpanah, H. Amiri, M. Yousefzadeh, **Ceramics International**, 2014, 40, 5, 6713-6718.

[24] L. Yang, G. Xi, J. Liu, **Ceramics International**, 2015, 41, 3 (A), 3555-3560.

[25] S. A. Seyyed Ebrahimi, S. M. Masoudpanah, **Journal of Magnetism and Magnetic Materials**, 2014, 357, 77- 81.

[26] A. Sutka, G. Mezinskis, **Frontiers of Materials Science**, 2012, 6(2), 128-141.

[27] M. George, A. M. John, Swapna S. Naira, P.A. Joy, M. R. Anantharaman, **Journal of Magnetism and Magnetic Materials**, 2006, 302, 1, 190–195.

[28] A. C. F. M. Costa, M. R. Morelli, R. H. G. A. Kiminami, **Journal of Materials Synthesis and Processing**, 2001, 9(6), 347–352.

[29] A. S. Mukasyan, P. Epstein, P. Dinka, **Proceeding of the Combustion Institute**, 2007, 31(2), 1789-1795.

[30] K.H. Wu, T.H. Ting, M.C. Lia, W.D. Ho, **Journal of Magnetism and Magnetic Materials**, 2006, 298(1), 25–32.

[31] N.m. Ferreira, A. V. Kovalevsky, J.C. Waerenborgh, M. Quevedo-Reyes, A. A. Timopheev, F. M. Costa, J.R. Frade, **Journal of Alloys and Compounds**, 2014, 611, 57-64.

[32] M. Costa, M.F. Carrasco, R.F. Silva, J.M. Vieira**, High Tc superconducting fibers processed by conventional and electrical assisted laser floating zone: Chapter 4, In: Perspectives on Superconductivity Research** ,2005, Nova Science Publishers, Inc

[33] E.R.M. Andreeta, M.R.B. Andreeta, A.C. Hernandes, **Journal of Crystal Growth**, 2002, 234, 782–785.

[34] G. Dhanaraj, K. Byrappa, V. Prasad, M. Dudley, **Handbook of Crystal Growth: Chapter 13**, 2010, Springer-Verlag Berlin Heidelberg.

[35] S. Erdei, F.W. Ainger, **Journal of Crystal Growth**, 1997, 174, 293-300.

[36] S.M. Koohpayeh, D. Fort, J.S. Abell, **Progress in Crystal Growth and Characterization of Materials**, 2008, 54, 121-137.

[37] V.V. Prokofiev, J.P. Andreeta, C.J. de Lima, M.R.B. Andreeta, A.C. Hernandes, J.F. Carvalho, A.A. Kamshilin, **Optical Materials**, 1995, 4, 433–436.

[38] S. Erdei, L. Galambos, I. Tanaka, L. Hesselink, L.E. Cross, R.S. Feigelson, F.W. Ainger, H. Kojima, **Journal of Crystal Growth**, 1996, 167, 670–680.

[39] R.S. Feigelson, **Journal of Crystal Growth**, 1986, 79, 1-3 (2), 669-680.

[40] D.R. Ardila, M.R.B. Andreeta, S.L. Cuffini, A.C. Hernandes, J.P. Andreeta, Y.P. Mascarenhas, **Journal of Crystal Growth**, 1997, 177, 52–56.

[41] I. Sharifi, H. Shokrollahi, S. Amiri, **Journal of Magnetism and Magnetic Materials**, 2012, 324, 6, 903-915.

[42] D. S. Mathew, R-S. Juang, **Chemical Engineering Journal**, 2007, 129, 51–65.

[43] B. Tural, N. Ozkan, M. Volkan, **Journal of Physics and Chemistry of Solids**, 2009, 70, 5, 860-866.

[44] Z. Karimi, L. Karimi, H. Shokrollahi, **Materials Science and Engineering: C**, 2013, 33, 5, 2465-2475.

[45] A. K. Gupta, M. Gupta, **Biomaterials**, 2005, 26, 3995-4021.

[46] J. Xie, C. Xu, Z. Xu, Y. Hou, K. L. Young, S. X. Wang, N. Pourmand, S. Sun, **Chemistry of Materials**, 2006, 18(23), 5401-5403.

[47] S. Wang, J. Tang, H. Zhao, J. Wan, K. Chen, **Journal of Colloid and Interface Science**, 2014, 432, 15, 43-46.

[48] K. M. Batoo, **Physica B**, 2011, 406, 382-387.

[49] U. I. Tomsdorf, N. C. Bigall, M. G Kaul, O. T. Bruns, M. S. Nikolic, B. Mollwitz, R.A. Sperling, R. Reimer, H. Hohenberg, W. J. Parak, S. Förster, U. Beisiegel, G. Adam, H. Weller, **Nano Letters**, 2007, 7, 2422–2427.

[50] J. H. Lee, Y. M. Huh, Y-W. Jun, J-W. Seo, J-T. Jang, H-T. Song, S. J. Kim, E-J. Cho, H-G. Yoon, J-S. Suh, J. Cheon, **Nature Medicine**, 2006, 13, 95–99.

[51] D.-H. Kim, H. Zeng, T. Ng, C.S. Brazel, **Journal of Magnetism and Magnetic Materials**, 2009, 321, 3899–3904.

[52] D-H. Kim, D. E. Nikles and C. S. Brazel, **Materials**, 2010, 3(7), 4051-4065.

[53] A. A. Momin, R. Parvin, A. K. M. Akther Hossain, **Journal of Magnetism and Magnetic Materials**, 2017, 423, 124–132.

[54] G. S. Parkinson, **Surface Science Reports**, 2016, 71, 272–365.

[55] U. Schwertmann, R. M. Cornell, **Iron Oxides in the Laboratory: Preparation and Characterization**, 2007, WILEY-VCH Verlag.

[56] Ü. Özgür, Y. Alivov, H. Morkoç, **Journal of Materials Science: Materials in Electronics**, 2009, 20, 9, 789–834.

[57] R.M. Cornell, U. Schwertmann, **The Iron Oxides: Structure, Properties, Reactions, Occurences and Uses**, Second Edition, 2004, WILEY-VCH Verlag.

[58] J. M. D. Coey, **Magnetism and Magnetic Materials**, 2010, Cambridge University Press.

[59] F. Bødker, M. F. Hansen, C. Bender Koch, K. Lefmann, S. Mørup, **Physical Review B**, 2000, 61, 10, 6826-6838.

[60] R. E. Vandenberghe, E. Van San, E. De Grave, G. M. da Costa, **Czechoslovak Journal of Physics**, 2001, 51, 7, 663–675.

[61] C. Luna, V. Vega, V.M. Prida, R. Mendoza-Reséndez, **Journal of Nanoscience and Nanotechnology**, 2012, 12, 7571–7576.

[62] C. Y. Cummings, F. Marken, L. M. Peter, A. A. Tahir, K. G. Upul Wijayantha, **Chemical Communications**, 2012, 48, 2027-2029.

[63] A. Kleiman-Shwarsctein, M. N. Huda, A. Walsh, Y. Yan, G. D. Stucky, Y.-S.Hu, M. M. Al-Jassim, E. W. McFarland, **Chemistry of Materials**, 2010, 22, 510-517.

[64] D. S. Mathew, R-S. Juang, **Chemical Engineering Journal**, 2007, 129, 1–3, 51-65.

[65] C.R. Vestal, J.Z. Zhang, **International Journal of Nanotechnology**, 2004, 1, 240-263.

[66] R. A. McCurrie, **Ferromagnetic Materials Structure and Properties**, 1994, Academic Press.

[67] C. Heck, **Magnetic Materials and their Applications**, 1974, Butterworth-Heinemann.

[68] W. Wu, Z. Wu, T. Yu, C. Jiang and W-S Kim, **Science and Technology of Advanced Materials**, 2015, 16, 023501.

[69] I. M. Mirza, K. Ali, A. K. Sarfraz, A. Ali, A. ul Haq, **Materials Chemistry and Physics**, 2015, 164, 183-187.

[70] F. Schrettle, Ch. Kant, P. Lunkenheimer, F. Mayr, J. Deisenhofer, A. Loidl, **The European Physical Journal B**, 2012, 85, 164.

[71] S-I. Akimoto and H. Fujisawa, **Journal of Geophysical Research**, 1965, 70, 2, 443-449.

[72] E. Gartstein and T. Mason, **Communications of the American Ceramic Society**, 1982, C 24-26.

[73] P. C. Fannin, C. N. Marin, I. Malaescu and N. Stefu, **Journal of Physics: Condensed Matter**, 2007, 19, 036104 (8pp).

[74] K.H. Lee, J. Lee and R. Dieckmann, **Bulletin of the Korean Chemical Society**, 2013, 34, 2, 629-632.

[75] C. Pecharromfin, T. Gonzfilez-Carrefio, J. E. Iglesias, **Physics Chemistry Minerals**, 1995, 22, 21-29.

[76] D. E. Dunstan, **Journal of Colloid and Interface Science**, 1994, 163, 1, 255-258.

[77] L. B. Slichter, M. Telkes, **Handbook of Physical Constants: Electrical Properties of Rocks and Minerals**, 1942, Geological Society of America.

[78] N.M. Ferreira, A.V. Kovalevsky, J.C. Waerenborgh, M. Quevedo-Reyes, A.A. Timopheev, F.M. Costa, J.R. Frade, **Journal of Alloys and Compounds**, 2014, 611, 57–64.

[79] A.K. Gupta, M. Gupta, **Biomaterials**, 2005, 26, 3995–4021.

[80] O. Veiseh, J. W. Gunn, M. Zhang, **Advanced Drug Delivery Reviews**, 2010, 62, 284–304.

[81] A. Tomitaka, T. Koshi, S. Hatsugai, T. Yamada, Y. Takemura, **Journal of Magnetism and Magnetic Materials**, 2011, 323, 10, 1398-1403.

[82] Zhiya Ma, Huizhou Liu, **China Particuology**, 2007, 5, 1–10.

[83] M. Ali, G. Ghosh, **Colloids and Surfaces B: Biointerfaces**, 2010, 75, 590–594.

[84] C. Sun, J. S.H. Lee, M. Zhang, **Advanced Drug Delivery Reviews**, 2008, 60, 1252–1265.

[85] T. Nakaya, Y. J. Li, **Progress in Polymer Science**, 1999, 24, 143–181.

[86] M. Mahmoudi, S. Sant, B. Wang, S. Laurent, T. Sen, **Advanced Drug Delivery Reviews**, 2010, 63, 24-46.

[87] T. Sen, I. J. Bruce, **Microporous and Mesoporous Materials**, 2009, 120, 246–251.

[88] L. Qu, S. Tie, **Microporous and Mesoporous Materials**, 2009, 117, 402–405.

[89] P. Yang, Z. Quan, Z. Hou, C. Li, X. Kang, Z. Cheng, J. Lin, **Biomaterials**, 2009, 30, 4786–4795.

[90] T. Sen, J. Lellouche, I.J. Bruce, **Journal of Magnetism and Magnetic Materials**, 2005, 293, 33–40.

[91] V. Raicu, C. Gusbeth, D. F. Anghel, G. Turcu, **Biochimica et Biophysica Acta (BBA) - General Subjects**, 1998, 1379, 1, 7-15.

[92] B. Fadeel, A. E. Garcia-Bennett, **Advanced Drug Delivery Reviews**, 2010, 62, 3, 362-374.

[93] P. Xu, X. Han, J. Jiang, X. Wang, X. Li, and A. Wen, **Journal of Physical Chemistry C**, 2007, 111 (34), 12603–12608.

[94] M. Fan, Z. He, H. Pang, **Synthetic Metals**, 2013, 166, 1-6.

[95] S. Laurent, J. L. Bridot, L. V. Elst and R. N. Muller, **Future Medicinal Chemistry**, 2010, 2, 3, 427-449.

[96] E. R. Monazam, R.W. Breault, and R. Siriwardane, **Industrial & Engineering Chemistry**, 2014, 53 (34), 13320–13328.

[97] J.P. Gavirıa, A. Bohe, A. Pasquevich, D.M. Pasquevich, **Physica B**, 2007, 389, 198–201.

[98] R. Hong, J. Li, S. Zhang, H. Li, Y. Zheng, **Applied Surface Science**, 2009, 255, 3485–3492.

[99] M. Latorre-Esteves, A. Cortés, M. Torres-Lugo, C. Rinaldi, **Journal of Magnetism and Magnetic Materials**, 2009, 321, 3061–3066.

[100] D. R. Saha, M. Mukherjee and D. Chakravorty, **Journal of Magnetism and Magnetic Materials**, 2012, 324, 4073-4077

[101] J. S. Xu and Y. J. Zhu, **Journal of Colloid and Interface Science**, 2012, 385, 58-65

[102] S. Larumbe, C. Gomez-Polo, J. I. Perez-Landazabal and J. M. Pastor, **Journal of Physics: Condensed Matter**, 2012, 24, 266007-266013

[103] A. Darmawan, S. Smart, A. Julbe and J. C. D. da Costa, **Materials**, 2011, 4, 448-456

[104] R. Pazik, E. Piasecka, M. Małecka, V.G. Kessler, B. Idzikowski, Z. Sniadecki, and R. J. Wiglusz, **RSC Advances**, 2013, 3, 12230-12243.

[105] E. Kang, J. Park, Y. Hwang, M. Kang, J-G. Park, and T. Hyeon, **Journal of Physical Chemistry B**, 2004, 108, 13932-13935.

[106] V. Blanco-Gutierrez, E. Climent-Pascual, R. Saez-Puche and M. J. Torralvo-Fernandez, **Physical Chemistry Chemical Physics**, 2016,18, 9186-9193.

[107] F. Perez-Robles, F. J. Garica-Rodriguez, S. Jimenez-Sandoval and J. Gonzalez-Hernandez, **Journal of Raman Spectroscopy**, 1999, 39, 1099-1104.

[108] C. Russel, **Journal of Non-Crystalline Solids**, 1997, 219, 212-218.

[109] L. E.W. LaConte, N. Nitin, O. Zurkiya, D. Caruntu, Ch. J. O'Connor, X. Hu, and G. Bao, **Journal of Magnetic Resonance Imaging**, 2007, 26, 1634 –1641.

[110] D. Maggioni, T. Orlando, G. D'Alfonso, P. Arosio, A. Manfredi, F. Orsini, E. Ranucci, and A. Lascialfari, **Dalton Transactions**, 2014, 43, 1172-1183.

[111] B. Baruwati, V. Polshettiwar and R. S. Varma, **Green Chemistry**, 2009, 11, 926–930.

[112] Y. Fu, P. Xiong, H. Chen, X. Sun, and X. Wang, **Industrial & Engineering Chemistry Research**, 2012, 51, 725–731.

[113] B. Sahoo, S. Kumar Sahu, S. Nayak, D. Dhara and P. Pramanika, **Catalysis Science & Technology**, 2012, 2, 1367–1374.

[114] E. Veena Gopalan, K. A. Malini, S. Saravanan, D. Sakthi Kumar, Y. Yoshida and M. R. Anantharaman, **Journal of Physics D: Applied Physics**, 2008, 41, 185005.

[115] A.A. Momin, Roksana Parvin, A.K.M. Akther Hossain, **Journal of Magnetism and Magnetic Materials,** 2017, 423, 124–132.

[116] M. A. Dar, R. K. Kotnala, V. Verma, J. Shah, W. A. Siddiqui, and M. Alam, **The Journal of Physical Chemistry C**, 2012, 116, 5277−5287.

[117] Sh. Sen, S. Konar, A. Pathak, S. Dasgupta, and S. DasGupta, **Journal of Physical Chemistry B**, 2014, 118, 11667−11676.

This page intentionally left blank

Chapter 3 - Experimental Characterization Methods

In this chapter, the experimental characterization methods used to analyze the prepared samples will be presented as well as all the mathematical formalisms.

3.1) X-ray Diffractometry

XRD is an analytical method primarily employed to identify a crystalline material phase and corresponding unit cell dimension and atomic spacing. It is based on constructive interference between monochromatic X-rays and a crystalline structure. The conventional X-ray spectrometer consists of three parts: The X-ray source unit, the spectrometer, and the measuring electronics (Fig. 3.1) [1, 2].

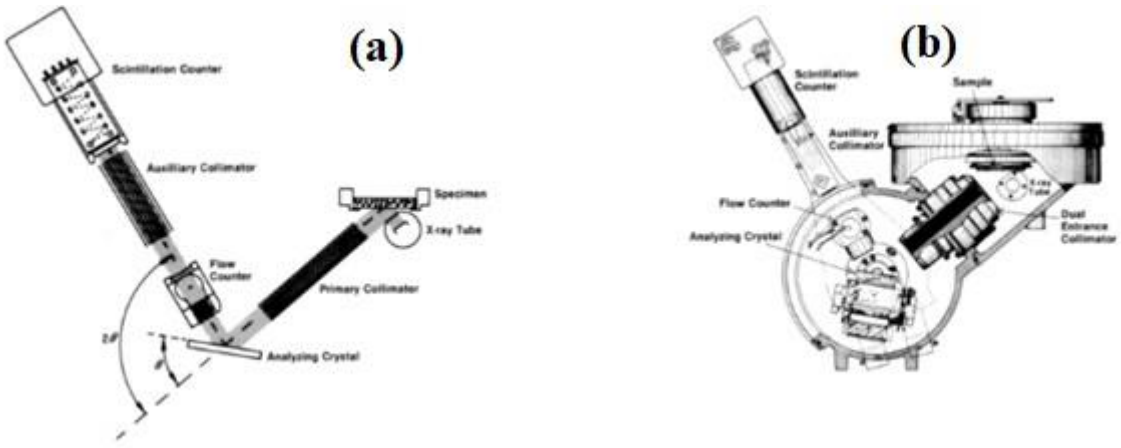

Fig. 3.1) The wavelength-dispersive spectrometer. (a) The parts of the wavelength-dispersive spectrometer (b) The same components as they appear in actual spectrometer [2].

The X-ray source has a very stable high-voltage generator, capable of providing up to around 3 kW of power at a potential of typically 60–80 kV, plus a sealed X-ray tube. The sealed X-ray tube has an anode of copper and delivers an intense source of continuous radiation (K-Alpha1: 1.54060 Å; KAlpha2: 1.54443 Å; K-Beta: 1.39225 Å). The spectrometer is made of a specimen holder support, a primary collimator, an analyzing crystal, and a detector. These components are geometrically arranged based on Bragg–Brentano configuration. [1, 2].

Fundamental principles of X-ray Powder Diffraction followed: first the cathode ray tube generates the X-ray radiation. This radiation is then filtered and collimated to produce monochromatic concentrated radiation, which is directed toward the sample. These diffracted X-rays are ultimately detected by the detector, processed and counted. By scanning the sample through a large range of 2θ, all possible diffraction directions of the lattice are attained a qualitative/quantitative phase analysis will be possible. The interaction of the incident rays with the sample produces constructive and nonconstructive interference. W. Bragg and L. Bragg postulated a condition, Bragg's Law, when the constructive diffracted ray is provided, expressed as [1]:

$$2d\sin\theta = n\lambda \tag{3.1}$$

where λ is the wavelength of the electromagnetic radiation, *d* is the atomic spacing and θ is the angle between the incident (or diffracted) ray and the relevant crystal planes. *n* is an integer, referred to as the order of diffraction, and is often unity. The total intensity of diffracted radiation at any 2θ position can be written as [2]

$$I_{(hkl)} = K \times \left|F_{(hkl)}\right| \times f_a e^{\frac{-B\sin^2\theta}{\lambda^2}} \times A \times L(\theta) \times P(\theta) \times m \tag{3.2}$$

where K is a constant independent of 2θ, $f_a e^{\frac{-B\sin^2\theta}{\lambda^2}}$ the temperature factor describing the average displacement of atoms from their equilibrium point due to the thermal fluctuation, $F_{(hkl)}$ is the crystallographic structure factor, A the absorption factor, L(θ) the Lorentz factor, P(θ) the polarization factor and m the multiplicity describing the number of equivalent planes that can diffract at a given Bragg angle. The shape of the diffracted signal is influenced by different factors including:

i) the instrumental broadening depending on the X-ray source, primary and secondary optics, detector, etc;

ii) compositional inhomogeneity within the analyzed crystallites which leads to a distribution of lattice constants and resulting in a broadening;

iii) the crystallite size effect;

iv) crystal defects such as dislocations, stacking faults, twins, etc;

v) heterogonous strains and microstrains.

Qualitative phase analysis can be performed via a comparison of the detected diffraction peaks with a well-known database. The International Center for Diffraction Data (ICDD) provides the main available database referring to the different scientific sources (http://www.icdd.com/). Quantitative phase content analysis can be performed using two distinct strategies. The first technique is based on the peak shape description using a mathematical function such as Gaussian, Lorentzian, Voigt, Pseudo-Voigt, Modified Cox-Hasting Voigt function, Pearson VII, etc. These functions can be used for profile refinements in such a case that instrumental details are non-known. Although, since the methods are based on the mathematical fitting, no physical information such as crystallite size and microstrain cannot be extracted. The second strategy, Rietveld profile refinement, is fundamentally a parameter approach, e.g. the evaluation is based on the simultaneous analysis of several peaks. In this method, the profile calculation is done by taking into account several structural, microstructural, and experimental parameters. The instrumental function can also be measured by using a standard without sample broadening. Generally, the standard SRM660a (LaB_6) is used, as the large crystallites of about 2 mm do not lead to a significant broadening of the peaks [3]. The refinement is performed by minimization of the function S given in

$$S = \sum_i u_i |y_{iobs} - y_{icalc}|^2 \tag{3.3}$$

where y_{iobs} the measured and y_{icalc} the calculated intensities at each 2θ position i and u_i. a weighting factor taken from the experimental error margins. The calculation of y_{calc} at each position i is a function of instrumental contribution, reflections of all present phases, backgrounds, etc. [3].

3.2) Thermal analysis

Thermal Analysis (TA) is defined as a group of physical-chemical techniques considering the investigation of materials and processes under conditions of programmed changings of the surrounding temperature [4]. Here we are going to consider differential thermal analysis (DTA) technique for the thermal measurement of the prepared composites. DTA is a technique in which the temperature difference between a substance and a reference material is measured

as a function of temperature while the substance and reference material are subjected to a controlled program [1]. The plot is called a DTA curve; the temperature difference ΔT should be plotted on the ordinate, with the endotherm processes shown downward and the exotherm processes in the opposite direction, and the temperature or time on the abscissa, increasing from left to right. DTA measurement was performed on as-prepared samples at the air with the given rate, depending on the sample preparation method, using Lenisis apparatus.

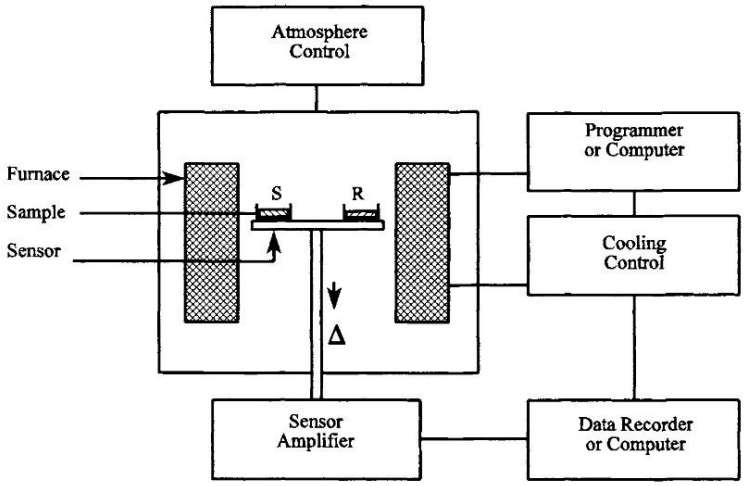

Fig. 3.2) Schematic of a DTA apparatus.

3.3) Raman spectroscopy

Raman spectroscopy is one of the vibrational spectroscopic techniques which provides information on molecular vibrations and crystal structures. In this technique, a laser light source is employed to irradiate a sample. The radiation results in a change in the polarizability of the molecule and the infinitesimal amount of Raman scattered light is generated and detected by a charge-coupled device (CCD) camera. The intensity of Raman scattered radiation as a function of its frequency difference from the incident radiation is defined as Raman spectrum. The characteristic fingerprinting pattern in a Raman spectrum makes it possible to identify substances including polymorphs and evaluate local crystallinity, orientation and stress. There are some benefits which can be addressed by Raman spectroscopy including:

i) non-contact and non-destructive analysis.
ii) high spatial resolution up to sub-micron scale.
iii) no sample preparation needed.

iv) both organic and inorganic substances can be measured.

v) samples in various states such as liquid, solution, solid, crystal, the emulsion can be measured.

vi) samples in a chamber can be measured through a glass window.

vii) fast technique.

viii) imaging analysis is possible by scanning the motorized stage or laser beam.

In the Raman spectroscopy, an laser beam (amplitude E_0; frequency υ_{1as}) interacts with phonons of frequency υ_{vib}, and the dipoles in solid will be excited. The polarization depends on the polarizability tensor $\bar{\bar{\alpha}}$:

$$\vec{P} = \bar{\bar{\alpha}} \times \overrightarrow{E_0} \cos(2\pi\nu_{1as}t) \tag{3.4}$$

where $\bar{\bar{\alpha}}$ term s are described as functions of the normal vibration coordinates Q using a Taylor approximation:

$$\alpha_{ij} = \alpha_{ij}^0 + \left(\frac{\partial\alpha_{ij}}{\partial Q}\right)_{Q=Q_0} \times Q \ (i,j = x,y \ or \ z) \tag{3.5}$$

$$P_i = \sum_j \alpha_{ij} \times E_j \sum_j \left[\left[\alpha_{ij}^0 E_{0j} \cos(2\pi\upsilon_{1as}t) + \frac{E_{0j}Q_0}{2}\right]\left(\frac{\partial\alpha_{ij}}{\partial Q}\right)_{Q=Q_0} \times [\cos(2\pi(\upsilon_{1as} - \upsilon_{vib})t + \cos(\upsilon_{1as} + \upsilon_{vib})t] + \cdots\right] \tag{3-6}$$

With the scattered electric field being proportional to $\vec{P}$, Eq. (3-6) predicts both quasi-elastic ($\upsilon \sim \upsilon_{1as}$) and inelastic ($\upsilon = \upsilon_{1as} \pm \upsilon_{vib}$) light scattering. The former is called the Rayleigh scattering and the latter, which occurs only if vibrations change polarizability ($\frac{\partial\alpha_{ij}}{\partial Q} \neq 0$), is the Raman scattering [5-6].

Raman scattering can be classified into two types, Stokes and anti-Stokes scattering (Fig. 3.2). Stokes scattering is a process in which an electron is excited from the ground level and falls to a vibrational level. It involves energy absorption by the molecule. Thus Stokes scattered light has less energy (longer wavelength) than the incident light. By contrast, anti-Stokes scattering is a process in which an electron is excited from the vibrational level to the ground level. It

involves an energy transfer to the scattered photon. Thus anti-Stokes scattered light has more energy (shorter wavelength) than the incident light.

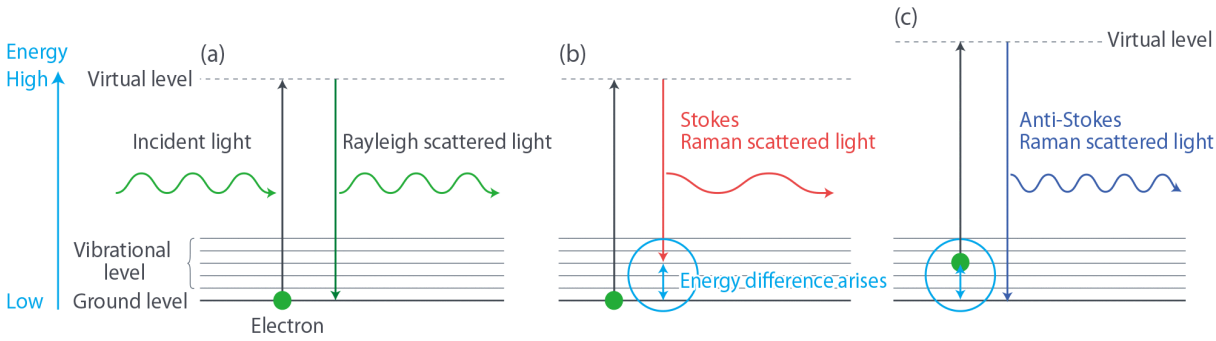

Fig. 3.3) An electron is excited from the ground level and falls to the original ground level. (b) An electron is excited from the ground level and falls to a vibrational level. (c) An electron is excited from a vibrational level and falls to the ground level [7].

The dominant process is Rayleigh scattering, and Raman scattering is an extremely weak process in that only one in every 10^6 - 10^8 photons scatters. In standard Raman measurement, Rayleigh scattered light is rejected using a filter and only the Stokes Raman scattering is recorded for simplicity. The ratio of Stokes Raman and anti-Stokes Raman scattering depends on the population of the various states of the molecule. At room temperature, the number of molecules in an excited vibrational level is smaller than that of in the ground level, thus generally the intensity of Stokes Raman light is higher than anti-Stokes Raman light. The intensity of anti-Stokes Raman light increases relative to Stokes scattering as the temperature rises. Thus the intensity ratio of anti-Stokes and Stokes light can be used to measure the temperature of a sample [7].

Raman spectroscopists normally refer to vibration modes by their wavenumber $\bar{\upsilon} = \frac{\upsilon_{vib}}{c}$ (c is the light speed, $\bar{\upsilon}$ in cm^{-1} unit) and the classical electromagnetic theory of radiations from an oscillating dipole demonstrates that Raman peaks have a Lorentzian shape:

$$I(\bar{\nu}) = I_0 \times \int_{Brillouin\ Zone\ (BZ)} \frac{d^3\vec{k}}{\left[\bar{\nu} - \bar{\nu}(\vec{k})\right]^2 + \left(\frac{\Gamma_0}{2}\right)^2} \tag{3.7}$$

In Eq. (3.7), $\bar{\nu}(\vec{k})$ represents the dispersion branch to which the mode belongs and $\frac{\Gamma_0}{2}$ is the half-width for the ordered reference structure.

The scattering of one photon ($\vec{k}\sim\vec{0}$) by n phonons (wavevectors $\vec{k}_i$) is governed by the momentum conservation rule:

$$\sum_{i=1}^{i=n} \overrightarrow{k_i} = \vec{k}_{scattered} - \vec{k}_{incident} \approx \vec{0} \quad (3.8)$$

Therefore, only vibrations from the center of Brillouin zone, BZ, (BZ_c), i.e., long wavelength phonons can be active in any one phonon process (first-order spectrum). However, not all BZc phonons are active in Raman spectra. According to Eq. (3-6), $\frac{\partial \alpha_{ij}}{\partial Q}$ terms must be different from zero, and this condition is governed by the symmetry of the crystals. Raman activity can, therefore, be predicted through Group Theory [7].

According to Eq. (3.5) Raman spectra are sensitive to both the electrical (α_{ij}) and mechanical (υ_{vib}) properties of the investigated materials. Therefore, the spectra are influenced by two kinds of parameters:

(i) Parameters acting on the ‘‘mechanics’’ like atomic mass, bond strength or the system geometry (interatomic distances, atomic substitutions) will set the peaks’ positions (the eigenfrequencies of matter vibrations).

(ii) Parameters acting on the ‘‘charge transfer’’ (iono-covalency, band structure, electronic insertion) will set intensity, by the vibration-induced charge variations occurring at the very bond scale.

Elements with high atomic numbers that are situated on the right side of the periodic table (covalent materials in general) are good Raman scatterers whereas ionic structures are difficult to analyze with Raman spectra. As for the metals, their surface plasmons limit the penetration of the light. Thus, their Raman signal is extremely weak [8].

Fig. 3.4 shows the principle of a Raman spectrometer. Up-to-date equipment would include holographic gratings, for improved excitation light rejection, a set of monochromators and Peltier effect-cooled CCD mosaic for detection [8]. In this thesis, the Raman spectroscopy of the samples was carried out in a T64000 Jobin Yvon SPEX spectrometer, using an Ar laser (λ

= 532 nm) as excitation font. The spectra were obtained, in a back-scattering geometry, in the given wavenumber range by the composition under the measurement.

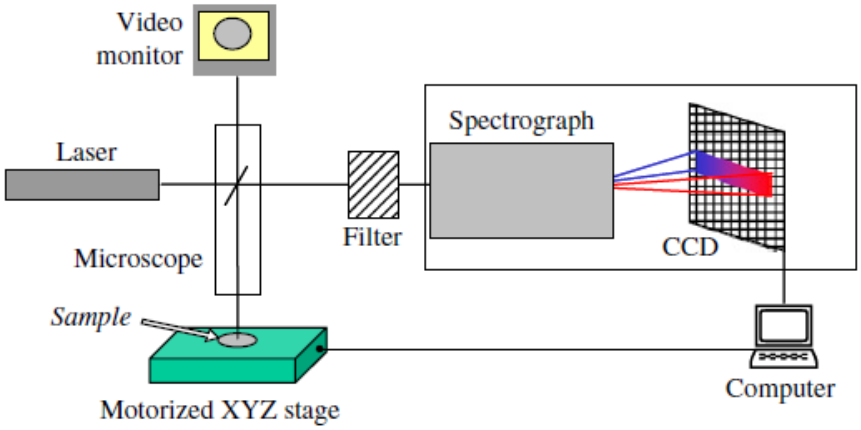

Fig. 3.4) Principle of a conventional micro-Raman spectrometer.

3.4) Scanning Electron Microscopy

A scanning electron microscope (SEM) produces images of a sample by scanning the surface with a focused beam of electrons. The electron beam is scanned in a raster scan pattern, and the beam's position is combined with the detected signal to produce an image. Due to multiple scattering of beam electrons in the specimen, the interaction volume extends. This results in a boost of the electron probe size, considerably (Fig. 3.5). The interaction of the primary electrons with the sample leads to a variety of signals utilized to gain information about the sample's surface topography and composition. The detected signal originally is from electrons emerged from the surface. Therefore, there is no restriction to thin electron-transparent samples. However, the interaction volume unfavorably causes that electrons are excited far away from the scan position. This leads to background noise and deteriorates the image quality. The intensity of the detected signal is converted to a grey-scale value, attributed to the current scan position. In this way, a grey-scale image evolves pixel by pixel.

A portion of the primary electrons is scattered back and escapes the sample. The detection of these backscattered electrons (BSEs) leads to intense material contrast because the backscatter efficiency strongly depends on the atomic number of the element.

Imaging with secondary electrons (SEs), which exhibit energies below 50 eV by definition, is widely used. The number of SEs released depends on the geometry of the sample and the angle

of incidence of the electron beam. In combination with a large depth of focus due to small cone angles of the beam, the well-known quasi-three-dimensional (3D) image impression is obtained.

There are several excitation processes for SE. The most important one is the excitation of plasmons (oscillations of the electron gas) by high-energy electrons and their subsequent decay, which may lead to the generation of SEs. SEs are generated in the whole interaction volume by primary and backscattered electrons, but due to their low energies, only those generated close to the surface can emit from the sample. SEs, which are excited by primary electrons, the so-called SE1, are highly localized and retain information about the sample area that is hit by the beam spot. Because BSEs emerge from inside the interaction volume, their travel range is not confined to the beam spot and the SE2 excited by them originate from a relatively wide emission zone. If BSEs hit the walls of the vacuum chamber or the electron column, SE3 are produced, which contribute to the background noise, thereby decreasing contrast.

If the electron beam reaches an edge on the sample, SE emission is no longer confined to the horizontal sample surface but may also take place at the vertical edge. This so-called blooming effect may obscure the exact position of the edge.

After impact ionization, the resulting vacancy in the shell may be filled by an electron from a higher energy level, thereby possibly emitting an X-ray photon specifically for the atomic element. These X-rays can be analyzed by energy-dispersive X-ray spectroscopy (EDS) to gain information about the elemental composition of the sample [9]. Surface morphology of the prepared composites was observed using VEGA3 TESCAN scanning electron microscopy (SEM), and phase's composition analyzed using EDS mode (25 kV,10 mA).

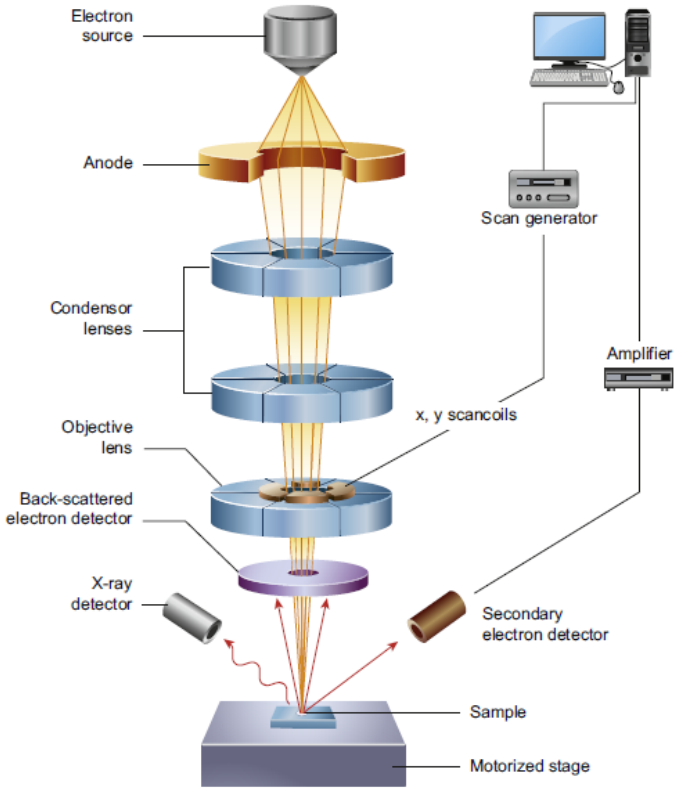

Fig. 3.5) A schematic figure of SEM instrument.

3.5) Transmission Electron Microscopy

The design of a transmission electron microscope is shown on the left side of Fig. 3.5. It resembles that of a transmission light microscope.

The electrons emitted by the source are accelerated (typically by 200 kV) on their way to the sample. Condenser optics is used to achieve a spatially uniform illumination on the electron-transparent specimen. After passing through the sample, the electrons are collected and imaged on a projection screen using electron optics. A scintillator converts the impinging electrons to light pulses that may also be detected by a CCD for direct image recording using a computer. The electrons are scattered, diffracted, and possibly absorbed by the specimen, depending on different sample properties, such as mass, thickness, elemental composition, and crystallinity. The image is generated by detecting electrons that are deflected within certain angular ranges, which are determined by the aperture of the imaging lens. Dark-field (DF) imaging uses only the deflected electrons for image formation, whereas in bright-field (BF) mode the beam of

undeflected electrons is registered. In high-resolution TEM mainly phase contrast is exploited. The sample acts as a phase object that distorts the wave front of the impinging electron wave. Under Scherzer defocus conditions, phase contrast is transformed into visible amplitude contrast [9]. For TEM analysis, Samples were prepared by the following method: adding a drop of an aqueous (ethanol) nanoparticle suspension to a copper grid. Sonication was used to disperse the nanoparticles further. This mesh was then dried in a vacuumed desiccator. TEM analysis were carried out on the dried mesh.

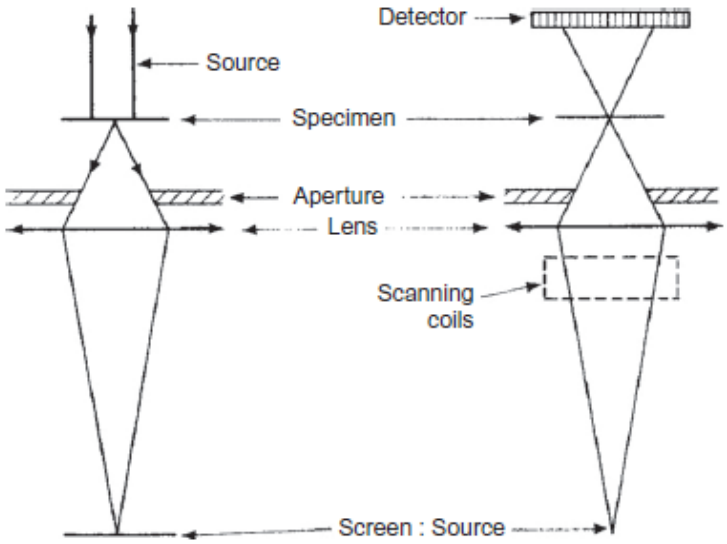

Fig. 3.6) The scheme of TEM microscopy.

3.6) Electrical and dielectric measurements

Electrical conductivity is a vital experimental tool to probe both the bulk transport properties of wide range materials like semiconductors and dielectrics and the electrochemical reactions at interfaces. The purpose of the present chapter is to investigate the alternating current (AC) and DC electrical conductivity of iron oxide-based materials. Association with the conduction mechanism study, the related dielectric parameters and also a brief description of the experimental setup which is used in this work to measure the electrical and dielectric characteristics of the compositions are given.

3.6.1) DC electrical measurement

The voltage developed across a standard resistance can be measured with a multimeter from which the current versus applied voltage could be readily known. By knowing the value of current, I, and voltage, V, across the sample, with cross-sectional area A and thickness d, the conductivity can be calculated using the relation 3.9 [10]:

$$\sigma = \frac{I}{V}\frac{d}{A} \tag{3.9}$$

where I is the current passed through the sample and V is the voltage drop across it, A the area of the electrodes, and d the thickness of the sample. The dependence of the conductivity with the temperature is often described by Arrhenius equation (3.10) [11]:

$$\sigma_{DC}(T) = \sigma_o \exp(\frac{-\Delta E}{k_B T}) \tag{3.10}$$

where k_B is Boltzmann constant, T is temperature, σ_0 is the conductivity at T=0 K and ΔE is the activation energy. A general condition for semiconducting behavior is that conduction can take place by the transfer of electrons from low-valence to high-valence states. Drift mobility is low owing to the strong interaction between the network and electrons. The potential well produced by this interaction deforms this network and traps transport electrons. Under a conventional electric field, electrons are forced to move in one direction, so that a net current is observed [12]. A schematic description of the hopping model is shown in Fig. 3.7 [13]. The initial state is represented by the dotted line, and an electron is trapped at site 1. The depth of the potential well and the difference in potential energy between sites 1 and 2 are given by E_D, E_P and r is the radius of the polaron. The general equation for small-radius hopping conduction is expressed as [13]:

$$\sigma(T) = \frac{\upsilon_{phonon} e^2 c(1-c)}{k_B TR}.\exp(-2\alpha R)\exp(\frac{-\Delta E}{k_B T}) \tag{3.11}$$

where c is the ratio between the two valences of the transition metal cations, k_B is the Boltzman´ constant, R is the hopping distance, α is the decay constant, and exp(−2αR) is the tunneling term.

Although usually semiconducting materials possess a temperature dependent activation energy. Therefore, the band conduction or nearest neighbor hopping models cannot explain their conduction mechanism. And the Ln(σ.T) as a function of 1/T does not show a linear relation. In such case the variable range hopping (VRH) conductivity model is employed as expressed by [14]:

$$\sigma=\sigma_o \exp[-(T_o/T)^p] \tag{3.12}$$

where σ_o, the pre-exponential factor, is either independent or slowly varying function of temperature. Also $T_o= \varepsilon^2/\varepsilon_r.a$, a^{-1} and ε_r being the electron localization range and the relative dielectric constant of the material, respectively. The exponent p is related to the grain size and the temperature range of measurements and ranged from 1/4 for Mott´s hopping [15] and 0.5 to 1.0 for Efro´s hopping [16]. It depends on the variation of density of states with energy within the Coulomb type electron-electron correlation, which leads to a weak gap near the Fermi level due to the exciton effect.

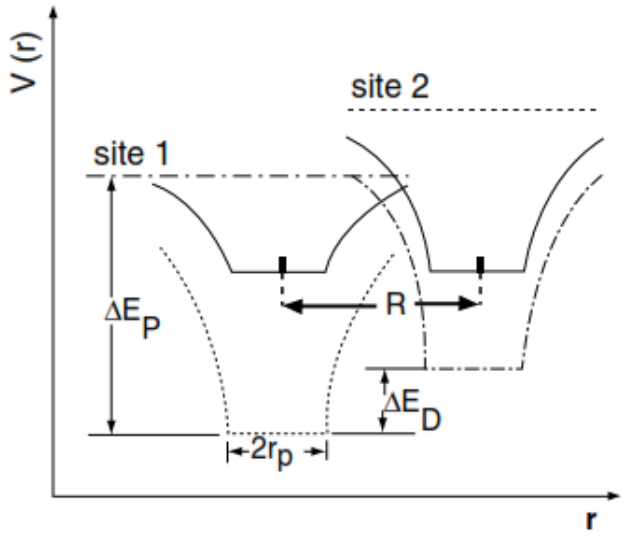

Fig. 3.7) Hopping mechanism in semiconductors [13].

3.6.2) AC electrical measurements

A.C. impedance spectroscopy is a useful tool to study both the bulk transport properties of materials and the electrochemical reactions at interfaces. Typically, A.C. impedance experiments are carried out over a wide range of frequencies from several hundred hertz to several megahertz. The resulting spectra can be interpreted by analogy to equivalent circuits involving simple components such as resistors and capacitors. Generally, such equivalent circuits are not unique and infinite set of different electrical circuits can represent any given impedance repsonse. It is common to select a physically plausible electrical circuit containing a minimal number of components and, in a somewhat *ad hoc* way, assign physical significance to the derived parameters. Often, meaningful insight into material behavior can be gained from such analyses. However, the *ad hoc* approach is lacking in mathematical and physical rigor and can lead one to overlook some of the more subtle, but significant, features of the data.

Impedance Spectroscopy (IS) can be used to study an external stimulus that influences the conductivity of an electrode-electrolyte system [17]. The parameters derived from the IS spectrum can be categorized into two. i) electrolytes, such as conductivity, dielectric constant, mobility of charges, equilibrium concentration of the charged species and bulk generation-recombination rates, etc., and ii) electrode-electrolyte interface, such as adsorbed reaction rate constants, capacitance of the interface region, diffusion coefficient of the neutral species present in the electrode, etc. [18]. The electrical response of solid electrolytes (SE) can be studied by interpretion of the complex impedance and complex admittance plane representations. Whereas, the dielectric response of SE is derived from the complex modulus and complex permittivity spectra.

The impedance (Z(t)) in its standard definition means the quotient of the vector voltage (V(t)) with the vector current (I(t)), calculated from small single sinusoidal measurement (eq. 3.13) [17].

$$Z(t) = \frac{V(t)}{I(t)} = \frac{V_0 . e^{i(\omega t)}}{I_0 . e^{i(\omega t - \theta)}} \tag{3.13}$$

The impedance is also a complex quantity ($Z^* = Z' - iZ''$), and therefore presents both magnitude $|Z|$ and phase angle θ and expressed as Eq. 3.14

$$Z(\omega) = |Z|\exp(-i\omega t) \quad (3.14)$$

In impedance technique, the real and imaginary parts of the impedance of the sample were measured simultaneously as a function of frequency. The measured impedance data can be represented in the other three forms, using the inter relations as follows:

Complex impedance, in R-C parallel configuration

$$Z' = \frac{R_p}{[1+(\omega R_p C_p)^2]} \quad \text{and} \quad Z'' = \frac{\omega R_p{}^2 C_p}{[1+(\omega R_p C_p)^2]} \quad (3.15)$$

Complex admittance

$$Y^* = \frac{1}{Z^*} = Y' + iY'' \quad (3.16)$$

Complex permittivity

$$\varepsilon^* = \varepsilon' - i\varepsilon'' = \frac{1}{i\omega C_o Z^*} \quad (3.17)$$

Complex modulus

$$M^* = M' + iM'' = i\omega C_o Z^* \quad (3.18)$$

where $i = \sqrt{-1}$, C_o, is the vacuum capacitance and $\omega = 2\pi f$ is the angular frequency. The admittance and permittivity are parallel functions that can be measured at low frequencies whereas the impedance and modulus are series functions at high frequencies [18].

The complex impedance spectrum of an ideal system with an equivalent circuit represented by the parallel combination R and C, R_p and C_p, shows a semicircle intersecting the real axis at a point R and origin and the difference between the intercepts of the semicircle with the real axis gives the grain resistance (R_g) of the system [6]. In the case of real solid electrolyte, the impedance spectrum shows an inclined straight line with the depressed semicircle respectively due to the presence of double layer capacitance of electrode-electrolyte interface and parallel combination of resistance and capacitance. The angle of inclination of the straight line and the angle of depression of the semicircle is due to the distributed microscopic material properties, termed as the constant phase element (CPE) and expressed as $Z^* = A(i\omega)^{-\alpha}$, $0<\alpha<1$ and

A=constant. The fractional power law dependence on frequency is referred to as a constant phase angle element [17].

Dielectric property is a characteristic of short-range electrical conduction of a material under the influence of an applied alternating electric field. According to Debye the resulting polarization due to applying an AC voltage to the material may be divided into two parts according to the time constant of the response:

i) An almost instantaneous polarization due to the displacement of the electrons concerning the nuclei, defined as the high-frequency dielectric constant, ε_∞;

ii) A time-dependent polarization due to the orientation of dipoles in the electric field corresponded to low-frequency dielectric constant ε_s.

Thus, expression 3.17 can be rewritten regarding ε_∞ and ε_s as following:

$$\varepsilon^* = (\varepsilon_\infty + \frac{(\varepsilon_\infty - \varepsilon_s)}{1+\omega^2\tau^2}) - i(\frac{\omega\tau(\varepsilon_\infty - \varepsilon_s)}{1+\omega^2\tau^2}) \quad (3.19)$$

Many materials show a non-Debye dielectric behavior characterized by a broader asymmetric loss peak and by a constant loss tangent at a frequency higher than the loss peak, where the relaxation effects of the sample begin. Cole-Cole, Davidson-Cole and empirical expression proposed by Havriliak-Negami, could describe the non-Debye behavior of the material [17].

The complex electric modulus M*, proposed by Macedo et al. [17], is defined by the reciprocal of the complex permittivity ε*.

$$M^* = M' + iM'' \quad (3.20)$$

where M' and M'' are real and imaginary parts of complex modulus. The complex electric modulus $M^*(\omega)$ spectra mainly reflect the electrical properties of a sample by suppressing the electrode polarization effects [18]. For an ideal material with a single relaxation time τ_σ, a plot of M´´ vs. log (f) shows a maximum, in just the same way that ε´´ shows a maximum for a dielectric relaxation process. However, often modulus spectra give a broad and asymmetric curve is deviating from the ideal Debye curve with the distribution of relaxation times. The variation of relaxation time is continuous and can be expressed by normalized distribution function of relaxation times that relaxation times $G(\tau_\sigma)$

$$M = M_s \int_0^{\infty} G(\tau_\sigma) \frac{i\omega\tau_\sigma}{1+i\omega}, \qquad M_s = \frac{1}{\varepsilon_s} \tag{3.21}$$

The decay function for the electric field after the imposition of a charge on the electrodes can be expressed by:

$$\phi'(t) = \exp -\frac{t}{\tau_\sigma} \tag{3.22}$$

The modulus is related to $\phi'(t)$ through the expression:

$$\frac{M}{M_s} = 1 - \left\{ \left(-\frac{d\phi'(t)}{dt} \right) \right\} \tag{3.23}$$

The function of $\phi'(t)$ can be rewritten regarding Kohlrausch-Williams-Watts (KWW) function which was proposed first by Moynihan.

$$\phi'(t) = \exp -(\frac{t}{\tau_\sigma})^{\beta} \quad , \qquad 0 < \beta < 1 \tag{3.24}$$

β is the full-width half maximum (FWHM) of the stretched exponent. The KWW function can be interpreted as resulting from the sum of many exponential decays weighted by a distribution of individual relaxation times.

Typical frequency dependence of conductivity spectrum of $10MnFe_2O_4$-$90SiO_2$ nanocomposite prepared by auto-combustion method measured at 400 K shown in Fig. 3.8 exhibits two distinguish regions:

1) plateau region in the low frequency region where the conductivity is frequency-independent;

2) dispersive region where a sharp increase in conductivity occurs in the high-frequency region.

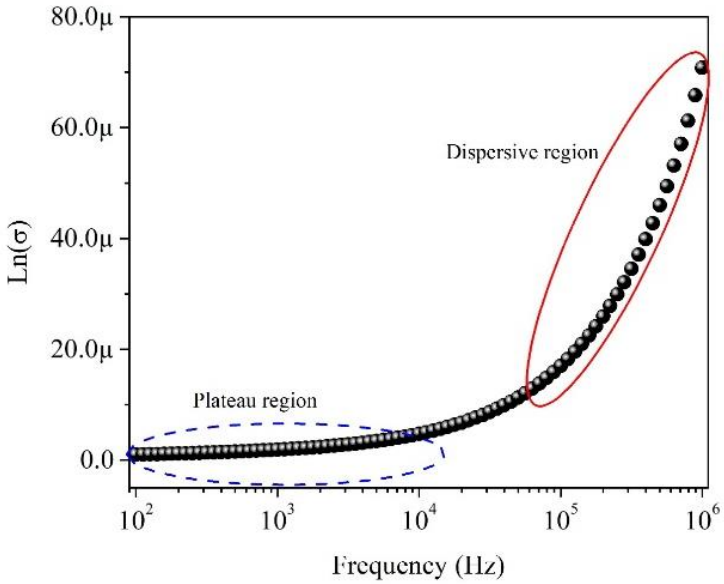

Fig. 3.8) Ln(σ) vs. Ln(frequency) plot of the Fe_2O_3 sample prepared by Pechini method. Low- frequency plateau and (b) an extended dispersion at high frequency.

The variation of conductivity in the low-frequency region is attributed to the polarization effects at the electrolyte (iron oxide pelted sample) and electrode interface. As the frequency reduces, more and more, accumulation occurs at the electrode and electrolyte interface and hence, drop in conductivity. In the intermediate frequency plateau region, conductivity is almost found to be frequency independent and is equal to dc conductivity, σ_{dc}. In the high-frequency region, the conductivity increases with the frequency. The frequency dependence of conductivity or so-called universal dynamic response (UDR) is related by a simple expression given by Jonscher power law [17]:

$$\sigma_{AC}(\omega) = \sigma_o + A\omega^n \qquad (3.25)$$

where σ_o is the limiting zero frequency conductivity, A is a pre-exponential constant and n is the power law exponent, which is between 0 and 1.

The measurement system is constructed of a quartz glass cryostat, a vacuum system, a specifically designed sample holder, various measurement sensors and devices, and a PC which are easily integrated. For electric measurements, the following instruments are used: A Keithley electrometer, model 617, for the DC measurements and an Agilent 4294A impedance analyzer for moderate to high frequencies (40–10^6 Hz). The cable type and quality is a critical issue and should not interfere with the sample electrical response [19].

The assembly sketch of the impedance spectroscopy setup, along with the cryostat and the sample holder used in this work is shown in Fig. 3.9.

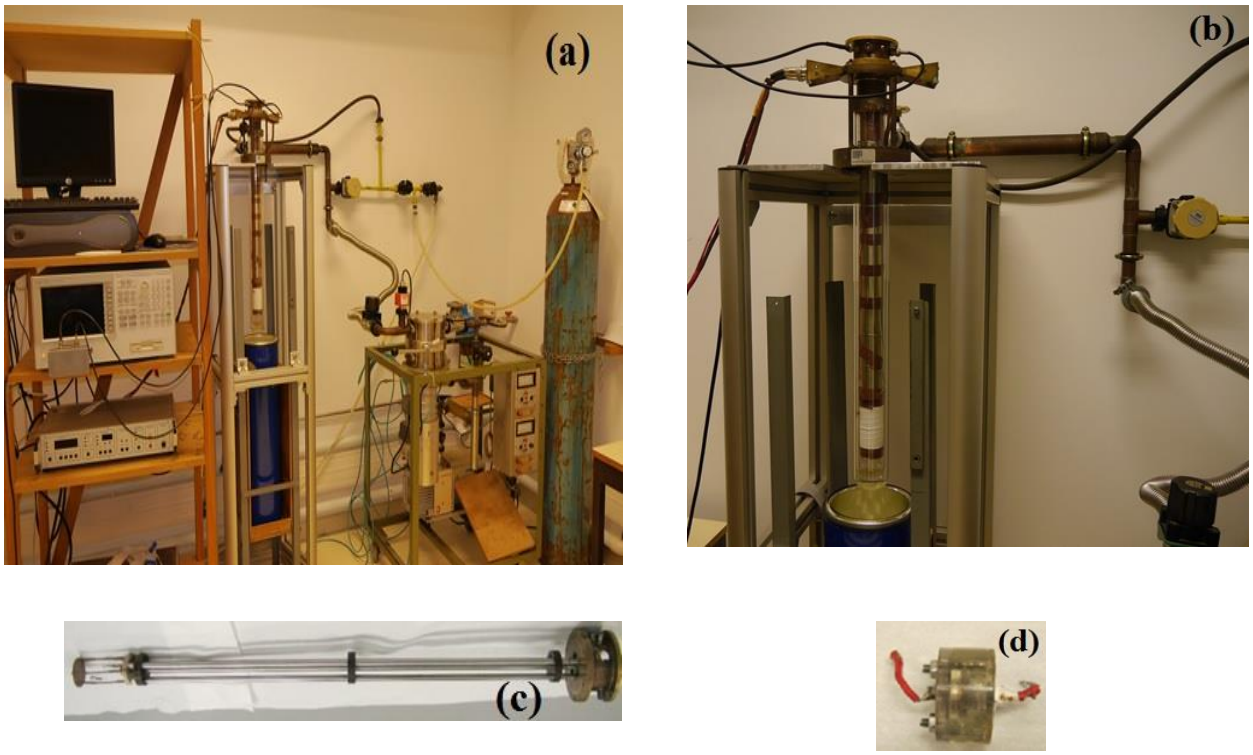

Fig. 3.9) Exterior images of a) the impedance spectroscopy setup, b) the cryostat, c) a close-up photograph of the cryostat and d) the pressured sample holder.

Usually, the samples are spring-loaded between two copper or steel electrodes. The ability to work at temperatures as low as 100 K, using liquid nitrogen as a cooling agent rather than liquid helium, is because one of the sample holder electrodes is connected to the body of the cryostat without insulation. The foremost heat insulation is a vacuum jacket surrounding the central core of the cryostat. The volume between the outer walls of the cryostat and central core of the cryostat is evacuated by a vacuum pump [20].

A LabVIEW™ program, custom made, controls and monitorizes all the electrical and dielectric experiences. The operator can choose the temperature range and steps of measurement and also the voltages (for DC measurements) and frequencies (for AC measurements) to be used in each temperature step. The temperature is controlled by an Oxford ITc4 and all communications between the personal computer (PC), and the terminals are done via the General Purpose Interface Bus (GPIB).

3.7) Magnetic measurements

The physics of nanoscale magnetic materials has been a vivid research subject in the last few decades not only for technological reasons but also for fundamental research point of view. In the last decades, thorough investigations have been made in the field of nanosized magnetic particles, because of their potential for biomedical applications such as improving the quality of MRI, hyperthermic treatment for malignant cells, site-specific drug delivery and manipulating cell membranes. However, the grand challenges in nanomagnetism require a fundamental mastery of the elementary concepts of the magnetic properties of the bulk condensed matter. Thus, in this introductory chapter, we present the field of magnetism, briefly surveying the underlying key theoretical concepts to its recent and rapid development in nanomaterials.

3.7.1) Magnetic ordering

The origin of magnetism lies in the magnetic moments (sometimes electron spins, sometimes an effective moment including contributions from both electron spin and orbital motion) are arranged and how these moments interact with one another. The magnetic ordering of materials can be categorized into the following four major groups:

a) diamagnetism;
b) paramagnetism;
c) ferromagnetism;
d) antiferromagnetism.

3.7.1a) Diamagnetism

In the diamagnetic substance, an applied magnetic field induces a magnetic moment in in the opposite direction and causing a repulsive force [21, 22].

3.7.1b) Paramagnetism

The paramagnetic material contains the atoms having a non-zero- magnetic moment due to unpaired electrons. In the presence of a magnetic field, the magnetic moments are aligned in the direction of the field, resulting in a net positive magnetization and positive susceptibility. However, by the magnetic field removal, the individual moments are directed randomly because of the very weak interaction of the magnetic moments on neighboring atoms with each other and the net magnetization is zero [21, 22]. The magnetic moment on an atom is associated with its total angular momentum $\vec{J}$ which is a sum of the orbital angular momentum $\vec{L}$ and the spin angular momentum $\vec{S}$ so that [23]:

$$\vec{J} = \vec{L} + \vec{S} \tag{3.26}$$

3.7.1.b.i) Curie law

Here with introducing a semiclassical approach, we formulate mathematically paramagnetism. In this approach we suppose $\vec{J} = \infty$ and it is ignored that the magnetic moments can be directed only along a particular alignment due to quantization. If we consider magnetic moments are lying at an angle between θ and θ+dθ in respect to the applied field $\vec{B}$ directed along the z-axis and they can sweep the semisphere with a radius of unity. The probability of occurrence of this situation at temperature T is $\exp(\frac{\mu B\cos\theta}{k_B T})\frac{1}{2}\sin\theta.d\theta$ and moments possess the energy with a net magnetic moment along $\vec{B}$ equal to μcosθ. Then, The net moment along $\vec{B}$ is then [23]

$$\langle \mu_z \rangle = \frac{\int_0^{\pi} \mu\cos\theta.\exp(\frac{\mu B\cos\theta}{k_B T})\frac{1}{2}\sin\theta.d\theta}{\int_0^{\pi} \exp(\frac{\mu B\cos\theta}{k_B T})\frac{1}{2}\sin\theta.d\theta} = \mu.\frac{\int_{-1}^{1} xe^{yx}dx}{\int_{-1}^{1} e^{yx}dx} \tag{3.27}$$

where $y = \mu B/k_B T$ and $x = \cos\theta$. This leads to

$$\frac{\langle \mu_z \rangle}{\mu} = \coth y - \frac{1}{y} \equiv L(y) \tag{3.28}$$

where $L(y)$ is the Langevin function. This function was simulated and is shown in Fig. 3.10.

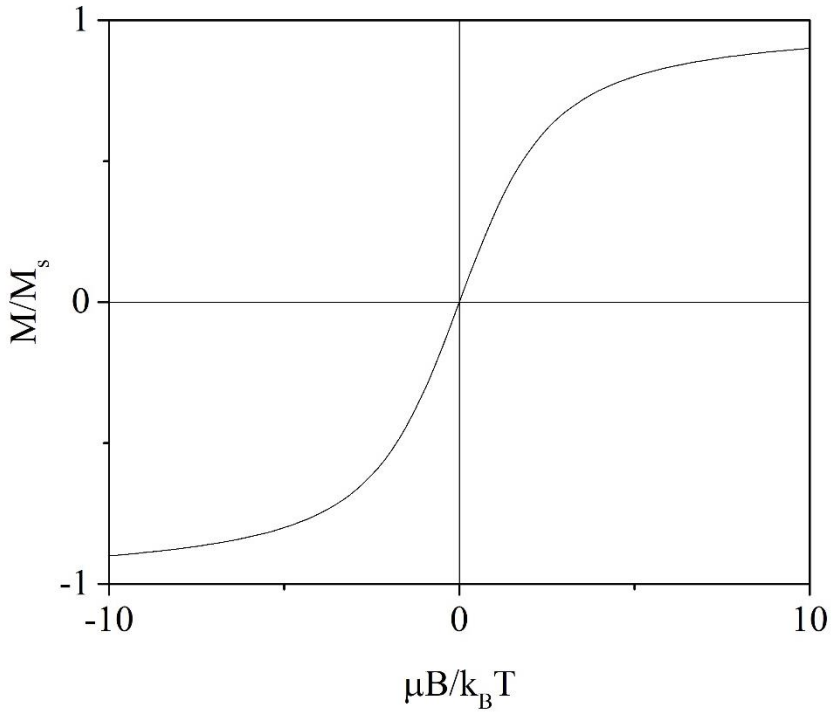

Fig. 3.10) The magnetization of a classical paramagnet described by the Langevin function.

The total magnetization is stated as $M = n\langle \mu_z \rangle$ where n stands for the number of magnetic moments per unit volume. The saturation magnetization, M_S, is the maximum magnetization in the case that all magnetic moments are aligned so that $M_s = n\mu$.

Thus we have [21]

$$\frac{M}{M_s} = \frac{\mu B}{3k_B T} \tag{3.29}$$

and small if the field is small enough and we can define the susceptibility as $\chi = \frac{M}{H}$ and

$$\chi = \frac{n\mu_o \mu^2}{3k_B T} = \frac{C}{T} \text{ and } C = \frac{n\mu_o \mu^2}{3k_B} \tag{3.30}$$

Therefore, the magnetic susceptibility is inversely proportional to the temperature, which is known as Curie's law and C is called Curie constant [21].

3.7.1.b.ii) the Brillouin function

Considering a general case from the quantum mechanical point of view, we assume that J can take any integer or half-integer value. Then, the function of total magnetization, M, is given by:

$$M = M_s . B_J(y) \tag{3.31}$$

where $M_s = n g_J \mu_B J$ is the saturation magnetization and $B_J(y)$ is the Brillouin function given by [21-23].

$$\mathrm{B_J(y)} = \left(\frac{2J+1}{2J}\right)\coth\left(\frac{2J+1}{2J}\,y\right) - \left(\frac{1}{2J}\right)\coth\left(\frac{1}{2J}\,y\right) \tag{3.32}$$

This function was simulated and is plotted in Fig. 3.11 for various values of J.
The Brillouin function has the appropriate limits. When J=∞ it reduces to a Langevin function:

$$\mathrm{B_\infty(y) = L(y)} \tag{3.33}$$

and when $J = \frac{1}{2}$ it reduces to a tanh function [21, 23]:

$$B_{\frac{1}{2}}(y) = \tanh(y) \tag{3.34}$$

Hence for the case of a low magnetic field, the susceptibility is given by

$$\chi = \frac{M}{H} \approx \frac{\mu_o M}{B} = \frac{n\mu_o \mu_{eff}^{\ 2}}{3k_B T} = \frac{C}{T} \tag{3.35}$$

Where the effective moment is expressed by

$$\mu_{eff} = g_J \mu_B \sqrt{J(J+1)} \tag{3.36}$$

So according to the Curie's law, the susceptibility has a linear relation with T^{-1}[23].

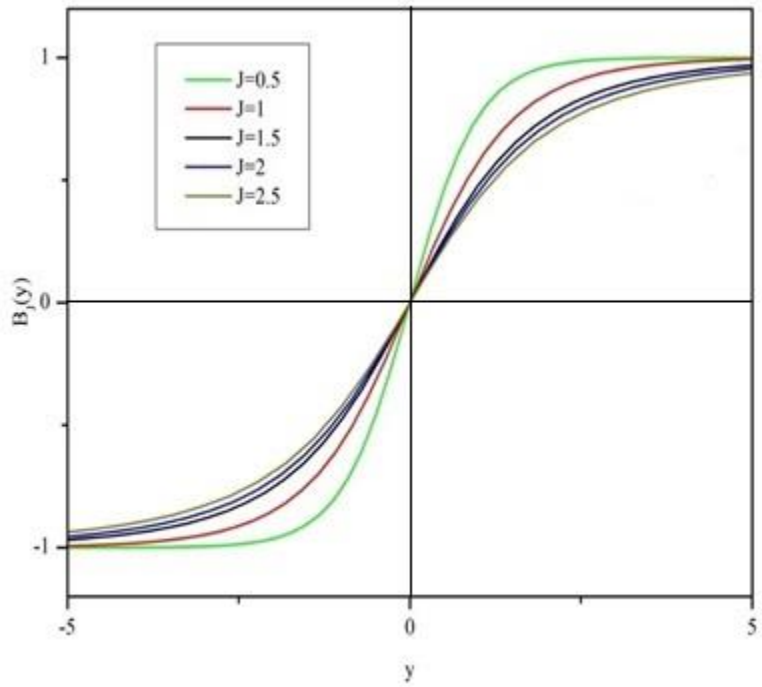

Fig. 3.11) Brillouin function, $B_J(y)$, for different values of J.

3.7.1.c) Ferromagnetism

When the interaction between the magnetic moments of each atom is considered, the substance demonstrates an interesting magnetic properties. In ferromagnetic material, the moments are aligned one parallel to another, even in the absence of any external magnetic field. This results in the possibility of obtaining a large value of susceptibility and non-zero magnetic moment even at zero applied a magnetic field (so-called spontaneous magnetization) [25].

Based on the molecular filed approach postulated by Weiss, if in equation 3.29 we substitute the applied magnetic field B with $B+\lambda_E M$, magnetization of a ferromagnet is expressed by [24],

$$M = M_S B_J\left(\frac{g_J \mu_B J}{k_B T} B + \frac{g_J \mu_B}{k_B T} \lambda_E M\right) \tag{3.37}$$

where λ_E is called Weiss coefficient. The magnetic susceptibility of ferromagnetic material can be calculated by [25]

$$\chi = \frac{M}{H} = \frac{C}{T - \lambda_E C} \tag{3.38}$$

where C is identified as the paramagnetic Curie constant (if no ferromagnetic order exists, i.e., $\lambda_E=0$). The Curie temperature, $\Theta_P=T_C=\lambda_E C$, is a critical temperature below which a ferromagnetic compound have a nonzero magnetization in the absence of an applied magnetic field. Above T_C, the sample shows paramagnetic characteristics and the moments within are disordered.

3.7.2.d) Antiferromagnetism

A simple antiferromagnet can be visualized as consisting of two magnetic sublattices (A and B) the atomic magnetic moments belonging to different sublattices have an antiparallel orientation. So, an antiferromagnet exhibits zero net magnetization (at least at zero Kelvin) [25]. The anti-alignment effect only occurs at a temperature below the Neel temperature, T_N. Below T_N the antiferromagnetic material becomes paramagnetic [25]. Above this temperature, they become paramagnetic as in the case of ferromagnetic materials.

3.7.2.e) Ferrimagnetism

Ferrimagnetism is observed only in compounds with complex crystal structures. In ferrimagnetic the magnetic moment associated with sublattice A atom is larger than those of sublattice B atoms. So they do not cancel each other and there a net magnetization, however, lower than ferromagnetic materials [24].

To Summarize, the temperature dependence of the magnetization M and the reciprocal susceptibility χ^{-1} in various types of magnetic materials have been shown in Fig. 3.12.

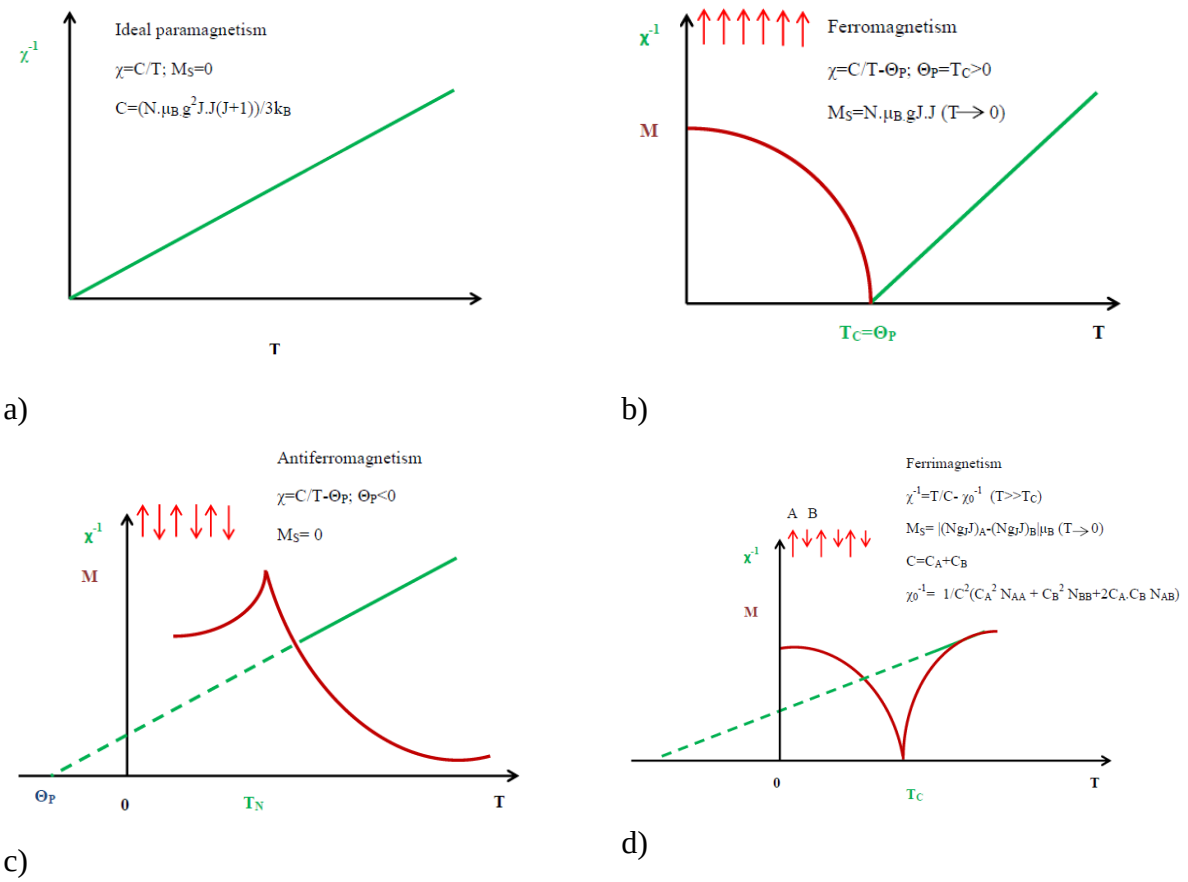

Fig. 3.12) Summary of the temperature dependence of the magnetization M, the reciprocal susceptibility χ-1 in a) ideal paramagnetism b) ferromagnetism c) antiferromagnetism d) ferrimagnetism [26].

3.7.2) Magnetic Interactions

The main types of magnetic interactions leading to having a long-range order in the iron oxides are explained in the following.

3.7.2.i) Dipole-dipole interaction

Two magnetic dipoles with moments and separated by a distance vector have the potential energy [27]:

$$E = \frac{\mu_0}{4\pi r^3}\left[\vec{m}_1.\vec{m}_2 - \frac{3}{r^2}(\vec{m}_1.\vec{r})(\vec{m}_2.\vec{r})\right] \qquad (3.39)$$

This interaction is long-range and anisotropic. The strength of this interaction depends on their separation and degree of mutual alignment. The dipolar interaction is much too weak to account for the ordering of most magnetic materials since most of the magnetic materials order at much higher temperature. However, in magnetic nanoparticle systems, where each nanoparticle has a moment $m \approx 10^3 – 10^5 \mu_B$, the energy may correspond to an ordering temperature of a few tens of Kelvins [54].

3.7.2.ii) Exchange interaction

The exchange interaction arises from the interplay of electromagnetism with quantum mechanics. This interaction usually lies at the heart of the long-range magnetic order. When the electrons on neighboring magnetic atoms undergo exchange interaction, this is known as a direct exchange. Hence, direct exchange interaction will play a leading role in nanoparticle assemblies, where the surfaces of the particles are in close contact [27]. If the exchange interaction is negative, the molecular field is oriented such that it is favorable for the nearest neighbor magnetic moment to lie antiparallel to one another.

3.7.2.iii) Superexchange interaction

When the matrix is insulating, superexchange interaction can occur via intermediate atoms or ions (e.g., oxygen) depending on the structure and the nature of the matrix and the bonding at the particle-matrix interface [28]. Exchange interactions are short ranged in insulating magnetic materials, but if the bonding is favorable, superexchange interactions may extend over large distances.

3.7.3) Magnetic anisotropy

The term magnetic anisotropy is used to describe the dependence of the internal energy on the direction of the spontaneous magnetization, creating easy and hard directions of magnetization. In the following sections, we will briefly characterize four different contributions to magnetic

anisotropy: magnetocrystalline anisotropy, shape anisotropy, strain anisotropy and surface anisotropy.

Magnetic anisotropy describes the dependence of the internal energy on the direction of spontaneous magnetization. The thus defined magnetic anisotropy energy density has the crystalline symmetry of the material and is known as crystal magnetic anisotropy or magnetocrystalline anisotropy [27].

The simplest forms of crystal anisotropies are uniaxial anisotropy in the case of a hexagonal and cubic anisotropy in the case of a cubic crystal. For example, hexagonal cobalt exhibits uniaxial anisotropy, which makes the stable direction of internal magnetization (or easy direction) parallel to the c axis of the crystal at room temperature. For uniaxial symmetry, the (free) energy is given by

$$E_{uni}^{a} = K_1 V \sin^2\theta + K_2 V \sin^4\theta \tag{3.40}$$

About the shape anisotropy, the free poles on the surface of a perfectly spherical and homogeneous sample give rise to a demagnetizing field which is collinear and linearly proportional to the magnetization vector, as described by $\vec{H}_d = -\frac{4\pi}{3}\vec{M}$.

Another effect due to the surface is related to strains. Strain anisotropy is essentially a magnetostrictive effect. Because of magnetostriction, strains are effective in the magnetization direction. This kind of anisotropy is often described by a magnetostatic energy term

$$E_{strain}^{a} = -\frac{3}{2}\lambda_s \sigma . S \cos^2\theta' \tag{3.41}$$

where is the saturation magnetostriction, σ the strain value by surface unit, S the particle surface and the angle between magnetization and the strain tensor axis.

Surface anisotropy is caused by the breaking of the symmetry and a reduction in the nearest neighbor coordination at the surface. Surface anisotropy enhances the total anisotropy of fine particles [27, 28].

3.7.4) The Origin of Nanomagnetic Behavior

Magnetic particles in the nanometer size range are necessarily single-magnetic-domain (SMD) structures and thus magnetically saturated in the absence of an external magnetic field. It has been estimated that the critical size below which a spherical particle exists as a single-magnetic-domain is given by [29]:

$$R_{SDM} = \frac{6\sqrt{AK}}{\mu_0 M_S^2} \tag{3.42}$$

Here A, the exchange stiffness, is a constant characteristic of the material related to its critical temperature for magnetic ordering [29]. The response of nanoparticles to external magnetic fields reflects characteristically different spin dynamical processes compared to those of their bulk counterparts.

3.7.5) Superparamagnetism

3.7.5.a) Ideal superparamagnetism

As mentioned in the previous section, in a single-domain particle, when a magnetic field is applied, all the spins are aligned in the same direction, and since there are no domain walls to move, its magnetization will be reversed by spin rotation. The net magnetic moment can be represented by a well-isolated single domain particle with uniaxial anisotropy and in the case of the external perturbation presence; the magnetic energy can be expressed as follows:

$$E = KV\sin^2\phi - MB\cos(\theta - \phi) \tag{3.43}$$

where ϕ and θ are the angle between the magnetic moment of the particle and the applied field and the easy axis, respectively, KV is the energy barrier that separates both equilibrium states for zero applied field and B is the applied field. Considering the case of uniaxial anisotropy when the energy barrier is much larger than the thermal energy of the system, i.e. $KV >> k_B T$. The relaxation of magnetization of these particles can be described by an Arrhenius-type law:

$$M(t) = M_o \exp(-\frac{t}{\tau}) \tag{3.44}$$

where M_o is the initial magnetization and τ is the characteristic relaxation time. Such relaxation time is a function of the energy barrier and the temperature:

$$\tau = \tau_o \exp(-\frac{KV}{k_B T}) \tag{3.45}$$

where τ_o is inversely proportional to the jump attempt frequency of the particle magnetic moment between the opposite directions of the magnetization easy-axis. For τ_m = 100 s one obtains the well-known result:

$$T_b \approx \frac{KV}{25k_B} \tag{3.46}$$

For $k_BT > KV$ case where the thermal equilibrium was already reached, an assembly of isotropic single-domain particles behaves like a paramagnet, instead of atomic magnetic moments and there is now a giant (super) moment, μ, inside each particle. This magnetization corresponds to the saturation magnetization M_S:

$$\frac{M}{M_S} = \coth(\frac{\mu H}{k_B T}) - \frac{k_B T}{\mu H} \tag{3.47}$$

In order to verify if a system behaves as an ideal superparamagnet, one should initially analyze three aspects: (i) if the reduced magnetization (M/M_S), plotted as a function of $M_S(H/T)$, results in an universal curve, known as "classical scaling law of superparamagnetism", (ii) if the magnetization isotherms are anhysteretic and (iii) if the fitted size distribution is (almost) temperature independent. In real systems, however, there are several reasons for not obtaining a good fit of an experimental curve, such as the existence of a distribution of grain sizes, a random anisotropy axis distribution, surface anisotropy (anisotropic superparamagnetism), or interparticle magnetic interactions (interacting superparamagnetism).

3.7.5.b) Interacting superparamagnetic (ISP) systems

By now we discussed the superparamagnetic models which neglecting the interaction effects of nanoparticles. Considering the role of magnetic interactions on the macroscopic physical properties, leads to compelling phenomena such as spin-glass-like behaviour, shift of blocking temperature, the existence of a slight hysteresis in fully superparamagnetic systems, the coercivity shift with concentration, the lack of agreement between magnetic and structural data and interesting remarks about the effect of magnetization on the giant magnetoresistance [30]. Taking into account the magnetic interactions between nanoparticles which have a strong influence on the superparamagnetic relaxation, the behavior of the system becomes more complicated.

Among main types of magnetic interactions which already were discussed briefly, Dipolar interactions are almost always present in a magnetic particle system and are typically the most relevant interactions. They are of a long-range character and are anisotropic. From an experimental point of view, the problem of inter-particle interactions is very complex in two aspects. First, it is very complicated to separate the effects of interactions from the effects caused by the random distributions of sizes, shapes, and anisotropy axes. Second, several interactions can be present simultaneously in one sample. [30] Furthermore, in real with more concentration systems besides the combined effect of interactions, nanoparticle shape, distribution of sizes and anisotropy axes, surface effects and surface-core should be mentioned interactions which make extremely difficult to model these systems theoretically. As the particles size decreases, a large percentage of all the atoms in a nanoparticle are surface atoms, which implies that surface and interface effects become more important [30].

3.7.6) Vibrating Sample Magnetometry system (VSM)

The VSM is based upon Faraday's law according to which an electromagnetic force (e.m.f.) is induced in a conductor by a time-varying force magnetic flux. The operation of the VSM follows as; A magnetic sample is placed on a long rod and then driven by a mechanical vibrator. The rod is positioned between the pole pieces of an electromagnet, to which detection coils have been mounted. The sample is attached to the lower end of the rod and made oscillate

vertically typically over 0.1-1.5 mm at a frequency of 85 Hz. The oscillatory motion of the magnetized sample will induce a voltage in the detection coils. The induced voltage is proportional to the sample's magnetization, which can be varied by changing the dc magnetic field produced by the electromagnet. The AC induced voltage is given by [31]:

$$\mathrm{E} = -N\frac{d}{dt}(BA\cos\theta) \tag{3.48}$$

where N is the number of wire turns in the coil, A is the coil turn area, and θ is the angle between the B field and the direction normal to the coil surface. The coils are matched, and so reject the voltage induced in the coil system by any externally applied field change. The lock-in amplifier (LIA) is tuned to the vibration frequency using a reference signal from the vibrator controller and detects the in-phase voltage from the sense coils. The sketch of our VSM is depicted schematically in Fig. 3.13.a, and a photograph of the apparatus and Variable Temperature Insert (VTI) pump and helium gas dump area is shown in Fig. 3.13.b and c .

The vibrator is driven by a sinusoidal signal from a digital function generator. The second channel of the generator supplies a rectangular signal to the Reference of the LIA. The field direction is vertical, and the VSM sense coils are designed to measure the vertical component of magnetic moment. LabVIEW™ program provides experimental control and data acquisition. The program produces a calibrated analog signal, through a National Instruments data acquisition card (DAQ), which sets the current of the power supply to provide the desired magnetic field. The program then sweeps the field from high to low, and then back to high, in steps determined by the user. At each field setting, the induced signal read by the lock-in amplifier is transferred to the computer through the GPIB bus, and the output of the thermometer probe is measured through the DAQ. Once the program completes a field cycle, the data are plotted and saved to a text file. All measurements could just as well be made using the DAQ card and analog outputs from the instruments.

Cooling materials to cryogenic temperatures have traditionally used liquid cryogens (helium). Cryo-cooler requires only mains power to operate a compressor. The compressor drives moving pistons with regenerators. The cooling takes place by the controlled expansion of the compressed helium gas.

The VSM used in the present work is a Lakeshore 7407 VSM, situated at the Department of Physics at the University of Aveiro.

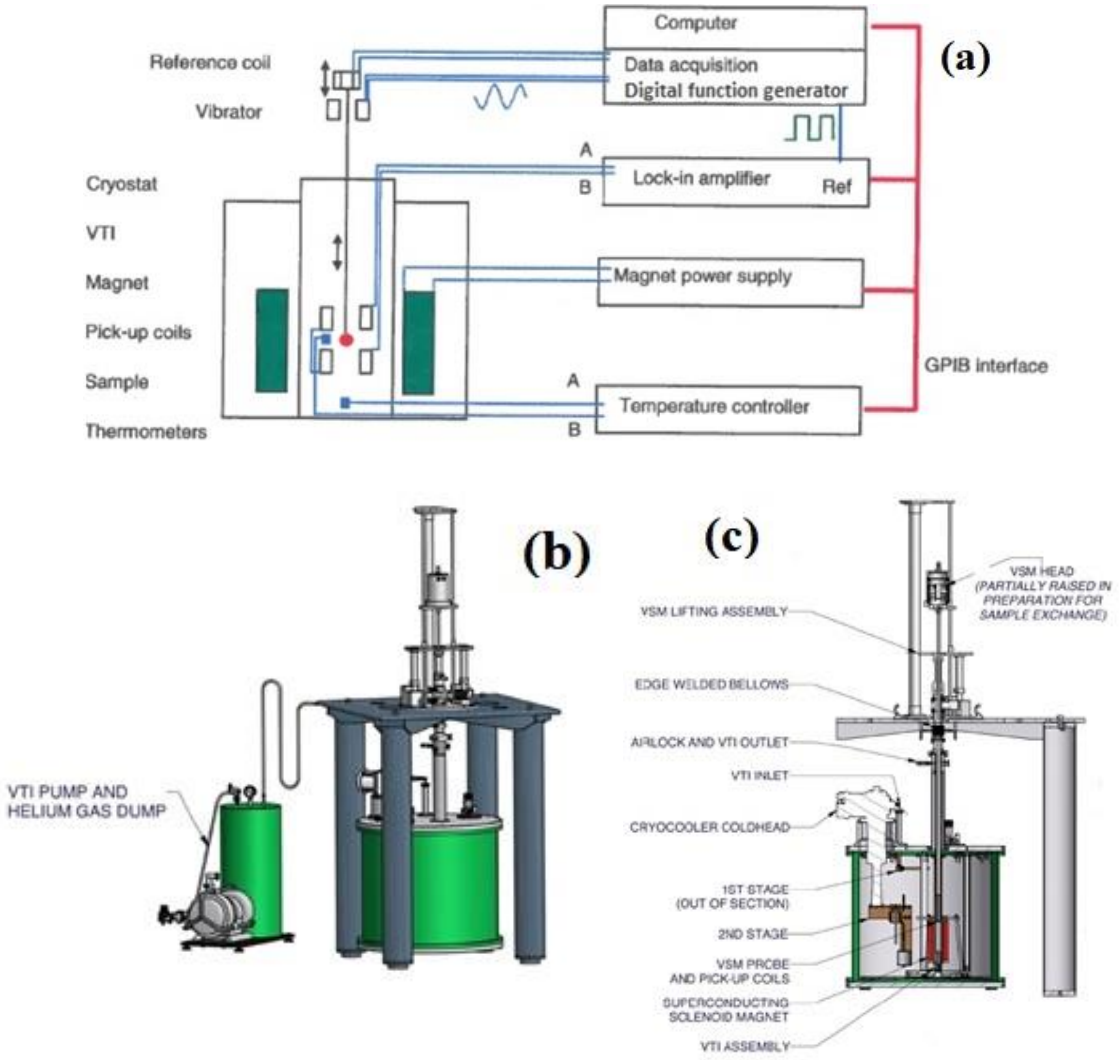

Fig. 3.13) a) Principle of a Vibrating Sample Magnetometer, b) the exterior feature of the VSM and c) the internal and external components of the VSM.

3.8) Atomic/Magnetic Force Microscopy (AFM/MFM)

The invention of atomic force microscopy (AFM) in 1986 caused a revolution in various material science disciplines [32]. The AFM technique can produce quantitative topographic images of surfaces at a magnification of up to 10^7 (subnanometer scale, some 10^3 times better than possible using an optical microscope). AFM system consists of a micro-machined cantilever probe, a sharp tip mounted to a Piezoelectric (PZT) actuator, and a position sensitive photo detector. The AFM principle is surface scanning and using a sharp tip and the measurement of atomic forces between the tip and the specimen. Forces on the tip affect the position of the cantilever, whose instantaneous position is measured by reflection of a laser beam onto the position-sensitive detector [33, 34] (Fig. 3.14).

Various techniques can be derived from the AFM depending on the forces exist between tip and surface. Beside atomic forces (van der Waals, chemical interactions, etc.), electrostatic and magnetic forces are mainly detected. While atomic forces are short-range (the van der Waals interaction energy between induced point dipoles falls off as $1/r^6$), magnetic forces are long-range (interaction between magnetic permanent dipoles falls as $1/r^3$) [35]. Thus, a magnetic force microscope (MFM) is, simply speaking, an AFM in which a magnetic probe is used to scan the sample surface while interacting with the magnetic fields of the sample [36, 37].

The most common method for MFM is called the “Two-Pass Technique” or “Hover Mode Scanning Method” [38-40]. The two-pass technique consists in measuring first a topographical image for each scan line and in the second time to produce an MFM image. The advantages of this method are easy implementation of the sample and providing high phase contrast in ambient condition [37]. Fig. 3.14 presents a schematic feature of AFM/MFM imaging techniques.

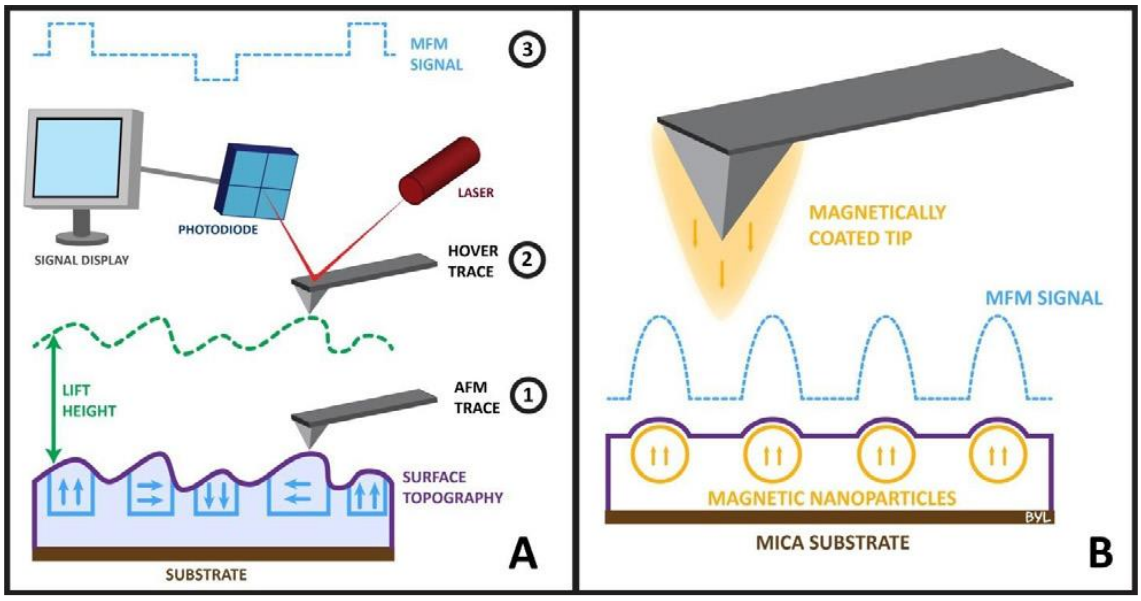

Fig. 3.14) Schematic of AFM and MFM imaging techniques [32].

As illustrated in the Fig. 3.14, on the first pass over the sample, the cantilever directly scans the surface of the sample, in its intermittent contact or "tapping" mode and the cantilever is mainly sensed by atomic interactions (e.g. Van der Waals forces). This results in a topographical image, as it would from AFM. In the second pass, the cantilever scans the sample at a small z-offset to record long-range magnetic forces and subsequently the MFM image is produced reflecting the magnetic properties of the sample [32, 35].

3.9) References

[1] R. A. Meyers (Editor), **Encyclopedia of Physical Science and Technology; Analytical Chemistry**, 2009, Springer-Verlag New York.

[2] G. Huebschen, I. Altpeter, R. Tschuncky, and H.-G. Herrmann, **Materials Characterization Using Nondestructive Evaluation (NDE) Methods: X-ray diffraction (XRD) techniques for materials characterization**, 2016, Wood head publishing.

[3] G. Will, **Powder Diffraction: The Rietveld Method and The Two-Stage Method**, 2006, Springer-Verlag.

[4] P. J. Haines, M. Reading and F. W. Wilburn, **Differential Thermal Analysis and Differential Scanning Calorimetry: Handbook of Thermal Analysis and Calorimetry. Principles and Practice**, 2004, Springer-Verlag.

[5] G. Gouadec, P. Colomban, **Progress in Crystal Growth and Characterization of Materials**, 2007, 53, 1-56.

[6] D.A. Long, **Raman Spectroscopy**, 1977, McGraw-Hill, New York.

[7] R. Yakimova, T. Paskova, I. Ivanov, K. Germanova, M. Peev, **Semiconductor Science and Technology**, 1993, 8, 2, 179-184.

[8] H. Poulet, J.P. Mathieu, **Vibration Spectra, and Symmetry of Crystals, Gordon and Breach**, 1976, New York.

[9] R.F. Egerton, **Physical Principles of Electron Microscopy: An Introduction to TEM, SEM, and AEM**, 2016, Springer.

[10] D. S. Mathew, R-Sh. Juang, **Chemical Engineering Journal**, 2007, 129, 1–3, 51-65.

[11] U. Ozgur, Y. Alivov, H. Morkoc, **Journal of Materials Science: Materials in Electronics**, 2009, 20, 789–834.

[12] C. R. Vestal, J. Z. Zhang, **International Journal of Nanotechnology**, 2004, 1, 240-263.

[13] R. A. H. El-Mallawany, **Tellurite glasses handbook: physical properties and data**, 2001, CRC Publishing.

[14] M. P. F. Graça, **Electrical measurements, Introduction, Concepts and Applications**, 2018, Nova Science Publisher.

[15] N. F. Mott and E. A. Davis, **Electronic Processes in Non-Crystalline Materials**, 2nd ed., 1979, Clarendon Press, Oxford.

[16] A L Efros and B I Shklovskii, **Electronic Properties of Doped Semiconductors**, (Berlin: Springer, 1984)

[17] E. Barsoukov, J. Ross, Macdonald, **Impedance Spectroscopy: Theory, Experiment, and Application**, 2005, Wiley and Sons.

[18] Andrzej Lasia, **Electrochemical Impedance Spectroscopy, and its Applications**, 2005, Springer.

[19] Y. Melman, S. Batltiansaki, and Y. Tsur, **Instrumentation Science and Technology**, 2005, 33, 279-287.

[20] B. Igarashi, T. Christensen, E. H. Larsen, N. B. Olsen, I. H. P. T. Rasmussen and J. C. Dyre, **Review of Scientific Instruments**, 2008, 79, 045105.

[21] S. Blundell, **Magnetism in Condensed Matter**, 2001, New York: Oxford University Press.

[22] J. M. D. Coey, **Magnetism and Magnetic Materials**, 2010, Cambridge University Press.

[23] S. Bedanta, W. Kleemann, **Topical Review: Supermagnetism**, 2009, Journal of Physics D: Applied Physics, 42, 013001.

[24] N. Magnani, **Ferromagnetism, Encyclopedia of Condensed Matter Physics**, 2005, 201-210.

[25] A. P. Guimarães, **Principles of Nanomagnetism**, 2009, Springer-Verlag Berlin Heidelberg.

[26] G. C. Papaefthymiou, **Review: Nanoparticle magnetism, Nano Today**, 2009, 4, 438-447.

[27] R.C. O'Handley, **Modern Magnetic Materials: Principles and Applications**, 2000, John Wiley and Sons, New York.

[28] J. Jorzick, C. Kramer, S. O. Demokritov, B. Hillebrands, B. Bartenlian, C. Chappert, D. Decanini, F. Rousseaux, E. Cambril, E. Sondergard, M. Bailleul, C. Fermon, A. N. Slavin, **Journal of Applied Physics**, 2001, 89, 7091–7095.

[29] M. R. Scheinfein, K. E. Schmidt, K. R. Heim, G. G. Hembree, **Physical Review Letter**, 1996,76, 9, 1541.

[30] A.H. Morrish, **The Physical Principles of Magnetism**, 1965, Wiley, New York.

[31] S. Foner, **Journal of Applied Physics**, 1996, 79, 4740.

[32] G. Cordova, B. Y. Lee and Z. Leonenko, **Nano World Journal**, 2016, 1, 2, 10-14.

[33] N. Jalili, K. Laxminarayana, **Mechatronics**, 2004, 14, 8, 907-945.

[34] P. Eaton, P. West, **Atomic Force Microscopy**, 2010, Oxford.

[35] H. H. Hans, P. Oepen, **Magnetic Microscopy of Nanostructures**, 2005, Springer-Verlag Berlin Heidelberg.

[36] A. de Lozanne, **Microscopy Research and Technique**, 2006, 69(7), 550-562.

[37] V. Karoutsos, **Journal of Nanoscience and Nanotechnology**, 2009, 9(12), 6783-6798.

[38] C. W. Hsieh, B. Zheng, S. Hsieh, **Chemical Communications**, 2010, 46(10), 1655-1657.

[39] G. Cordova, S. Attwood, R Gaikwad, F. Gu, Z. Leonenko, **Nano Biomedicine and Engineering**, 2014, 6(1), 1-12.

[40] C. S. Neves, P. Quaresma, P. V. Baptista, P. A. Carvalho, J. P. Araújo, **Nanotechnology**, 2010, 21(30), 305706.

This page intentionally left blank

Chapter 4 - Effect of iron oxide concentration on the dielectric properties of iron oxide doped silica glasses prepared by Sol-gel method

4.1) Introductory remarks

Recently, iron oxide-silica nanocomposites have been extensively investigated for diverse applications, for instance; in magnetic hyperthermia due to their biocompatibility property [1], in the microwave and electronic devices [2], in catalysts [3] as well as sensors [4]. Iron oxide nanocomposites can be synthesized by several methods including chemical methods such as sol-gel, coprecipitation, hydrothermal [4-6] or physical methods like laser ablation, mechanical milling and sputtering [7-9]. Among these methods, the sol-gel process has been employed extensively for fabrication of nonmetallic sieving matrices with nano scale pores [2]. For technological applications, it is important that the nanosize particles systems should not agglomerate by decreasing the particle diameter to the superparamagnetic range. Therefore, the size of magnetic nanoparticles and the magnetic interaction between should be considered [1]. In sol-gel method several organic or inorganic materials including polymers, dextran, chitosan or silica have been employing to coat the magnetic nanoparticles [10]. Among them silica is is most commonly used [10]. Using of $Si(OC_2H_5)_4$ with $Fe(OC_2H_5)_3$ or iron (III) acetylacetonate were led to α-Fe_2O_3 nano particles [11]. It has been observed that replacing $Fe(NO_3)_3$ with $Fe(OC_2H_5)_3$ as starting materials formed γ-Fe_2O_3 for heat treatment less than 900 ^oC and α-Fe_2O_3 at higher temperature [2]. However, the introduction of magnetic nanoparticles into silica matrix is resulted in reducing in net magnetization. The behavior can be described in term of the occurrence of surface spin induced by silica coating. Such a core-shell structure modifies the magnetic response the nanoparticles and determines their physical properties [1].

On another side, the electrical properties of iron oxide nano particles dispersed in the insulating amorphous silica can be described regarding each component, the degree of dispersion and the interaction between components [12, 13]. The addition of iron oxide fillers can lead to significant enhancement in the electrical conductivity of the compositions [13].

In this chapter, the effect of Fe/Si ratio on the electrical and structural properties of heat treated iron oxide nano particles embedded in silica matrix prepared by the sol-gel method will be investigated. Different composition of dried gels (0.5%, 1%, 2%, 10% and 20% mole of Fe_2O_3 in a SiO_2 matrix) were heat-treated (HT), in air, at temperatures up to 1400 ^oC. The structure and morphology of the obtained glasses and glass–ceramics were studied by X-ray powder diffraction (XRD), Raman spectroscopy and scanning electron microscopy (SEM). The dc electrical conductivity (σdc) was measured in the temperature range 140–400 K by the two probe method using a Keithley 617 programmable electrometer/source. The impedance spectroscopy measurements were carried out at room temperature, in the frequency range of 1 Hz-100 kHz using an Agilent 4294A precision impedance analyser, in the Cp-Rp configuration. The dc magnetic measurements were performed on powder samples (50–100 mg) using a vibrating sample magnetometer-VSM (Cryogenic–Cryofree). The dc mag-netization was recorded on field-cooled (FC) under 0.1 T, between 5 and 300 K. Typical hysteresis curves were ob-tained at several temperatures (5-300 K), for all samples in magnetic field up to 10 T. The magnetic parameters such as saturation magnetization (Ms), coercivity (Hc) and mag-netic moment are obtained from the VSM results.

4.2) Experimental procedure

In this work iron nanoparticles embedded in the SiO_2 glassy matrix were synthesized by sol-gel method. In the preparation of each batch of samples, firstly, clear solutions were prepared using 5 ml tetraethylorthosilicate (TEOS-Merck), ethanol (C_2H_5OH-Merck) and deionized water (H_2O) in the molar ratio of 1:3:8, respectively. To increase the hydrolysis velocity, HCl was added to this solution (pH≈1). After iron nitrate ($Fe(NO_3)_3.9H_2O$-98%-Merck) was mixed to the previous solution to reach the Fe:Si molar ratios of 1:99 (sample 1Fe/Si), 2:98 (sample 2Fe/Si), 10:90 (sample 10Fe/Si) and 20:80 (20Fe/Si). For the polymerization and condensation reactions, the final solution was stirred for 2 h at room temperature. After, it was poured into Petri dishes and allowed to gellify and dried at 40 ^oC for 2 weeks. The dried samples were heat-treated in air conditions, in an electric furnace, using different heating rates of 5, 10 and 20 ^oC/min up to 1400 ^oC, and a dwell time of 4 hours for all experiences. The preparation process is shown schematically in Fig. 4.1.

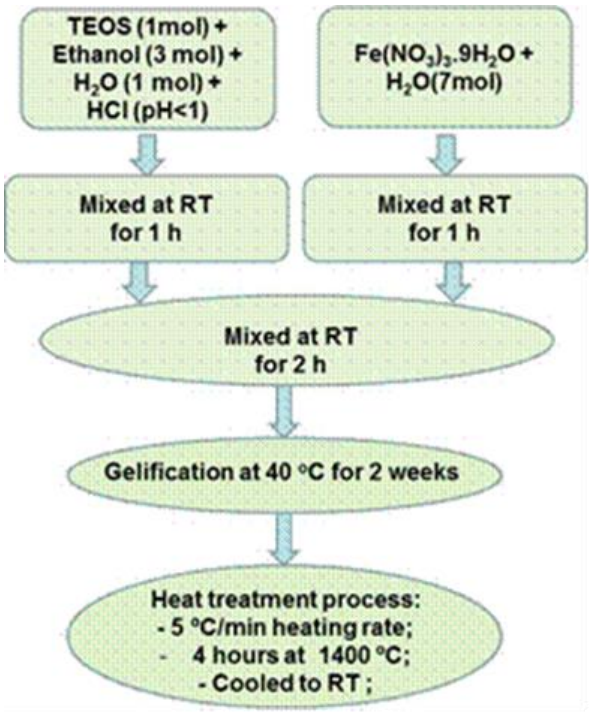

Fig. 4.1) Scheme of the solgel process for the preparation of iron oxide-silica compositions heat treated with rate of the 5 ºC/min up to 1400 ºC.

X-ray diffraction patterns were obtained at room temperature, in a Philips X'Pert system, with a Kα radiation (λ=1.54056) at 40 kV and 30 mA, with a step of 0.04º and a scan step time of 40 s. The Raman spectroscopy of bulk samples was carried out in a T64000 Jobin Yvon SPEX spectrometer, using an Ar laser (λ = 532 nm) as excitation font. The spectra were obtained, in a back-scattering geometry, between 100 and 1000 cm^{-1}. The microstructure of the samples was assessed using scanning electron microscopy (SEM) in a Hitachi S4100-1.

For the electrical measurements, the opposite sides of the bulk samples were painted with silver paste. The dc electric conductivity (σ_{dc}) was measured with a Keithley electrometer, model 617, as a function of the temperature (80–370 K). The impedance spectroscopy measurements were carried out at room temperature, in the frequency range of 1 Hz–100 kHz using an Agilent 4294A precision impedance analyzer, in the Cp-Rp configuration.

The dc magnetic measurements were performed on powder samples (50–100 mg) using a vibrating sample magnetometer-VSM (Cryogenic–Cryofree). The dc magnetization was recorded on field-cooled (FC) under 0.1 T, between 5 and 300 K. Typical hysteresis curves were obtained at several temperatures (5–300 K), in magnetic field up to 10 T. The magnetic

parameters, such as saturation magnetization (Ms), coercivity (B_c) and magnetic moment, were obtained from the VSM results.

4.3) Structural and morphologic results

The effect of the heating rate on the crystallization of the prepared glasses was studied. Therefore three compositions, 1Fe/Si, 2Fe/Si and 10Fe/Si, were heat treated with three different rate R= 5, 10 and 20 ºC/min) up to 1000 ºC for 4h. According to Fig. 4.2, overally the degree of crystallinity increase when the sample is heat treated rapidly.

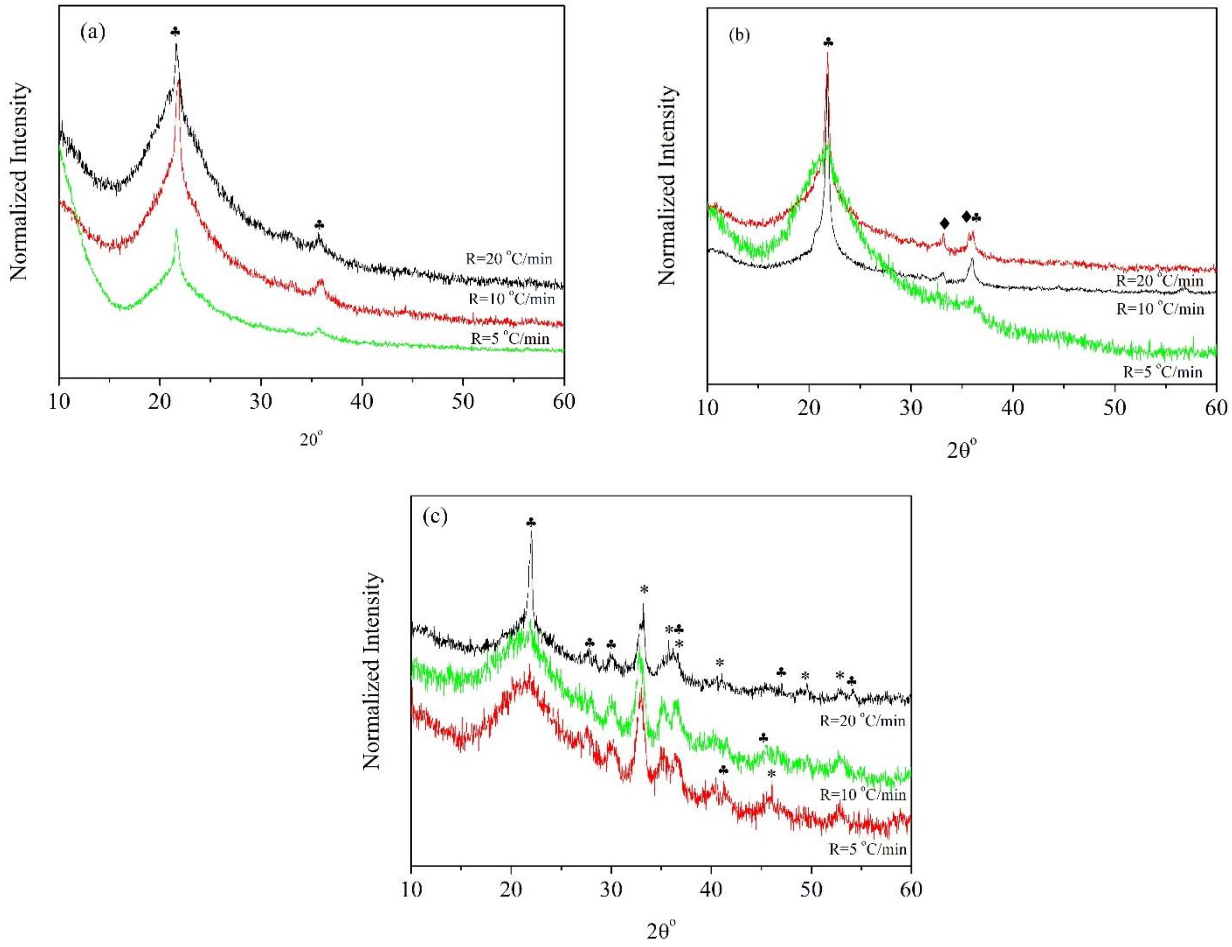

Fig. 4.2) XRD patterns of a) 1Fe/Si, b) 2Fe/Si and c) 10Fe/Si samples treated at 1000 ºC with different rates (5, 10 and 20 ºC/min) for 4h. (♣ and ♦ denote cristobalite and hematite, respectively.)

the XRD results show that high heating rates only led to an increase in the size of the cristobalite crystallites without any significant promotion in the iron oxide phase crystallization. It is also found that the crystalline formation of hematite phase depends on the iron oxide concentration. Moreover, there was no detectable crystallization of iron oxide phase in 1Fe/Si, independently of heating rate. Only 2Fe/Si heat treated with the highest rate shows the appearance of a nanoscale hematite phase. It can be said the heat treatment with the lowest rate, 5 ºC/min, reduce the possibility of forming the cristobalite phase. Therefore, the heat treatment rate of 5 ºC/min was selected as the optimized heating rate.

The evolution of the microstructure of the glass-ceramic as a function of iron oxide concentration is displayed in Fig. 4.3.

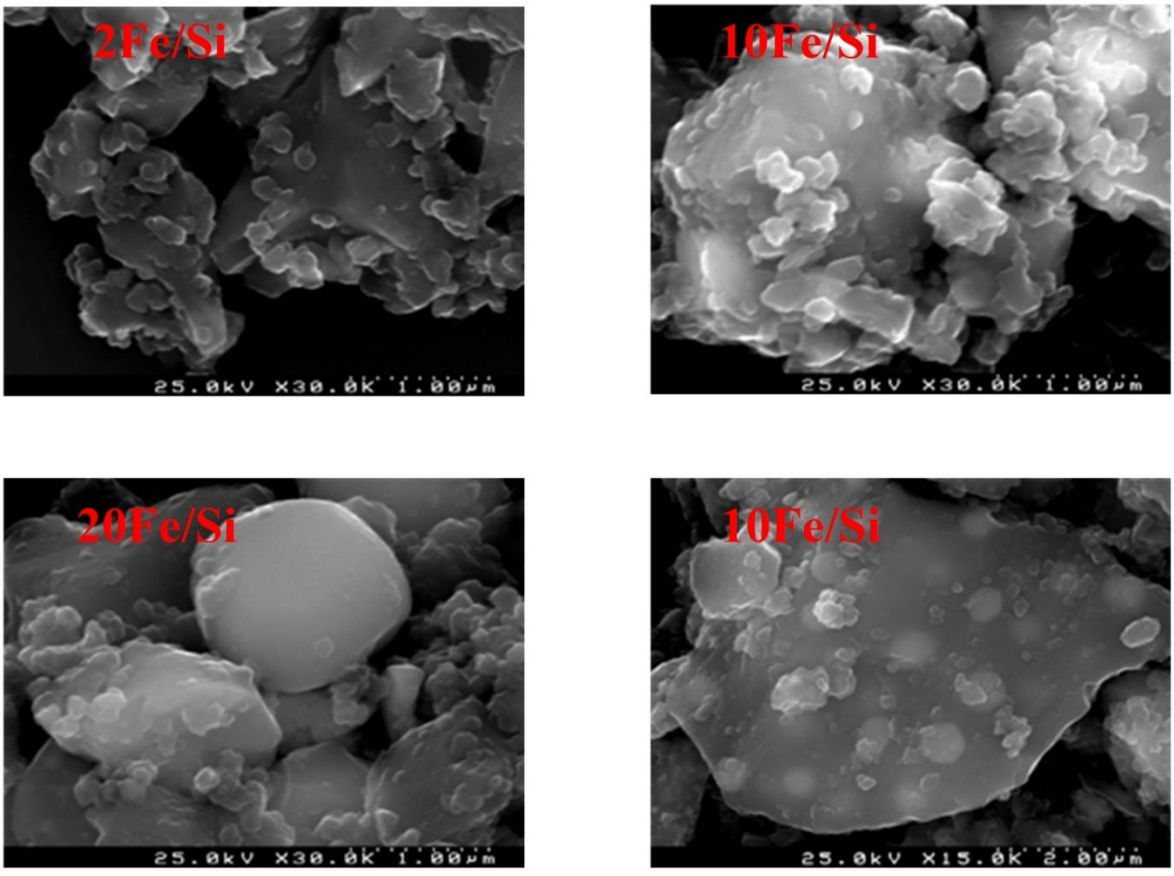

Fig. 4.3) SEM micrographs of samples treated with a heating rate of 5 ºC/min at 1000 ºC for 4h.

Polygonal crystals (200 nm to 1 μm in length) were presented after heat treatment at 1000 ºC. The final microstructure of 2Fe/Si consists of a few polymorph crystals of with a large amount of glassy matrix. In consistency with XRD results, the crystallinity is improved when the iron oxide content of glass composition increases.

From the XRD and SEM results, it can be suggested that the heat treatment temperature is insufficient to form the iron oxide crystallines specifically in the case of the compositions with low Fe_2O_3 content. Therefore, we applied an increase in the heat treatment temperature, up to 1400 ºC, and study the effect of the Fe/Si molar ratio on the physical properties of the glass ceramics heat treated at 1400 ºC with a heating rate of 5 ºC/min for 4 h.

Fig. 4.4 shows the XRD patterns of all samples treated at 1400 ºC with a heating rate of 5 ºC/min. In all samples the SiO_2, cristobalite, the phase is observed. Hematite (Fe_2O_3) phase starts to be detected in the samples with an iron concentration higher than 2.0%.

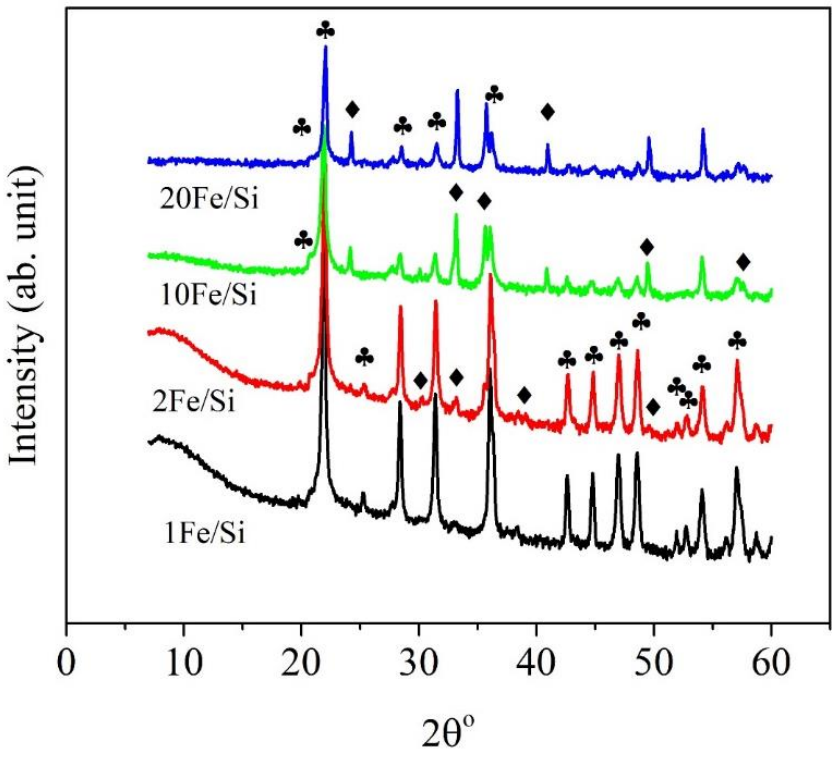

Fig. 4.4) XRD spectra of all samples treated at 1400 ºC with a heating rate of 5 ºC/min for 4 h (♦ α-Fe_2O_3; ♣ SiO_2).

Raman spectrum of the samples treated with the heating rate of 5 ºC/min at 1400 ºC is presented in Fig. 4.5. For each spectrum, the baseline was initially corrected the background effect removed and then the baseline-corrected spectrum was normalized with respect to the most intense peak in each spectrum. It can be seen that for samples with iron concentration below 20%, broad bands are present suggests the existence of an amorphous phase. The increase of the iron concentration leads to a decrease in the broadness of the bands due to an increase in the crystallinity of the samples, agreed with XRD results.

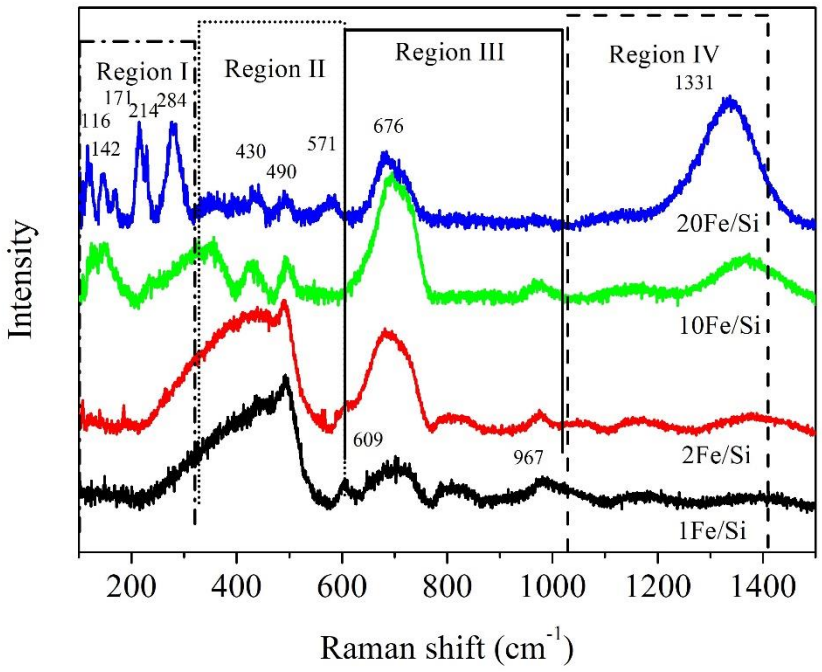

Fig. 4.5) Raman spectra of the samples with 1 < x < 20 % of Fe_2O_3 treated with a heating rate of 5 ºC/min at 1400 ºC for 4 h.

The Raman spectra are divided into the 4 regions. In the region, I, the bands below 200 cm^{-1} corresponds to the SiO_4 transition mode [14] which are absent in the sample with an iron concentration below 10%. Moreover, in the low-frequency region, the bands at 214 and 284 cm^{-1} are assigned to A_{1g} and E_g modes of α-Fe_2O_3 phase, respectively. As the iron content increases, the appearance of these bands gradually changes from a shoulder-like hump to intense and sharp bands. The presence of the bands at 214 and 284 cm^{-1} in 1Fe/Si and 2Fe/ Si, shows that this crystal phase already exists in those samples. However, the size is not big enough to be detected by the XRD. The band at around 430 cm^{-1} assigned to Si-O-Si in amorphous silica [15] whose intensity decrease with iron concentration. The bands at 490 and

571 cm^{-1} are related to FeO_4 vibration mode in hematite [16]. The last band is more apparent in 20Fe/Si. The band at 676 cm^{-1} located in the mid-range frequency region is related to Fe-O band assigned to the longitudinal optical (LO) E_u mode of hematite [16, 17] and it is diminished as the iron oxide molar ratio decreases. In addition, shoulder-like mark at 609 cm^{-1}, only found in 1Fe/Si, is identified as transverse optical (TO) E_g mode in hematite [17]. On the other side in region III there is a small band of 967 cm^{-1} corresponding to Fe-O-Si vibration mode due to distortion of silicate tetrahedral structural units [14]. In the high-frequency region, Region IV, and the band at 1331 cm^{-1} is attributed to the second order magnon Raman scattering in hematite [18]. This band strongly depends on the molar ratio of iron oxide; with increasing of the iron concentration in glass ceramic, the intensity, and area of this bands increase.

4.4) Electrical results

DC electrical conductivity measurements have been carried out for all composite. DC conductivity Vs. the iron oxide content plot of the samples, measured at room temperature, is presented in Fig. 4.6.

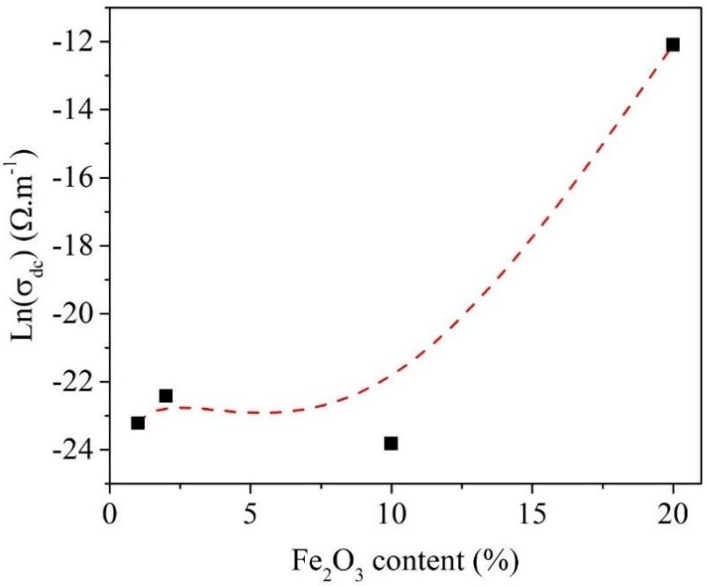

Fig. 4.6) DC conductivity measured at room temperature in function of the iron oxide content of samples treated with a heating rate of 5 ºC/min at 1400 ºC for 4 h. (the dashed line is a guide for the eye.)

According to the Fig. 4.6, there is significantly rising in dc conductivity for the sample containing 20% iron oxide as a result of the presence of the pre-dominant number Fe ions in the silicate glass structure as network modifiers and enhancement in the charge carriers' mobility. [19]. It has been indicated that the dc conductivity in the system Fe_2O_3–SiO_2 can be described in term with small polaron hopping between Fe^{2+} and Fe^{3+} sites [13].

The Ln (σ_{dc}) plots as a function of $1000.T^{-1}$ for the investigated samples are illustrated in Fig. 4.7. The nearest-neighbor-hopping (NNH) model can explain the conduction mechanism of the compositions containing semiconductors using the following equation [20]:

$$\sigma_{dc}=\sigma_o \exp(-\Delta E_{NNH}/k_B T) \quad (4.1)$$

where σ_o is a constant, $k_B=1.38\times10^{-23}$ J.K^{-1} is the Boltzmann constant and ΔE_{NNH} is defined as the activation energy of the nearest neighbor hopping.

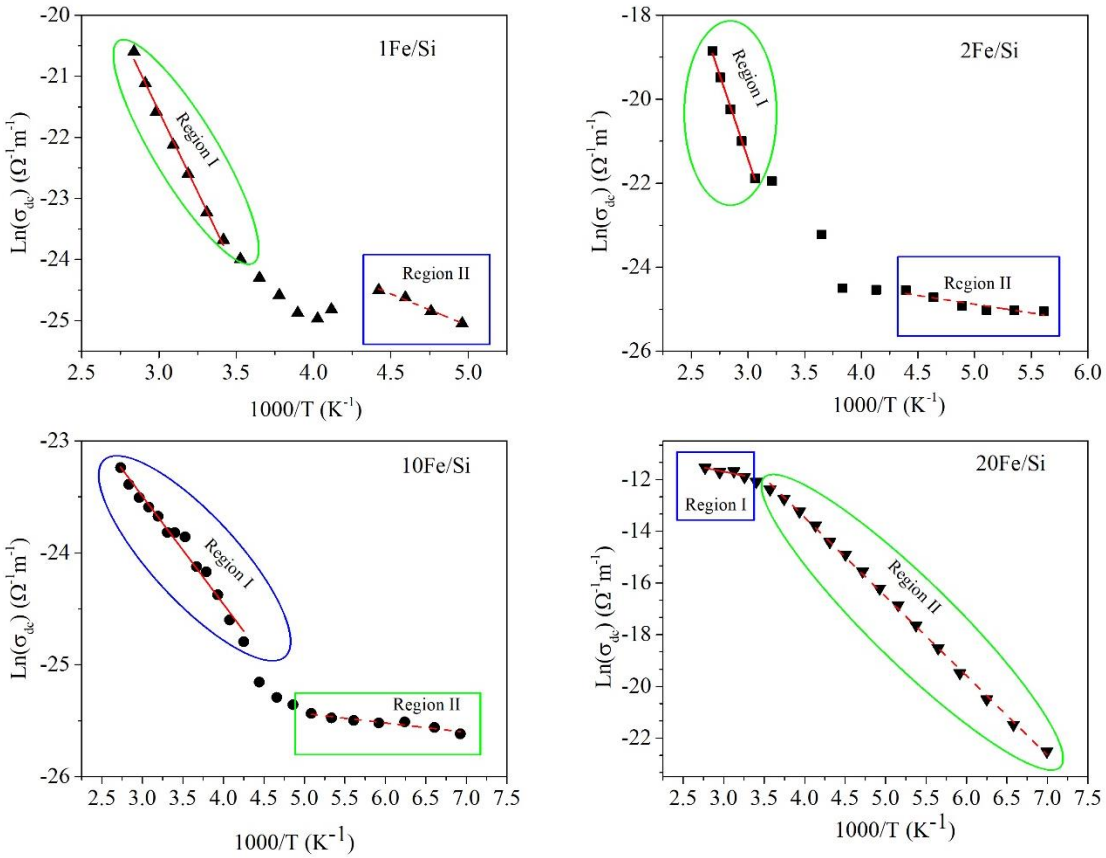

Fig. 4.7) DC conductivity in function of 1000/T of samples treated with a heating rate of 5 ^oC/min at 1400 ^oC for 4 h.

As depicted in Fig. 4.7, each graph can be divided into the high-temperature region, region I, and the low-temperature region, region II. The ΔE_{NNH} values are obtained by linear fitting of the curves for each region according to the equation and listed in table 4.1. As seen in the table, the activation energy value of the region I, for all sample expect to 20Fe/Si, was found to be much bigger than one of the region II.

Table 4.1) The derived data from the fitting to equation 4.1.

Sample	ΔE_{NNH} (Region I) ($kJ.mol^{-1}$)	ΔE_{NNH} (Region II) ($kJ.mol^{-1}$)
1Fe/Si	43.74	8.63
2Fe/Si	66.63	3.48
10Fe/Si	8.01	0.70
20Fe/Si	5.20	30.44

As seen in Fig. 4.8 from the dependence of dielectric constant with temperature at 100 kHz, the ε´ maintains almost constant in the temperature range between 200 and 380 ºC for the samples containing 0.5, 1, 2 and 10% iron oxide, showing that low amount Fe_2O_3 in the compositions cannot influence the structural modification. While for the 20Fe/Si, one can observe the highest dielectric constant which attributed to the increase in the number of Fe_2O_3 crystallites dispersed in the glass network [19].

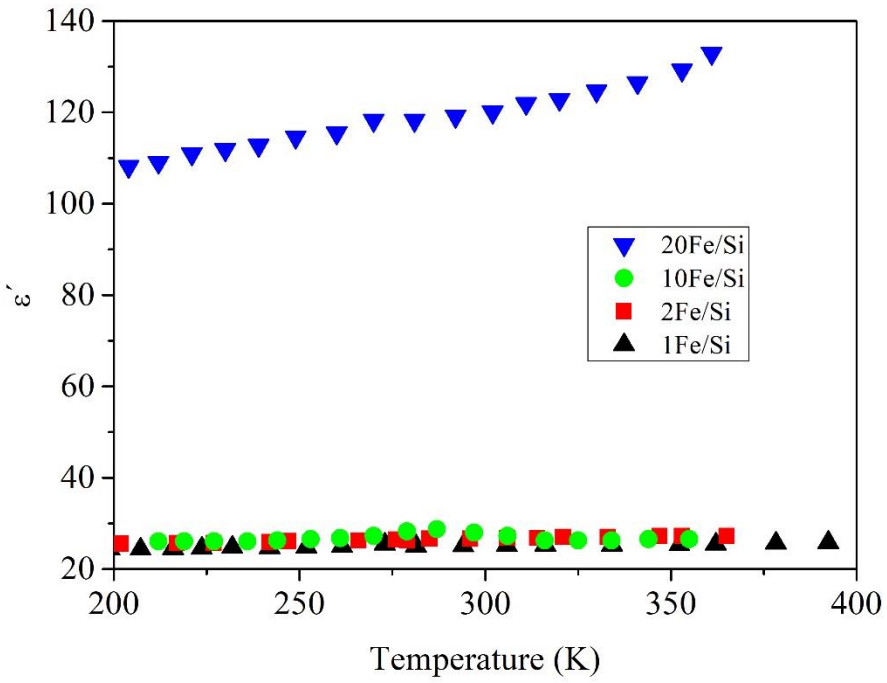

Fig. 4.8) Dielectric constant in function of temperature at 100 kHz of samples with a heating rate of 5 ºC/min at 1400 ºC for 4 h.

The dielectric constant plot (ε′) as a function of temperature at selected temperatures for all samples are shown in Fig. 4.9. The ε′ decreases slowly with increasing in frequency. The high ε′ value in the low-frequency region is due to the ionic, space charge and interface polarization contributions [20]. Also, the dielectric constant value in the low-frequency region values in lower frequencies get bigger as the temperature rises up confirming the relaxation process is thermally activated [20]. At higher frequencies, dielectric constant becomes independent of frequency. These results from the fact that the electric dipoles are unable to follow the rapid alternation of the applied field [21].

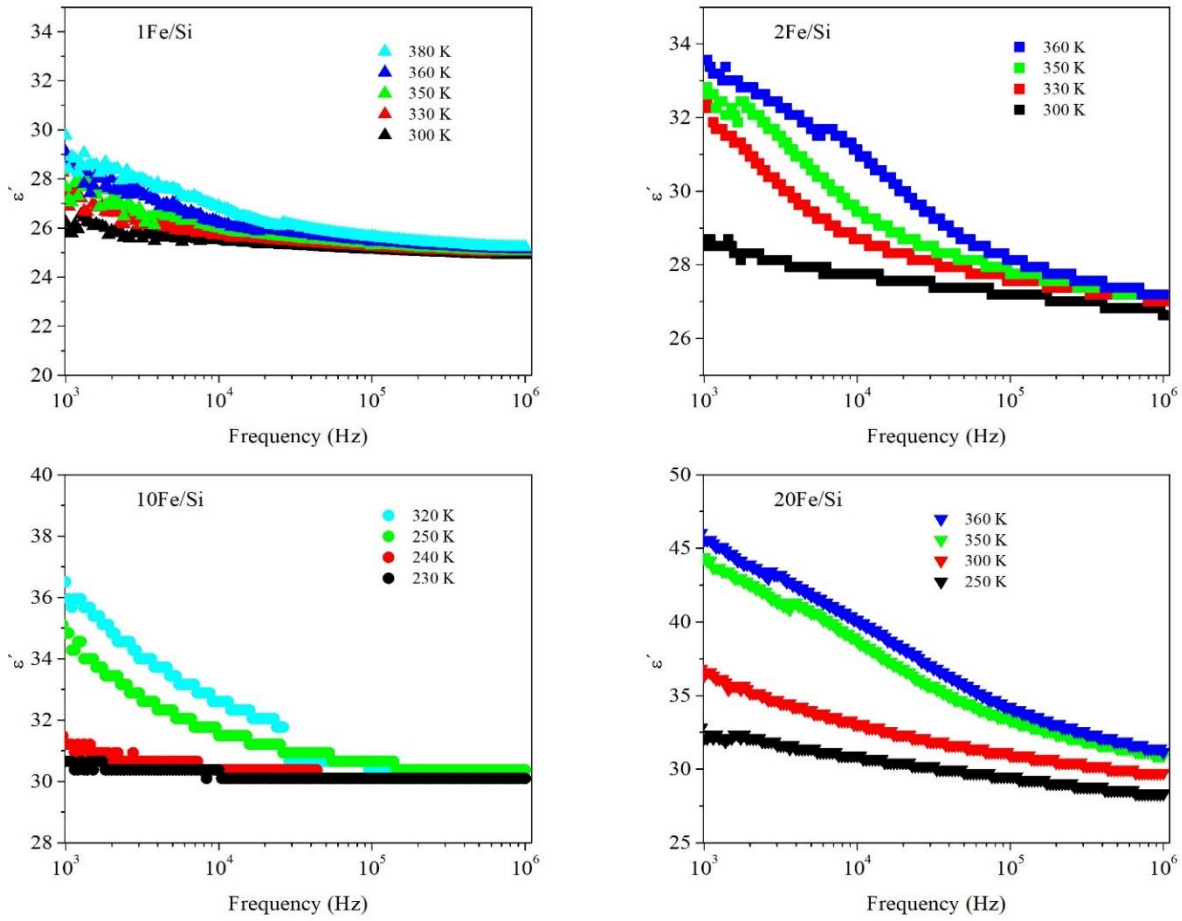

Fig. 4.9) Frequency dependence of dielectric constant of the heat treated xFe/Si (x=1, 2, 10 and 20) with a heating rate of 5 ºC/min at 1400 ºC for 4 h, measured at selected temperatures.

Fig. 4.10 shows the frequency dependence of ε´´ measured at several temperatures. It is observed that the dispersion feature of ε´´ is similar to the one for ε´ in 1Fe/Si. While the variation of ε´´ with frequency in other samples exhibits the relaxation steps which shift towards lower frequencies with decreasing temperature.

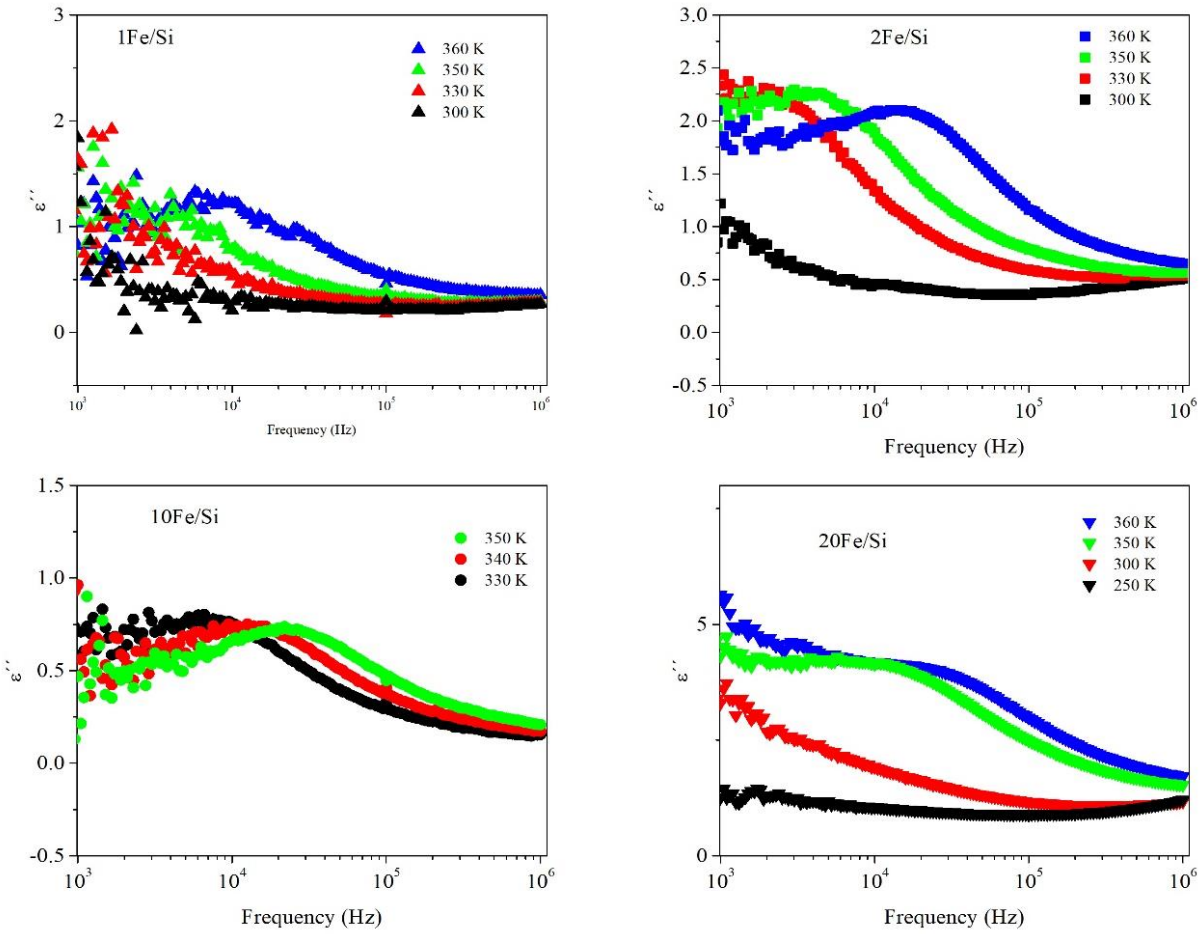

Fig. 4.10) The imaginary part of permittivity in function of frequency measured at several temperatures for all samples treated with a heating rate of 5 ºC/min at 1400 ºC for 4 h.

To investigate the dielectric relaxation of the samples, the dielectric modulus spectra as a function of frequency have been derived. As illustrated in Fig. 4.11, in the samples consisting Fe_2O_3 higher than 1%, the interfacial relaxation process can be assigned to the polarization of dipoles formed between the samples surface and the electrodes. Also, the existence of non-symmetric maximum for M´´ confirms that there is a distribution of relaxation time. Moreover, the M´´ maximum shifts to higher frequency when the measurement temperature rises which can be related to a decrease in the relaxation time due to easier depolarization, as well as the dielectric relaxation mechanism, is thermal activated [22, 23].

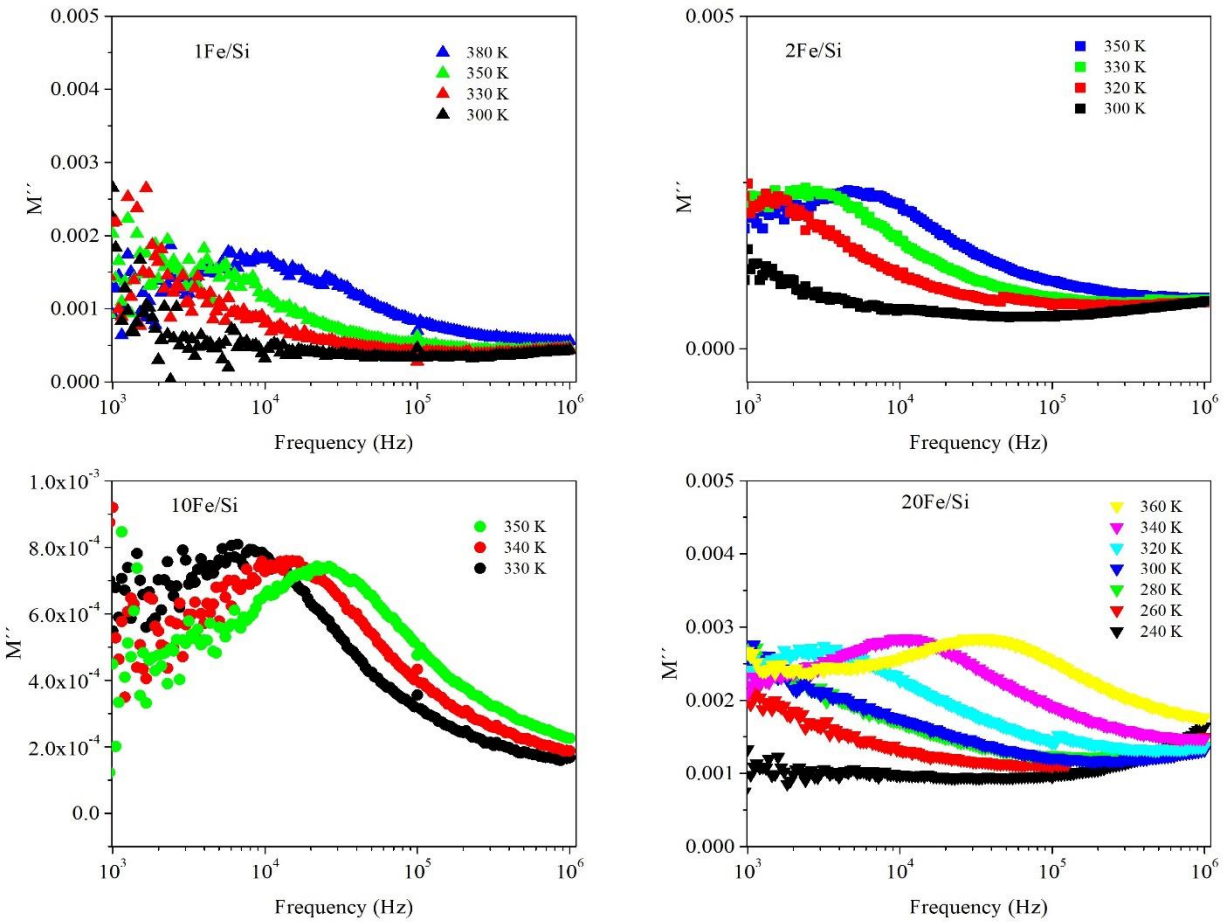

Fig. 4.11) Imaginary part of the dielectric modulus in function of frequency, for xFe/Si samples (x=1, 2, 10 and 20%) treated with a heating rate of 5 ºC/min at 1400 ºC for 4 h.

4.5) Magnetic results

Fig. 4.12 depicts the magnetic hysteresis (M–H) loops of 1Fe/Si and 2Fe/Si heat-treated at 1400 ºC derived at 300 K and 5 K. As it can be seen the saturation magnetization for 5 K for both samples larger than that in 300 K. At low temperature the thermal energy is neglected and the magnetic moments can follow external field and the total magnetic moment increases. As the temperature increases, the thermal energy played a dominant role and the magnetic moments became more disorder which made the total magnetic moment decrease. Additionally the magnetic moment in 2Fe/Si almost 2 times bigger than that of 1Fe/Si. It is not surprising that with an increase in the iron concentration in the glass-ceramic the number of magnetic moments and corresponding interactions between them increases resulting in the enhancement of the total magnetization.

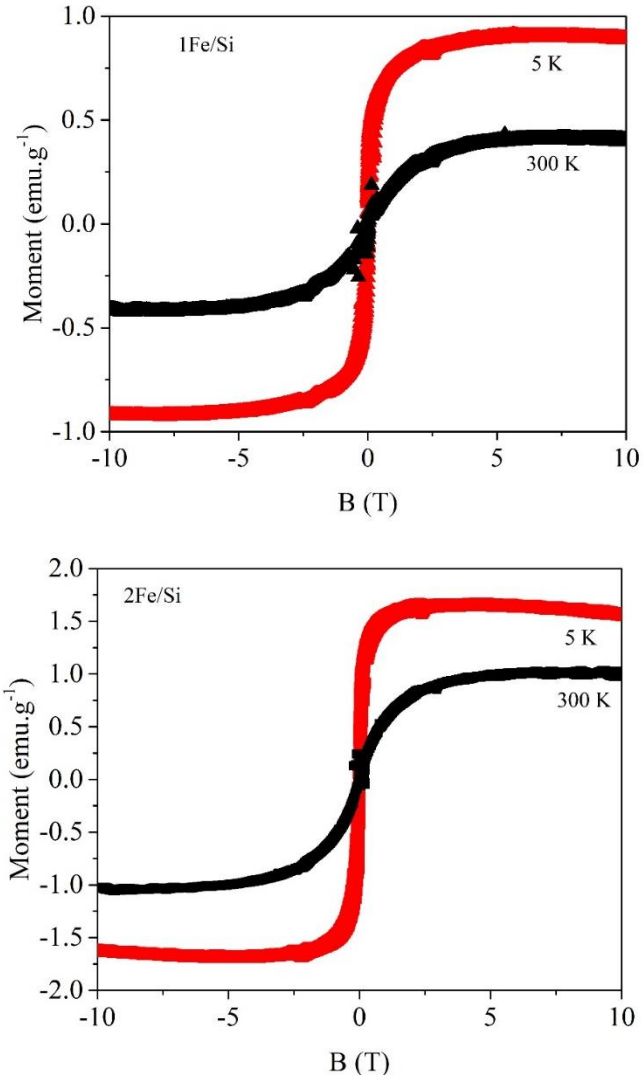

Fig. 4.12) Magnetic hysteresis curves at 5 K and 300 K for 1Fe/Si and 2Fe/Si compositions heat-treated with a heating rate of 5 ºC/min at 1400 ºC for 4 h.

Fig. 4.13 shows the variation of magnetization as a function of temperature for 1Fe/Si and 2Fe/Si in both Field Cooled (FC) and zero Field Cooled (ZFC) states, respectively presenting a superparamagnetic behavior for the samples. The ZFC curves exhibit a peak, T_b, indicating a transition from a magnetically blocked state (at low temperature) to a superparamagnetic state (at high temperature) [24]. The T_b value was found to be 8.3±0.1 K and 11.6±0.1 K for 1Fe/Si and 2Fe/Si, respectively. It is expected that T_b increases when the nanoparticle size increases. From the blocking temperature T_b and the magnetic anisotropy energy constant, K_{eff}

(taken from table 2.3), of the particles, the volume of particles can be calculated by using equation 3.46. We consider the particles formed in the glass matrix are hematite and in a spherical shape. Therefore, the particle size, d, was obtained to be 4.2±0.1 nm and 4.7±0.1 nm for 1Fe/Si and 2Fe/Si, respectively.

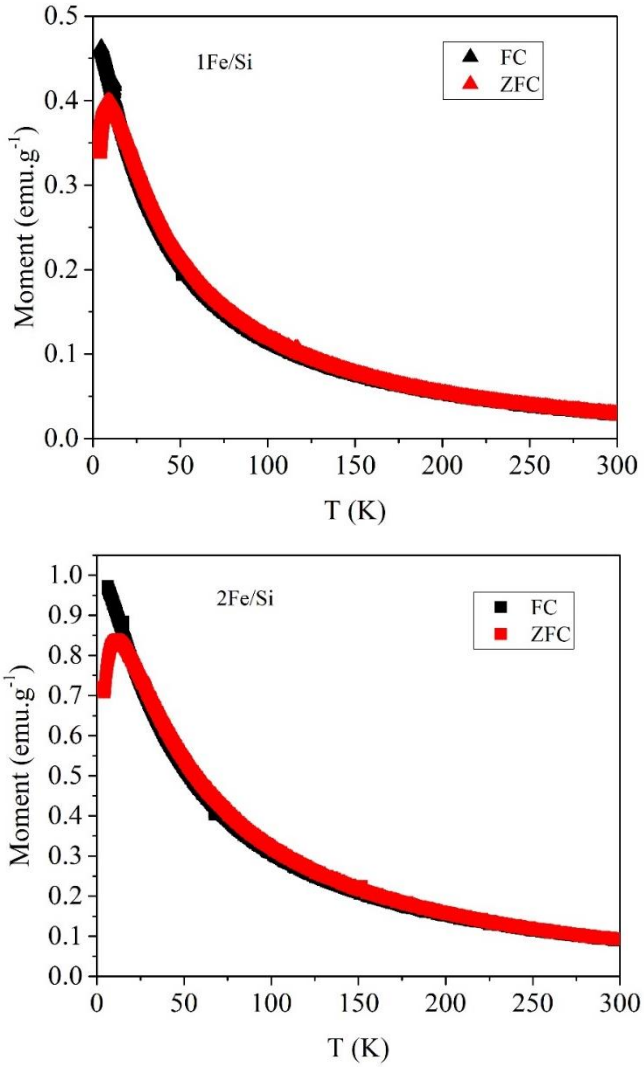

Fig. 4.13) FC and ZFC curves of 1Fe/Si and 2Fe/Si heat treated with a heating rate of 5 ^{o}C/min at 1400 ^{o}C for 4 h.

Finally, a systematic analysis was performed of magnetic loops (M-B) of 1Fe/Si, and 2Fe/Si measured at 300 K using Langevin function (equation 3.47). This temperature is well above T_b, and any hysteretic behavior is not observed in the measured loop. The experimental and fitted M-B curves at 300 K are indicated in Fig. 4.14.

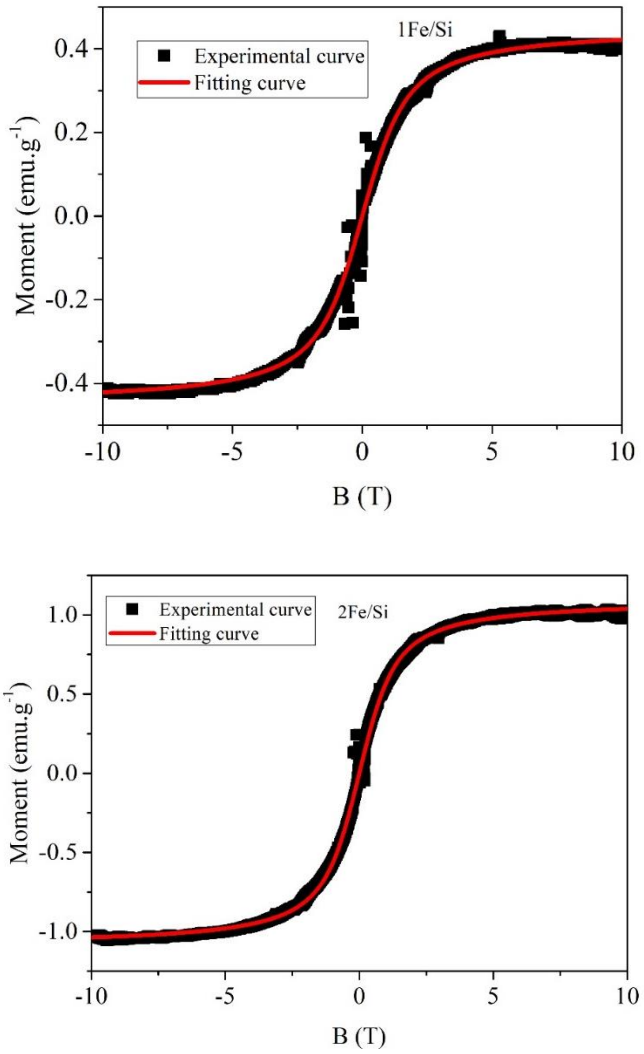

Fig. 4.14) The experimental hysteresis loops of 1Fe/Si and 2Fe/Si measured at 300 K along with the theoretical fitting curves to the Langevin equation.

It is obvious that the Langevin equation characterizing the superparamagnetic behavior perfectly fits the experimental curves. From fitting data, the magnetic moments per particle, m_p, dispersed in each composition was extracted using $m_p=\pi d^3 M_S/6$ [25]. Here, d is the mean particle size which was determined previously and M_S, saturation magnetization, is the fitting parameter. The M_S fit parameter was found to be 0.45199 and 1.09 emu/g for 1Fe/Si and 2Fe/Si, respectively. Therefore, the m_p value was obtained 379 μ_B and 660 μ_B for 1Fe/Si and 2Fe/Si, respectively. The obtained values are in good agreement with with other findings

regarding the bare hematite nanoparticles [26] and hematite (α-Fe_2O_3) nanoparticles embedded in an amorphous silica matrix [27]. Thus, the formation of bigger iron oxide nanoparticle in the sample with higher iron concentration results in an enhancement of the magnetic moments per particle and consequently the interactions between the moments and higher total magnetization. Fig. 4.15 and Fig. 4.16 show the hysteresis loops of 10Fe/Si and 20Fe/Si, respectively, measured at 5 and 300 K. A wasp-waisted feature is observed in the hysteresis curves measured at 300 K. It was reported that either mixture of different grain sizes or combination of particles with distinct magnetic characteristics could be the reasons for the wasp-waisted hysteresis loop [28].

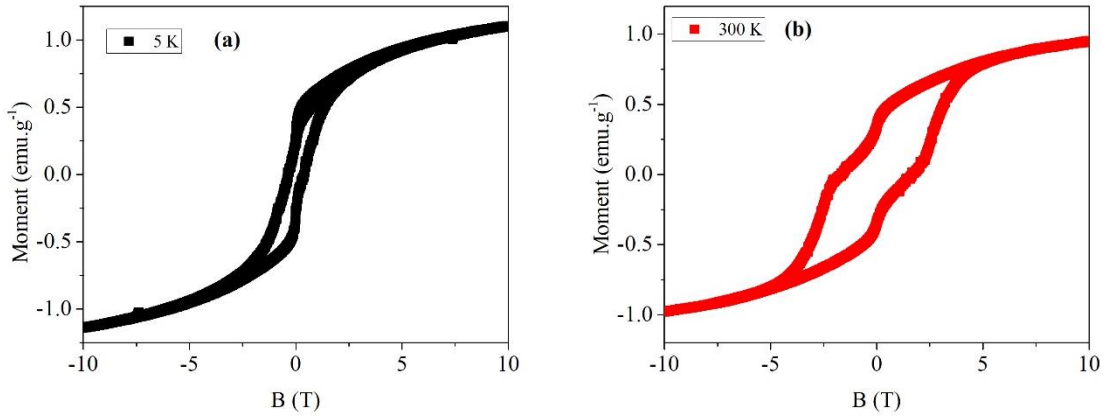

Fig. 4.15) The experimental hysteresis loops of 10Fe/Si measured at a) 5 K and b) 300 K.

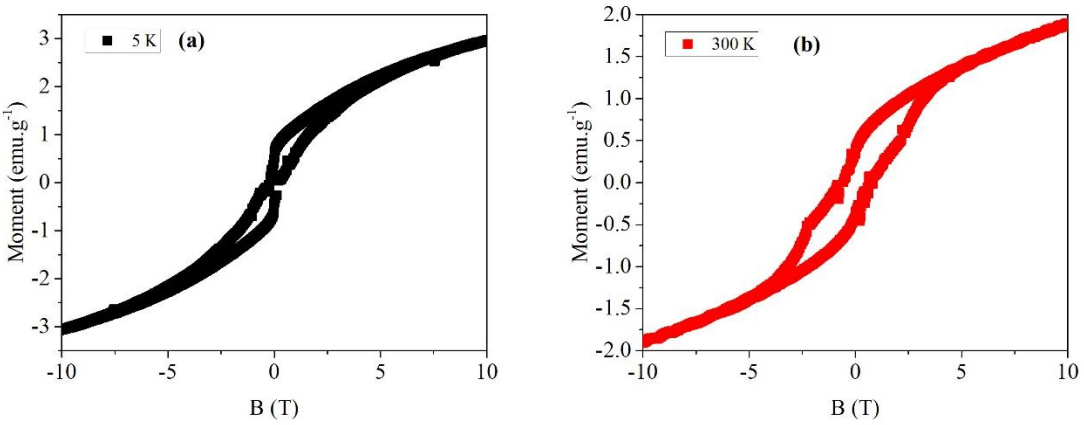

Fig. 4.16) The hysteresis loops of 20Fe/Si measured at a) 5 K and b) 300 K.

Table 4.2 summarizes the magnetic properties of xFe/Si glass ceramics measured at 5 and 300 K.

For 1Fe/Si and 2Fe/Si the coercivity (B_c) measured at 300 K are equal to zero and have low values at a temperature of 5 K. The M_r values increases with the iron oxide concentration, regardless of the measurement temperature. For both 10Fe/Si and 20Fe/Si the B_C values measured at 300 K are greater than the ones at 5 K. The largest value of the magnetization is observed for the sample with x = 20. Although, the magnetization of 10Fe/Si anomalously is lower than the M_S of the sample with x = 2.

Table 4.2) Magnetic properties of xFe/Si glasses.

Sample	**Measured at 5 K***			**Measured at 300 K***		
	M_S (emu.g^{-1})	**B_C (T)**	**M_r (emu.g^{-1})**	**M_S (emu.g^{-1})**	**B_C (T)**	**M_r (emu.g^{-1})**
1Fe/Si	0.893	0.03	0.08	0.405	0.0	0.02
2Fe/Si	1.57	0.027	0.177	0.993	0.0	0.145
10Fe/Si	1.10	0.387	0.268	0.945	1.638	0.337
20Fe/Si	3.06	0.168	0.469	1.88	0.649	0.349

* All values have error of ±2%

We suggest that the presence of the hematite in bigger size favors the antiparallel alignment of the iron ions in 10Fe/Si which can be responsible for the reduction in magnetization [29].

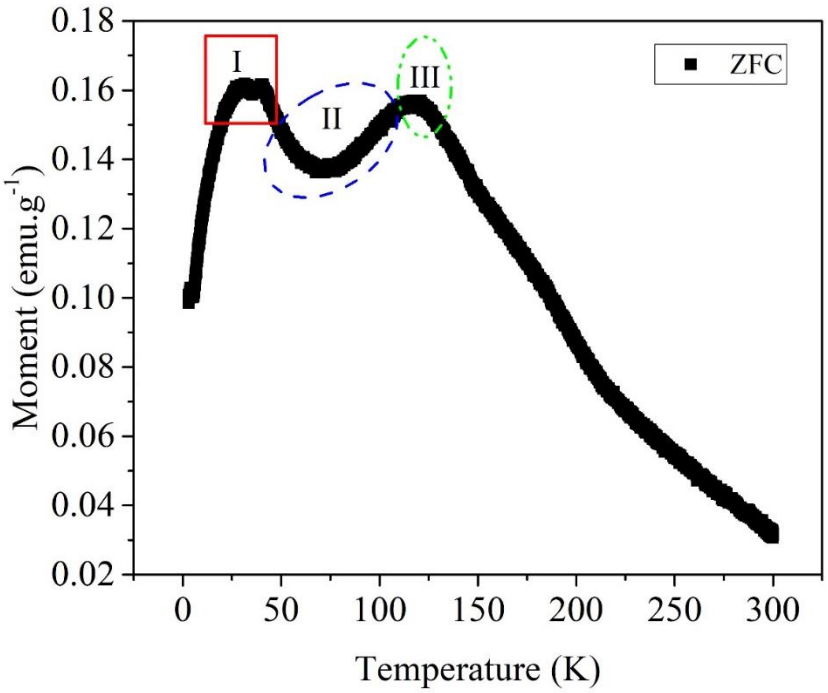

Fig. 4.17) The magnetization vs. temperature curve of 20Fe/Si measured at a constant field of 0.1 T in ZFC mode.

Fig. 4.17 shows the ZFC curve of 20Fe/Si depicting three clear features. The bimodal ZFC magnetization curve (regions I and III) might be due to the presence of two magnetic phases with different the mean size distribution relaxing at two different temperatures. The low temperature peak at region I is due to the extremely small particles, while the the broader second peak at the region III indicates the particles are widely distributed. This results are in good agreements with findings from other air dried xerogels and aerogels containing Ni-nanoparticles [30]. The appearance of region II in the temperature interval of 75-115 K, is supposed to be an indicator of the Verwey transition in this sample because of formation magnetite crystalline phase resulted in the highest magnetization. The Verwey transition can be shifted to much lower temperature in the partially oxidised magnetite (maghemite magnetite mixture) as already observed in other reports [31].

It is worthy to note that the presented findings from XRD, Raman, and magnetic characterization are insufficient to have a clear idea regarding the exact nature of magnetic phases formed in the samples with the iron oxide concentration higher than 10 %. To have a better inspection of the structural and magnetic properties of these samples, more precise measurements such as Mossbauer spectroscopy and high-resolution transmission electron

microscopy (HRTEM) are required which are not available in our lab. So further investigation on magnetic properties of 10Fe/Si and 20Fe/Si is excluded from this work.

4.6) Final remarks

In this chapter, iron-silicate glass-ceramics were successfully prepared by sol-gel. It was shown that the optimized heating rate is 5 ^{o}C/min. Moreover, Fe_2O_3 crystalline phase growth is promoted in the samples with concentrations higher than 2% and heat treated up to 1400 ^{o}C. The crystallization was found to be dependent on the iron oxide ratio. Raman spectroscopy showed new vibration bands related to Fe-O interactions in crystalline structures. Raman analysis supports the observation obtained from XRD measurements and SEM images. The DC conductivity measurements showed that 20Fe/Si is the highest conductive sample among all prepared samples.

Also, the highest dielectric constant was found to be for 20Fe/Si. A dielectric relaxation phenomenon was observed in the samples containing iron oxide more than 1%.

The dielectric relaxation shifts to higher frequencies with the increase of the temperature confirming its thermal actively nature. The superparamagnetic feature was observed for 1Fe/Si and 2Fe/Si with a blocking temperature of 8.3 and 11.6 K, respectively. By means of the blocking temperature values, we could estimate the size of iron oxide crystallites formed in the glass matrix. The experimental M-B loops of 1Fe/Si and 2Fe/Si measured at 300 K successfully was fitted to the theoretical Langevin model. Using the data extracted from the fitting a larger the magnetic moment per particle, 660 μ_B, was obtained for 2Fe/Si compared with 379 μ_B for 1Fe/Si. It also was observed that samples with the iron concentration of 10 % in mol only show present hysteretic behavior due to a high number of magnetic interactions between the magnetic phases with larger particle size. The maximum magnetization was observed in 20Fe/Si, while the abnormal reduction in magnetization of 10Fe/Si can be resulting from the presence of hematite in a bigger size with the antiparallel alignment of the iron ions.

4.7) References

[1] S. Larumbe, C. Gomez-Polo, J. I. Perez-Landazabal, and J. M. Pastor, **Journal of Physics: Condensed Matter**, 2012, 24, 266007.

[2] J. Xu, S. Thompson, E. O'Keefe, and C. C. Perry, **Materials Letters**, 2004, 58, 1696-1700.

[3] M. Zaharescu, M. Crisan, A. Jitiannu, and D. Crisan, **Journal of Sol-Gel Science and Technology**, 2000, 19, 631-635.

[4] A. Darmawan, S. Smart, A. Julbe, and J. C. D. da Costa, **Materials**, 2011, 4, 448-456.

[5] B. Wen, J. Li, Y. Lin, X. Liu, J. F. H. Miao and Q. Zhang, **Materials Chemistry and Physics**, 2011, 128, 35–38.

[6] X-Y. Xue, C-H. Ma, C-X. Cui, and L-L. Xing, **Solid State Sciences**, 2011, 13, 1526-1530.

[7] S. Moussa, G. Atkinson, M. Samy El-Shall, **Journal of Nanoparticle Research**, 2013, 15, 1470.

[8] R.Y. Hong, H.P. Fu, G.Q. Di, Y. Zheng and D.G. Wei, **Materials Chemistry and Physics**, 2008, 108, 132–141.

[9] Y. Masubuchi, Y. Sato, A. Sawada, T. Motohashi, H. Kiyono, S. Kikkawa, **Journal of the European Ceramic Society**, 2011, 31, 2459–2462.

[10] Z. Karimi, L. Karimi and H. Shokrollahi, **Materials Science and Engineering C**, 2013, 33, 2465-2475.

[11] S. Laurent, J–L. Bridot, Luce Vander Elst, and Robert N Muller, **Future Medicinal Chemistry**, 2010, 2(3), 427-449.

[12] M. El Hasnaoui, A. Triki, M.P.F. Graça, M.E. Achour, L.C. Costa and M. Arous, **Journal of Non-Crystalline Solids**, 2012, 358, 20, 2810-2815.

[13] D. Das, S. Roy, J. W. Chen, and D. Chakravorty, **Journal of Applied Physics**, 2002, 91,4573.

[14] A. Chopelas, **American Mineralogist**, 1991, 76, 1101-1109.

[15] S. W. da Silva, R. C. Pedroza, P.P. C. Sartoratto, D. R. Rezende, A. V. da Silva Neto, M. A. G. Soler, and P. C. Morais, **Journal of Non-Crystalline Solids**, 352, 2006, 1602-1606.

[16] A. M. Jubb and H. C. Allen, **Applied Materials & Interfaces**, 2010, 2, 10, 2804–2812.

[17] D. Bersani, P. P. Lottici, and A. Montenero, **Journal of Raman Spectroscopy**, 1999, 30, 355-360.

[18] I. Cesar, K. Sivula, A. Kay, R. Zboril and M. Gratzel, **The Journal of Physical Chemistry C**, 2006, 113, 772–782.

[19] M. P. F. Graça, M. G. Ferreira da Silva, and M. A. Valente, **Solid State Sciences**, 2009, 11, 570–577.

[20] S. Mukherjee, R. Gupta, and A. Garg, **AIP Advances**, 2013, 3, 052115-052118.

[21] R. S. Yadav, I. Kuřitka, J. Vilcakova, J. Havlica, J. Masilko, L. Kalina, J. Tkacz, J. Švec, V. Enev and M. Hajdúchová, **Advances in Natural Sciences: Nanoscience and Nanotechnology**, 2017, 8, 045002-045016.

[22] M. A. Valente, M. Peres, C. Nico, T. Monteiro, M.P.F. Graça, A.S.B. Sombra and C.C. Silva, **Optical Materials**, 2011, 33, 1964–1969.

[23] M. A. Valente, L. Bih, and M. P. F. Graça, **Journal of Non-Crystalline Solids**, 2011, 357, 55–61.

[24] K. Chesnel, M. Trevino, Y. Cai, J. M. Hancock, S. J. Smith, and R G Harrison, **Journal of Physics: Conference Series**, 2004, 521, 012004.

[25] T. Ozkaya, M. S. Toprak, A. Baykal, H. Kavas, Y. Koseoglu, B. Aktas, **Journal of Alloys and Compounds**, 2009, 472, 18-23.

[26] F. Bødker, M. F. Hansen, C. Bender Koch, K. Lefmann, S. Mørup, **Physical Review B**, 2000, 61, 10, 6826-6838.

[27] L. Kopanja, I. Milosevic, M. Panjan, Vesna Damnjanovic, Marin Tadic, **Applied Surface Science**, 2016, 362, 380–386.

[28] L. H. Bennetta, and E. Della Torre, **Journal of Applied Physics**, 2005, 97, 10E502.

[29] M. G. Ferreira da Silva, M. A. Valente, **Materials Chemistry and Physics**, 2012, 132, 2-3, 264-272.

[30] V. Thiruvengadam, S. Vitta, **RSC Advances**, 2013, 3, 12765-12773.

[31] R. Strobel, S. E. Pratsinis, **Advanced Powder Technology**, 2009, 20, 2, 190-194.

This page was intentionally left blank

Chapter 5 – $10Fe_2O_3$-$90SiO_2$ glass fibers prepared by LFZ method, investigation on magnetic domains and redox state due to the pulling rate.

5.1) Introductory remarks

Silica-based glasses have gained increasing attention due to a wide variety of emerging applications in the industry due to their unique physical and chemical properties, including chemical durability, abrasion resistance, specific electrical transport features and biocompatibility. Moreover, silica glasses show reasonably high ionic mobility along with a high concentration of weakly-bonded mobile ions [1, 2].

The addition of transition metal ions like iron to the silica base glasses is expected to improve their electrical, dielectric and magnetic features. Regardless of the original oxidation state of the iron in the starting glass batch, the final glass contains Fe^{3+} (in both tetrahedral and octahedral coordination environments) and Fe^{2+} ions in octahedral coordination. [3]. The redox variation of iron cations in the glasses and consequently their physicochemical properties can be affected by several working conditions such as temperature and oxygen partial pressure [4]. Laser floating zone technique is a suitable method to simulate the nonequilibrium conditions that characterize the redox process. Moreover, being a unique technique to obtain high-quality single crystals [5-8], eutectic structures [9] and highly oriented polycrystalline materials [10-11]. LFZ method also allows to deeply study phase transformation kinetics, diffusion phenomena and how to control the crystallization/amorphization degree in the sample's crystallization path [4].

The previous investigation on crystallization of iron-doped Magnesium Alumino Silicates (MAS) glass system fibers prepared the LFZ method showed that iron oxidation state and local environment is affected by the fiber growth rate, as a result of kinetic limitations imposed by specific conditions of the LFZ method [8, 11]. Moreover, it was found that the presence of a significant Fe^{3+} fraction on MAS glass and corresponding Fe^{2+}/Fe^{3+} redox interactions exerts a noticeable effect on the electrical conductivity, however, still there is no satisfactory description of this phenomenon, and more work is needed.

In this chapter, the behavior of silica glass system, containing 10 mol% of iron oxide, prepared by LFZ under various pulling rates is studied. The selected amount of iron implies that it will be rather incorporated into the glass as a network modifier. The prepared samples were characterized by structural, morphological, electrical and magnetic measurements in order to assess the effects of the pulling rate on redox properties of iron oxide in silica glasses.

5.2) Experimental procedure

According to the molar composition $90SiO_2$-$10Fe_2O_3$, the raw powders (MERCK, with > 99.0 % purity) were weighed and after mixed inside the agate container of a planetary ball milling system for 40 min at 250 rpm. The pedestal source material was then prepared by the cold extrusion process, using an organic binder (PVA) [11], obtaining 150 mm long an 1.75 mm diameter rod samples. These rods were used as feed and seed precursor. The growth process was carried out with a continuous CO_2 Spectron SLC laser (λ=10.6 μm; 200 W) in room temperature conditions and with four different pulling rates: 100, 150, 200 and 400 mm/h. Because of this, the fibers are hereafter labeled as LFZ100, LFZ150, LFZ200, and LFZ400 respectively.

X-ray diffraction (XRD) was performed using an X'Pert MPD Philips diffractometer (Cu Kα radiation, λ = 0.154056 nm, 2θ=15–70°, step 0.04° and exposition 1.3 s) at 40 kV and 30 mA, and the obtained spectra were analyzed using the Joint Committee on Powder Diffraction Standards (JCPDS) database. Surface morphology of the fibers was observed using a VEGA3-TESCAN scanning electron microscopy (SEM), and phase's composition analyzed using energy dispersion spectroscopy (EDS - BRUKER) mode (25 kV, 10 mA). The topography and magnetic structure of the LFZx fibers were studied using an NTEGRA Aura (NT-MDT SI) scanning probe microscope equipped by the magnetic probe MFM01 (70 kHz, 3 N/m). The Raman spectroscopy of the powder samples was carried out in an HR800 Jobin Yvon SPEX spectrometer, using an Ar laser (λ = 532 nm) as excitation font. The spectra were obtained, in backscattering geometry, between 200 and 1100 cm^{-1} at room temperature.

For the electrical measurements the opposite sides of the fibers, with a thickness of about 1 mm, were painted with silver paste. Impedance spectroscopy measurements were performed

in a wide temperature range from 100 K to 400 K and between 10^2 -10^6 Hz, using an Agilent 4294A Network Analyzer in the C_p-R_p configuration.

The magnetic susceptibility measurements were performed using a vibrating sample magnetometer (VSM) from Cryogenics. The magnetic properties as a function of temperature were acquired in field cooling (FC) and zero field cooling (ZFC) modes, applying a magnetic field of 0.1 Tesla on LFZ grown fibers, and magnetization versus magnetic field in the wide range of temperatures between 5 – 300 K. The magnetic measurements were made by placing the samples in the parallel position relative to the direction of the applied magnetic field. It should be mentioned that the positioning the sample with respect to the magnetic field does not have any effect on the magnetic properties of the fibers. To survey that the samples were positioned in the perpendicular direction relative to the applied magnetic field. The results obtained are in similarity with the ones obtained from the parallel positioning. As seen in the following this shows there is no directional crystallization for magnetic phases formed in the fibers.

5.3) Structural and morphologic results

Fig. 5.1 exhibits the X-ray diffraction (XRD) patterns of LFZ powdered fibers. According to the reflection peak positions and relative intensities, the XRD patterns show the presence of M: magnetite - Fe_3O_4 (ICDD: 00-019-0629), IS: iron silicate - Fe_2SiO_4 (ICDD: 01-070-1861), F: fayalite – 2(FeO). SiO_2 (ICDD: 00-011-0262), H: hematite - α-Fe_2O_3 (ICDD: 00-001-1053), γ: maghemite - γ-Fe_2O_3 (ICDD: 01-070-1861), W: wustite - F_xO, with $0.83 \leq x \leq 0.95$, (ICDD: 01-074-1880) phases in all fibers.

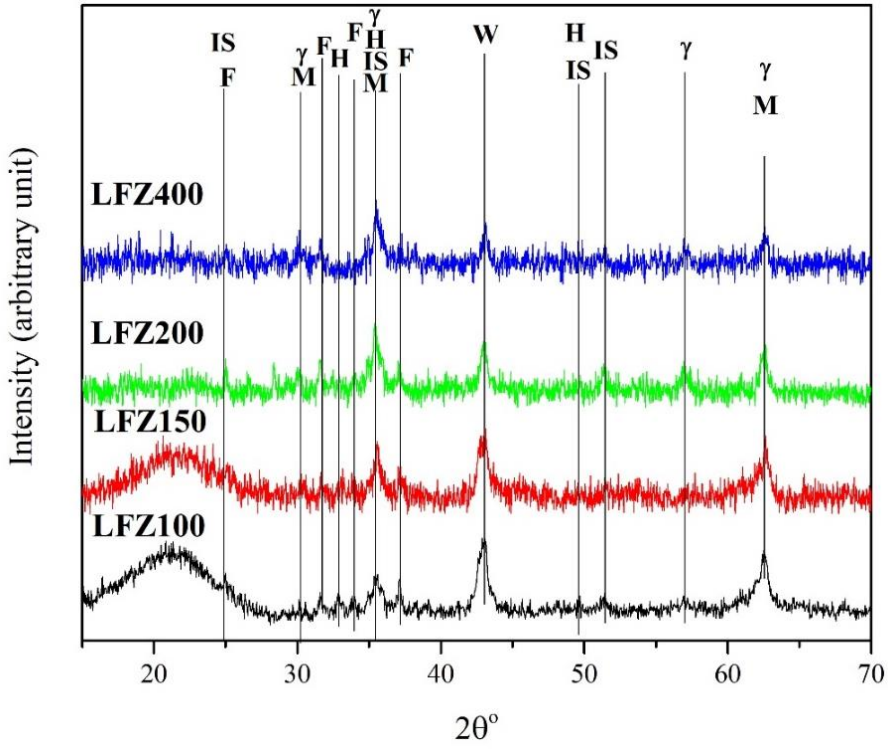

Fig. 5.1) XRD pattern of all powdered fibers. M: Magnetite - Fe_3O_4 (ICDD: 00-019-0629), IS: iron silicate - Fe_2SiO_4 (ICDD: 01-070-1861), F: Fayalite - 2FeO. SiO_2 (ICDD: 00-011-0262), H: Hematite - α-Fe_2O_3 (ICDD: 00-001-1053), γ: Maghemite - γ-Fe_2O_3 (ICDD: 01-070-1861), W: Wustite - F_xO (ICDD: 01-074-1880).

It should be noted that no crystalline phase of silica was detected in the XRD patterns of the fibers. The appreance of a broad hump around $2\Theta = 21^o$, characteristic of the silica glasses with the short-range order [12], is confirmed in the samples LFZ100 and LFZ150. Whereas, the formation of silica vitreous structure is not observed in LFZ200 and LFZ400. In the following, we present the reduction-oxidation reactions occurring during the LFZ process to understand the findings obtained from XRD analysis.

As described in the experimental procedure, the raw materials are SiO_2 and Fe_2O_3 powders. In a reducing atmosphere, such as the high temperature melting zone during the LFZ preparation [4], the conditions met for the formation of fayalite - Fe_2SiO_4 or iron silicate (Eq. 5.1 and 5.2), Wustite - F_xO (Eq. 5.3) and Magnetite - Fe_3O_4 (Eq. 5.4) follow as:

$$2Fe_2O_3 + 2SiO_2 \leftrightarrow 2Fe_2SiO_4 + O_2 \quad (5.1)$$

$$2Fe_3O_4 + 3SiO_2 \leftrightarrow 3Fe_2SiO_4 + O_2 \quad (5.2)$$

$$2Fe_2O_3 \leftrightarrow 4FeO + O_2 \quad (5.3)$$

$$3Fe_2O_3 \leftrightarrow 2Fe_3O_4 + O_2 \quad (5.4)$$

According to Eq. 5.1 and 5.2 the decreasing in the pulling rate and the longer time for oxidation can attribute in the formation of a lower quantity of fayalite or iron silicate, with more silica melt for the glass formation, originating for the wide hunch at LFZ100 and LFZ150 XRD patterns. Therefore, the melting made in air at atmospheric pressure, i.e., an oxidative atmosphere, may cause the decomposition of fayalite with the crystallization of hematite (Eq. 5.1) and magnetite (Eq. 5.2) [13]. Moreover, the hematite can be reduced in wustite and magnetite (Eq. 5.3 and 5.4 respectively).

As seen in Fig. 5.1, the major part of the observed peaks can be attributed to more than one crystalline phase. This fact only allows us to calculate the diameter of the crystallites of the Wustite, F_xO, which has the diffraction peak with the greatest intensity at $2\Theta = 43.6^o$, using Debye-Scherrer (D-Sch)'s equation

$$< D >_{D-Sch} = \kappa \lambda/(\beta \cos\Theta) \quad (5.5)$$

where λ is X-ray wavelength, κ a constant, β is line broadening measured at half height from the most intense peaks of XRD and θ is Bragg angle.

Fig. 5.2 shows that the Wustite crystallites have nanometer dimensions and the size tends to diminish with the decreasing of the pulling rate with the minimum size for the sample LFZ150 but similar to the one calculated for the LFZ100 sample.

The main peak of the fayalite phase ($2(FeO).SiO_2$) at $2\Theta \cong 31.59^o$ is observed in all the samples. The peak at $2\Theta \cong 33.27^o$ corresponds to hematite (α-Fe_2O_3) and increases with the decrease in the growth rate of the fibers. The peak at $2\Theta \cong 57^o$ can be ascribed to the maghemite (γ-Fe_2O_3) phase diminishes with the decrease of the pulling rate.

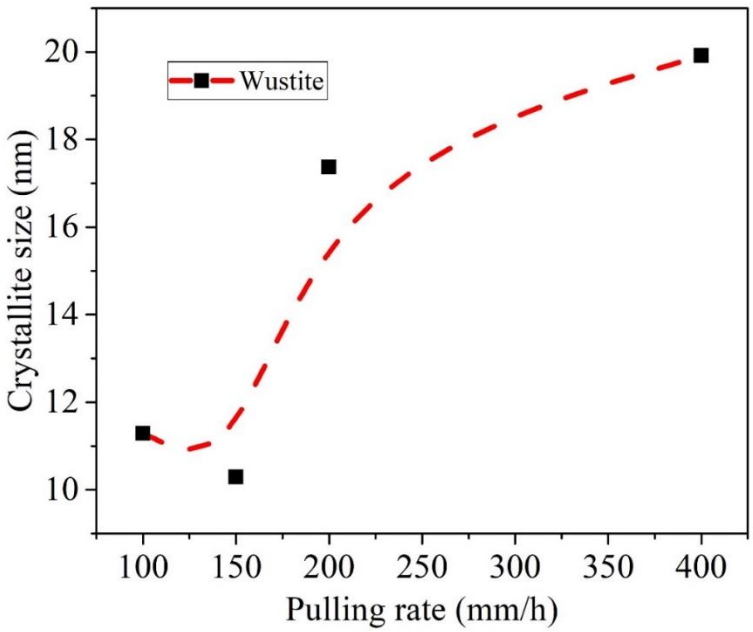

Fig. 5.2) Crystallite size of wustite phase vs. the pulling rate calculated using Debye-Scherer equation.

It is noteworthy that the observed broadening in XRD lines with the increasing of the pulling velocity can be interpreted in terms of lower crystallinity [14] of these samples. However, the major problem is that the observed peaks with higher intensity may have contributions of several crystalline phases. Thus, the peak at $2\Theta \cong 35.5^{\circ}$ can be the overlapping of peaks due to magnetite, hematite, wustite and iron silicate crystalline phases and the diffraction peak at $2\Theta \cong 62.6^{\circ}$ can be attributed to magnetite, hematite, wustite phases in the sample.

Based only on the XRD results it is hard to know how the observed crystalline phases vary as a function of the growth rate of the samples. This justifies the need for a more precise phase identification. For this purpose, Raman spectroscopy, commonly used for determination of the structure, environment, and dynamics of glassy materials, was analyzed. The experimental Raman spectra of all fibers were obtained at room temperature. For each spectrum, first, the baseline was corrected in order to remove the background effect and secondly the baseline-corrected spectrum was normalized with respect to the most intense peak in each spectrum. The Raman spectra were deconvoluted into individual Gaussian peaks (Fig. 5.3) in order to identify and assign all possible vibration bands, as described precisely in [15].

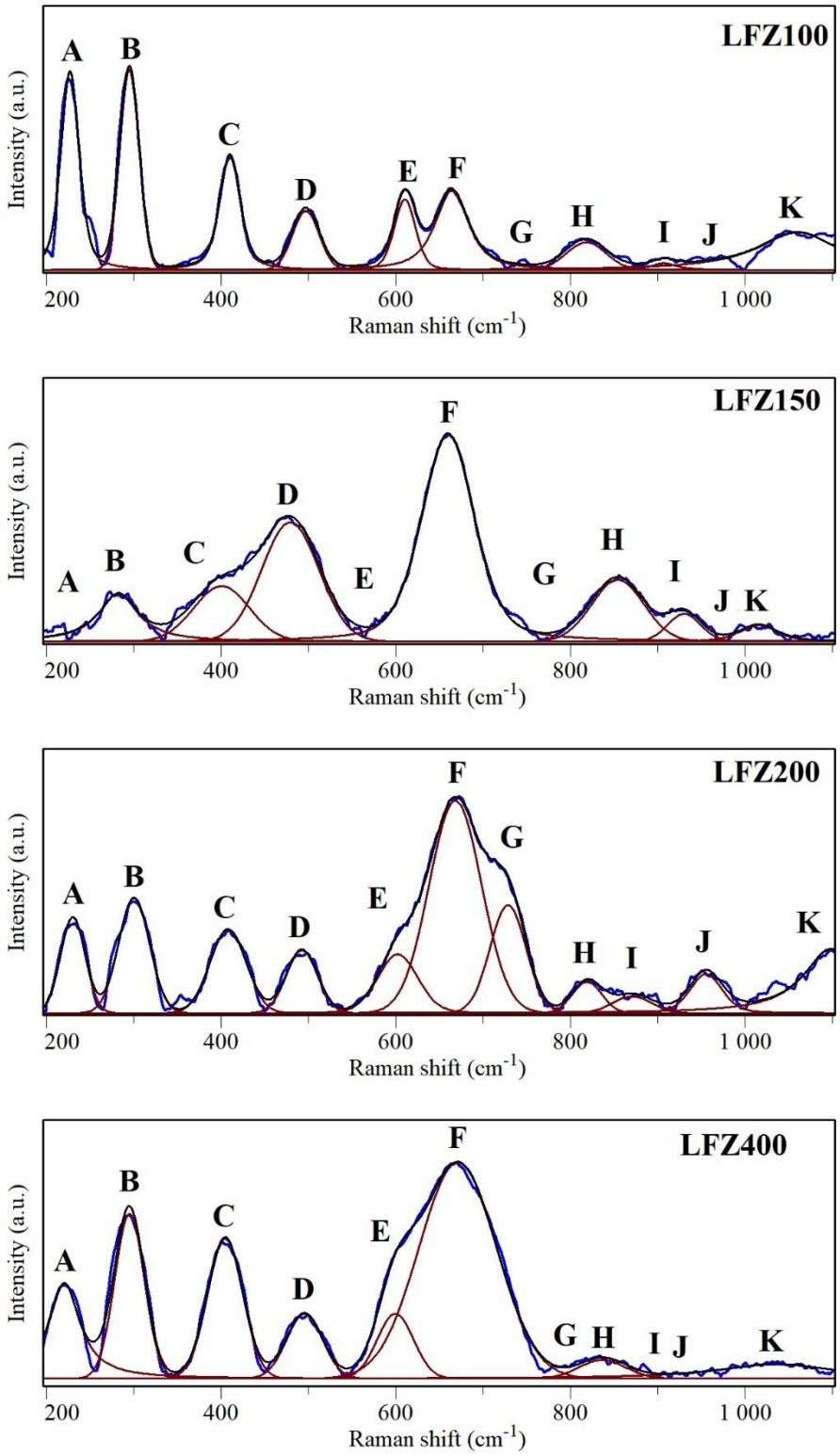

Fig. 5.3) The normalized and deconvoluted into individual Gaussian peaks of the Raman spectra.

All observed vibration bands were identified by comparison with the literature data [7, 16-28], labeled in alphabetic order and along with their corresponding assignments are given in table 5.1.

The first observed feature is the bands in LFZ100 are sharper and more symmetric compared with the equivalent bands in the fibers grown in higher pulling rates. Inhomogeneous and asymmetric broadening of the Raman peaks is usually observed in amorphous compositions in which the chemical composition, crystal size, molecular chain length, morphology or local environment can vary significantly for different parts of the sample [29].

According to the Raman analysis all fibers, with the exception of LFZ150 fiber, showed a band around 220 cm^{-1} (Fig. 5.3 - labeled by A) that can be ascribed to the A_{1g} mode in α-Fe_2O_3 crystallite [16]. In LFZ150 fiber there is no evidence of band at ~ 620 cm^{-1} (Fig. 5.3) assigned to E_g mode for hematite phase. These two peaks are attributed to hematite and do not have any contribution from maghemite or magnetite phases [17]. The absence of these two peaks can be related to structural changes within LFZ150 accompanied by hindering of formation of α-Fe_2O_3 phase [18]. Oppositely, the band F, in the range of 660-675 cm^{-1}, is a characteristic signature of magnetite [7].

Considering the band F, specific for Fe_3O_4, as a criterion for the abundance of Fe^{2+} ions in the fibers, it is possible to calculate the ratio between the area of the band F and the area of the other bands due to Fe ions. The ratio $[Fe^{2+}]/[Fe_{tot}]$ for each sample was calculated from the relation:

$$R_{[Fe2+]/[Fetot]} = \text{Area}_{[\text{Band F}]} / \sum \text{Area}_{[\text{Fe Bands}]} \qquad (5.6)$$

where $\sum \text{Area}_{[\text{Fe Bands}]}$ is the sum of all band areas attributed to Fe structural units. The graph of $[Fe^{2+}]/[Fe_{tot}]$ ratio vs. the pulling rate is in Fig. 5.4. From this criterion, it is observed that the content of Fe^{2+} increases as the pulling rate of the fibers increases. A consequence of the increase in $[Fe^{2+}]/[Fe_{tot}]$ ratio is the appearance of new oxygen bridging atoms [30].

Table 5.1) Raman band position and corresponding assignment of the LFZx fibers [7, 16-28].

	Raman band wavenumbers (cm^{-1})				Assignment
Band notation	LFZ100	LFZ150	LFZ200	LFZ400	
A	225	-	231	220	Fe-O stretching bond hematite crystalline
B	295	281	300	295	asymmetric bends oxygen with respect to Fe in hematite and magnetite
C	411	394	409	401	Si-O-Si symmetric stretching bending in quartz
D	498	477	492	495	Si-O-Si bond bending vibration
E	614	-	613	601	Fe-O bond in hematite
F	663	662	673	669	A_{1g} mode in magnetite
G	-	-	731	-	$\nu_3(+\nu_1)$ vibration of SiO_4 in fayalite
H	816	858	822	830	Si-O-Fe due to distortion of silicate tetrahedra structural units
I	904	930	890	-	
J	964	-	951	-	
K	1048	1014	1037	1036	

As seen in table 5.1, the bands recognized in the range of 410-500 cm^{-1} and ~800-1000 cm^{-1} are attributed to Si-O-Si vibrations in Silicate structural units [19-22] (Table 5.1). Although, band J at ~960 cm^{-1} barely was detected at LFZ100. Besides that any trace of the band I was not observed for LFZ400.

In fact, the bands around 850 (H), 900 (I), 950 (J), and 1100 (K) cm^{-1} correspond symmetric Si-O stretching vibrations of SiO_4 tetrahedral with four, three, two and one non-bridging oxygen atoms, respectively [3]. Therefore, it is an indicator of a random configuration of bridging and non-bridging oxygen in LFZ samples. Similar behavior is most often associated with melts that contain high field charge divided by the square of the cation-oxygen distance, modifying cations (Mg^{2+}, La^{3+}) [31]. The type of modifying cation impacts on the distribution of the chain lengths appearing as a shift to the higher wavenumbers when the field strength of the modifying cation increases [32]. The change in the structure seen in Raman spectra and table 5.1 is a result of the difference in strength of Fe–O and more covalent Si–O bonds present in the network.

To complement these data, it is possible to calculate the relative areas of the bands pertaining to hematite entity, the peaks A and E to determine, at least qualitatively, its variation as a function of the pulling rate. We could approximately, assess the fraction of hematite in fibers R_{Fe2O3} from the summation of the peaks area of bands A and E, designated for α-Fe_2O_3, and the total area of the bands associated with all iron species, $\sum$Area [Fe Bands], viz,

$$R_{Fe2O3}=(\text{Area}_{[\text{Band A}]}+ \text{Area}_{[\text{Band E}]})/\sum\text{Area}_{[\text{Fe Bands}]} \quad (5.7)$$

Fig. 5.4 shows the dependence of hematite fraction in LFZx samples on the pulling rate, based on the previous equation.

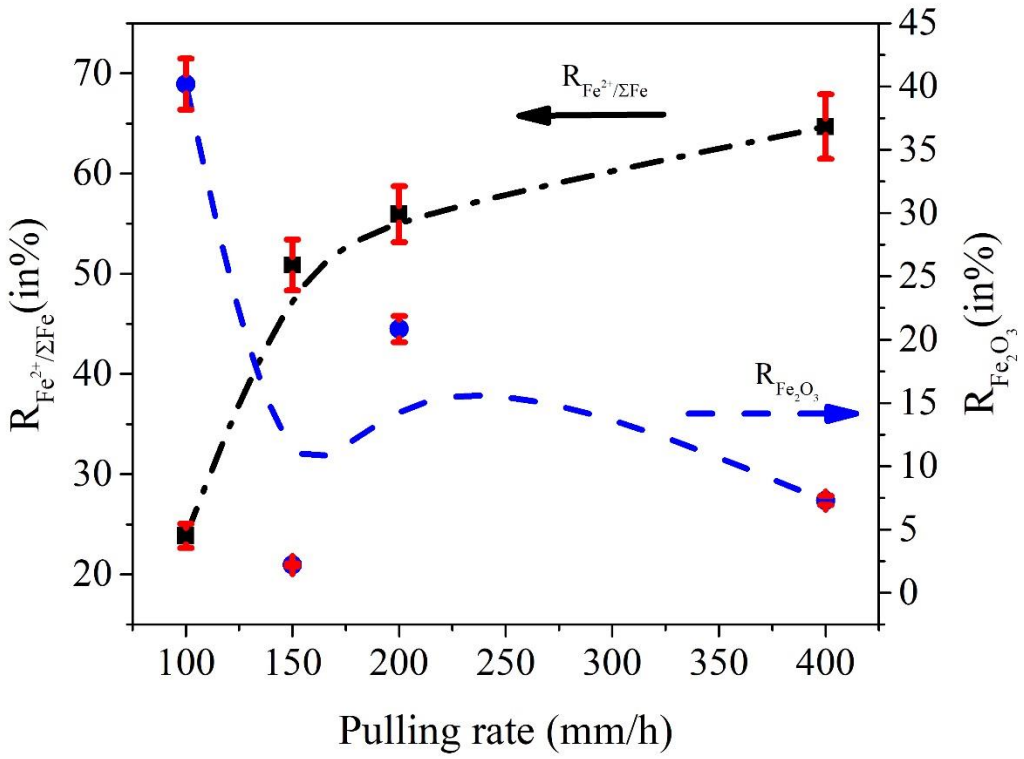

Fig. 5.4) $[Fe^{2+}]/[Fe_{total}]$ and $R_{Fe2O3}/[Fe_{total}]$ ratio as a function of the pulling rate (The dash lines are guides for eyes).

The fraction drops abruptly as the pulling rate increases from 100 to 150 mm/h; after a drastic increase in the proportion of hematite phase with the increase in the pulling rate up to 200 mm/h, again the fraction decreases gradually when the pulling rate increases.

It should be taken into account that it is difficult to ensure that this dependence exactly is correlated to the Fe^{3+} quantity in the fiber because we did not consider the bands which are assigned to both hematite and magnetite phases consisting Fe^{3+} ions [24-28]. From this graph, we could imply the increase of magnetite amount with the pulling rate while the hematite decrease with the pulling rate, which is in agreement with the result observed for the LFZ on hematite growth [7].

Fig. 5.5 shows the transversal section microstructure of the $10Fe_2O_3$-$90SiO_2$ LFZ fibers grown at the different rates ranging from 100 mm/h to 400 mm/h. Moreover, in order to study the distribution of elements in the fiber matrices, along with the SEM images, the element mapping of each LFZ fiber is also brought.

Sample	Ampilfied SEM image (2.5 kx)	Elemental Mapping
LFZ100	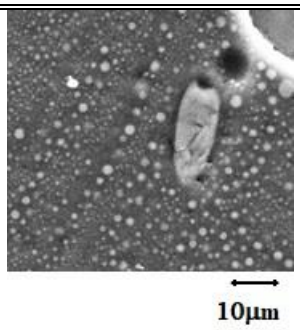	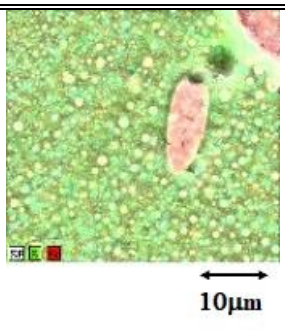
LFZ150	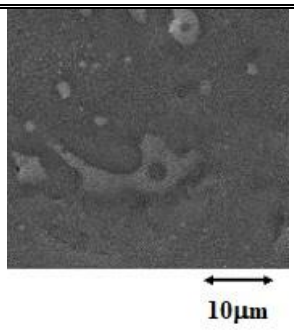	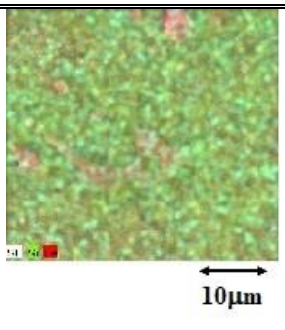
LFZ200	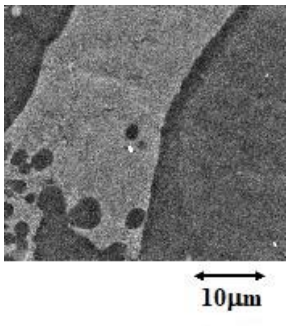	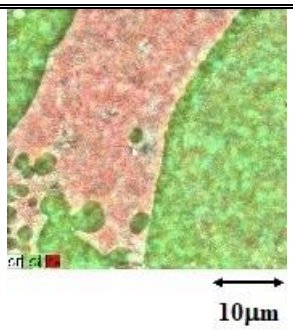
LFZ400	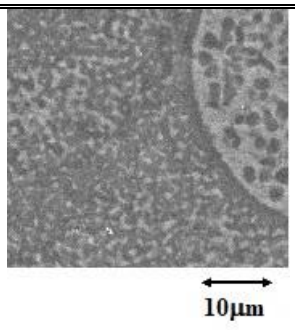	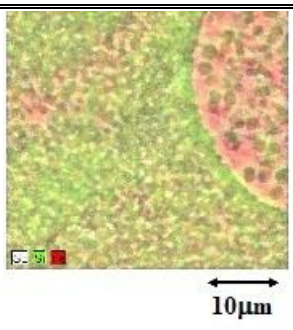

Fig. 5.5) SEM and elemental mapping of transversal section micrographs of LFZx samples. (In the elemental mapping the red and green colors indicate the distribution of iron and Si, respectively)

There are some pores, cracks and internal defects are observed in LFZ100 and LFZ200 probably due to the velocity of the pulling and/or polishing processes.

The morphology, moreover, is an indication of phase separation. we emphasize that the chemical composition of the residual glass is inhomogeneous after crystallization, consistent with the elemental mapping micrographs.

We can see that the microstructure of the LFZ fibers is dependent on the pulling rate. For LFZ400, as shown in Fig. 5.5, SEM investigation evidenced signs of simultaneous surface crystallization of Fe-rich skeletal dendrites coexisting with a coarser Fe-rich microstructure developed by the aggregation of dendritic skeletal morphology as well as the fine circular grains dispersed in Si-rich matrix. The dendritic skeletal structure is due to both supercooling and solidification heat, which produces a negative gradient of temperature in the interface between the glass matrix and crystalline phases. The stability of the interface decreases and leads to growth by thermal diffusion [33]. In other words, diffusion in the supercooled residual melts is too rapid causing disequilibration of the system and the formation of some impurity phases and this impurity phase will seriously degrade the electrical properties of the system. The elemental mapping analysis reveals that the surface plate-like crystalline structure is more iron-enriched than the dendritic skeletal pattern and small grain accumulations. As the crystallization time increased with decreasing the pulling rate, crystals nucleated and grew in random locations. The grains continued to grow in size until they impinged on one another thus forming spherical regions of a crystalline phase, and then their grain boundaries become faint due to the formation of the amorphous phase. Although the glass ceramics grown in low pulling rates still possess a dense Fe-enriched microstructure.

The examination of the microstructure along the longitudinal section revealed that there is no orientation along the fiber axis (nor any other axes). The misoriented circular grains structure, as well as the coarser intergrain spacing, were found anywhere in the fibers (Fig. 5.6).

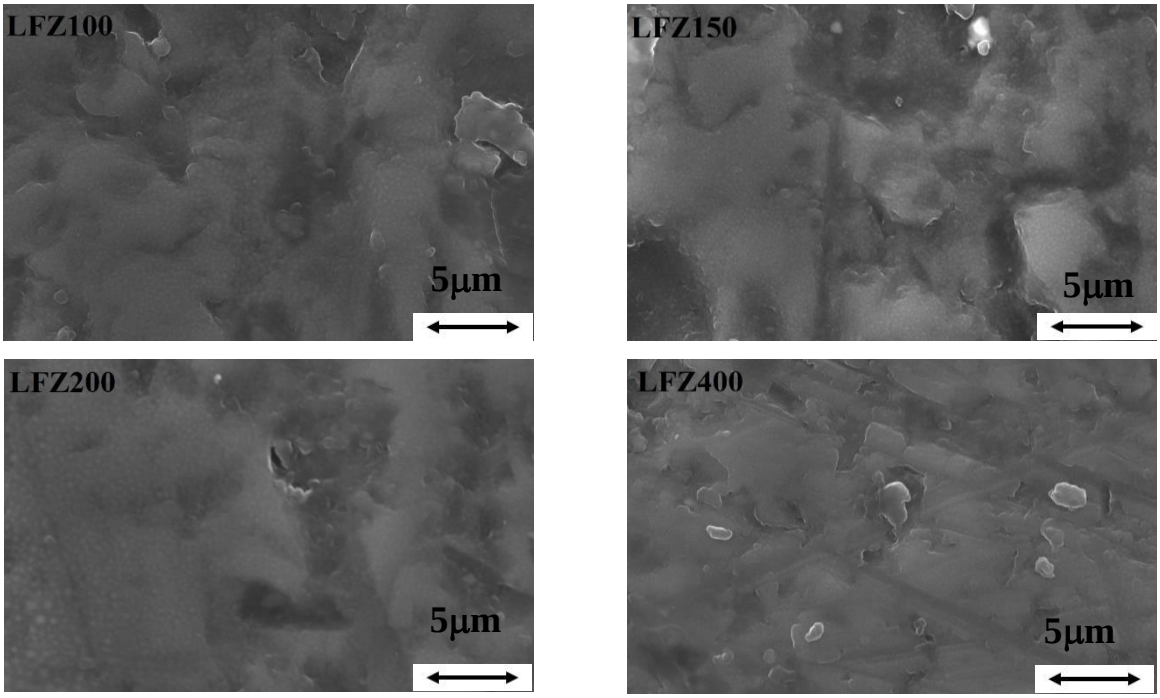

Fig. 5.6) The SEM micrographs of the fibers taken from the longitudinal section.

Fig. 5.7 presents AFM and MFM scan images of the LFZx fibers. The dark/bright contrast in the MFM images is associated with the magnetic interactions between a ferromagnetic tip and the iron oxide clusters formed in the LFZx fibers. The AFM images support the phase separation, confirming the observation obtained from SEM micrographs. The MFM results demonstrate an alteration of the magnetic domain structure as the pulling rate increases.

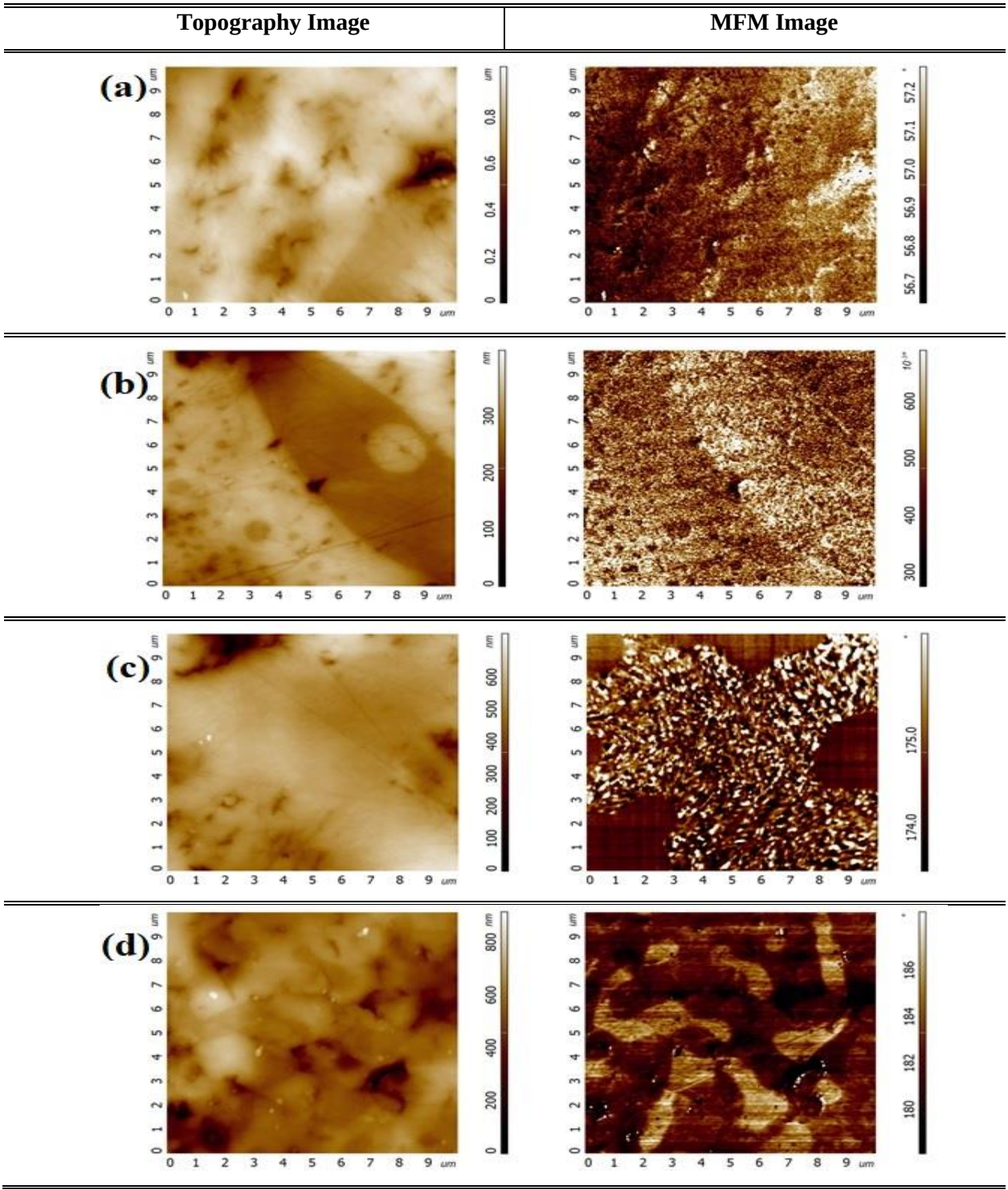

Fig. 5.7) AFM/MFM images of a) LFZ100, b) LFZ150, c) LFZ200 and d) LFZ400 mm/h. (the topography and MFM response images are presented in left and right panel, respectively).

Generally, the samples LFZ100 and LFZ150 demonstrate weak MFM contrast which is partly affected by the topography. However, the LFZ150 fiber exhibits the areas where MFM response is not influenced by the morphology, and the inherent magnetic domain structure can be revealed (Fig. 5.7 b). The LFZ200 sample demonstrates a clear magnetic domain structure consisting of opposite state domains with the dimension of about 100 nm, as seen in Fig. 5.7 c. The LFZ400 fiber reveals clear, big and elongated monodomain states with the size of ~1 x 4 μm (Fig. 5.7 d). Thus, the AFM/MFM results are fully consistent with the Raman study. The glass fibers grown at the lower rates, LFZ100 and LFZ150, with a low $Fe^{2+}/[Fe]_{total}$ ratio, demonstrate a stronger tendency to bulk crystallization of the hematite phase presenting a poor MFM response. As the pulling rate increases, ferrimagnetic monodomains of magnetite with a high $Fe^{2+}/[Fe]_{total}$ ratio are formed, as a result giving a strong MFM response. This observation is further supported by magnetic measurement.

5.4) Electrical measurements

Fig. 5.8 shows the frequency dependence of dielectric constant for the LFZ fibers. Generally, the dielectric constant of a material is determined by electronic, ionic, dipolar and space polarization [34]. Out of these, the space charge contribution depends on the homogeneity and "crystalline perfection" of the samples. Its influence is generally negligible at low temperatures and noticeable in the low-frequency region [35]. The dispersion of ε´ at low frequency is due to the interfacial polarization and existence of depletion layers near the sample–electrode contacts [36]. The magnitude of ε´ decreases with the increase of frequency before leaving off a constant value at higher frequencies. At high frequencies, reversal of the external electrical field takes place too "rapidly" so that the dipoles cannot align themselves and there is no charge accumulation at the interface resulting in constant ε´ values [34-36]. As the temperature rises, the dielectric constant increases and at higher temperatures (400 K) it increases very rapidly. This behavior is typical of polar dielectrics in which the orientation of dipoles is facilitated with rising temperature and thereby the dielectric constant is increased. At low temperatures, the contribution of electronic and ionic components to the total polarizability will be small. The electronic contribution is temperature independent. In the case of ionic polarization, in low temperature, insufficient thermal excitation energy hinders the ions shifting in the

directional of the external field [37]. The increase in dielectric constant of the sample with an increase in temperature can be due to:

(i) the weakening of the intermolecular forces, and hence enhancement of the orientational vibration.

(ii) increasing in the thermal agitation, and therefore strongly disturb in the orientational vibrations [35].

The dielectric constant becomes larger at low frequencies and high temperatures which is a commonly observed feature in oxide glasses. The dielectric dispersion curve and the constant at lower frequency region for LFZ400 can be explained on the basis of Koop's phenomenological theory due to Maxwell–Wagner interfacial type of polarization [35, 38]. From previous studies, it is seen that the Fe^{2+} ions are maximum for the sample LFZ400. The polarization in this sample is determined mainly by local displacement of electrons in the direction of an applied field, which is due to the electron exchange interaction, $Fe^{2+} \Leftrightarrow Fe^{3+}$ [35, 36]. The electrons attain the grain boundary through hopping of charge carriers which results in the interfacial polarization. However, as the frequency increases, the possibility of charge accumulation in grain boundaries decreases, which results in a decrease in the interfacial polarization.

Besides this, the LFZ fibers consist of cracks, pores, and other defects and due to inhomogeneity, there are regions with different permittivity. It is assumed that there should be two layers which are well-conducting materials (ferrite grains) and separated by the layers of lower conductivity (grain boundaries) that are effective at higher and lower frequencies respectively in the inhomogeneous dielectric structure. It can be also explained on the basis of space charge polarization explained by Maxwell and Wagner resulted from differences among the conductivities of the various phases present. It is worth mentioning that the dielectric data of LFZ200 over the whole range of frequency was anomalously found be the highest. The true physical reason for this observation is ambiguous and open for further investigation.

The values of AC electrical conductivity measured at 100 kHz and room temperature, are shown in Fig. 5.9. The results of AC conductivity are in similar range with those reported for other silica glasses containing iron oxide [38, 39]. Conductivity is strongly affected by the pulling rate, suggesting a dependence on the fraction of the crystalline phase. To understand the conduction process in partially crystallized glasses, microstructure including the size and

the boundary of crystallized grains and the nature of crystalline phases must be considered [40].

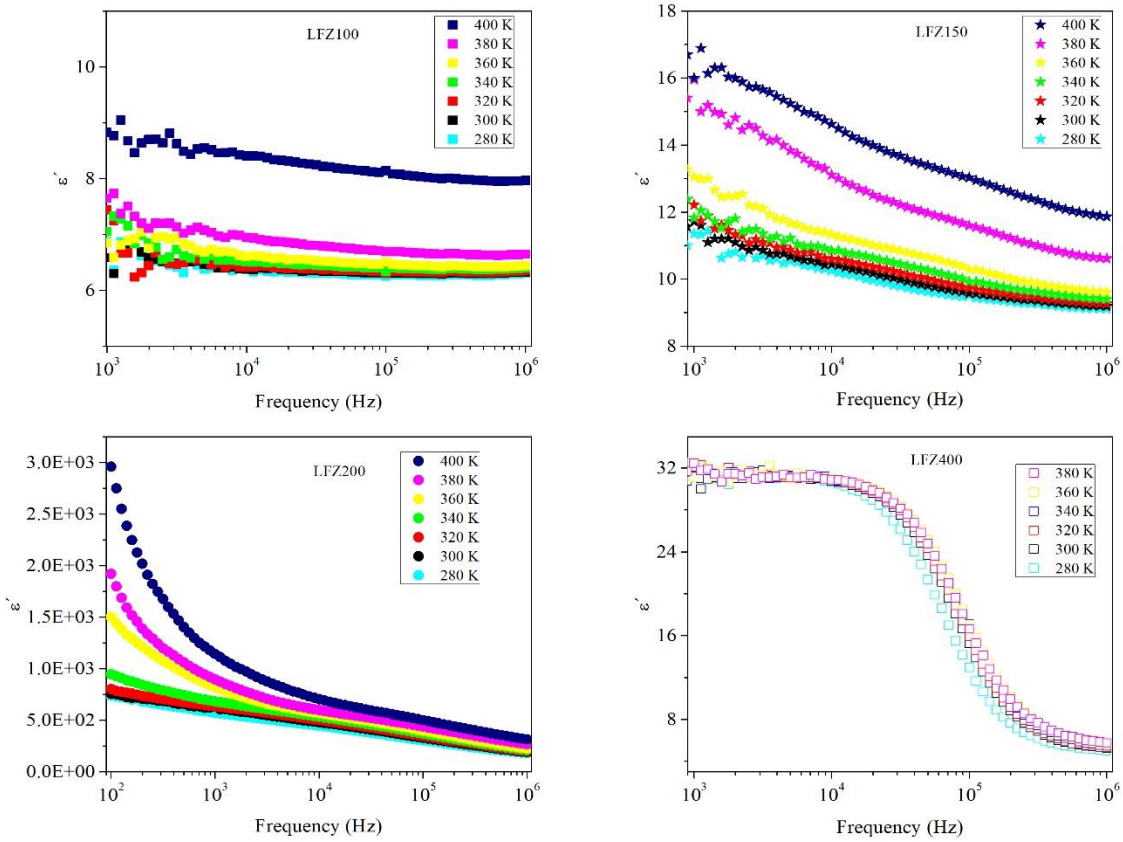

Fig. 5.8) Dispersion of dielectric constant of LFZ fibers.

Generally, when a glass undergoes crystallization conductivity drops significantly and shows a several order lower magnitude than that of the parent glass. This is the case where we are facing for our fibers. Formation of microsize crystallites with increasing the pulling rate causes a drop in electrical conductivity due to the blocking of the conduction pathways for the electron hopping between Fe sites at the crystal/glass matrix interfaces. So in more heterogeneous glass fibers where the clusters are rich in Fe^{2+}, there is a higher tendency to form Fe_2SiO_4 crystallites which are randomly distributed in the glass matrix. Besides that, only Fe^{2+} ions are incorporated in Fe_2SiO_4 crystallites, thus their crystallization induces a cause to hinder the hopping process and consequently lowering in the conductivity. Another explanation for the electrical conductivity behavior could be the influence of α-Fe_2O_3 volume in the fibers on the conductivity. Agreed with the data provided from Raman analysis (see Fig. 5.3), the larger

inclusion of α-Fe_2O_3 in LFZ100, LFZ200 and LFZ400, with conductivity values several orders of magnitude lower than magnetite can greatly decrease the conductivity [41]. Hence, conductivity can be used as an indicator of the quantity of hematite in fibers. Thus we can suggest that the conductivity in the LFZx glass fibers is not controlled only by the polaron hopping between iron ions and the crystallization of microsize crystallites, high Fe^{2+}/Fe_{total} ratio, but also the amount of inclusion α-Fe_2O_3 phase in the fibers. The maximum conductivity was found in LFZ150 which is the less heterogeneous sample. The increase in conductivity is probably due to the coexistence of both valence states and the redistribution of Fe^{n+} ions situated in some kind of clusters in the continuous residual amorphous phase. Charge transport then takes place along clusters.

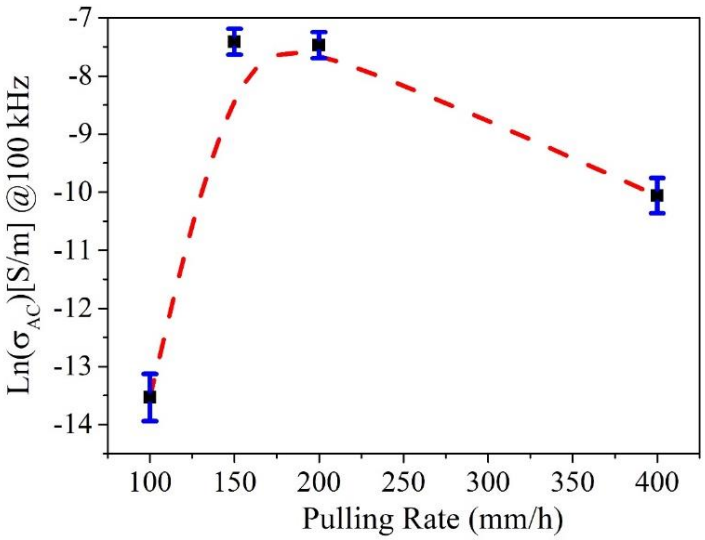

Fig. 5.9) AC conductivity at room temperature and 100Hz vs the pulling rate. (The dashed line is a guide for eyes.)

5.5) Magnetic measurements

The ZFC and FC curves measured, with an applied field of 0.1 T, of all LFZ samples are shown in Fig. 5.10.

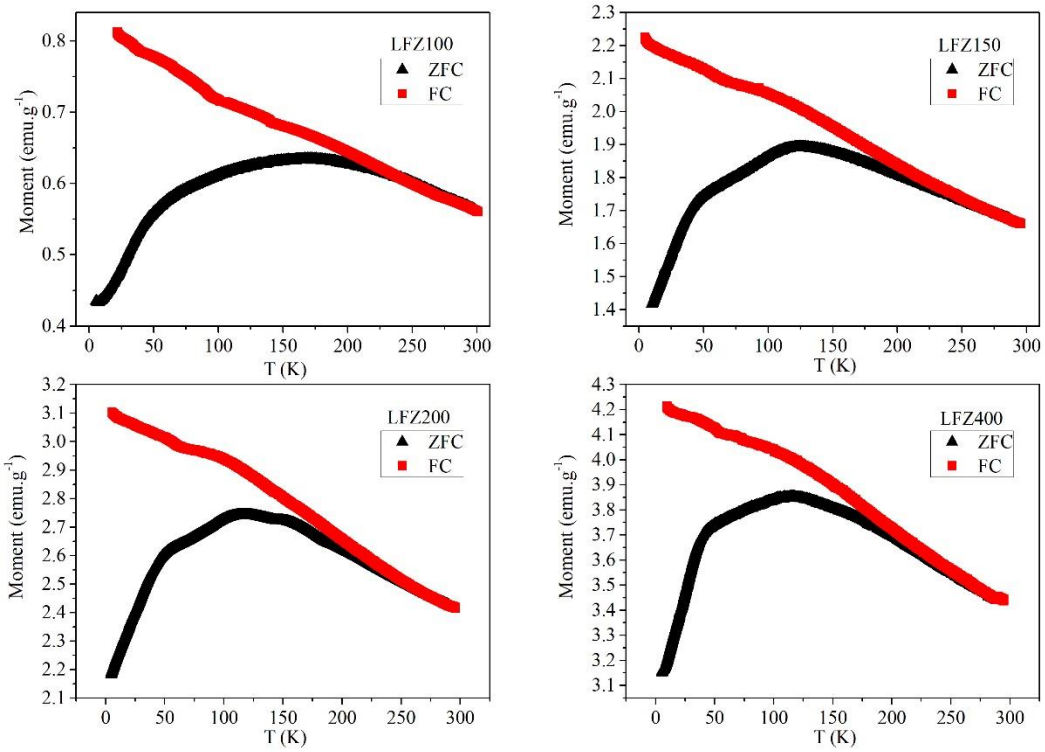

Fig. 5.10) ZFC and FC curves measured under an applied field of 0.1 T of the fibers.

The remarkable features of these curves are mentioned as follows:

(a) The FC and ZFC curves diverge for all prepared samples at a particular temperature, called irreversible temperature T_{irr}. This temperature is very similar for samples prepared at grow rates equal or greater than 150 mm/h (T_{irr}=250 K) and has a significantly lower value for the sample grown at 100 mm/ h (T_{irr} = 233 K);

(b) The ZFC curves of the samples exhibit superparamagnetic-like (SPM) characteristics signifying a broad peak centered at a temperature defined as T_P. The T_P values were determined and given in table 5.2. The T_P shifts progressively towards lower temperatures and gets closer to T_V = 120 K, the Verwey transition temperature, with an increase in the pulling rate. As mentioned before in Raman studies, higher growth rate amounts to increase of Fe^{2+} content (Fe_3O_4) within the fibers. Thus, the T_P behavior against the pulling rate is very coherent with the results achieved from the Raman analysis. Moreover, the peak broadness is a consequence of the size distribution of the crystallites and, in turn, the energy barriers, i.e., the spread in relaxation time occurring due to different sizes and random orientation of anisotropy axis [42]. As the measuring temperature increases, the moments gradually become aligned along with the applied field, resulting in the enhancement of the magnetization. The temperature T_P

attributes to the highest blocking temperature associated with the large population of crystallite in which moments get lined up with the particular applied field. Beyond T_P, thermal energy prevails the applied field ensuing into a reduction of magnetization value progressively;

(c) However, there are also small "anomalies" evident in the ZFC measurements; In the LFZ400, LFZ200 and LFZ150 ZFC graphs, a change of the slope of the curve at around T=60 K is distinguishable. This change is not so clear for the LFZ100 sample graph. Furthermore, from the ZFC results of the sample LFZ200, a small cusp is also observed at a temperature between 150 K and 200 K. In table 2.3 (see Chapter 2) we presented the magnetic structure, the transition temperatures and the saturation magnetization of the magnetic phases identified from the XRD patterns of the samples. By comparison between tables 2.3 and 5.2, it is possible to admit that the detected anomaly at T_F = 65 K can be due to the antiferromagnetic transition of fayalite [43]. In addition, the small band seen in the LFZ200 ZFC graph in the vicinity of 200 K can be ascribed to the wustite crystalline phase that is paramagnetic at room temperature with a Neel transition, T_N, at around 200-210 K. The T_N of wustite depends on the concentration of the defects in this phase [44];

(d) The value of magnetization at any temperature increases with increase in pulling rate (invoking $Fe^{2+}/\sum Fe$ total ratio increasing).

Table 5. 2) The T_P, T_{irr} , and ΔT obtained in the ZFC and FC measurements.

Sample	$T_{irr}(\pm1)$ (K)	T_P (±0.5) (K)	$\Delta T=T_{irr}-T_P$ (K)
LFZ100	233	169	64
LFZ150	251	125	126
LFZ200	252	117	135
LFZ400	248	114	134

In Fig. 5.11 it can be seen the hysteresis loops (magnetic moment vs. B) at 300 K (Fig. 5.11 a) and 25 K (Fig. 5.11 b) of the studied samples. Due to the lower thermal fluctuation of the magnetic moments, the magnetization at 25 K is clearly larger than that at 300 K for all samples. It is not observed a complete saturation of the magnetization even for the highest field (B =10 T). The inobservance of the saturation for the magnetic moment can be attributed to the surface spin disorder, the canting of spins in the ferrimagnetically ordered ferrite particles

(magnetite and maghemite) [45], as well as to the antiferromagnetic and paramagnetic phases (hematite, wustite, and fayalite) present in the samples. The maximum magnetic value measured with a magnetic field of 10 T at the room temperature vs. the pulling rate is plotted in Fig. 5.12.

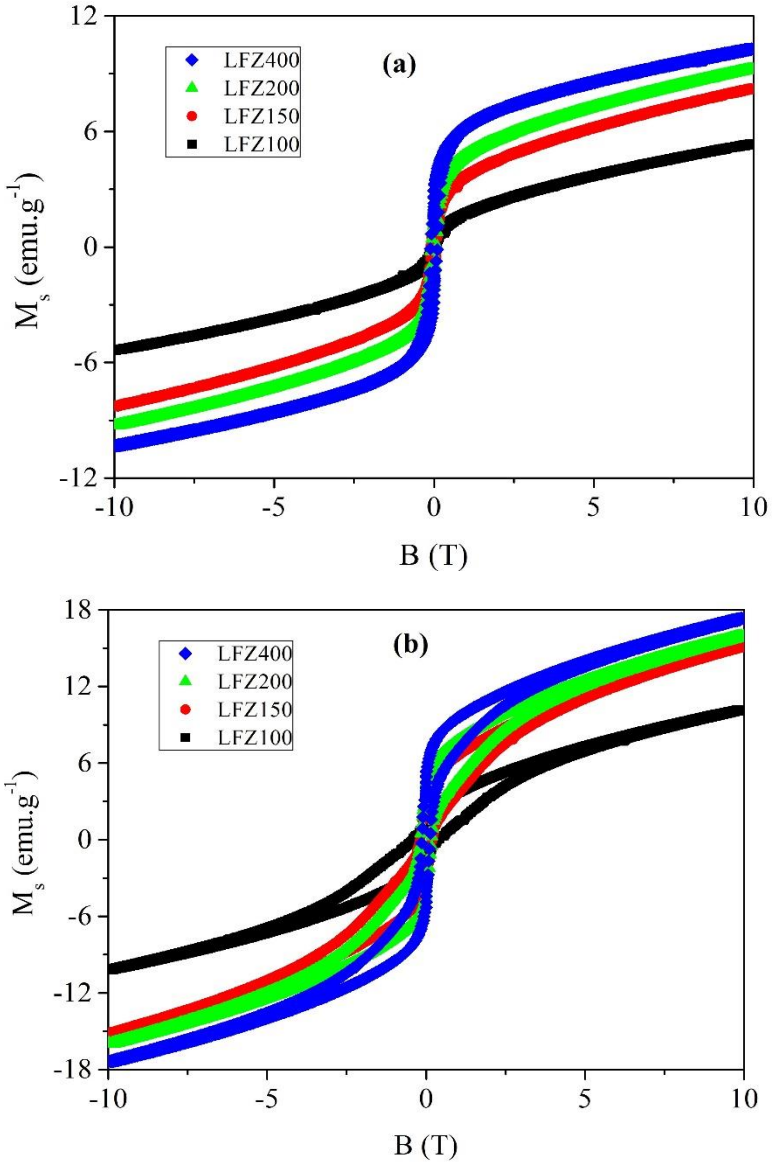

Fig. 5.11) Magnetization curves measured at a) 300 K and b) 25 K up to maximum field 10 T for the LFZ fibers.

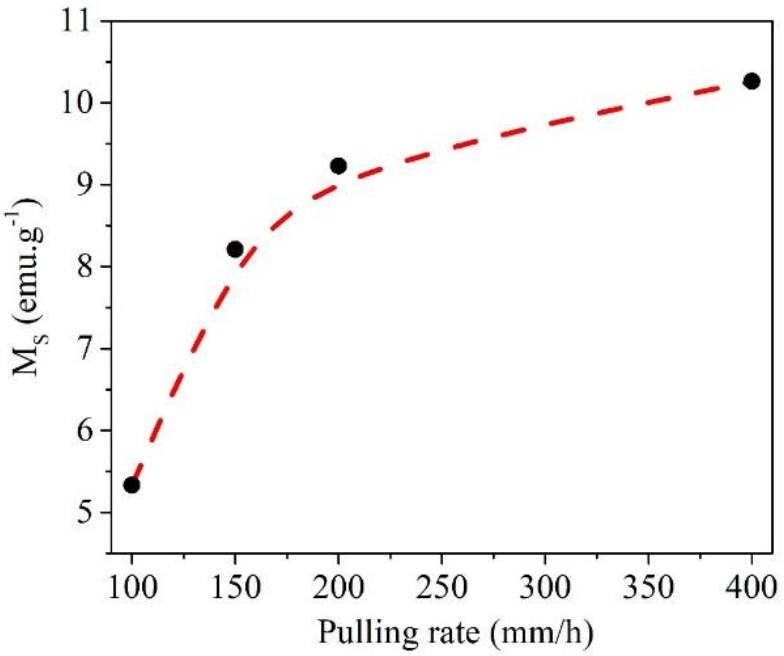

Fig. 5.12) Dependence of the M_S value measured at room temperature on the pulling rate. (The dashed line is a guide for eyes).

The maximum magnetic value increases from 5.33 to 10.26 emu/g, as the pulling rate increases from 100 to 400 mm.h^{-1}. The observed behavior can be correlated to the data provided by the Raman analysis and AFM/MFM scan images. As already mentioned in Raman analysis and supported by magnetic force microscopy, the $Fe^{2+}/\sum Fe_{total}$ ratio increases with increasing the pulling rate. The Fe^{2+} is known to couple predominantly ferromagnetically while the main interaction in Fe^{2+}-Fe^{3+} and Fe^{3+}-Fe^{3+} pairs is antiferromagnetic and this interaction is much stronger than the ferromagnetic coupling within the pairs [44] resulting in higher magnetization in the fibers with the higher $Fe^{2+}/\sum Fe_{total}$ ratio. Magnetite has an inverse spinel structure with a mixed (Fe^{2+} and Fe^{3+}) iron oxide content composed of a cubic close-packed oxygen array [44]. Its formula is written as $Fe^{3+}{}_A[Fe^{3+}Fe^{2+}]_BO_4$, and in its unit cell, all tetrahedral sites are occupied by Fe^{3+} ("A" sites), and octahedral sites are occupied by both Fe^{3+} and Fe^{2+} ("B" sites) [45]. The electron spins in the Fe^{2+} and Fe^{3+} ions in the octahedral sites are coupled, and the spins of the Fe^{3+} ions in the tetrahedral sites are coupled as well, but anti-parallel to the former. Fe^{3+} and Fe^{2+} ions with octahedral coordination are ferromagnetically coupled through a double-exchange mechanism. On the other hand, the Fe^{3+} ions in tetrahedral and octahedral sites are coupled anti-ferromagnetically via the oxygen atom. In this configuration, all Fe^{3+}

spins cancel each other out and thus the unpaired spins of Fe^{2+} ions in octahedral sites contribute to the overall magnetization [45].

Additionally, and as determined by Raman analysis, the LFZ100 has a high fraction of α-Fe_2O_3, 40%, with very low magnetization (0.3 $emu.g^{-1}$ at room temperature) due to the antiferromagnetic coupling between Fe^{3+} ions [48]. Therefore, LFZ100 manifests a sharp drop in the total magnetization and poor MFM response compared with the other fibers containing a lower quantity of hematite phase. Moreover, all fibers show non-vanishing coercivity even at room temperature. Therefore, the magnetic feature of the particles in spherical aggregates indicates a divergence from the ideal superparamagnetic behavior, resulted from a relatively strong interparticle interaction in the fibers [45].

The temperature-dependence of saturation magnetization can be described by the modified Bloch's law associated with spin-wave excitations of the form [46]

$$M_S = M_S(0)\left(1-\left(\frac{T}{T_0}\right)^{\alpha}\right) \tag{5.8}$$

Here $M_S(0)$ is the saturation magnetization at 0 K, T_0 is the temperature at which the spontaneous magnetization of the sample reaches zero. The exponent α is known as the Bloch's exponent where α = 3/2 for bulk materials [46]. Bloch derived the $T^{3/2}$ law by considering the magnon excitation of long wave-length spin-waves at low temperatures. Several studies [47, 49] reported the deviation of the saturation magnetization from Bloch's law in nanoparticles at low temperatures. The modified Bloch's law for nanoparticles was shown to have a similar form to the Bloch's law for bulk materials but with Bloch's exponent α which could have values larger and smaller than 3/2 [49, 50]. For these fits, all parameters are left free to deduce the actual contribution into the equation. Typical plots of saturation magnetizations with measuring temperature along with theoretical fits to the data based on modified Bloch's law for the fibers are given in Fig. 5.13. The fit parameters are illustrated in table 5.3. The value of the Bloch factor is ranged from α =0.62 to 0.80 for different fibers. The results have a significant deviation with the $T^{3/2}$ dependence of M_S and in LFZ fibers the saturation magnetization decreases much slower with increasing temperature than in the case of a bulk sample (α= 1.5), but this result is consistent with other results found for cobalt ferrites [47] and $Zn_xMg_{1-x}Fe_2O_4$

nanoparticles [48]. The obtained α values can be explained on the basis of size-effect on the energy band structure in the density of states in spin-wave spectrum [49].

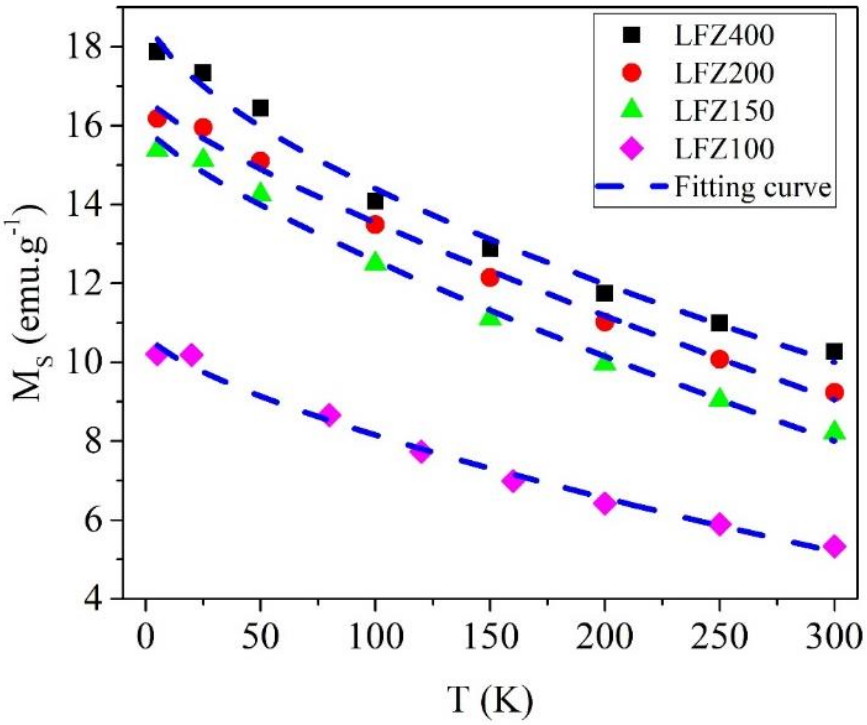

Fig. 5.13) Saturation magnetization as a function of temperature for the LFZ fibers. The dashed lines showed the best-fits to experimental data based on modified Bloch's law.

The temperature dependence of the coercive fields in particulate media has been observed to follow Kneller's law [46-49]:

$$B_C(T) = B_C(0)\left(1-\left(\frac{T}{T_b}\right)^{\beta}\right) \tag{5.9}$$

Where $B_C(0)$ is the coercive field at absolute zero temperature, T_b is the block temperature and β=0.5 is for uniaxial non-interacting single domain particles [40]. We have fitted our experimental data of B_C with the Kneller's law and the fitting plots are shown in Fig. 5.14.

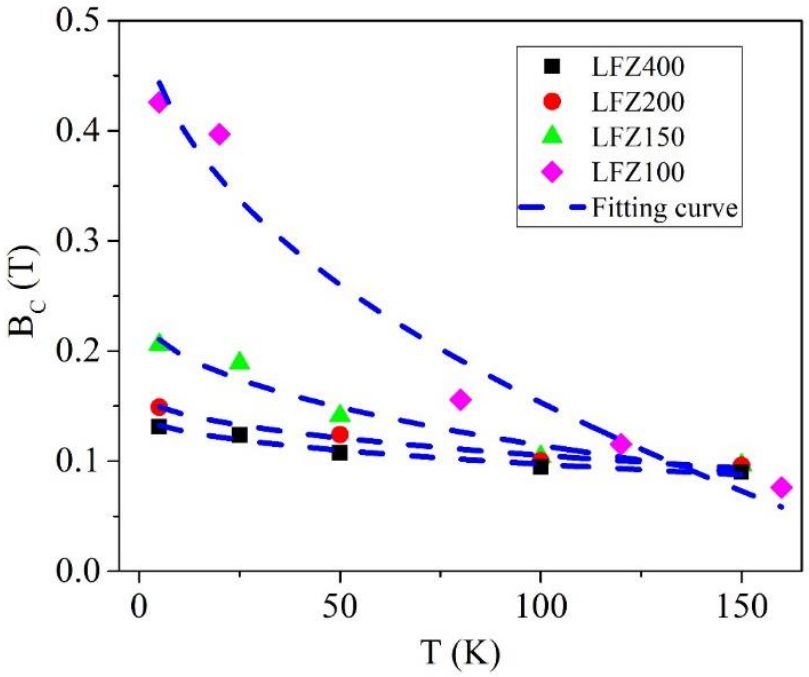

Fig. 5.14) Fitting of the temperature dependence of coercivity based on modified Kneller's law (the dashed line).

A reasonable fitting of the data, for the temperatures below 200 K, can be seen. However, due to fluctuations in B_C that occurred at temperatures above 200 K, it was not possible to include the Bc values measured at the temperature range of 200-300 K in the fitting. The obtained results from the fitting are presented in table 5.3 and Fig. 5.14. The derived values for β from the fitting are near to consistent with β=0.5, however, the theoretical values of T_b are considerably larger than the T_P values. Furthermore, the T_b increases as the pulling rate go up; unlike the pulling rate dependence of the T_P. It should be kept in mind that the Kneller equation is strictly valid for uniaxial non-interacting single domain particles. Thus, the occurrence of magnetic interactions would contribute to the detected behavior [46]. Also, the $[Fe^{2+}]/[Fe_{tot}]$ ratio increases with the pulling rate resulting in the formation of more Fe_3O_4 which is not a uniaxial material [49]. Therefore, the determination of T_b via Eq. (5.10) may give a larger error in the fibers grown at higher pulling rate. These two factors should be taken into account to explain the observed behavior for T_b.

Table 5.3) Parameters obtained from the fittings to the modified Bloch's law and Kneller's law, respectively, along with the experimental values of T_P.

Sample	Fitting parameters derived from the modified Bloch law				Fitting parameters derived from the modified Kneller law			
	$M_S(0)$ (emu.g^{-1})	α	T_0 (K)	χ^{2*}	$B_C(0)$ (T)	T_b (K)	β	χ^{2*}
LFZ100	10.74	0.69	781	0.990	0.54	204	0.47	0.984
LFZ150	15.99	0.77	735	0.993	0.24	418	0.44	0.978
LFZ200	16.72	0.80	793	0.994	0.16	1012	0.43	0.989
LFZ400	18.88	0.62	1006	0.988	0.14	1254	0.43	0.985

* correlation coefficient

Moreover, we demonstrate the influence of pulling rate on the coercivity and remanence obtained at two different temperatures, 25 K, and 300 K, in table 5.4. the coercivity was found to decrease with increasing the growth rate (provoking enhancing in the Fe^{2+}/Fe^{3+} ratio). The Stoner–Wohlfarth theory can explain such a trend. Based on this model, the coercivity (B_C) of single-domain particles can be expressed in respect of the anisotropy constant (K) and the saturation magnetization (M_S) as [50]:

$$B_C=2K/\mu_o M_S \qquad (5.10)$$

where μ_0 is the permeability constant of the vacuum.

Table 5.4) Experimental magnetic parameters measured at 25 K and 300 K.

Sample	@25 K*				@300 K*			
	Mr (emu.g^{-1})	Ms (emu.g^{-1})	B_c (T)	SQ	Mr	Ms	Bc	SQ
LFZ100	1.86	10.18	0.39	0.18	0.51	5.33	0.10	0.09
LFZ150	3.53	15.09	0.19	0.23	1.64	8.20	0.10	0.20
LFZ200	4.41	15.95	0.18	0.28	2.31	9.23	0.09	0.25
LFZ400	4.90	17.33	0.12	0.28	2.89	10.26	0.10	0.28

* All values have an error of ±1%.

Thus, the decrease of the coercivity with increasing the Fe^{2+} content within the fibers is consistent with a reduction in the anisotropy constant and the increase of the saturation magnetization.

Opposite to B_C, the remanent magnetization is enhanced as the pulling rate rises ups. The enhancement of remanence and the reduction in B_C have a linear correlation for the fibers grown in the rate range of 100 to 400 mm/h, associated to decrease in the anisotropy of the fibers [51].

The reduced remanence (squareness) values, $SQ=M_r/M_s$, calculated from the hysteresis loops at the 25 K and 300 K are enlisted in table 5.4. They are found to be in the range of 0.1 to 0.3 which is significantly smaller than the theoretical value SQ = 0.5 indicating soft magnetic properties of the fibers [44].

5.6) Final remarks

The $10Fe_2O_3$-$90SiO_2$ fibers were grown with pulling rates between 100 and 400 mm/h using the LFZ technique. Through XRD, Raman and SEM analysis we investigated the trend of crystallization and heterogeneity as a function of the pulling rate. Using Raman spectra, we concluded that the $Fe^{+2}/\sum Fe_{total}$ ratio increases with the pulling rate. The SEM images confirm the occurrence of phase separation in all samples due to the pulling rate. The acquired MFM images have shown a trend towards to the formation of the elongated magnetic monodomains and the incorporation of a high ratio Fe^{2+} ion in the crystalline structure of the fibers grown at the high pulling rate (400 mm/h). The pulling rate dependence of AC conductivity could be explained in terms of the polaron hopping between iron ions, the crystallization of microsize crystallites, induced by high Fe^{2+}/Fe_{total} ratio and also the amount of inclusion α-Fe_2O_3 phase in the fibers in agreement with the results provided from Raman, XRD, SEM and AFM/MFM measurements. The ZFC-FC curves of the fibers showed a superparamagnetic-like behavior, characterized by a T_P near to the Verwey transition and T_{irr} ranged from 200 to 250 K. However, the ZFC-FC curves are influenced by the magnetic interaction between the particles with different sizes within the fibers. The increasing in magnetization with pulling rate can be correlated to the sharp increase of the Fe^{2+}/Fe_{tot} ratio. The temperature-dependence of saturation magnetization has been fitted by a modified Bloch's law and the obtained parameters

can be explained base on size-effect of the energy band structure in the density of states in the spin-wave spectrum. Also, the modified Kneller´s law has been used to account for the temperature dependence of the coercivity in the fibers. The obtained results from the fittings are in good consistency with Raman, and morphological studies. It was proved that the pulling rate has a crucial role in the redox state of iron ions and formation of the magnetic domains dispersed into the glass network of the fibers.

5.7) References

[1] I. Fanderlick, **Silica Glass, and its Application,** Elsevier Science Publishers, Amsterdam, 1991.

[2] N.M. Ferreira, A.V. Kovalevsky, M.A. Valente, N.A. Sobolev, J.C. Waerenborgh, F.M. Costa, J.R. Frade, **Ceramics International**, 2016, 42, 2693-2698.

[3] N.M. Ferreira, A.V. Kovalevsky, J.C. Waerenborgh, M. Quevedo-Reyes, A.A. Timopheev, F.M. Costa, J.R. Frade, **Journal of Alloys and Compounds**, 2014, 611, 57-64.

[4] N.M. Ferreira, M. C. Ferro, M. A. Valente, J. R. Frade, F. M. Costa, A.V. Kovalevsky, **Dalton Transactions**, 2018, 47, 5646-5651.

[5] M.R.N. Soares, S. Leite, C. Nico, M. Peres, A.J.S. Fernandes, M.P.F. Graça, M. Matos, R. Monteiro, T. Monteiro, F.M. Costa, **Journal of the European Ceramic Society,** 2011, 31, 501-506.

[6] J. Llorca, V.M. Orera, **Progress in Materials Science**, 2006, 51, 711–809.

[7] N.M. Ferreira, A. Kovalevsky, M.A. Valente, F.M. Costa, J. Frade, **Applied Surface Science**, 2013, 278, 203-206.

[8] R.G. Carvalho, F.J. Oliveira, R.F. Silva, F.M. Costa, **Materials & Design**, 2014, 61, 211-216.

[9] M.F. Carrasco, R.F. Silva, J.M. Vieira, F. M. Costa, **Superconductor Science and Technology**, 2004, 17, 612-619.

[10] F.M. Costa, N.M. Ferreira, Sh. Rasekh, A.J.S. Fernandes, M.A. Torres, M.A. Madre, J.C. Diez, A. Sotelo, **Crystal Growth & Design**, 2015, 15, 2094-2101.

[11] A.V. Kovalevsky, A.A. Yaremchenko, E.N. Naumovich, N.M. Ferreira, S.M. Mikhalev, F.M. Costa, J.R. Frade, **Journal of the European Ceramic Society**, 2013, 33, 13-14, 2751-2760.

[12] D. R. Smith, R. F. Cooper, **Journal of Non-Crystalline Solids**, 2000, 278, 145-163.

[13] H. St. C. O'Neill, **American Mineralogist**, 1987, 72, 67–75.

[14] A.A. Bunaciu, E.G. Udriştioiu and H.Y. Aboul-Enein, **Critical Reviews in Analytical Chemistry**, 2015, 45, 4, 289-299.

[15] S.A. Salehizadeh, B.M.G. Melo, F.N.A. Freire, M.A. Valente, M.P.F. Graça, **Journal of Non-Crystalline Solids**, 2016, 443, 65-74.

[16] D.L.A. de Faria, S.V. Silva, M.T. de Oliveira, **Journal of Raman Spectroscopy**, 1997, 28, 873-878.

[17] A.M. Jubb, H.C. Allen, **ACS Applied Materials & Interfaces**, 2010, 2804-2812.

[18] O.N. Shebanova, P. Lazor, **Journal of Solid State Chemistry**, 2005, 1742, 424–430.

[19] P. Yuan, H.P. He, D.Q. Wu, D.Q. Wang, L.J. Chen, **Spectrochimica Acta Part A**, 2004, 60(12), 2941-2945.

[20] K.J. Kingma, R.J. Hemley, **American Mineralogist**, 1994, 79, 269-273.

[21] A. Chopelas, **American Mineralogist**, 1991, 76, 1101-1109.

[22] E. Huang, C.H. Chen, T. Huang, E.H. Lin, J.A. Xu, **American Mineralogist**, 2000, 85, 473-479.

[23] P.M. Sorensen, M. Pind, Y.Z. Yue, R.D. Rawlings, A.R. Boccaccini, E.R. Nielsen, **Journal of Non-Crystalline Solids**, 2005, 351, 1246-1253.

[24] L.V. Gasparov, D.B. Tanner, D.B. Romero, H. Berger, G. Margaritodo, L. Forro, **Physical Review B**, 2000, 62, 7639-7944.

[25] L. Slavova, M.V. Abrashev, T. Merodiiska, Ch. Gelev, R.E. Vandenberghe, I. Markova-Deneva, I. Nedkov, **Journal of Magnetism and Magnetic Materials**, 2010, 1904–1911.

[26] I. Chamriski, G. Burns, **Journal of Physical Chemistry B**, 2005, 109, 4965-4968.

[27] L. Stagi, J.A. De Toro, A. Ardu, C. Cannas, A. Casu, S.S. Lee, P. Ricci, **Journal of Physical Chemistry C**, 2014, 118, 5, 2857-2866.

[28] Y-S. Li, J.S. Church, A.L. Woodhead, F. Moussa, **Spectrochimica Acta Part A**, 2010, 76, 484–489.

[29] C.S.S.R. Kumar, **Raman Spectroscopy for Nanomaterials Characterization**, 2012, Springer-Verlag, Berlin.

[30] A. Moguš-Milanković, A. Šantić, S.T. Reis, K. Furić, D.E. Day, **Journal of Non-Crystalline Solids**, 2005, 351, 40–42, 3246-3258.

[31] P. Richet, B. Mysen, **Silicate Glasses and melts**, 2005, Elsevier

[32] R.K. Brow, **Journal of Non-Crystalline Solids**, 2000, 263-264, 1-28.

[33] M. Romero, J.M. Rincón, **Journal of American Ceramic Society**, 1999, 82, 1313-1317.

[34] M.M. Elkholy, L.M. Sharaf El-Deen, **Materials Chemistry and Physics**, 2000, 65, 192–196.

[35] R. Hassan, J. Hassan, M. Hashim, S. Paiman, R.S. Azis, **Journal of Advanced Ceramics**, 2014, 3(4), 306–316.

[36] A.K. Singh, T.C. Goel, R.G. Mendiratta, O.P. Thakur, C. Prakash, **Journal of Applied Physics**, 2002, 91 10, 15, 6626-6629.

[37] K.M. Gupta, Nishu Gupta, **Advanced Electrical and Electronics Materials: Processes and Applications**, 2015, Scrivener Publishing.

[38] C.G. Koops, On the dispersion of resistivity and dielectric constant of some semiconductors at audio frequencies, **Physical Review**, 1951, 83, 121.

[39] P.R. Rao, L. Pavić, A. Moguš-Milanković, V. Ravi Kumar, I.V. Kityk, N. Veeraiah, **Journal of Non-Crystalline Solids**, 2012, 23, 3255–3267.

[40] N.Ch. Ramesh Babu, M.A. Valente, N. Narasimha Rao, M.P.F. Graça, G. Naga Raju, M. Piasecki, I.V. Kityk, N. Veeraiah, **Journal of Non-Crystalline Solids**, 2012, 358, 23, 3175-3186.

[41] M.P.F. Graça, M.G. Ferreira da Silva, M.A. Valente, **Journal of Non-Crystalline Solids**, 2005, 351, 33–36, 2951–2957.

[42] S. Thota, J. Kumar, **Journal of Physics and Chemistry of Solids**, 2007, 68, 10, 1951-1964.

[43] F. Belley, E. C. Ferré, F. Martín-Hernández, M. J. Jackson, M. D. Dyar and E. J. Catlos, **Earth and Planetary Science Letters**, 2009, 284, 516–526.

[44] R. M. Cornell and U. Schwerthmann, **The iron oxides, Structures, Properties, Reactions and Uses, Second Edition**, 2003, Wiley-VCH Verlag.

[45] R. Zamiri, S.A. Salehizadeh, H. Abbastabar Ahangar, M. Shabani, A. Rebelo, J. Suresh Kumar, M.J. Soares, M.A. Valente, J.M.F. Ferreira, **Materials Chemistry and Physics**, 2017, 192, 330-338.

[46] S. Larumbe, C. Gomez-Polo, J.I. Perez-Landazabal, J.M. Pastor, **Journal of Physics: Condensed Matter**, 2012, 24, 266007-266013.

[47] I.M. Obaidat, B. Issa, B. A. Albiss and Y. Haik, **IOP Conference Series: Materials Science and Engineering**, 2015, 92, 012012.

[48] C. Vazquez-Vazquez, M.A. Lopez-Quintela, M.C. Bujan-Nunez, J. Rivas, **Journal of Nanoparticle Research**, 2011, 13, 4, 1663-1676.

[49] P. Masina, T. Moyo, H.M.I. Abdallah, **Journal of Magnetism and Magnetic Materials**, 2015, 381, 41-49.

[50] C. R. Vestal and Z. J. Zhang, **Chemistry of Materials**, 2002, 14, 3817.

[51] J. F. Qian, A. K. Nayak, G. Kreiner, W. Schnelle, and C. Felser, **Journal of Applied Physics**, 2014, 47, 305001.

This page was intentionally left blank

Chapter 6 - Manganese ferrite-silica nanocomposites obtained by auto-combustion

6.1) Introductory remarks

Nanostructured spinel ferrites have been extensively studied in recent years because of their excellent magnetic, catalytic, chemical stability and electrical conductivity properties [1, 2]. Manganese ferrite is a magnetic ferrite with a face-centered cubic (FCC) spinel structure owing two types of cations lattice sites: a tetrahedral lattice site and an octahedral lattice site occupied by 4 and 8 oxygen atoms, respectively [3]. Each unit cell consists of 8 A sites and 16 B sites [4]. Bulk $MnFe_2O_4$ adopts 20% inverse spinel structure (i.e the octahedral site is occupied by 20% of Mn^{2+} along with Fe^{3+} ions.) [5]. Several studies showed that the degree of inversion strongly depends on the synthesis procedure and the particle size of the magnetic phase [6]. Manganese ferrite nanoparticles (MnFe NPs) have shown a high value of the magnetic susceptibility when compared to other ferrite nanoparticles, high chemical stability, easy synthesis process, high resistivity, soft magnetic behavior and intermediate saturation magnetization [5, 7]. Because of these special characteristics, MnFe NPs have drawn potential merits in several technological applications including MRI [7], targeted drug delivery [8], microwave, inductance, magnetic recording media, electronic devices, magnetic storage devices [9] and gas sensors [10].

The variation of the microstructure will lead to the cation redistribution, which further impacts the electrical and magnetic properties of the ferrite nanocrystals [11, 12]. Moreover, the magnetic behavior is affected by interparticle interactions and the local environment of nanoparticles can be changed when they are dispersed in amorphous silica [13].

In this chapter, we report the effect of silica concentration on structural, morphological, electrical and magnetic properties of $xMnFe_2O_4$-$(100-x)SiO_2$ (x=100, 20, 15, 10 in mol%) nanocomposites prepared by citric acid assisted auto-combustion method. Various characterization techniques including XRD, Raman, SEM, BET, TEM, Dielectric measurements and VSM were employed to obtain the results discussed in this chapter.

6.2) Experimental Procedure

Analytical grade iron nitrate (99% purity), manganese nitrate (≥97% purity), TEOS (≥ 98% in solution), ammonia (≈30% in solution) and citric acid (98% purity) all from MERCK were used as raw materials to prepare, manganese ferrite-silica composite, $MnFe_2O_4$-silica. Below we describe the preparation process of $xMnFe_2O_4$-$(100-x)SiO_2$ (x=10, 15, 20 and 100 in mol%) compositions. According to the given molar percentage of Mn-ferrite and silica in the composite, aqueous solutions of iron - manganese nitrates (molar ratio of Fe:Mn=2:1) and citric acid (CA) with 1:1 molar ratio of metals to CA were prepared using appropriate amount of the raw materials. The aqueous solutions were stirred for 0.5 h separately and then mixed together. A small amount of ammonia was added into the metal-citrate solution to adjust the pH value to about 4, stabilizing the nitrate-citrate sol. During this procedure, the solution was continuously stirred and kept at room temperature. A silica precursor, TEOS in ethanol and water (TEOS/water/ethanol molar ratio of 1/10/4 was considered) was prepared and added up to the nitrate-citrate solution. For the preparation of pure $MnFe_2O_4$ nano-powders, the silica precursor was not added to the nitrate-citrate solution. After vigorous stirring for 24 h in air at a temperature in the range of 80-100 ^oC, the water and ethanol (for compositions containing silica precursor) contents were released and the sol was allowed to gelify. Subsequently, the gel was submitted to a thermal treatment at 300 °C in a preheated oven. The gel started to boil and after that, the temperature increased gradually until the dried gel simultaneously burnt in a self-propagating combustion manner and it is completely transformed into loose powder at 500-600 ^oC depending on the composition. Hereafter, we label the compositions as xMnFe/Si where x is the molar percentage of manganese ferrite.

6.3) Thermal analysis results

The DTA curve of the auto-combusted 15MnFe/Si composite (Fig. 6.1) displays in the low-temperature region few variations due to decomposition of organic components adsorbed on the surface during catalysis. Besides, this curve shows that the ferrite formation starts from 580 ^oC and a weight loss of 30 % on the TGA curve can be observed. The weight loss corresponds to the vigorous oxidation-reduction reaction or combustion reaction among citric acid, unreacted alkoxide organic ligand and nitrate ions. Additionally, two exothermic peaks at

around 700 and 900 °C were detected and can be due to the oxidation-reduction reaction of the residue organics in ashes.

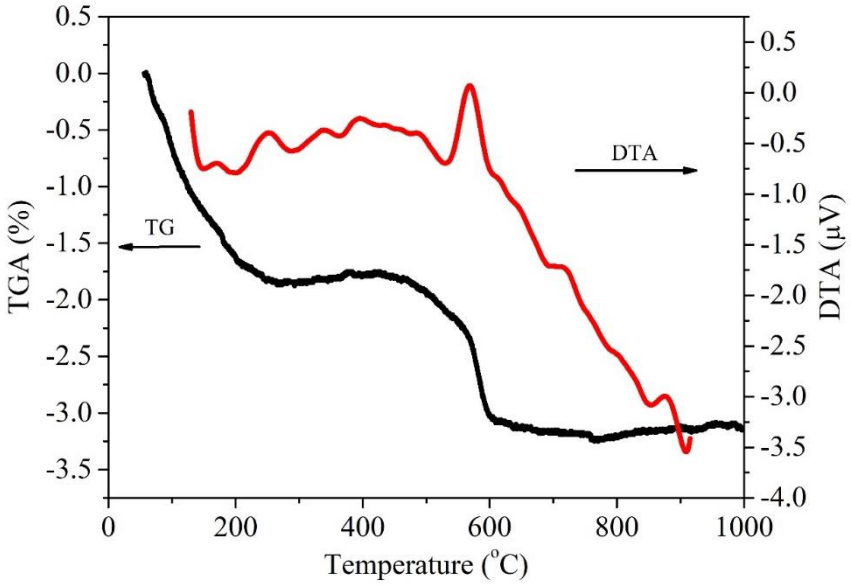

Fig. 6.1) DTA-TG curve of the auto-combusted 15MnFe/Si nanocomposite.

6.4) XRD pattern analysis

Fig. 6.2 shows XRD patterns of all as-prepared compositions measured at room temperature. The patterns confirm the formation of single phase cubic spinel structure of $MnFe_2O_4$ without any signature of secondary phase in 100MnFe/Si, 15MnFe/Si and 10MnFe/Si in agreement with the JCPDS no. 04-016-8331. X-ray diffraction patterns of all compositions indicate a preferable growth along the (220), (311), (400), (333) and (440) directions belonging the face-centered-cubic (FCC) close packing structure of $MnFe_2O_4$. However, for 20MnFe/Si composition, the sample contains some impurities which are due to the α-Fe_2O_3 phase. The peaks are sharper and more intense for the pure manganese ferrite nanopowders compared with ones for the compositions containing silica. While the broadening of the peaks is more pronounced in 20MnFe/Si. Moreover, the broad and low-intense hump at $2\theta \sim 22^o$ observed in the $MnFe_2O_4$-silica compositions is due to the short-range correlations in the amorphous silica phase. According to the Scherrer equation, the broad diffraction maxima reveal a nanometric particle size of manganese ferrite for all samples in comparison with those typical diffraction

patterns corresponding to bulk materials [14]. The average $MnFe_2O_4$ crystallite sizes of the samples are estimated through applying the Debye-Scherrer equation into the broad maximum at $2\theta \sim 35^o$ after considering corrections for instrumental contribution. The crystallite size of the samples is represented in table 6.1.

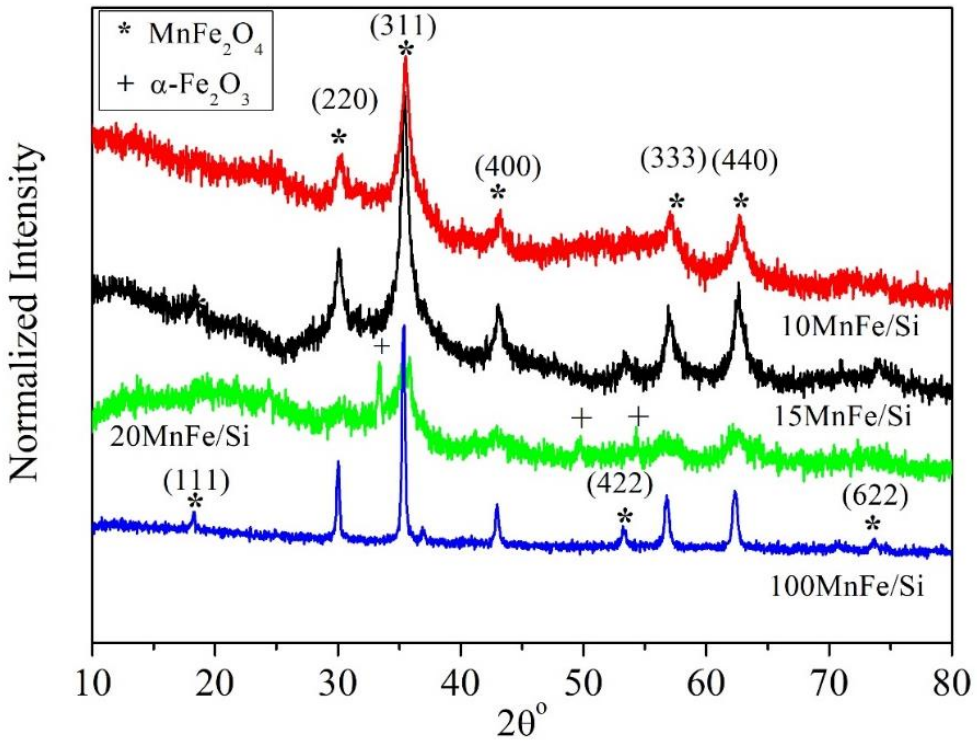

Fig. 6.2) XRD pattern of xMnFe/Si.

Usually for nanosize materials, X-ray diffraction profiles are influenced not only by the crystallite size but also by the lattice strain and lattice defects such as O^{2-} vacancies [15]. While Scherer's formula does not consider the strain contribution in the line broadening of a Bragg reflection, the Williamson–Hall (W-H) approach can be employed for calculating the crystallite size and strain contribution to the X-ray line broadening (β) in the nanocomposites [16]. The study of microstrain assuming uniform energy density model had established that microstrain in nanostructured samples [17].

Table 6.1) Mean particle size obtained from W-H ($<D>_{W-H}$), D-Sch ($<D>_{D-Sch}$), BET ($<D>_{BET}$), TEM ($<D>_{TEM}$) approaches along with the values of the specific surface area, S, the strain, η, and the deviation extracted from log-normal function, ς, and the density, ρ, of xMnFe/Si samples. (*Due to the existence of α-Fe_2O_3 impurities, it is hard to distinguish that the particle observed in TEM image whether are $MnFe_2O_4$ or hematite. A Debye-Scherrer survey showed that the 20MnFe/Si sample contains α-Fe_2O_3 impurities with an average size of 30 nm.)

Sample	$<D>_{W-H}$ (nm)	$<D>_{D-Sch}$ (nm)	$<D>_{BET}$ (nm)	η ($\times10^{-3}$)	$<D>_{TEM}$ (nm)	ς	S ($m^2.g^{-1}$) (±0.2)	ρ ($g.cm^{-3}$) (±0.05)
100MnFe/Si	54±8	33±0.5	116±1	8.73	33	0.98	9.7	5.33
20MnF/Si*	5 ±0.5	9±0.5	115±1	-	7	0.25	24.7	2.11
15MnFe/Si	13±0.5	12±0.5	48±0.5	1.62	8.5	0.09	41.2	3.03
10MnFe/Si	12±0.5	12±0.5	27±0.5	1.38	6	0.29	77.8	2.86

The contributions to integral-breadth of crystallite size and the strains can be evaluated by the adoption of an integral-breadth method relating the crystallite size, expressed as the average apparent diameter, δ, with the mean value of the strain, η [17]:

$$(\frac{\beta^*}{d^*})^2 \approx \frac{1}{\delta}\frac{\beta^*}{(d^*)^2} + (\frac{\eta}{2})^2 \qquad (6.1)$$

where $\beta^*=\beta\cos\theta/\lambda$ and $d^* = 2\sin\theta/\lambda$. β and d are the integral breadth and the interplanar distance, respectively.

Fig. 6.3 shows the $<D>_{W-H}$ and η values versus $MnFe_2O_4$ concentration obtained from equation 6.1. It can be seen that the variations of $<D>_{W-H}$ and η both are in a similar manner. The strain and crystallite size are found to be maximum for the sample 100MnFe/Si, however, the crystallite size of 20MnFe/Si is the smallest. The result of strain for 20MnFe/Si is not shown because the fitted data gave a negative value which has no physical meaning. This primarily comes from the huge contribution of internal strain and the defects due to the existence of α-Fe_2O_3 impurities. Consequently, the de-convolution of XRD peaks is affected by the close proximity of coexisting hematite and manganese ferrite. So the peak broadening and the complexity of the polycrystalline composition effect in the evolution of the strain [18]. Moreover, the average crystallite size for $MnFe_2O_4$-silica compositions is observed to be

smaller than pure $MnFe_2O_4$. To prevent a particle growth, the motion of grain boundary must be impeded. The resistance of the motion of grain boundaries can be explained by Zener-Pinning effect [19]. This motion has prevented either precipitation of secondary phase or contamination at the surface of $MnFe_2O_4$. When the moving boundaries attach the amorphous silica pores, moving boundaries are obstructed by the generation of retarding force. If the retarding force is more than the driving force of the grain growth, the particles cannot grow any longer. It is noticeable that for the sample 20MnFe/Si, the combined effect of the presence of α-Fe_2O_3 impurities and amorphous silica cause more retarding force and consequently the growth of crystal grains is prohibited excessively and the crystallite size is reduced extensively.

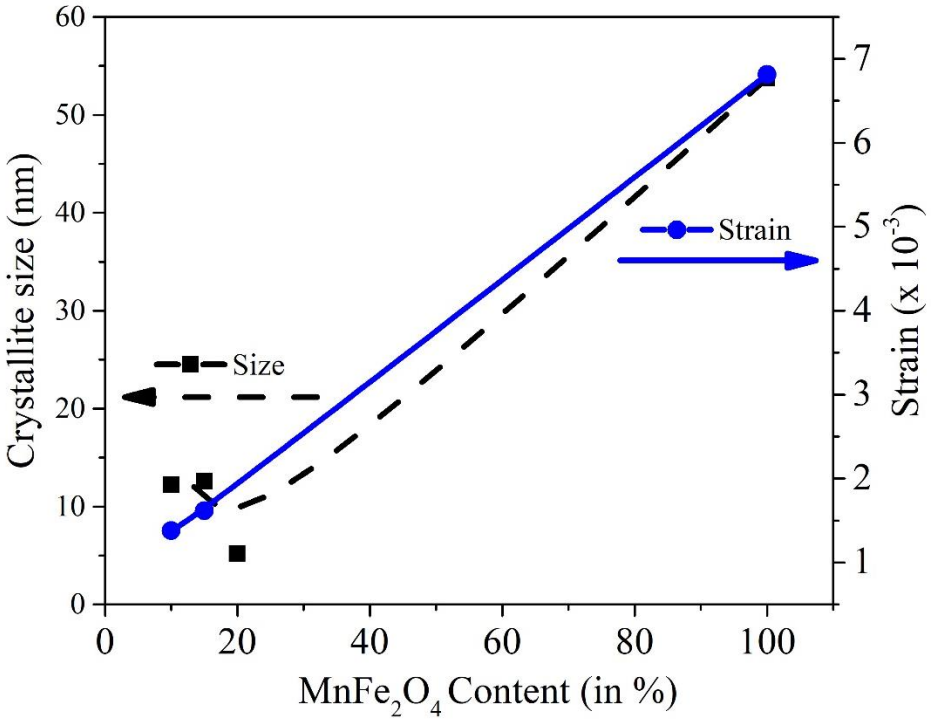

Fig. 6.3) Size-strain plot of xMnFe/Si.

To investigate the effect of thermal treatment on crystalline phase evolution, the sample 15MnFe/Si was calcined up to 800 and 1000 ^oC with a rate of 5 ^oC/min for 2h in the air. In addition, the same composition went under a heat-treatment process in nitrogen atmosphere. For this calcination process, the sample was heated up to 1000 ^oC/min with rate of 10 ^oC/min for 2 h and then was cooled with the same rate down to room temperature. During the process, nitrogen gas passed through the tubular reactor continuously.

The XRD patterns of the auto-combusted 15MnF/Si nanocomposite, the samples calcined for 2h in air atmosphere at 800 ^{o}C and 1000 ^{o}C in air and nitrogen atmospheres are illustrated in Fig. 6.4.

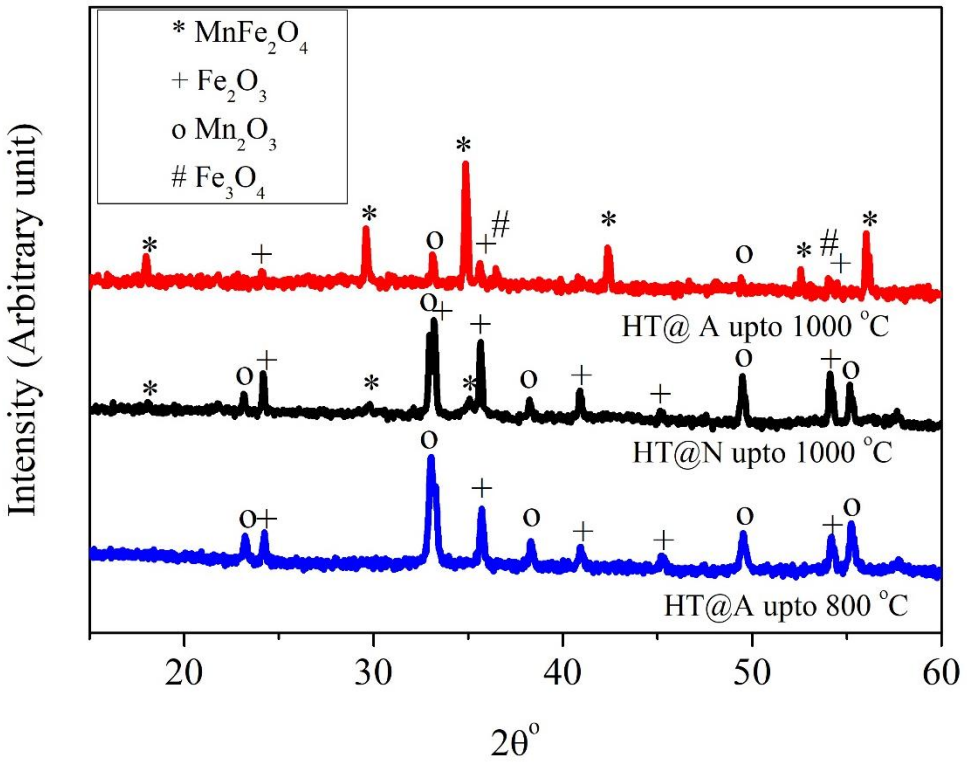

Fig. 6.4) XRD patterns of 15MnFe/Si after heat-treatment in the different conditions. (A and N denote air and nitrogen atmosphere, respectively.)

As Fig. 6.4 shows the calcination treatments result in huge variations in the XRD spectra. With heating up to 800 ^{o}C at air atmosphere, the manganese ferrite, $MnFe_2O_4$, is totally decomposed to Mn_2O_3 and α-Fe_2O_3, 52% and 48%, respectively. While when the composition is heated up to 1000 ^{o}C in the air, the XRD spectrum shows the presence of Mn_2O_3 and hematite phases, 34% and 62% respectively, with only 4% of manganese ferrite. Seemingly, an increase in the heat-treat temperature from 800 to 1000 ^{o}C causes the formation of some $MnFe_2O_4$ crystalline raised from the internal redox reaction Mn_2O_3 and Fe_2O_3 with free O_2 ions existing in the residue organics and amorphous silica. The decomposition of manganese ferrite and consequently the formation of the hematite and manganese oxide phases during the thermal treatment in the air can be related to the large positive free energy change associated with the reaction [20] and can be described according to the following equation:

$$2MnFe_2O_4 + 1/2\ O_2 \leftrightarrow 2Fe_2O_3 + Mn_2O_3 \quad (6.2)$$

Moreover, the peaks of α-Fe_2O_3 and Mn_2O_3 phases, become sharper as the heat treatment temperature increases. The Fig. 6.4 reveals that when the thermal treatment process is carried out in a nitrogen atmosphere, $MnFe_2O_4$ remains as the major phase with 69% quantity and the remaining is transformed to the secondary phases Mn_2O_3, α-Fe_2O_3, and Fe_3O_4, with 16%, 10% and 5% quantity, respectively.

So oxidative/non-oxidative atmosphere and temperature are two crucial parameters which should be controlled for the formation of ferrite crystalline phase. It was already experienced that pure phase of $MnFe_2O_4$ would be expected to be present after vacuum heat treatment ($p \sim 10^{-7}$ atm) up to 700 ^oC [1], while heat treatment in air at a higher temperature of 900 °C should result in oxidation to other phases such as Mn_20_3 and Fe_20_3 [21].

6.5) Density and BET measurements analysis

Nitrogen adsorption-desorption isotherms of the prepared nanocomposites were measured using a micromeritics equipment, Gemini V2 (USA). The specific surface area of the samples was measured based on the Brunauer-Emmett-Teller (BET) equation [22] and the obtained values are listed in table 6.1.

The average particle size ($<D>_{BET}$) using the specific surface area measurement can be calculated in accordance with the following equation [22]:

$$< D >_{BET} = \frac{6 \times 10^6}{(S\rho)} \quad (6.3)$$

Where S is the specific surface area of the particle and ρ is the density of the nanocomposites. The density measurement was done via the Archimedes method at room temperature and using ethanol (with 99% purity) as the immersion liquid. The results of $<D>_{BET}$ and ρ are given in table 6.1. A minimum density was observed for sample 20MnFe/Si, maybe due to high inclusion and nonuniform distribution of the silica matrix in this sample. Moreover, the specific surface area increase as the $MnFe_2O_4$ content decreasing in the compositions. Table 6.1 shows

that the values of $<D>_{BET}$ are much larger than those obtained from XRD analysis. The calculation of particle size from the specific surface area usually takes into account the effectively absorbed surfaces of the grains or agglomerates which consisting of several ultrafine crystallines. The highest BET surface area was observed in 10MnFe/Si indicating that the clusters in this composition have a mesoporous structure.

6.6) Morphology results

Fig.s 6.5 a and b shows the SEM images for the 100MnFe/Si and 10MnFe/Si nanocomposite, respectively. The agglomerated spongy-shaped particles are observed for 100MnFe/Si. The length of spongy-shaped $MnFe_2O_4$ is about 100–200 nm. In Fig. 6.5 b, it is found that the 10MnFe/Si nanocomposite still retains the morphology of spongy shape and the agglomeration tends to become into the particles with the bigger surface area which is in agreement with the BET results.

The size and morphology of the synthesized particles were determined using TEM analysis and micrographs for the powder are shown in Fig.s 6.6-6.8. Fig. 6.6 a-d presents the TEM image of $MnFe_2O_4$-SiO_2 composites. For 100MnFe/Si, (Fig. 6.6 a) a wide range of morphology and size is observed. Small size particles are usually spherical whereas the sample of well-matured particles are elliptical and polymorph like. The selected area electron diffraction (SAED) pattern of the image (Fig. 6.6 a) indicates that the concentric rings with bright and large spots confirming the nanosize crystalline nature of the $MnFe_2O_4$ self-ignited nanocomposite. The superimposition bright spots designate the polycrystalline nature of nanoparticles [23]. In 20MnFe/Si, small spherical particles formed loose aggregates and were randomly distributed in amorphous silica matrix (Fig. 6.6 b). The TEM image of 15MnFe/Si demonstrates that the nanoparticles have a core-shell structure with light contrast silica shells and dark contrast cores of $MnFe_2O_4$, implying that the hydrophilic $MnFe_2O_4$ NPs were successfully uniformly distributed and coated by a silica shell. The SAED pattern of core-shell $15MnFe_2O_4$-$85SiO_2$ nanoparticles exhibits the lattice fringes corresponded to the typical cubic inverse spinel structure (Fig. 6.7 c). For 10MnFe/Si, the smaller spherical particles compared with the ones in 15MnFe/Si, indiscriminately are dispersed in amorphous silica. The random dispersion of the ultrafine nanoparticles is evidenced by the slender bright spots distributed non-uniformly around the lattice fringes, according to the SAED

pattern of 10MnFe/Si nanocomposite. To determine the size and size distribution of the nanoparticles, at least 50 particles randomly selected from the TEM micrographs. The average diameter of such nanoparticles was estimated using ImageJ to obtain the histogram of the size distribution. The histogram for each sample then was fitted to a log-normal function:

$$f(D) = \frac{A}{\sqrt{2\pi}\varsigma D}\exp\left[\frac{-Ln(\frac{D}{D_o})^2}{2\varsigma^2}\right] \qquad (6.4)$$

The mean diameter $\langle D\rangle_{TEM}=D_o.\exp(\varsigma^2/2)$ and the deviation, ς, were determined using fit results and the obtained results listed table 6.1. The $\langle D\rangle_{TEM}$ values are consistent with the $\langle D\rangle_{D\text{-}Sh}$ values. The highest value of ς was observed for 100MnFe/Si evidencing the polycrystalline nature of the sample. While the lowest value is for 15MnFe/Si meaning that the spherical $MnFe_2O_4$ nanoparticles are well-uniformly dispersed in the silica shell.

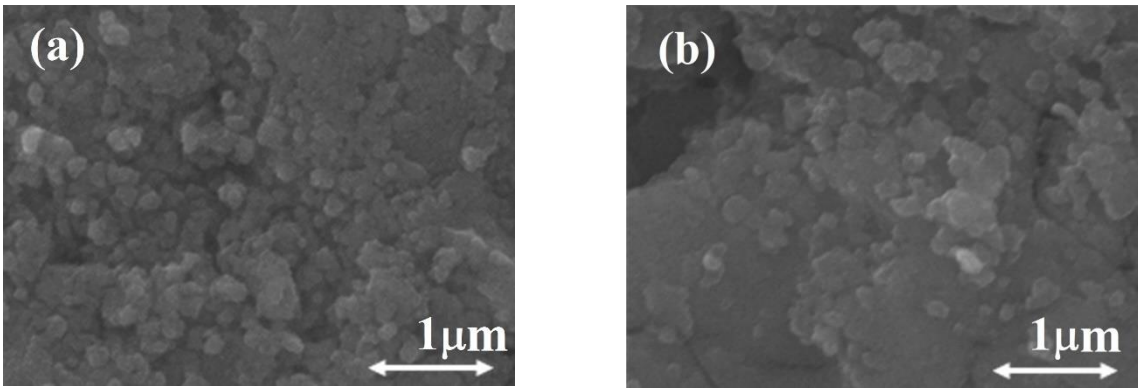

Fig. 6.5) SEM micrographs of: a)100MnFe/Si and b)10MnFe/Si samples.

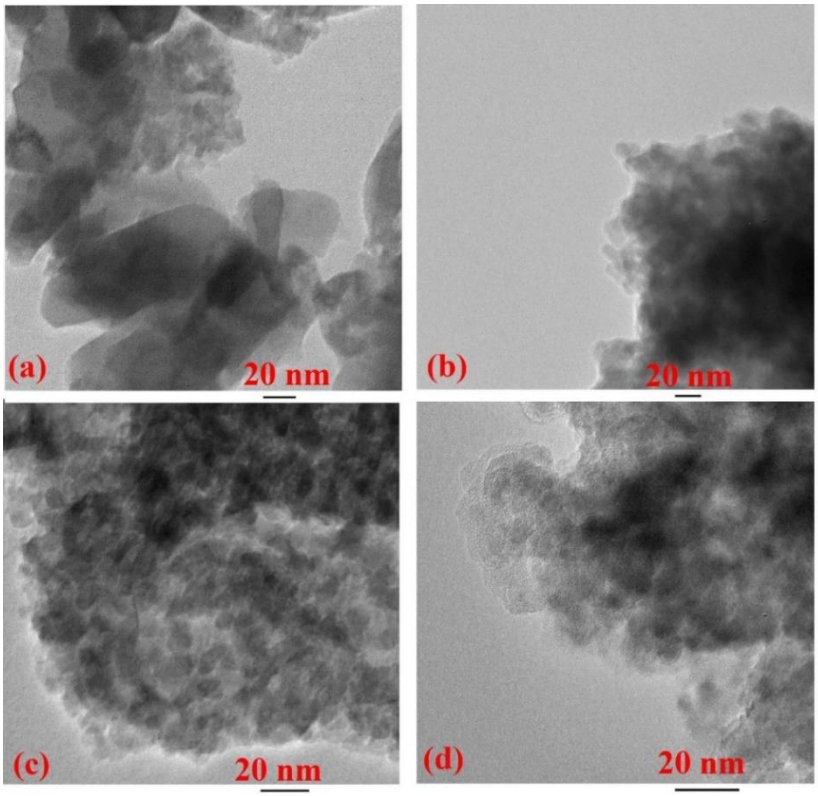

Fig. 6.6) TEM micrographs of a) 100MnFe/Si, b) 20MnFe/Si, c) 15MnFe/Si and d) 10MnFe/Si.

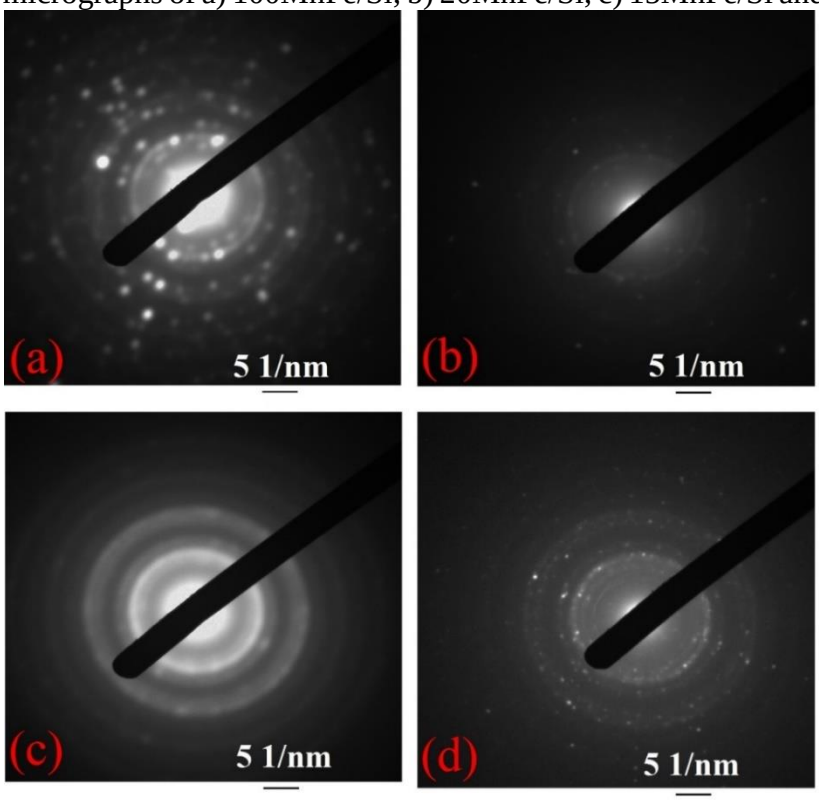

Fig. 6.7) The selected area electron diffraction patterns of the xMnFe/Si.

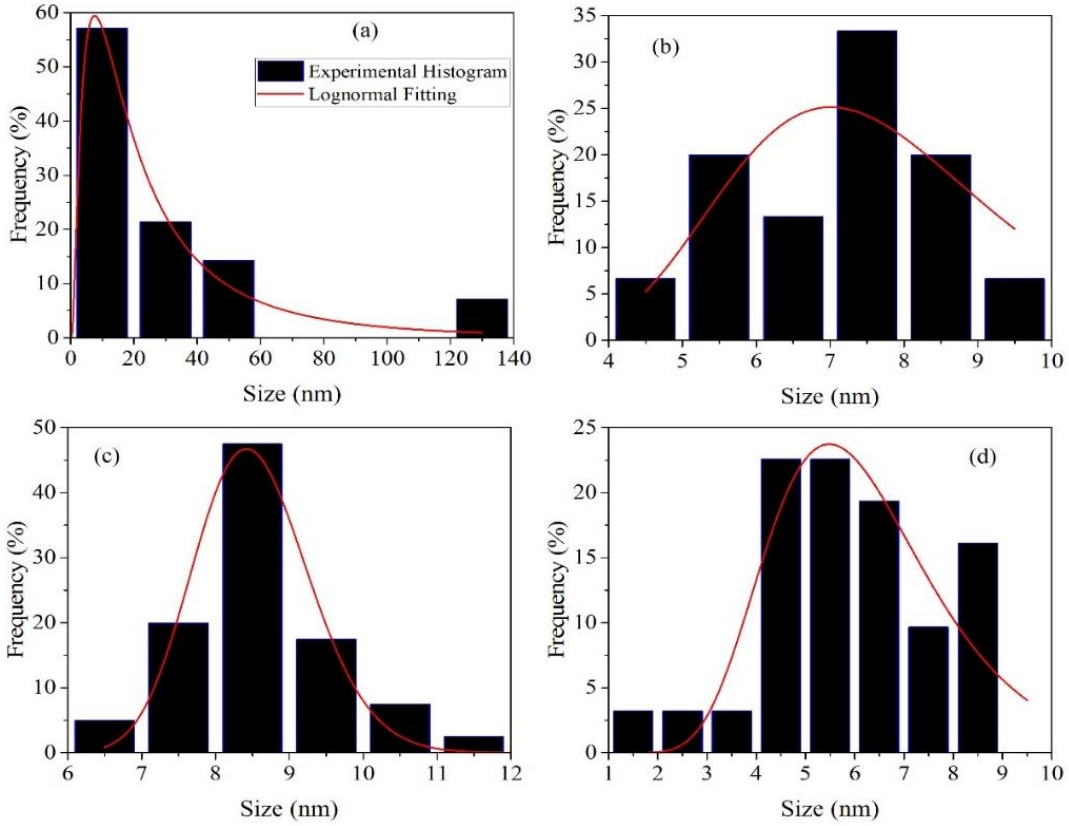

Fig. 6.8) Histogram of particle size distribution of a) 100MnFe/Si b) 20MnFe/Si c) 15MnFe/Si and d) 10MnFe/Si.

6.7) FTIR and Raman spectroscopic analysis

As an example, the Fourier-transform infrared (FT-IR) analysis was performed on 15MnFe/Si in the wavelength range of 400-4000 cm^{-1} by means of a Perkin Elmer Analyst 100 atomic absorption spectrometer (Fig. 6.9).

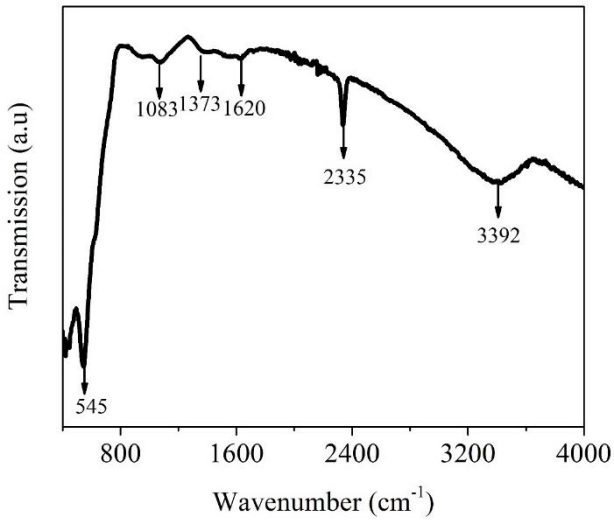

Fig. 6.9) FT-IR spectra of 15MnFe/Si.

The broadband absorption peaks appeared at 3392 cm^{-1} and 1620 cm^{-1}, were ascribed to the stretching modes of the O-H groups in the sample. The characteristic band at 1373 cm^{-1} is related to the symmetric vibrations of the NO^{3-} group [24]. The peak at 2335 corresponds to H–O–H bending vibration of the free or absorbed water [25]. Generally, the metal oxide vibrations occur below 1000 cm^{-1}. The band around 545 cm^{-1} is regarded to the intrinsic vibrations of octahedrally coordinated metal ions in the spinel structure, confirming that the prepared samples are spinel in structure attributed to the intrinsic vibrations of octahedrally coordinated metal ions in the spinel structure, confirming that the prepared samples are spinel in structure [24]. The band at 1083 cm^{-1} was assigned to the vibration of the Si-O bonds, demonstrating the existence of SiO_2 shell on the surface of $MnFe_2O_4$ [26] as confirmed by TEM images. It is worth mentioning that other samples showed similar spectroscopic behavior. Raman spectra of $MnFe_2O_4$-SiO_2 compositions measured in the spectral region between 200 and 1000 cm^{-1} at room temperature are represented in Fig. 6.10. First, each spectrum was baseline corrected in order to remove the background effect and then the spectrum was normalized with respect to the most intense peak in each spectrum. Identification of all possible vibration modes in each spectrum was obtained by deconvolution into individual Gaussian peaks as described precisely in [27] and given in table 6.2.

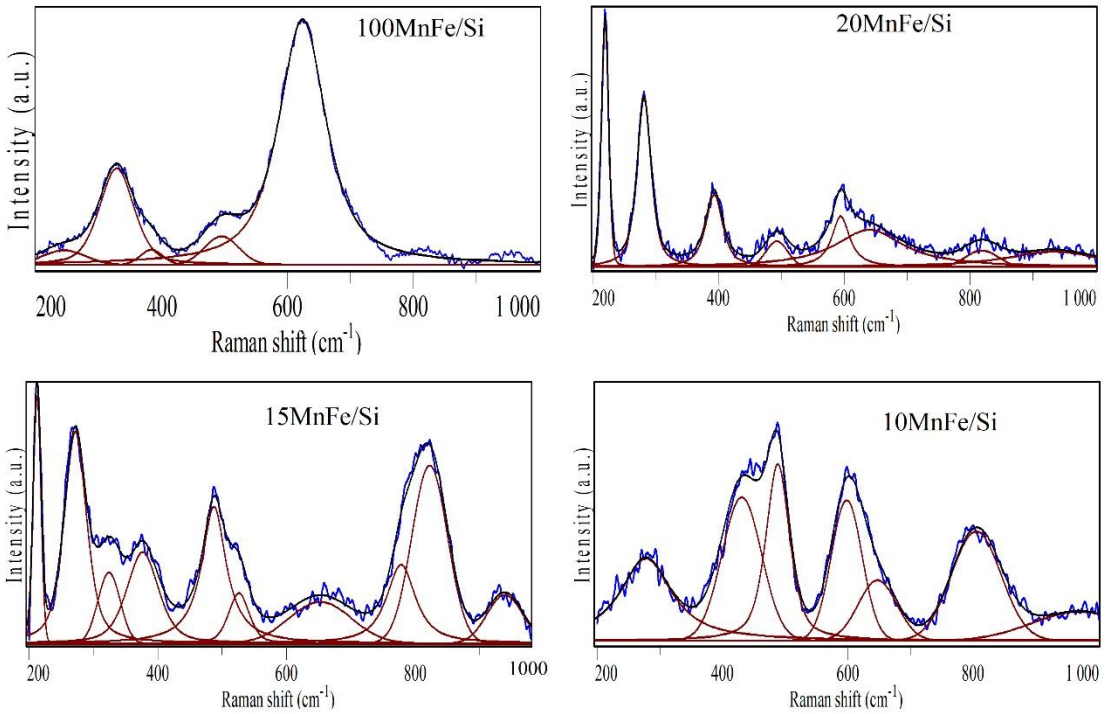

Fig. 6.10) Raman spectra and deconvolution curves of all samples.

For 100MnFe/Si Raman active bands were detected at 245, 327, 381, 497 and 622 cm^{-1}. These bands correspond to five first-order Raman active mode (A_{1g}, E_g, and $3T_{2g}$) characteristic of the cubic inverse-spinel structure O^7_h ($Fd\bar{3}m$) space group [28]. The A_{1g} appeared at 622 cm^{-1} is the symmetric stretch of tetrahedral FeO_4. The E_g at 327 cm^{-1} is regarded as symmetric bending of oxygen ions with respect to Fe. The T_{2g} (1) at 245 cm^{-1} is reflected the translational motion of Fe–O in manganese ferrite. The peak at 381 cm^{-1} is caused by the anti-symmetric stretch of Fe and O assigned as T_{2g} (2) mode. T_{2g} (3) at 497 cm^{-1} is due to an anti-symmetric bending of oxygen with respect to Fe [29, 30]. With the addition of SiO_2 to the composition, some bands related to the silica matrix are observed. Raman features at 440 and 810 cm^{-1} observed is regarded to the Si-O-Si stretching mode in SiO_4 structure. Moreover, the bands observed in the 900-1000 cm^{-1} range are attributed to OH impurity content in organic residue ash [31, 32]. On the other hand, a larger number of Raman bands is observed in the compositions containing silica. The extra Raman features can be attributed to the lowering of space group symmetry due to lattice distortion and also random cation distribution over tetrahedral and octahedral sites induced by the inclusion of the amorphous silica matrix [33]. Due to the short range orderness of the cations distributed at the octahedral site, domains with

lower space group symmetry are formed. As mentioned previously, the modes detected above 600 cm^{-1} mostly correspond to the motion of oxygen in tetrahedral AO_4 groups, while other low-frequency modes ranged from 350 to 500 cm^{-1} correspond to octahedral–metal stretching, $M_{octa}\leftrightarrow O$, the characteristics of the octahedral sites (BO_6) [34].

It is worthy mentioning that the number of allowed Raman modes in 10MnFe/Si decreases. It can be explained in terms of the particle size effect on the Raman features. With decreasing in size, the bands become wider, and adjacent broad Raman peaks are superimposed consequently some of the modes cannot be detected. Similar behavior already was observed in nanosized $CoFe_2O_4$ particles [35].

It should be noted that in the case of 20MnFe/Si, the existence of hematite impurity also maybe give rise to the excess of permitted Raman modes and the broadening of the bands. However, since the Raman bands of hematite are in close proximity to the ones for $MnFe_2O_4$ [36] the contribution of each phase in the Raman band is hardly distinguishable.

Table 6.2) Raman vibration modes of all samples.

100MnFe/Si	**20MnFe/Si**	**15MnFe/Si**	**10MnFe/Si**	**Assignment**
-	219	212	-	the translational motion of Fe–O
245	280	272	276	
327	-	322	-	symmetric bending of oxygen
381	393	375	-	ions with respect to Fe
-	-	-	438	O-Si-O band
497	489	489	487	an anti-symmetric bending of oxygen with respect to Fe
-	594	524	589	octahedral–metal stretching in the octahedral sites
622	649	663	641	symmetric stretch of tetrahedral FeO4
-	820	818-(781)*	800	Si-O-Si band
-	937	941	971	Si-O-H band

6.8) DC electrical measurements

The dc electrical conductivity measurements as a function of temperature are illustrated in Fig. 6.11 for xMnFe/Si (x = 100, 20, 15 and 10) samples. The conductivity behavior is essentially the same for all samples exhibiting semiconducting nature for the studied temperature range. Basically, the samples containing insulator silica have lower conductivity compared with 100MnFe/Si. However, the minimum conductivity was found for 20MnFe/Si (2-3 order smaller than other samples). This anomaly is due to the formation of α-Fe_2O_3 impurity with lack of Fe^{2+} sites. Therefore, the hopping process of $Fe^{2+} \leftrightarrow Fe^{3+}$ is obstructed resulting in the unexpected low conductivity in the sample.

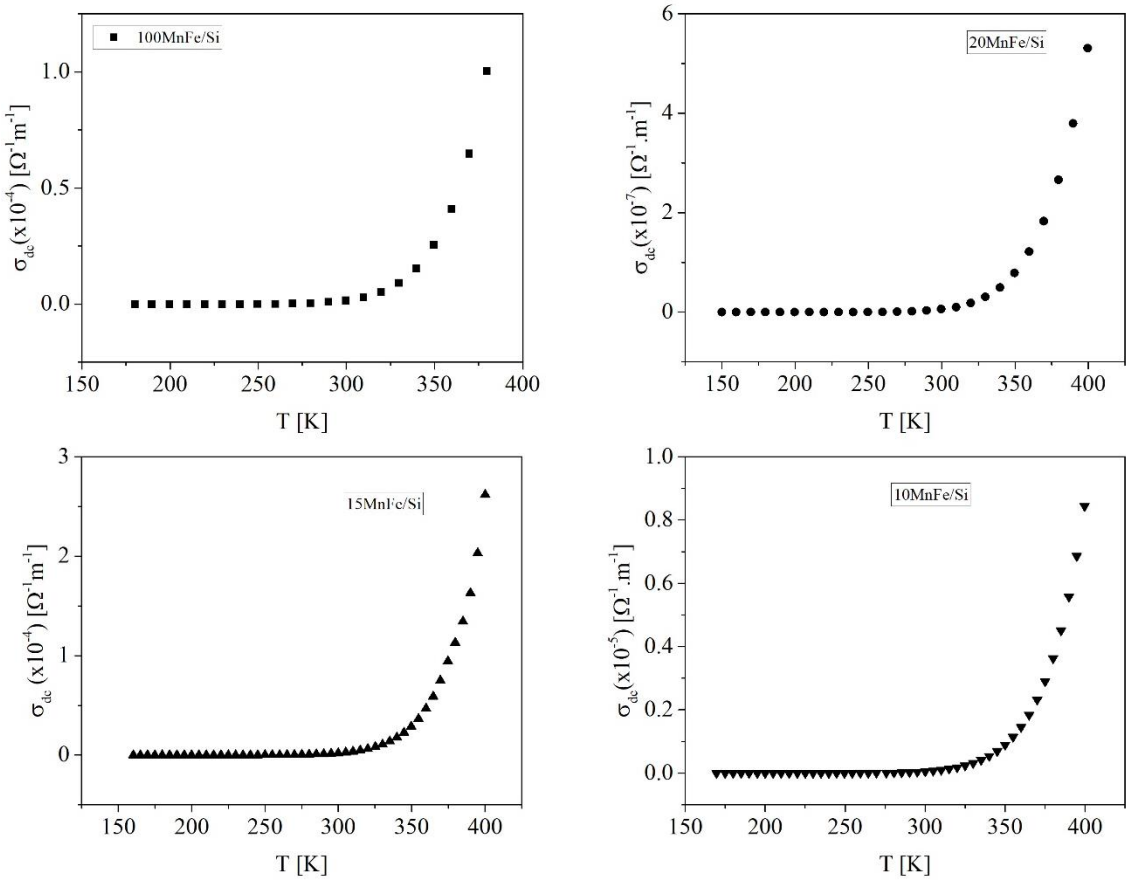

Fig. 6.11) The dc conductivity as a function of temperature for xMnFe/Si.

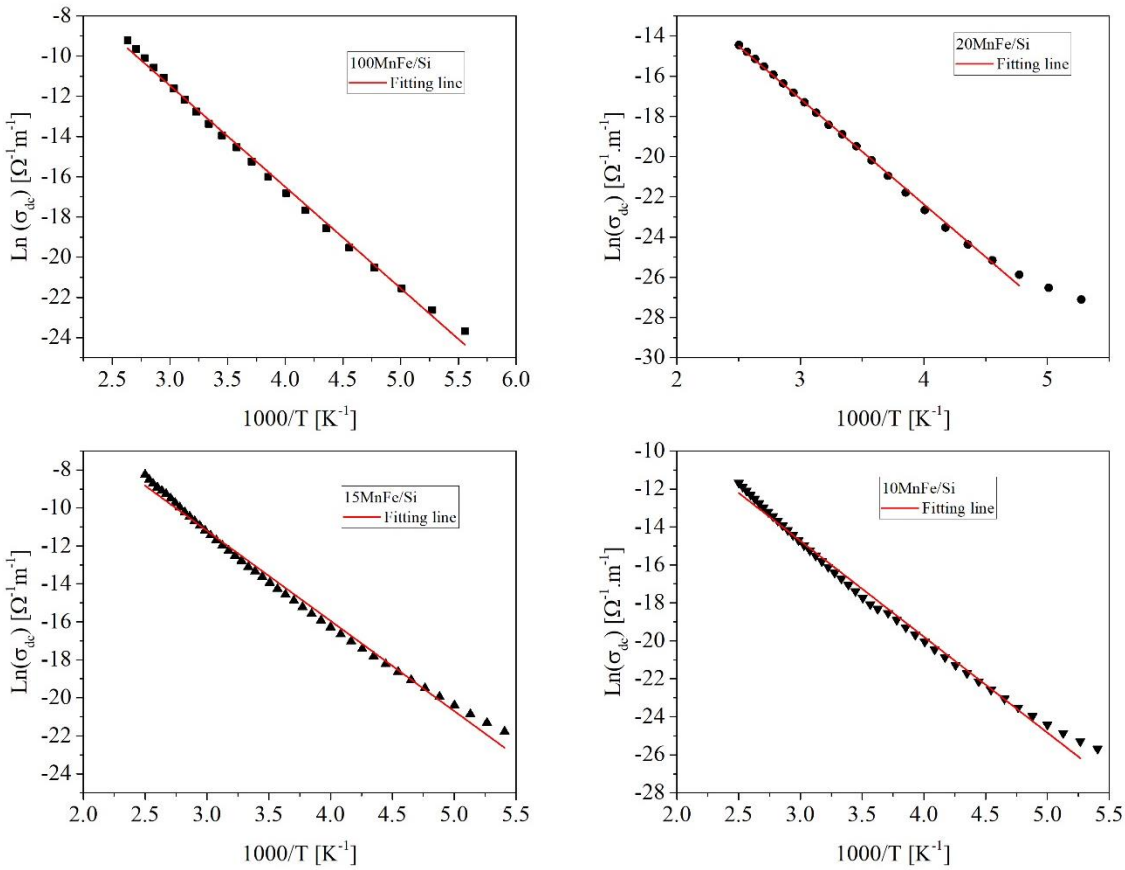

Fig. 6.12) The dependence of Ln(σ_{dc}) to the inverse of the temperature 1000/T; the linear fitting was performed according to the NHH model.

According to the nearest-neighbor-hopping (NNH) conduction model, the dc conductivity (σ_{dc}) of the spinel ferrite can be stated by the Arrhenius equation yielding [37]:

$$\sigma_{dc}=\sigma_o \exp(-\Delta E_{NNH}/k_B T) \quad (6.5)$$

where σ_o is a constant, $k_B=1.38\times10^{-23}$ J.K^{-1} is the Boltzmann constant and ΔE_{NNH} is defined as the activation energy of the nearest neighbor hopping.

The ln σ_{dc} plots as a function of 1000.T^{-1} for the investigated samples are shown in Fig. 6.12. The ΔE_{NNH} values are obtained by linear fitting of the curves to the equation and listed in table 6.3.

Table 6.3) DC electrical parameters of xMnFe/Si samples (the activation energy according to the NHH, Mott, and E-S models, ΔE_{NHH}, ΔE_{Mott} and $\Delta E_{E\text{-}S}$, respectively; the characteristic temperature and hopping distance based on Mott and E-S model, T_{Mott}, R_{Mott} and $T_{E\text{-}S}$, $R_{E\text{-}S}$, respectively; the density of localized states at the Fermi level, $N(E_F)$.)
(** calculated at 300 K). (All values have an error less than 1%.)

Sample	**ΔE_{NHH} (eV)**	**$T_{o(Mott)}$ (eV)**	**$T_{o(E\text{-}S)}$ (eV)**	**$N(E_F)$**	**ΔE_{Mott} ** (eV)**	**R_{Mott}** (Å)**	**$\Delta E_{E\text{-}S}$** (eV)**	**$R_{E\text{-}S}$** (Å)**
100MnFe/Si	0.43	-	3.97E5	4.78E27	-	-	0.47	5.83
20MnFe/Si	0.45	-	-	-	-	-	-	-
15MnFe/Si	0.41	5.99E9	-	3.22E16	0.18	341	-	-
10MnFe/Si	0.44	7.45E9	-	2.59E16	0.19	360	-	-

A more precise explanation of the conduction model can be assessed by ignoring the influence of a particular conduction mechanism on the evaluation of the activation energy. The model satisfying this condition is called Mott's variable-range-hopping (VRH) conduction. Mott proposed that the hopping range can increase with decreasing in temperature and become larger than the distance between neighboring sites due to the lower activation energy involved at lower temperatures [38]. This model is generally expressed as:

$$\sigma_{dc}=\sigma_{cons.}\exp(-T_o/T)^P \qquad (6.6)$$

where σ_{cons} is as a constant. T_o equals to $3\xi^{-3}2^{1/4}/[2\pi k_B N(E_F)]$ in which $N(E_F)$ is the density of localized states at the Fermi level and α is the decay factor of the localized wave function. If we introduce the parameter ξ as the distance between nearest between Mn and Fe ions. In addition, the exponent can take one of the values of 1/4, 1/3, and 1/2 depending on the investigated material and corresponding conduction mechanism [39]. The exact value of P can be obtained by the evolution of the activation energy of the bulk conductivity (ΔE_a) given by [38]:

$$\Delta E_a = -d[\ln(\sigma_{dc})]/d[1/k_BT] \qquad (6.7)$$

As illustrated in Fig. 6.13 the results show that ΔE_a decreases with temperature for all samples apart from 20MnFe/Si. Therefore, the temperature dependency of ΔE_a for 100MnFe/Si, 15MnFe/Si and 10 MnFe/Si are in agreement with the VRH model and inconsistent of the NNH conduction model. According to the NNH conduction model, the activation energy is supposed to be constant as temperature varies [38]. In the case of 20MnFe/Si, two distinct trends are observed; the ΔE_a stays fairly steady in the temperature range of 260 to 400 K and blow 260 K, with decreasing of temperature, the ΔE_a drops sharply.

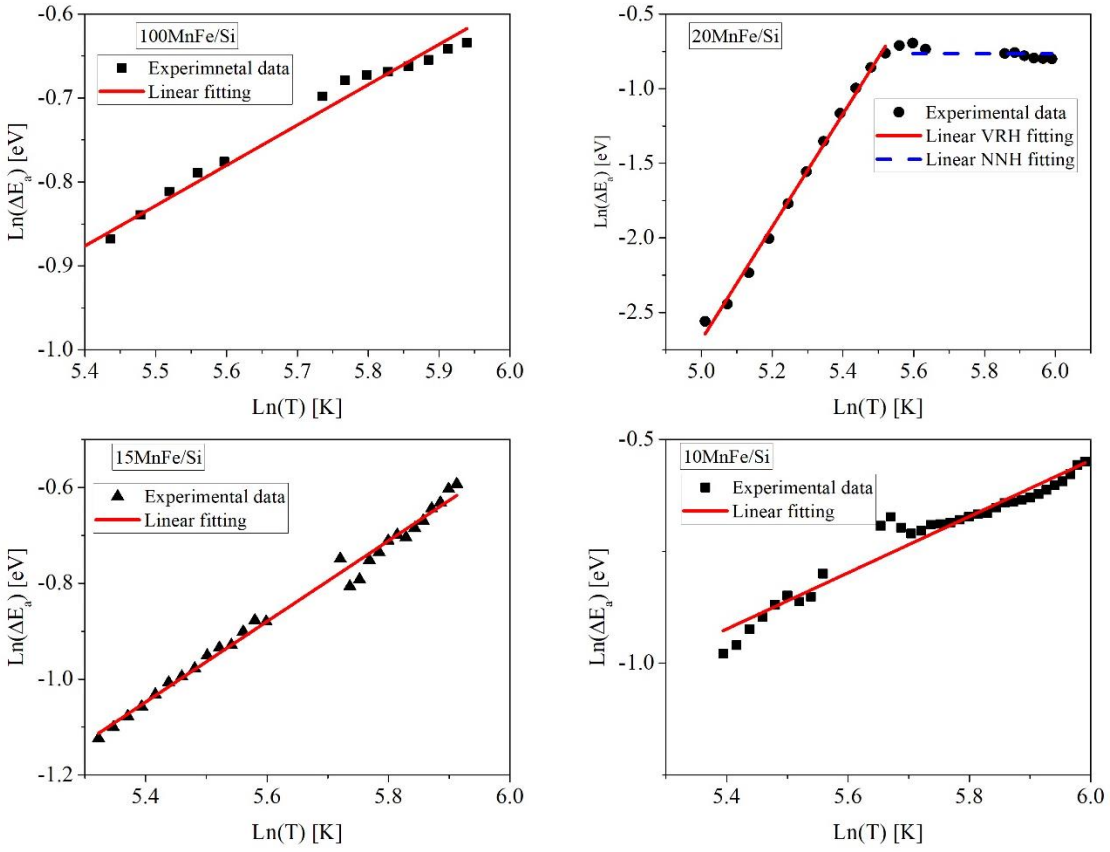

Fig. 6.13) Plots of Ln(ΔE_a) vs Ln(T). The red straight line shows the linear fitting according to the VRH model. The blue dashed line depicts the fitting of NNH conduction model for the 20MnFe/Si sample.

Moreover, by comparison of eq (6.6) and eq (6.7), we can say $1 - p$ equals to the slope of the Ln (ΔE_a) vs Ln (T) plot. The slope values were calculated from the linear fit of the Ln (ΔE_a) vs Ln (T) plot, obtaining 0.46, 0.64 and 0.82 for 100MnFe/Si, 15MnFe/Si and 10Mn/Si, respectively. This means the value of "p" most probably is ½ for 100MnFe/Si while for both

samples of 15MnFe/Si and 10MnFe/Si the value of ¼ can be considered. Although, subject to 20MnFe/Si the value of the slope was determined 3.72 pointing out p has a negative value without any physical meaning. Hence, the VRH model in the temperature range below 260 K, cannot be applicable to 20MnFe/Si. While, at temperatures higher than 300 K, the ΔE_a behavior obeys NNH model.

Excluding 20MnFe/Si, we go deeper through the analysis of the charge transport mechanism of the remaining samples based on the VRH conduction mechanism. We suggest that Mott VRH conduction model explains the charge transport mechanism in the sample 15MnFe/Si and 10MnFe/Si. Mott predicted that in the three-dimensional systems (alike to our samples) when electron-electron interaction effects are ignorable, conduction process occurs via phonon-assisted quantum-mechanical tunneling. In this case, p can take a value of 1/4 and equation (6.6) is stated as $\sigma_{dc}=\sigma_{cons}.\exp(-T_o/T)^{1/4}$. In 15MnFe/Si and 10MnFe/Si, the Coulomb interaction can be ignored because the nanoparticles within these samples are well-separated by a silica shell (as previously shown in TEM image) and electrons far from each other to interact significantly so that the Mott VRH model can support the conduction mechanism of these samples. If the Coulomb interactions between charge carriers are significant, Efros and Shklovskii (E-S) derived that the temperature dependence of the dc conductivity can be rewritten as $\sigma_{dc}=\sigma_{cons}.\exp(-T_o/T)^{1/2}$. In the case of 100MnFe/Si, the particles are well-matured and agglomerated (see the TEM image). Hence, charge carriers are close enough, and the long-range electron-electron interactions should be considered. Therefore, the (E-S) VRH theory can justify the conduction behavior of 100MnFe/Si. Accordingly, the linear fit of Ln (σ_{dc}) with $1/T^p$ ($p_{E-S}=1/2$ for 100MnFe/Si; $p_{Mott}=1/4$ for 15MnFe/Si and 10MnFe/Si) is presented in Fig. 6.14.

As seen in Fig. 6.14, the fitted curves are well consistent with the experimental data in the whole measured temperature range.

The extracted slope values of the linear fittings are used to calculate the characteristic temperature of T_o corresponding to each sample (100MnFe/Si, 15MnFe/Si, and 10MnFe/Si) and the obtained values are listed in table 6.3. Using the obtained value of T_o, the most probable hopping distance, R, and the average hopping activation energy (ΔE) at a certain temperature of T for each conduction model, Mott, and Efros-Shklovskii, are respectively expressed by [39]:

$$R_{Mott} = 3/8\xi(T_o/T)^{1/4} \quad (6.8)$$

$$\Delta E_{Mott} = 0.25 k_B T_o^{1/4} T^{3/4} \quad (6.9)$$

$$R_{E\text{-}S} = 1/4\xi(T_o/T)^{1/2} \quad (6.10)$$

$$\Delta E_{E\text{-}S} = 0.5 k_B T_o^{0.5} T^{0.5} \quad (6.11)$$

The ΔE_{Mott}, R_{Mott}, $\Delta E_{E\text{-}S}$, $R_{E\text{-}S}$ at selected temperatures were calculated and the obtained values are listed in table 6.3. It is worth to note that all the determined values of R and ΔE at different temperatures can satisfy the necessary condition for VRH model: $\Delta E > kT$ and $R/\xi > 1$ [40]. As mentioned before, the VRH model is not valid for 20MnFe/Si. Due to the existence of α-Fe_2O_3 impurity in this sample, the separate Fe^{3+} ions oriented to different directions increases the ξ, thus R/ξ is too small and the VRH model cannot be applied any longer.

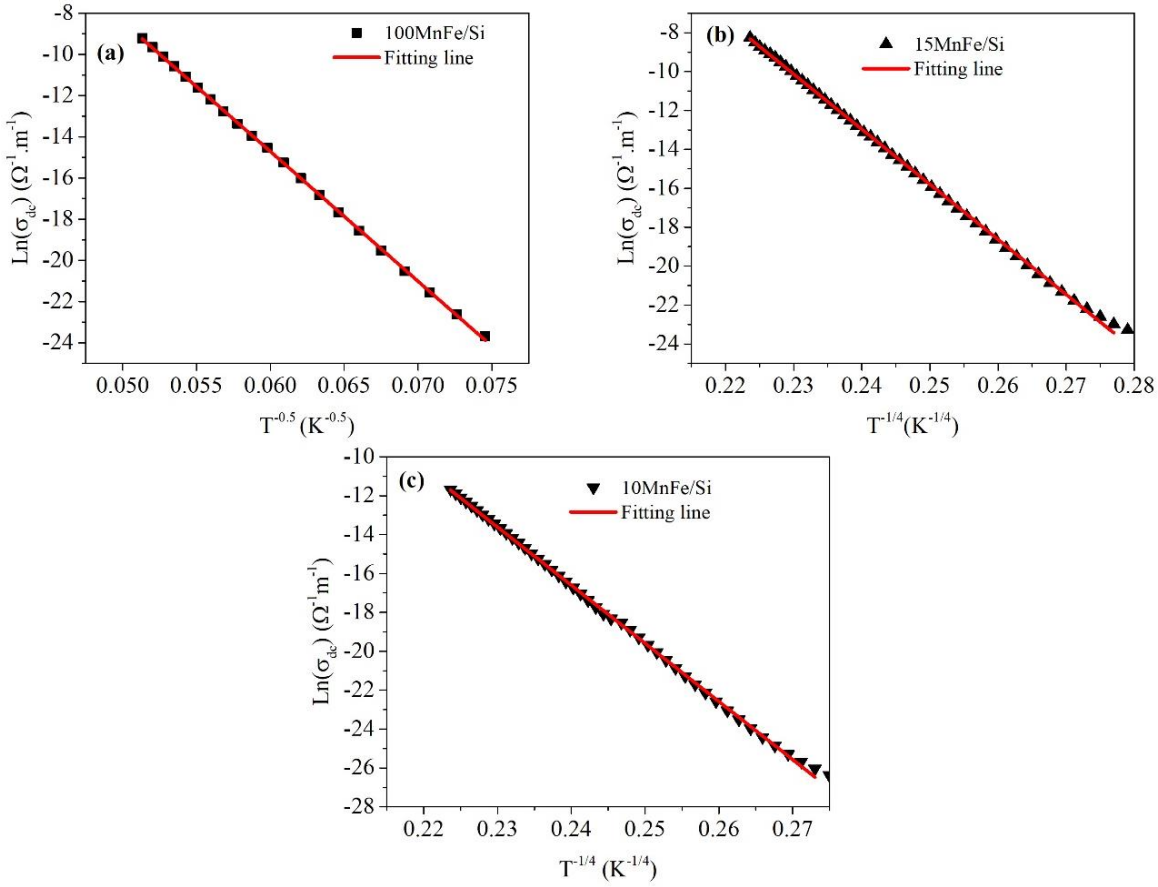

Fig. 6.14) Plots of $Ln(\sigma_{dc})$ vs T^{-p} for 100MnFe/Si, 15MnFe/Si and 10MnFe/Si.

6.9) AC electrical measurements

The variation of the real part of dielectric permittivity (ε´) with frequency at selected temperatures for all samples are depicted in Fig. 6.15.

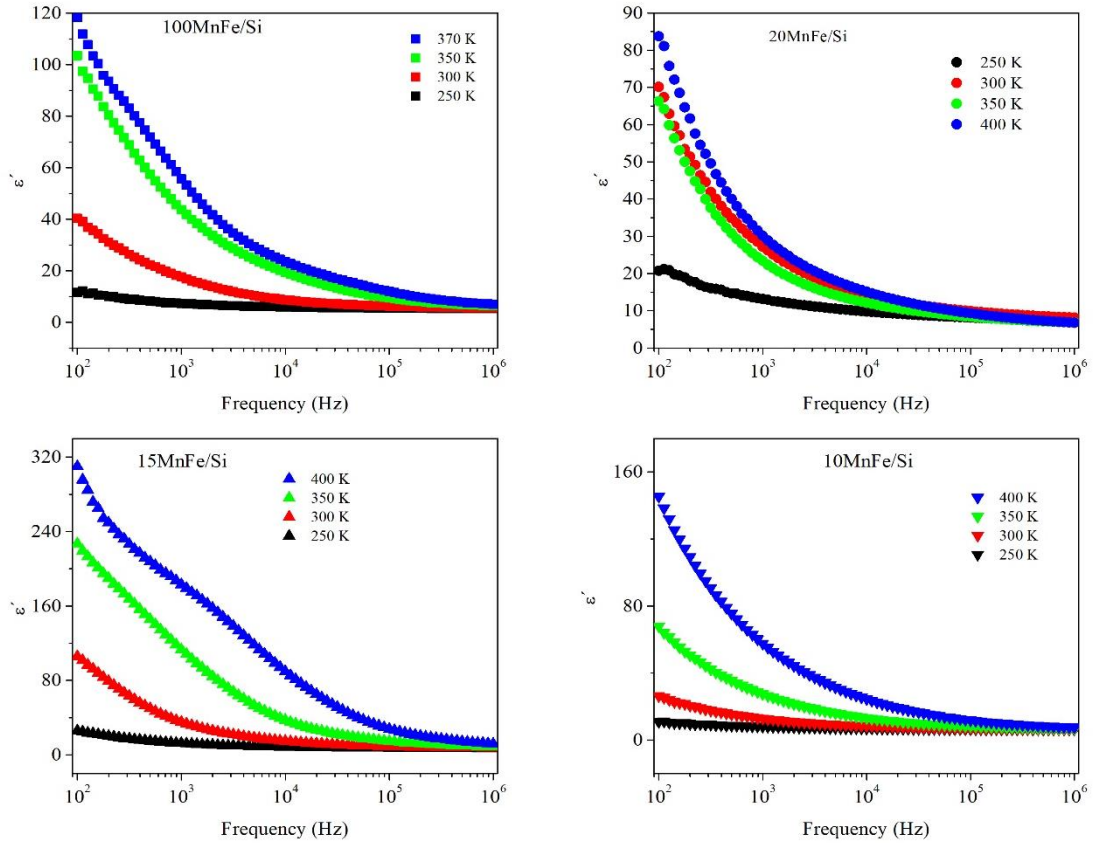

Fig. 6.15) Dielectric dispersion of 100MnFe/Si, 20MnFe/Si, 15MnFe/Si and 10MnFe/Si.

The ε´ values monotonously decrease in as the frequency increases [41]. The dielectric behavior of ferrite can be explained on basis of the Maxwell–Wagner theory of interfacial polarization [42] in consonance with the Koops phenomenological theory [43]. In this model, the ferrite system is considered as a heterogeneous system with low resistivity grains and high resistivity grain boundaries. The grain boundaries and grains are more effective at low and high frequencies, respectively [44-45] in manganese ferrite, the electrons exchanging between Fe^{2+} and Fe^{3+} ions and the holes that transfer between Mn^{3+} and Mn^{2+} ions present in different sites are responsible for conduction and dielectric polarization. Electrons and holes should pass through the conductive grains and the resistive grain boundaries. At higher frequencies, the

frequency of electron/hole exchange will not be able to follow the alternation of applied AC electric field and consequently the polarization decreases [46]. With a reduction in frequency, the electrons get in high resistance grain boundaries and therefore the material has larger ε' value in the low-frequency range. In addition, the dangling bonds and oxygen vacancies accumulated in the grain boundaries act as active charge carrier traps leading to form an enhanced space charge polarization. The thickness of this high capacitive barrier layer is proportional to the ratio of the concentration of trapped charge carriers (n_t) to free charge carriers (n_f). As the temperature rises up, n_t and n_f decrease and increase, respectively, consequently the barrier layer thickness decrease with the temperature and the dielectric constant increases [47]. Thus, Maxwell-Wagner polarization is an effective mechanism, but it is not the main mechanism responsible for the dielectric behavior of the samples. Another parameter that can be taken into account is the oxygen deficiency at the surface, which can arise from the synthesis process [48].

In the case of material under study, 15MnFe/Si, it is suggested these contributions combined together will results in the anomalous high dielectric constant at low frequency region. It is notable that in 20MnFe/Si, the dielectric constant at 350 K is slightly lower than ε' at 300 K. the observed deviation is due to thermal fluctuation the dipoles with random arrangement in which an increase in temperature is insufficient to form polarization [48].

Fig. 6.16 (part I and II) depict the Nyquist plots (complex impedance spectra) of xMnFe/Si compositions measured at different temperatures over a wide range of frequency range (100 Hz–1 MHz).

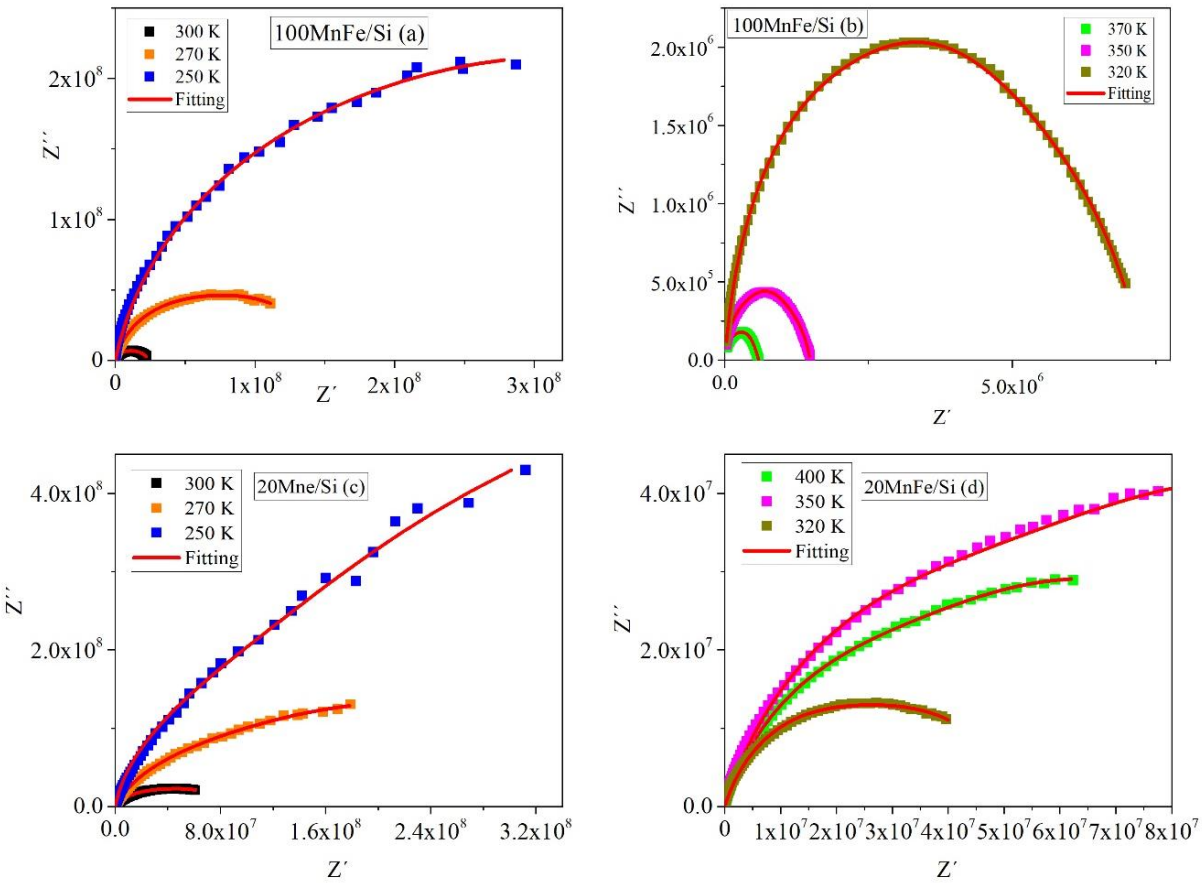

Fig. 6.16 part I) Complex impedance spectra of (a-b) 100MnFe/Si and (c-d) 20MnFe/Si at different temperatures.)

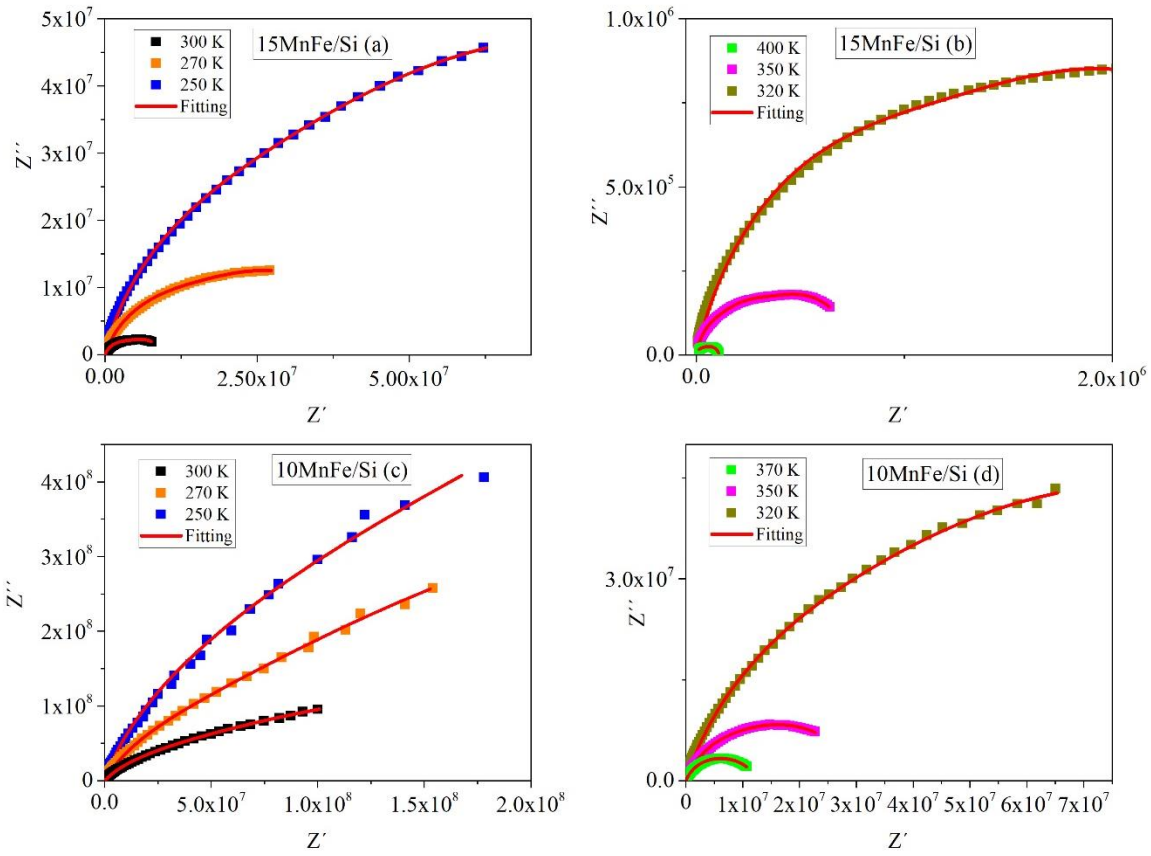

Fig. 6.16 part II) Complex impedance spectra of (a-b) 15MnFe/Si and (c-d) 10MnFe/Si at different temperatures.

The impedance plots of xMnFe/Si clearly show depressed single semi-circles suggesting the presence of a non-Debye type of relaxation in our compositions due to the heterogeneous grain size and grain boundary effect [49]. Therefore, due to this non-Debye nature, a relaxation time distribution is expected in the samples instead of a single relaxation time [44]. Moreover, it is observed that the diameters of the semicircles decrease as the temperature increases, showing the semiconducting nature of the samples with a negative temperature coefficient of resistance in the measured temperature range [50]. It also confirms that the conduction process in these samples is thermally activated [51]. In order to correlate between the impedance spectra and microstructure of the samples, we postulate an equivalent electrical circuit drawing.

The proposed equivalent circuit consists of a series combination $CPE_1||R_1$ and $CPE_2||R_2$ (CPE, R circuit element in a parallel configuration), each representing contribution of grain and grain boundary. The constant phase element (CPE) in the circuit suggests a deviation from the ideal Debye response. The capacitance value of the CPE element is given by $C=Q^{1/n}R^{(1-n)/n}$ where

the n value ranges from zero to unity (zero for pure resistive behavior and 1 for capacitative behavior) [48].

From the fitted curves, the values of grain resistance (R_g), grain boundary resistance (R_{gb}), interior grain capacitance (C_g) and grain boundary capacitance (C_{gb}) were obtained and listed in table 6.4 and 6.5.

Table 6.4) The grain and grain boundary capacitance, C_g and C_{gb}, grain and grain boundary resistance, R_g and R_{gb}, values extracted from the fitting of the proposed equivalent circuit for 100MnFe/Si and 20MnFe/Si (with an error value less than 2%).

100MnFe/Si				
Temperature (K)	**R_g (MΩ)**	**C_g (pF)**	**R_{gb} (MΩ)**	**C_{gb} (pF)**
250	200	2.81	364	6.86
270	98.1	10.09	52.8	3.21
300	8.61	3.32	15.3	13.1
320	3.13	3.23	4.09	19.3
350	0.464	3.84	1.02	9.80
360	0.222	4.53	0.694	7.10
370	0.103	5.83	0.480	5.44

20MnFe/Si				
Temperature (K)	**R_g (MΩ)**	**C_g (pF)**	**R_{gb} (MΩ)**	**C_{gb} (pF)**
250	151	3.03	1160	3.51
270	94	4.06	314	9.43
300	32.5	4.04	56.2	23.5
320	21	3.85	32.7	29.7
350	45.7	3.8	122	27.4
380	79.8	4.34	115	20.8
400	31.2	4.68	81.6	28.5

Table 6. 5) The grain and grain boundary capacitance, C_g and C_{gb}, grain and grain boundary resistance, R_g and R_{gb}, values extracted from the fitting of the proposed equivalent circuit for 15MnFe/Si and 10MnFe/Si (with an error value less than 2%).

15MnFe/Si				
Temperature (K)	**R_g (MΩ)**	**C_g (pF)**	**R_{gb} (MΩ)**	**C_{gb} (pF)**
250	24.4	11.4	121	23.1
270	13.8	11.6	32.9	60.4
300	3.53	12.2	6.40	127
320	1.07	10.5	2.27	75.9
350	0.25	10.6	0.537	99.4
400	0.574	9.44	0.532	201

10MnFe/Si				
Temperature (K)	**R_g (MΩ)**	**C_g (pF)**	**R_{gb} (MΩ)**	**C_{gb} (pF)**
250	448	5.34	3850	6.69
270	48.4	5.82	739	5.39
300	47	10	329	17.1
320	29.8	10.1	116	25
350	9.59	11.1	21.2	39.9
370	6.20	10.8	6.35	77.2

According to table 6.4 and 6.5 and Fig. 6.17, the C_g and C_{gb} variations with temperature for each sample show their own unique behaviors. Although, $C_{gb}>C_g$ is the common feature observed in all samples. Similarly, the grain boundary resistance R_{gb} is bigger than R_g on the whole temperature range for all xMnFe/Si compositions.

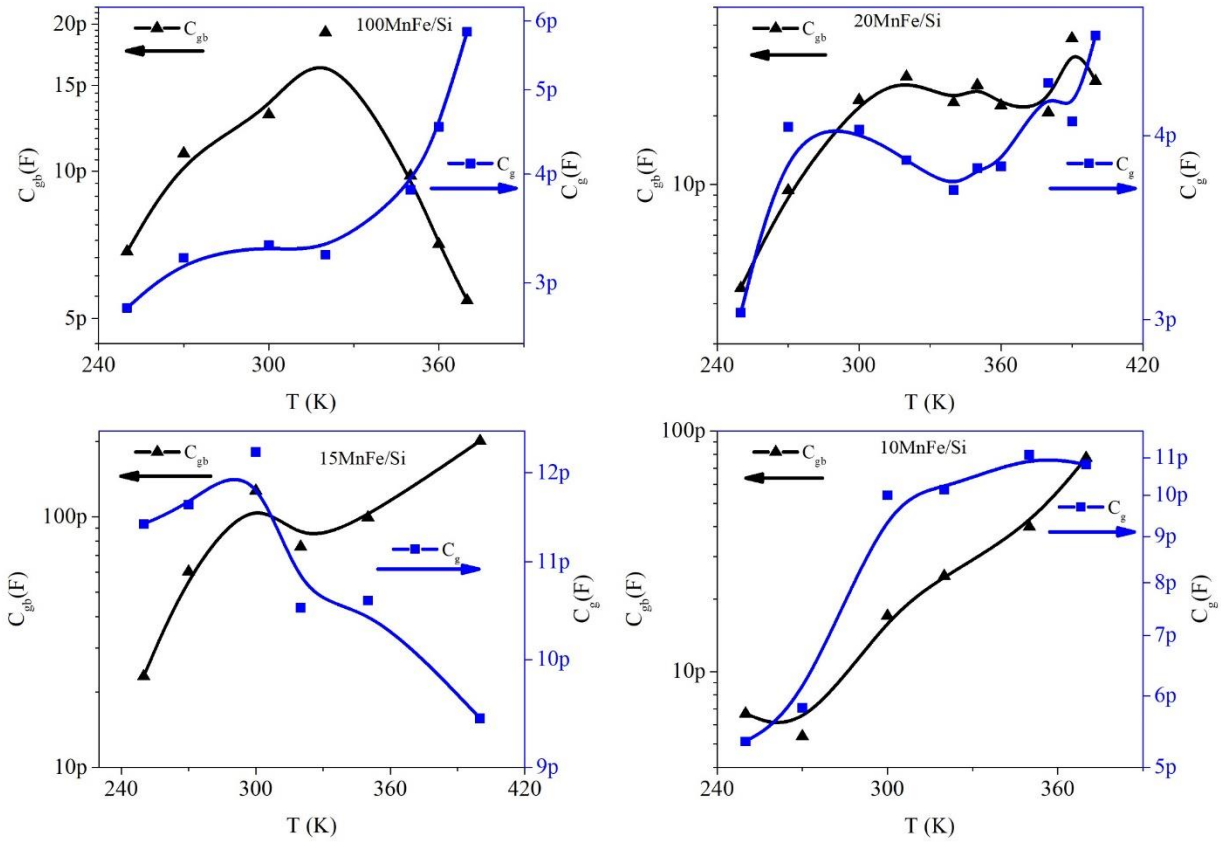

Fig. 6.17) Temperature variation of C_g and C_{gb} for xMnFe/Si compositions.

We also could obtain the grain and grain boundary conductivity, σ_g and σ_{gb}, using the following equation:

$$\sigma_{g,gb}=L/(A.R_{g,gb}) \qquad (6.12)$$

where A and L are the area and thickness of the sample, respectively.

The temperature variation of σ_g and σ_{gb} for all the samples are plotted in Fig. 6.18.

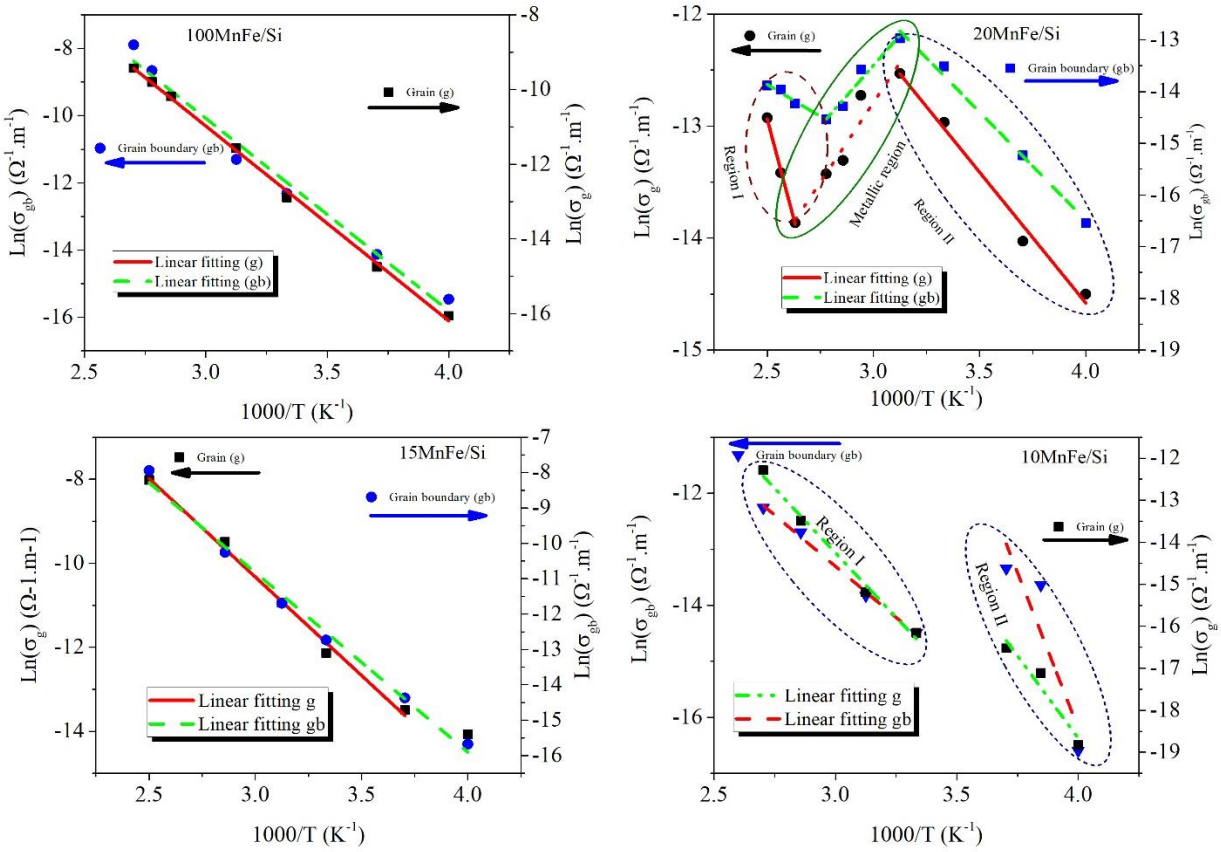

Fig. 6.18) NNH plots for grain and grain boundary contributions in xMnFe/Si compositions.

As shown in Fig. 6.18, the linear behavior of both these plots for 100MnFe/Si over the measured temperature range indicates the polaronic conduction in both grain and grain boundary [52]. Based on the NNH model, for a wide temperature range, the temperature dependence of σ_g and σ_{gb} can be expressed by:

$$\sigma_{g,gb} = \sigma_{g,gb(o)}.\exp(-\Delta E_{a(g,gb)}/k_B T) \qquad (6.13)$$

Where $\Delta E_{a(g)}$ and $\Delta E_{a(gb)}$ are the activation energy of the grain and grain boundary, respectively. From the slopes of the linear fittings, we have calculated the values of $\Delta E_{a(g)}$ and $\Delta E_{a(gb)}$ for 100MnFe/Si and listed in table 6.6.

Table 6. 6) The grain and grain boundary activation energy values ($\Delta E_{a(g)}$ and $\Delta E_{a(gb)}$) for xMnFe/Si compositions (error<1%).

Sample	**$\Delta E_{a(g)}$ (Region I) (eV)**	**$\Delta E_{a(g)}$ (Region II) (eV)**	**$\Delta E_{a(gb)}$ (Region I) (eV)**	**$\Delta E_{a(gb)}$ (Region II) (eV)**
100MnFe/Si	0.45	-	0.49	-
20MnFe/Si	0.61	0.20	0.36	0.21
15MnFe/Si	0.40	-	0.44	-
10MnFe/Si	0.54	0.48	0.27	0.65

It was found that in 100MnFe/Si the $\Delta E_{a(gb)}$ value is slightly higher than $\Delta E_{a(g)}$ conferring that the grain boundary has a prevailing impact on the resistive behavior of the sample. In the case of 20MnFe/Si, the plot indicates a non-monotonous trend. In the temperature range 250 to 320 K, referred to as region I, the observed reduction in the resistance of grain and grain boundary is due to thermal activation of the localized charge carries. The variation of the carrier density and carrier mobility with temperature will determine the temperature dependence of resistivity. In manganese ferrites, conduction comes from the hopping of localized d electrons of transition metal ions residing in oxygen lattices. Due to the electrostatic interaction via superexchange paths Fe^{3+}-O-Fe^{2+} and Mn^{2+}-O-Mn^{3+}, the cations 3d level is splitted into less stable doubly degenerate e_g levels and more stable triply degenerate t_{2g} levels. In the region I, the density of hopping carriers within the grain decreases, arising from the formation of the secondary phase of hematite and reduction in Fe^{2+} sites. Moreover, in the presence of some electronic traps and disorder surface/core spin, the energy of e_g electrons (E_k) is lower than that applied by the grain boundary and the electrons will be localized [53]. Therefore, in the region I, the sample has a semiconducting behavior. However, with a further increase in temperature above 320 K, the localized states become delocalized along with the alignment of surface/core spins and effective conductive channels are formed and the sample presents a metallic nature. Above 380 K, due to disordering of surface/core spin and also non-magnetic elements, the localized states reformed and the semiconducting feature reoccurs. Alike to 100MnFe/Si, both grain and grain boundary conductivity of 15MnFe/Si decreases monotonously with temperature. The explanation of the determined values of activation energies, presented in table 6.5, is similar to one for 100MnFe/Si. In the case study of 10MnFe/Si, the plot shows two distinct regions

(region I and II) with different activation energy values (for both g and gb contribution as presented in table 6.5). This can be explained in terms of the existence or distribution of localized trap centers and surface defects having multiple activation energies.

Fig. 6.19 shows the frequency dependence of the real part of ac conductivity in selected temperatures. The σ_{ac} variation with frequency can be divided into two regions: in the low-frequency region a plateau of conductivity while the conductivity is frequency dependent in the high-frequency region. The extrapolation of low-frequency σ_{ac} gives dc conductivity σ_{dc} which is attributed to the long-range translation motion of carriers.

The origin of the frequency dependence of conductivity lies in the relaxation phenomena arising due to mobile charge carriers [52]. With increasing in temperature, the AC conductivity increases due to thermally generated charge carriers. Further, the AC conductivity follows the Johnscher's power law given by [51]

$$\sigma_{ac}(\omega)= \sigma_{dc}+A\omega^{n} \qquad (6.14)$$

where σ_{dc} is the extrapolated dc conductivity, A is material specific temperature dependent constant and determines the strength of polarizability, ω is the angular frequency and n ($0 \leq n \leq 1$) is a temperature and frequency dependent exponent and represents the degree of interaction between mobile ions with the environments surrounding them.

The AC conductivity data were fitted to Eq. (6.14) and the n values were obtained. Several models have been developed based on the behavior of n such as QMT (Quantum tunneling mechanism, where value of 'n' is independent of temperature), OLPT (Overlapping large polaron tunneling, where n reaches a minimum followed by increases with temperature), and CBH (Correlated barrier hopping, where n decreases with temperature) [51]. Variation for universal exponent n as a function of temperature is shown in Fig. 6.20.

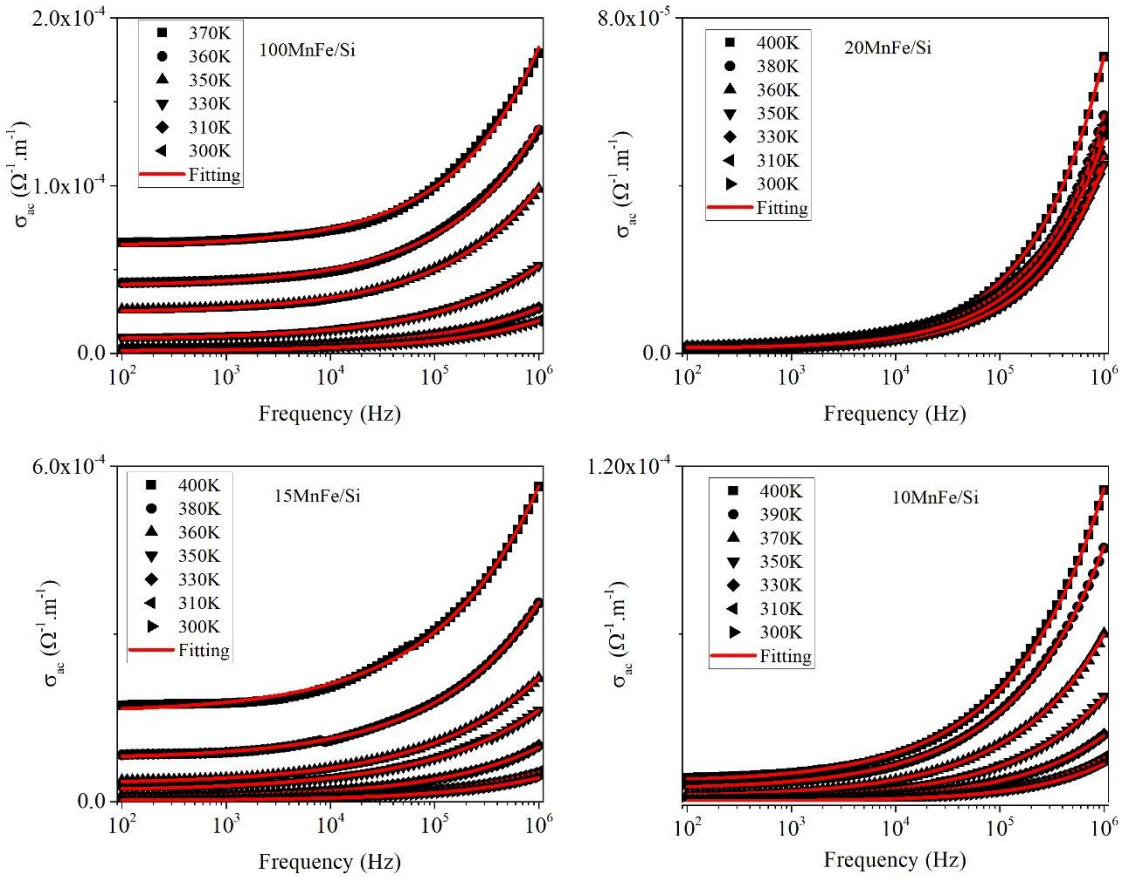

Fig. 6.19) σ_{ac} vs. frequency plots at temperatures for xMnFe/Si.

According to Fig. 6.20, the exponent n depends on temperature. In 100MnFe/Si, 15MnFe/Si and 10MnFe/Si the n value drops with rising temperature to a minimum value and then increases, as temperature rises. This result suggests that the OLPT model is the most suitable model to characterize the electrical conduction mechanism in these compounds. For 20MnFe/Si, the value of n decreases with increase in temperature and reach to a minimum followed by increases in the value with further rising of the temperature up to 360 K. Above 360 K the n is saturated and becomes constant. Therefore, in 20MnFe/Si below 360 K, the OLPT explain the conduction process while above 360 K the mechanism obeys the QMT model.

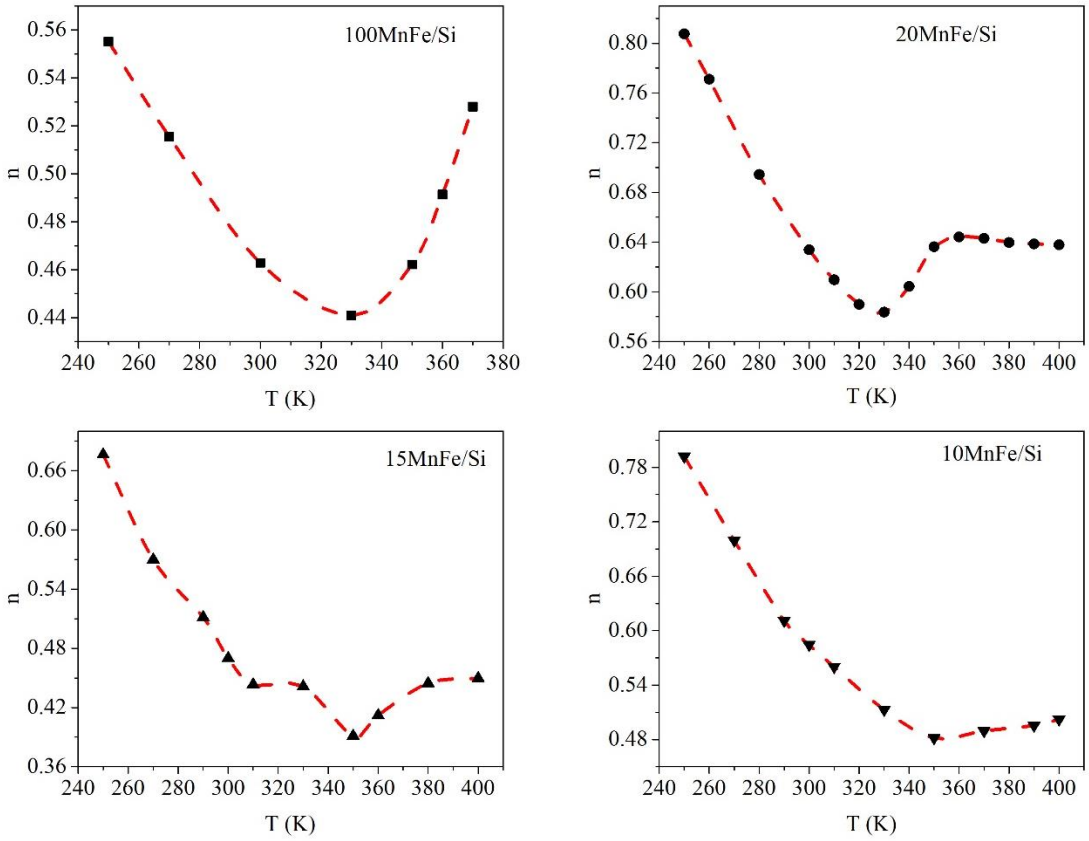

Fig. 6.20) Variation for universal exponents n as a function of temperature.

6.10) Magnetic measurements

Fig. 6.21 (a-b) depicts the magnetic hysteresis loops collected at 10 K and room temperature for the as-synthesized samples. As expected the sample 100MnFe/Si has the highest saturation magnetization in both temperatures. Moreover, 20MnFe/Si shows an unexpected low saturation magnetization due to the presence of a secondary phase of hematite with smaller magnetization compared with $MnFe_2O_4$. ZFC and FC curves of all samples measured in an applied magnetic field of 100 Oe are given in Fig. 6.22.

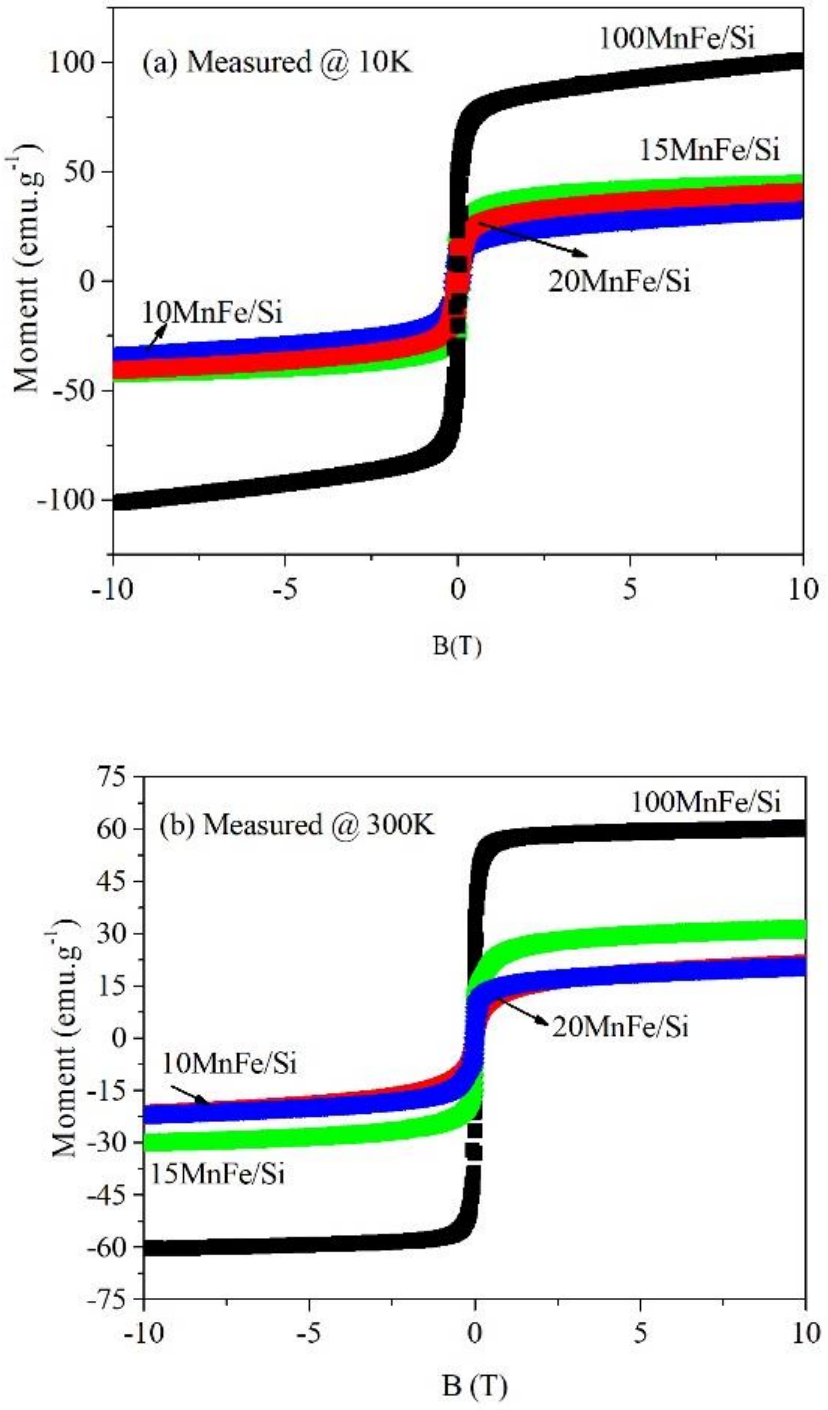

Fig. 6.21) Magnetic hysteresis loops of all samples at 10 K and 300 K.

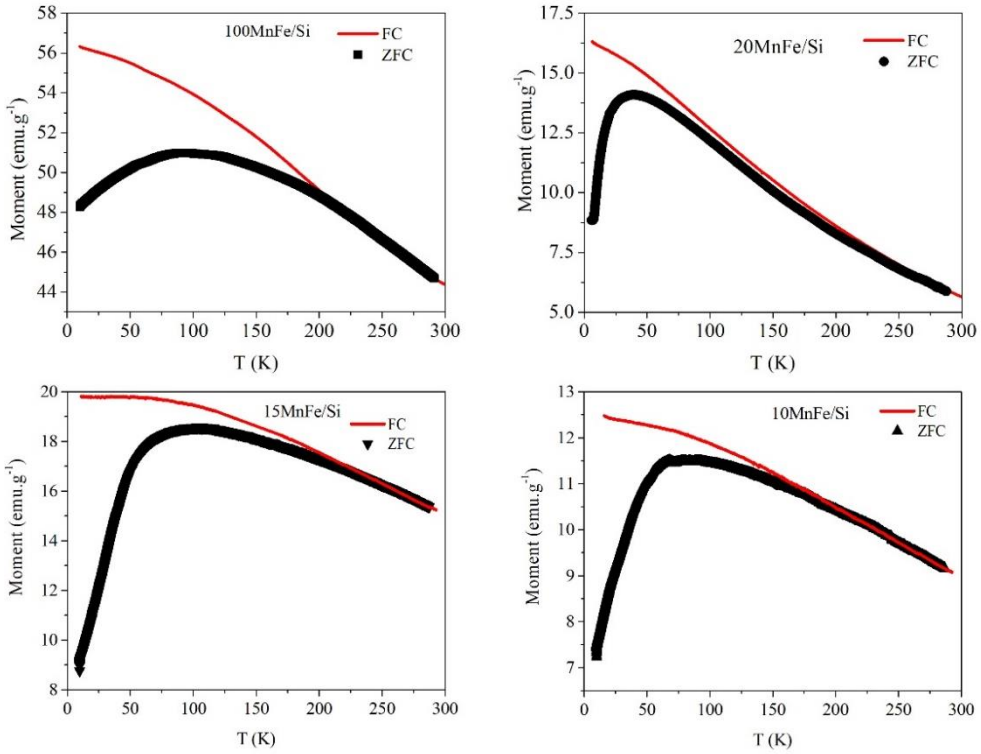

Fig. 6.22) ZFC and FC curves of all samples.

The ZFC curves exhibit a maximum and the corresponding Temperature, T_b, is for noninteracting particles directly proportional to the average blocking temperature which ranged from 85 to 103 K for xMnFe/Si compositions. Also, we define T_{irr} as the temperature where ZFC and FC curves diverge from each other. (Table 6.7) The difference between T_b and T_{irr}, ΔT, provides a qualitative measure of the width of blocking temperature distribution, i.e., of the size distribution in the absence of interparticle interactions. Clearly, the maximum value of T_{irr} was found for 20MnFe/Si, despite a relatively narrow size distribution according to the TEM analysis. Therefore, a strong interaction between $MnFe_2O_4$ and α-Fe_2O_3 crystalline phases with distinct anisotropy energies causes the highest T_{irr} and ΔT values for 20MnFe/Si.

Furthermore, for all samples, the magnetization measured in FC mode at temperatures below T_b constantly increases seemingly an indication of the ideal noninteracting superparamagnetic (SP) behavior.

Table 6.7) Magnetic parameters extracted from experimental ZFC/FC and the hysteresis loops of the samples (with an error of less than 1%).

Sample	T_b (K)	T_{irr} (K)	ΔT (K)	M_s @ 10 K ($emu.g^{-1}$)	M_s @ 300 K ($emu.g^{-1}$)
100MnFe/Si	93	210	117	100.90	60.69
20MnFe/Si	36	257	167	40.60	21.40
15MnFe/Si	103	207	154	43.05	30.75
10MnFe/Si	85	203	122	33.38	21.39

To check that if an ideal noninteracting superparamagnetic picture can satisfactorily explain the magnetic behavior of the present compositions, we have carried out a comprehensive study. In fact, magnetic nanoparticles are considered to be in superparamagnetic regime if i) the corresponding anhysteretic curves mannerly can be fitted to a single Langevin function or a weighted sum of Langevin functions and ii) the scaling of M/Ms with the ratio M_S(B/T) is observed [54].

Fig. 6.23 represents the reduced magnetization curves M/M_S of 100MnFe/Si as functions of the B/T ratio in the temperature region above the blocking temperature. These experimental curves perfectly are superimposed on one single curve indicating the classical ideal noninteracting superparamagnetic scaling law satisfies for 100MnFe/Si.

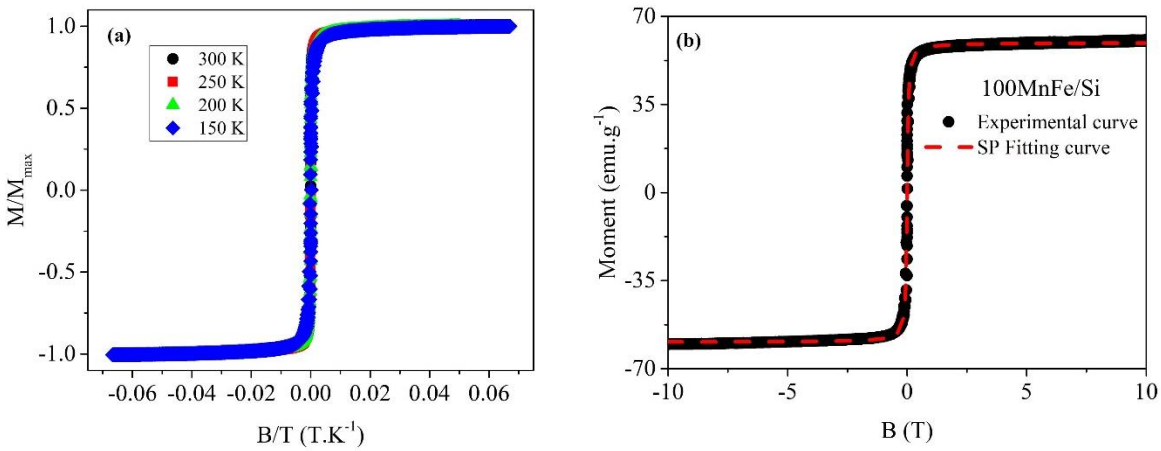

Fig. 6.23) a) Reduced magnetization behavior M/M_S of 100MnFe/Si as a function of B/T measured at different temperatures, b) Hysteresis loop of 100MnFe/Si measured at 300 K along with the theoretical fitting curve.

For the 20MnFe/Si, although, the scaling of M/M_S with the ratio $M_S(B/T)$ is not observed, as seen in Fig. 6.24 a.

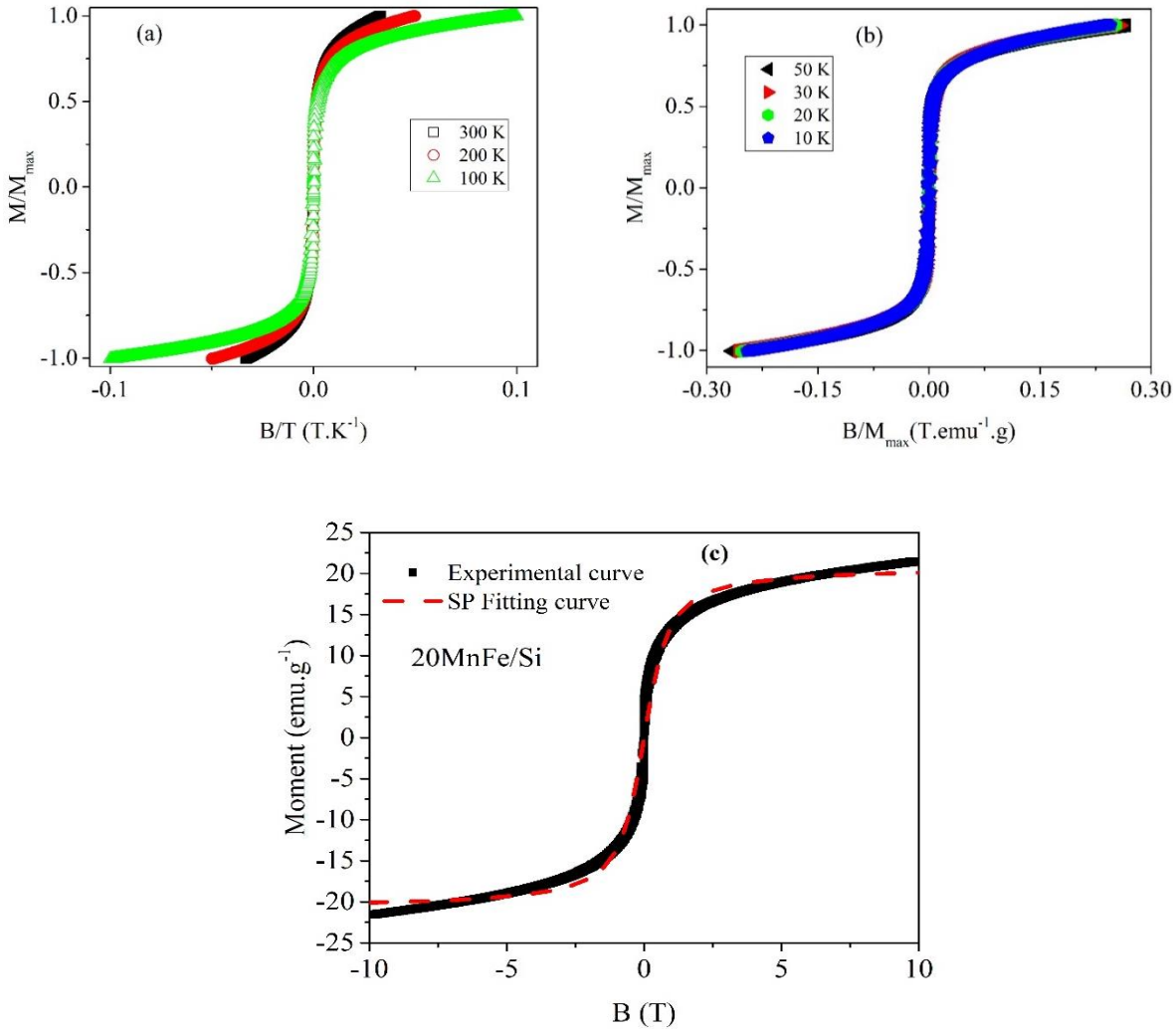

Fig. 6.24) Reduced magnetization behavior M/M_S as a function of 20MnFe/Si a) B/T and b) B/M_S measured at different temperature regions. c) Hysteresis loop of 20MnFe/Si measured at 300 K along with the supposed theoretical fitting curve.

On the other hand in the low-temperature regime the reduced magnetization curves scale with the ratio of B/M_S convincing that the interacting superparamagnetic (ISP) regime can be applied to this sample in the low-temperature regime [54]. Moreover, the Langevin function fitting to the experimental curve deviates, according to Figure 6.24 c. Therefore, the long-range interactions among isolated magnetic moments are effective and should be considered.

This shows ideal non interacting superparamagnetic model cannot be matched with the magnetic behavior of 20MnFe/Si and the dipolar interactions between the particles seem to be critical.

As illustrated in Fig. 6.25 (a-b), the hysteresis loops of 15MnFe/Si and 10MnFe/Si measured at 300 K do not saturate even for our highest field (B) (10 T). This indicates a magnetically hard component that can be associated with the surface spin disorder [55]. The observed behavior also might be addressed to the canting of spins in the ferrimagnetically ordered Mn-ferrite particles due to strong A–B superexchange interactions [56].

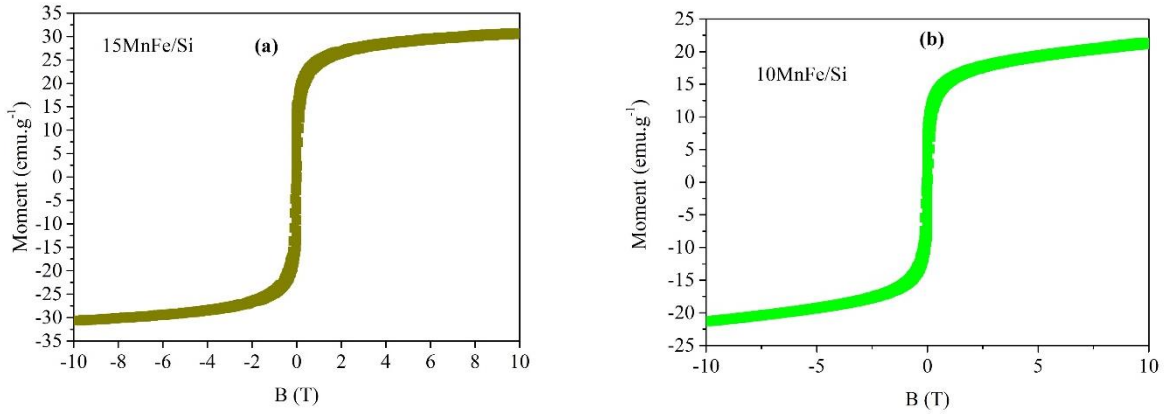

Fig. 6.25) Hysteresis loop of a) 15MnFe/Si and b) 10MnFe/Si measured at 300 K.

To prove the effect of surface spins on the magnetism of these two samples nanoparticles, we have performed a systematic analysis of magnetic loops (M-B) measured at 300 K where is well above T_b and any hysteretic behavior was not observed, using the modified Langevin function [53]:

$$M(B)=M_S^{SP}[\coth(\mu\mu_o B/k_bT)-(\mu\mu_o B/k_bT)^{-1}]+C^{PM}\cdot B \qquad (6.15)$$

where M_S^{SP} is the saturation magnetization of the superparamagnetic (SP) part and μ is the average magnetic moment of SP particles. C^{PM} is the susceptibility of the paramagnetic (PM) contribution, that is, linear with the magnetic field B.

We note that the large disorder spins on nanoparticles surface (called dead layer) and crystallographic interfaces do not align with field and hence their magnetization shows a linear dependence on applied field. This leads to a reduction in the number of spins aligned with the external field. To simulate the behavior of these surfaces and interfacial spins towards the hysteresis curves of 15MnFe/Si and 10MnFe/Si, we have added a linear term to the Langevin function [53].

We apply the theoretical model of 6.15 to the experimental fitted M-B curves of 15MnFe/Si and 10Mnfe/Si and the fitted data are presented in Fig. 6.26.

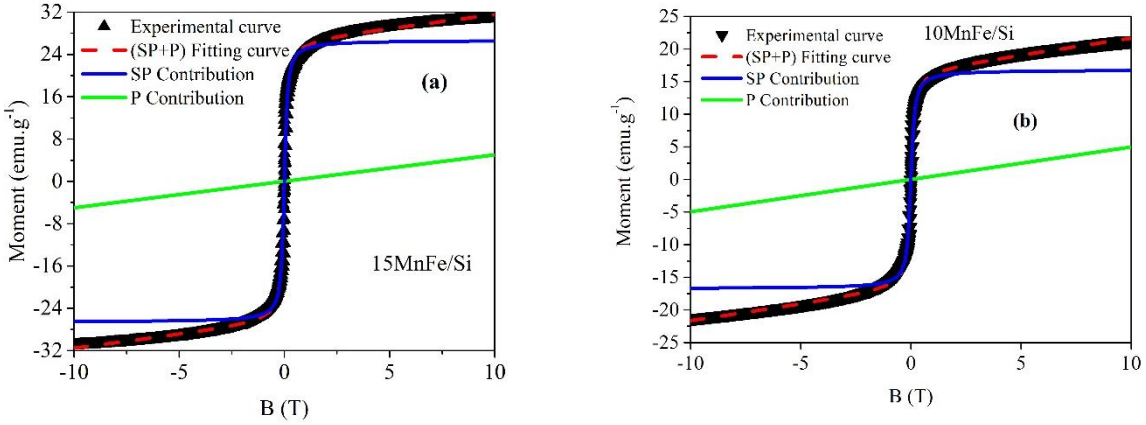

Fig. 6.26) The M-H curves at 300 K are fitted (red) to Eq. (6.15); the green and blue curves represent the simulated PM and SP contributions extracted from the experimental M-H data using the fitting parameters for (a) 15MnFe/Si and (b) 10MnFe/Si.

From fitting data, it was extracted that SP susceptibility contributes 84.2 % to the total magnetic moment, while the rest of it (15.8 %) comes from the PM susceptibility for the M-B loop measured of 15MnFe/Si. For the loop measured of 10MnFe/Si, however, the SPM susceptibility contributes 77.2% to the total magnetic moment and the 22.8% contribution comes from the PM susceptibility. Since a highly linear contribution to the magnetization results mainly from the uncompensated spins at the shell surfaces and crystallite interfaces, our findings suggest a larger number of disordered surface spins (a stronger surface spin effect) present in the composition with the highest silica content. Fig. 6. 27 summerise the effect of in-situ encapsulation on the spin configuration of Mn-ferrites.

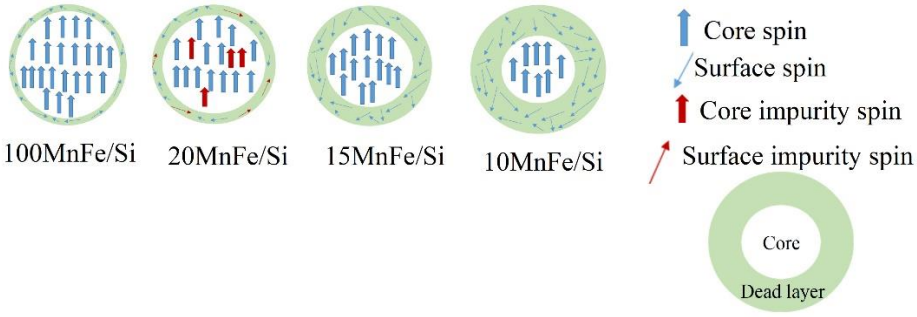

Fig. 6.27) Schematic spin configuration of xMnFe/Si compositions and imapct of the in-situ silica encapuslation on the spin structure.

6.11) Final remarks

$xMnFe_2O_4$-$(100-x)SiO_2$ nanocomposites (xMnFe/Si: x=100, 20, 15 and 10) were successfully synthesized by a one-pot auto-combustion route. XRD patterns confirmed the formation of $MnFe_2O_4$ with cubic spinel structure in all samples. However, the presence of a secondary phase of hematite with the size of 30 nm in 20MnFe/Si was confirmed. Moreover, the XRD results showed that the highest crystallinity is found for 100MnFe/Si. The effect of heat treatment at two different ambient (air and N_2) also investigated. It was shown that less $MnFe_2O_4$ phase is mainly decomposed to Mn_2O_3 and α-Fe_2O_3 phases if the thermal treatment carries on in both N_2 and air atmospheres. The calculation of the crystallite size by means of BET and TEM analyses confirmed the results obtained from XRD patterns. The BET measurement showed that the highest BET surface area was observed in 10MnFe/Si indicating the clusters in this composition has a mesoporous structure. Morphology of the nanocomposites was studied by TEM and SEM. The narrowest size distribution was found to be for 15MnFe/Si. In addition, the formation of a core/shell structure was observed by TEM analysis. The most conductive sample was detected to be 100Mn/Si. While due to high inclusion hematite nanosize crystallites with very low conductivity in 20MnFe/Si, this ample is the most insulating nanocomposite among other samples. According to Raman findings, by increasing the silica content, Mn cations tend to be distributed in the octahedral site and the inversion degree increases. A detailed study showed that only the NNH model can represent a picture from the conduction mechanism in 20MnFe/Si. While, the Mott VHR and Efros-Shklovskii VHR models are truly valid to describe the conduction mechanism in 100MnFe/Si and 15-10MnFe/Si, respectively. The dielectric behavior of xMnFe/Si samples can be

explained on basis of the Maxwell–Wagner theory of interfacial polarization in consonance with the Koops phenomenological theory. The impedance measurement revealed a non-Debye and thermally activated relaxation phenomena in all samples. A proper equivalent circuit was applied to complex impedance spectra of xMnFe/Si pointing out both contribution of grain and grain boundary in conduction. The Jonscher power law was successfully conducted to the AC conductivity of xMnFe/Si samples. It was suggested that the OLPT model is the most suitable model to characterize the electrical conduction mechanism in 100MnFe/Si, 15MnFe/Si, and 10MnFe/Si. But in the case of 20MnFe/Si, both OLPT and QMT model can explain the conduction nature over a whole measured temperature range.

Static magnetization measurements were used to investigate the magnetic behavior of Mn-ferrite/silica nanocomposites. The highest magnetization was found for 100MnFe/Si. All ZFC curves exhibit a peak at a temperature below 150 K depending on the composition. The ideal non-interacting superparamagnetic picture nicely adjusted to 100MnFe/Si. By using a modified Langevin equation, the contribution of the surface spins was quantitatively calculated in 15MnFe/Si and 10MnFe/Si. It was found that as the silica concentration increases from 85% to 90%, the surface spins contribution in the total magnetization increases from 15.8% to 22.8%.

6.12) References

[1] R. Pązik, E. Piasecka, M. Małecka, V. G. Kessler, B. Idzikowski, Z. Śniadecki and R. J. Wiglusz, **RSC Advances**, 2013, 3, 12230-12243.

[2] Aakash, R. Choubey, D. Das, S. Mukherjee, **Journal of Alloys and Compounds**, 2016, 668, 33-39.

[3] K. Vamvakidis, M. Katsikini, D. Sakellari, E. C. Paloura, O. Kalogirou, and C. Dendrinou Samara, **Dalton Transactions**, 2014, 43, 12754-12765.

[4] Z. J. Zhang, Z. L. Wang, B. C. Chakoumakos, and J. S. Yin, **Journal of the American Chemical Society**, 1998, 120, 1800-1804.

[5] J. R. Huang and C. Cheng, **Journal of Applied Physics**, 2013,113, 033912.

[6] C. Liu, B. Zou, A. J. Rondinone, and Z. J. Zhang, **Journal of the American Chemical Society**, 2000, 122 (26), 6263–6267

[7] R-R. Gao, Y. Zhang, W. Yu, R. Xiong, J. Shi, **Journal of Magnetism and Magnetic Material**, 2012, 324, 2534-2538.

[8] G. Wang, Y. Ma, L. Zhang, J. Mu, Zh. Zhang, X. Zhang, H. Che, Y. Bai, J. Hou, **Journal of Magnetism and Magnetic Material**, 2016, 401, 647-650.

[9] S. Güner, M. Amir, M. Geleri, M. Sertkol, A. Baykal, **Ceramics International**, 2015, 41, 10915–10922.

[10] Z. Z. Lazarevic, C. Jovalekic, A. Recnik, V. N. Ivanovski, M. Mitri, N. Paunovi, B.D. Cekic, N. Z. Romcevic, M. J. Romcevic, **Journal of Alloys and Compounds**, 2011, 509, 9977–9985.

[11] W. Wang, Z. Ding, X. Zhao, S. Wu, F. Li, M. Yue, and J. P. Liu, **Journal of Applied Physics**, 2015, 117, 17A328.

[12] D. K. Pradhan, S. Kumari, V. S. Puli, P. T. Das, D. K. Pradhan, A. Kumar, J. F. Scott, and R. S. Katiyar, **Physical Chemistry Chemical Physics**, 2017,19, 210-218.

[13] A. Baykal, S. Esir, A. Demir, S. Guner, **Ceramics International**, 2015, 41, 1, 231-239.

[14] V. Blanco-Gutierrez, E. Climent-Pascual, R. Saez-Puche and, Marıa J. Torralvo-Fernandez, **Physical Chemistry Chemical Physics**, 2016, 18, 9186-9193.

[15] G. Madhu, K. Maniammal and V. Biju, **Physical Chemistry Chemical Physics**, 2016,18, 12135-12148.

[16] R. Zamiri, H. Mahmoudi Chenari, H. F. Moafi, M. Shabani, S. A. Salehizadeh, A. Rebelo, J. Suresh Kumar, M. P. F. Graça, M. J. Soares, J. M. F. Ferreira, **Ceramics International**, 2016, 42, 11, 12860-12867.

[17] Z. Sherafat, I. Antunes, C. Almeida, J. R. Frade, M. H. Paydar, G. C. Mather, D. Fagg, **Dalton Transactions**, 2014, 43, 934.

[18] S. D. Shenoy, P.A. Joy, M.R. Anantharaman, **Journal of Magnetism and Magnetic Materials**, 2004, 269, 217–226.

[19] S. Singhal, J. Kaur, T. Namgyal, R. Sharma, **Physica B**, 2012, 407, 1223-1226.

[20] J. Ding, P.G. McCormick, R. Street, **Journal of Magnetism and Magnetic Materials**, 1979, 171, 309-314.

[21] A. R. O. Rodrigues, J. M. F. Ramosa, I. T. Gomes, B. G. Almeida, J. P. Araújo, M. R. P. Queiroz, P. J. G. Coutinho and E. M. S. Castanheira, **RSC Advances**, 2016, 6, 17302-17313.

[22] Ch. Fu, Xi. Long, W. Cai, G. Chen, X. Deng. **Ferroelectrics**, 2014, 460, 1, 157-161.

[23] V. Manikandan, A. Vanitha, E. Ranjith Kumar, S. Kavita, **Journal of Magnetism and Magnetic Materials**, 2017, 426, 15, 11-17.

[24] S. Kanagesan, S. B. A. Aziz, M. Hashim, I. Ismail, S. Tamilselvan, N. B. B. M. Alitheen, M. K. Swamy and B. P. C. Rao, **Molecules**, 2016, 21, 312-321.

[25] P. Sivakumar, R. Ramesh, A. Ramanand, S. Ponnusamy, C. Muthamizhchelvan, **Materials Research Bulletin**, 2011, 46, 12, 2204–2207.

[26] Z. Rashid, H. Naeimi, A-H. Zarnani, M. Nazari, **RSC Advances**, 2016, 6, 36840-36848.

[27] S. A. Salehizadeh, H. Mahmoudi Chenari, M. Shabani, H. Abbastabar Ahangar, R. Zamiri, A. Rebelo, J. Suresh Kumar, M. P. F. Graça and J. M. F. Ferreira, **RSC Advances**, 2018,8, 2100-2108.

[28] Z. Z. Lazarevic, C. Jovalekic, A. Recnik, V.N. Ivanovski, M. Mitric, M.J. Romcevic, N. Paunovic, B. D. Cekic, N. Z. Romcevic, **Journal of Alloys and Compounds**, 2011, 509, 9977– 9985.

[29] Y. Zhou, B. Xiao, Sh-Q. Liu, Z. Meng, Z-G. Chen, C-y. Zou, C-B. Liu, F. Chen, X. Zhou, **Chemical Engineering Journal**, 2016, 283, 266-275.

[30] S. W. da Silva, R. C. Pedroza, P.P. C. Sartoratto, D. R. Rezende, A. V. da Silva Neto, M. A. G. Soler, P. C. Morais, **Journal of Non-Crystalline Solids**, 2006, 352, 1602-1606.

[31] M. A. G. Soler, T. F. O. Melo, S. W. da Silva, E. C. D. Lima, A. C. M. Pimenta, V. K. Garg, A. C. Oliveira, P. C. Morais, **Journal of Magnetism and Magnetic Materials**, 2004, 272–276, 2357–2358.

[32] V. G. Ivanov, M. V. Abrashev, M. N. Lliev, M. M. Gospodinov, J. Meen, M. I. Aroyo, **Physical Review B**, 82(2), 2010, 024104.

[33] Z. W. Wang, P. Lazor, S.K. Saxena, G. Artioli, **Journal of Solid State Chemistry**, 2002, 165, 165–170.

[34] P. Chandramohan, M. P. Srinivasan, S. V. Narasimhan, **Journal of Solid State Chemistry**, 2011, 89-96.

[35] I. Chamritski, G. Burns, **The Journal of Physical Chemistry B**, 2005, 109, 4965-4968.

[36] H. Zheng, W. Weng, G. Han, and P. Du, **The Journal of Physical Chemistry C**, 2013, 117, 12966−12972.

[37] H. Han, C. Davis, III, and J. C. Nino, **The Journal of Physical Chemistry C**, 2014, 118, 9137−9142.

[38] Y-L. Huang, S-P. Chiu, Z-X. Zhu, Z-Q. Li and J-J. Lin, **Journal of Applied Physics**, 2010, 107, 063715.

[39] T. Abraham, C. Bansal, J. T. T. Kumaran, and, A. Chatterjee, **Journal of Applied Physics**, 2012, 111, 104318.

[40] A.K. Jonscher, **Nature**, 1977, 267, 673–679.

[41] C.G. Koops, **Physical Review**, 83, 1951, 121.

[42] K. W. Wagner, **American Journal of Physics**, 1973, 317, 40.

[43] C. Behera, R.N.P. Choudhary, P. R. Das, **Ceramics International**, 2015, 41, 13042–13054.

[44] E. Veena Gopalan, K. A. Malini, S. Saravanan, D. Sakthi Kumar, Y. Yoshida and M. R. Anantharaman, **Journal of Physics D: Applied Physics**, 2008, 41, 185005.

[45] N. Ponpandian, A. Narayanasamy, **Journal of Applied Physics**, 2002, 92, 2770.

[46] P. Lunkenheimer, V. Bobnar, A. V. Pronin, A. I. Ritus, A. A. Volkov, A. Loidl, **Physical Review B**, 2002, 66, 052105.

[47] I. Ahmad, M. J. Akhtar, M. M. Hasan, **Materials Research Bulletin**, 2014, 60, 474-484.

[48] C. Behera, R. N. P. Choudhary, P. R. Das, **Journal of Materials Science: Materials in Electronics**, 2015, 26, 4, 2343–2356.

[49] A. R. James, C. Prakash, G. Prasad, **Journal of Physics D: Applied Physics**, 2006, 42, 065413.

[50] J. Kolte, P.H. Salame, A. S. Daryapurkar, and P. Gopalan, **AIP Advances**, 2015, 5, 097164.

[51] K.K. Bhargav, S. Ram, S. B. Majumder, **Journal of Alloys and Compounds**, 2015, 638, 334-343.

[52] M. Younas, M. Nadeem, A. Atif and R. Grossinger, **Journal of Applied Physics**, 2011, 109, 093704.

[53] R. Zamiri, S. A. Salehizadeh, H. Abbastabar Ahangar, M. Shabani, A. Rebelo, J. Suresh Kumar, M. J. Soares, M. A. Valente, J. M. F. Ferreira, **Materials Chemistry and Physics**, 2017, 192, 330-338.

[54] P. Tiberto, G. Barrera, F. Celegato, M. Coisson, A. Chiolerio, P. Martino, **The European Physical Journal B**, 2013, 86, 173-179.

[55] G.F. Goya, T.S. Berquó, F.C. Fonseca, M.P. Morales, **Journal of Applied Physics,** 2003, 94, 3520-3528.

[56] D.L. Hou, X.F. Nie, H.L. Luo, **Applied Physics A**, 1998, 66, 109-114.

This page was intentionally left blank

Chapter 7 - Preparation and characterizations of single-phase hematite nanosize powders by Pechini method.

7.1) Introductory remarks

Hematite is an n-type semiconducting substance with E_g=2.1 eV and possesses the highest stability under ambient atmosphere compared with other iron oxides [1, 2]. In the magnetic point of view, in a temperature range below 300 K, it displays the Morin transition at 260 K. the electrical and magnetic properties of hematite strongly depend on the size of particles [3]. Particularly, as the size of the particle decrease, there is a reduction in the Morin temperature [4]. Hematite nano/microstructures extensively has been employed in several applications including; gas sensors [5], red pigment [6] photoinduced water splitting [7], catalysis [8], magnetic recording [9], drug delivery [10], tissue repair engineering [11], lithium-ion batteries [12] and spin electronic devices [13]. Up to now various methods have been employed to synthesize homogenous single-phase iron oxide particles such as sol-gel route [14] water-oil microemulsion [15], hydrothermal [16], combustion [17] and Pechini process [18]. Among the wet chemical methods, the Pechini method presents very interesting results due to its benefits such as better stoichiometric control, non-toxicity and being time-saving and low-cost method [1, 19].

In the Pechini process, the inorganic salts as precursors, citric acid as a chelating agent and polyethylene glycol (PEG) as a cross-linking agent are used to prepare nano/microstructured metal oxide powders [20]. During this process, the weakly bounded polybasic acids assist to chelate the metal ions. In the next step, the linkage between the chelates and polyhydroxyl alcohols leads to the polyesterification then a solid polymer resin containing homogeneously distributed metal cations is formed [1]. The highly branched polymer gives rise to a reduction in the cation mobility as the chelated solution undergoes to the heat treatment process, therefore the final product will have a good degree of homogeneity and minimum particle size [20].

In this chapter, a systematic study on the Pechini sol-gel method for the synthesis of the single-phase α-Fe_2O_3 nano-powders is presented. The XRD, DTA, Raman, SEM, electrical and VSM analyses are used to investigate extensively the crystallinity, thermal, structural, electrical and magnetic characteristics of the prepared samples.

7.2) Experimental Procedure

The preparation of the gel started by choosing the precursors, which were Iron(III) nitrate non-hydrate ($Fe(NO_3)_3$. $9H_2O$), Acid citric ($C_6H_8O_7$) and ethylene glycol ($C_2H_6O_2$) (purity> 99 %). The quantity of each component used was determined by establishing the molar ratio between the metallic cation, the acid and ethylene glycol 1:3:4.

Prior to the mixture of precursors together, the quantity of acid citric was mixed with ~ 30 ml of deionized water and stirred for about 30 min until at 60 ^oC reaching to a transparent solution. Then, the proposed iron nitrate was added to the solution and stirred for 2 hours at room temperature. In the next step, the quantity of ethylene glycol was poured into the mixture and stirred at room temperature for 24 hours. In order to dry the obtained gel, the heat treatment was done according to this procedure. First, the gel was kept in 80 ^oC for three days after the temperature has been raised gradually to 250 ^oC. In order to remove the smoking due to decomposition in the gel, the oven door was opened sometimes for few minutes and closed rapidly to avoid disturb in heat treatment process the sample was maintained in the final temperature for 24 hours and then cooled down to RT slowly.

The powder was firstly heat-treated to 500 ^oC at 4 h with a heating rate of 5 ^oC/min, (hereafter so-called as Pechini500) and the preheated powder was then re-ground and manually pelletized with 7 mm diameter using a disk-shaped mold. After pre-heating, the pellet was calcined at 800, 1000 and 1200 ^oC under ambient condition for 4 hours with a heating rate of 5 ^oC/min and hereafter are labeled as Pechini800, Pechini1000, and Pechini1200, respectively.

7.3) Results and discussion

7.3.1) XRD results

Fig. 7.1 demonstrates the XRD patterns of as-prepared and calcined initially at 500 ^oC. As seen in Fig. 7.1, the as-prepared sample contains mainly hematite phase and also a minor phase of maghemite. After initial calcination, the maghemite impurity phase almost disappears and the observed α-Fe_2O_3 peaks are intensified. The normalized XRD patterns of the final heat-treated (HT) samples are shown in Fig. 7.2. The powders calcined under the secondary heat treatment

process are well crystallized into hematite phase without any impurities. The observed peaks of the powders calcined at 800 °C and above (Fig. 7.2) are indexed in agreement with the standard XRD peaks in α-Fe_2O_3 (JCPDS standard data, Card No. 33-0664).

The average crystalline size of all patterns was calculated using the Debye-Scherrer formula and the obtained results are presented in table 7.1. Supported by SEM observation (discussed later), it can be observed that with an increase in the calcination temperature, the average size of the particles increases.

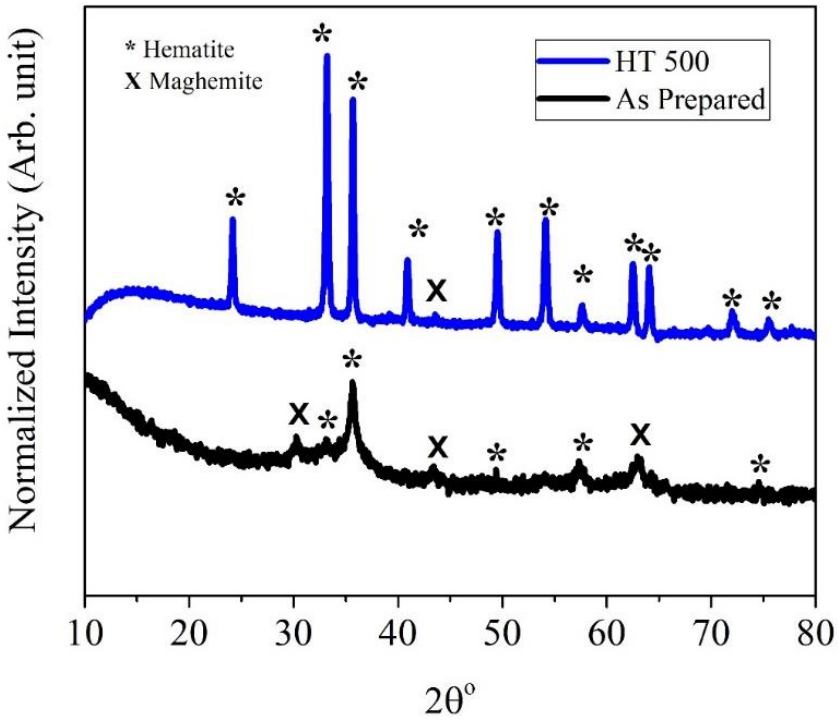

Fig. 7.1) XRD Patterns of as prepared and initial HT Fe_2O_3 using Pechini route.

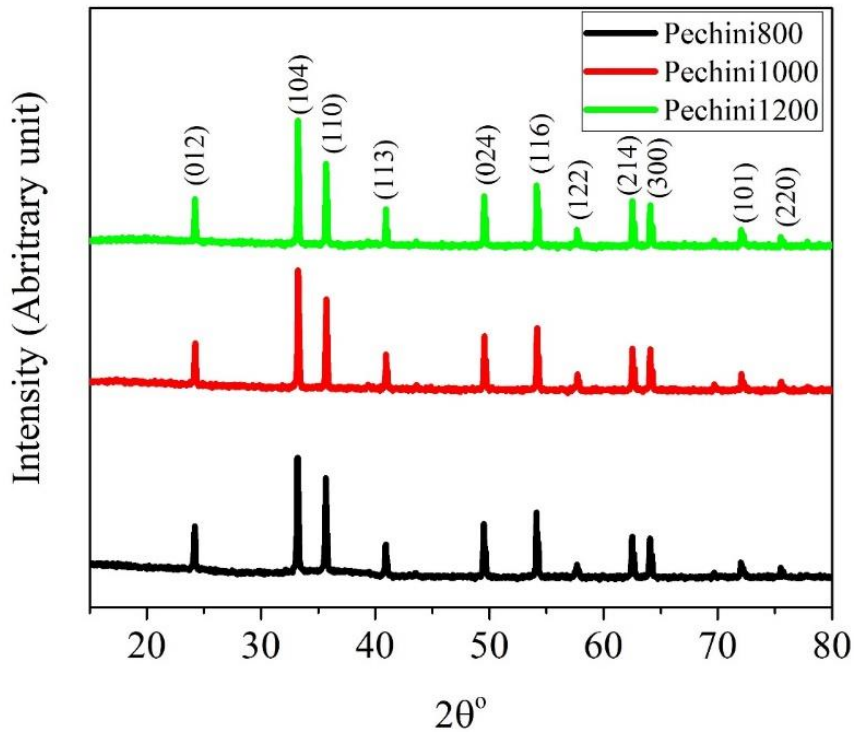

Fig. 7.2) XRD Patterns of the final HT α-Fe_2O_3 prepared by Pechini route.

Table 7.1) The crystallite size of the samples obtained using the Debye-Scherrer formula.

Sample	**As-prepared**	**Pechini500**	**Pechini800**	**Pechini1000**	**Pechini1200**
$D_{D\text{-}Sch}$ (nm)	13±1	46±2	-	-	-
D_{SEM} (nm)	-	-	295±85	386±154	756±210

7.3.2) DTA analysis

DTA curves performed in different heating rates are depicted Fig. 7.3. The DTA curves reveal two significant exothermic peaks. The first exothermic peak ranged from 323 °C to 350 °C depending on the heating rate, related to the combustion of citric acid and polyethylene glycol derivatives and the formation of α-Fe_2O_3 phase. It is also confirmed by the corresponding XRD patterns (Fig. 7.1).

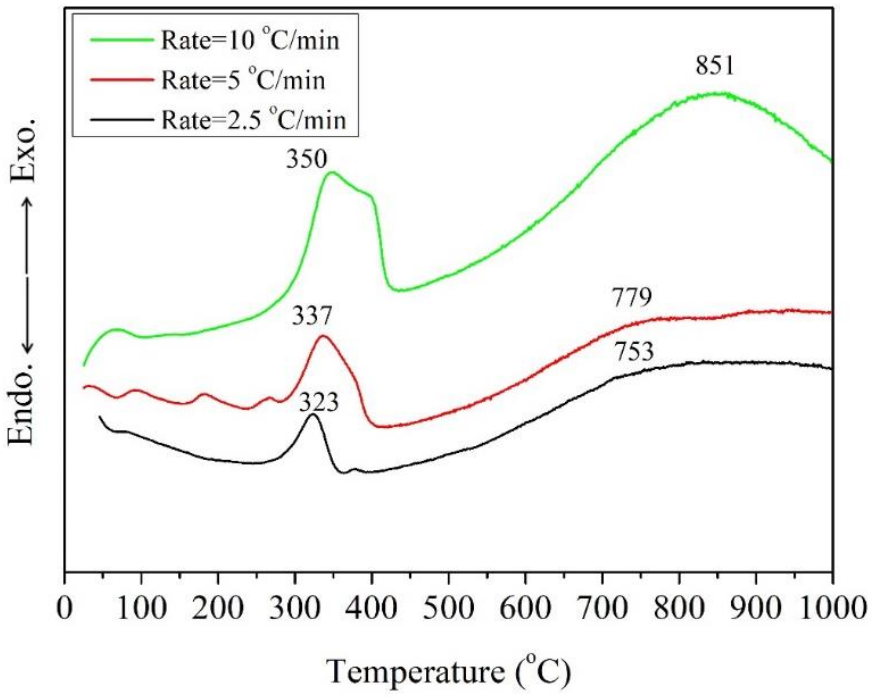

Fig. 7.3) DTA curves of as prepared Pechini sample at a different heating rate.

The second exothermic peak, attributed to the formation of pure α-Fe_2O_3, increases from 753 to 851 °C, with the heating rate enhancement from 2.5 to 10 °C/min. Another significant feature is that with a decrease in the heating rate the exothermic peaks are shifted to a lower temperature combined with a reduction in the intensity of the peaks.

Furthermore, it is noticed that in the curve performed at the rate of 10 °C/min there is a cusp mark attached to the peak at 350 °C. This shoulder-like feature gradually is diminished as the rate of heating is reduced. Besides that, for the curve with the rate of 5 °C/min, some peaks are detected at a temperature below 300 °C. The peaks between 25 and 200 °C can be correlated to the vaporization of water. Also, the peaks ranged from 200 to 300 °C can be related to the deformation of the polymer network mainly due to polyethylene glycol breakup and also combustion of the residue organic compound [1].

7.3.3) Raman spectra analysis

Fig. 7.4 exhibits the Raman spectra of the samples calcinated under the secondary heat-treatment process.

The occurrence of characteristic peaks of hematite (α-Fe_2O_3) at around 226 (A_{1g}), 245 (E_g), 295 (E_g), 410 (E_g), 500 (A_{1g}), and 610 (E_g) cm^{-1} all identified as transverse optical (TO) modes, can be observed in all samples [21, 22]. Also, a remarkable band at ~660 cm^{-1} is detected, assigned to the longitudinal optical (LO) E_u mode of hematite [23]. This band is supposed to be inactive in the perfect ordered hematite crystallites [24]. Hence, the appearance of this band in our samples can be due to the disorder within the hematite crystal lattice of the prepared samples. Additionally, the weak and broad band h at 820 cm^{-1} is corresponded to the first order magnon scattering in hematite [25]. Some contribution noticed in the range between 1000 and 1100 cm^{-1}, the bands i and j, can be attributed to lack of long-range order as well as to an impurity phase hence very often called “disorder bands” [23]. Besides that, band k at 1320 cm^{-1} is assigned to the second order magnon Raman scattering in hematite [21]. For a closer inspection of Raman analysis, the spectra were baseline-corrected then deconvoluted using Gaussian fitting and quantitative band parameters, such as peak maxima, widths, intensities, and areas were obtained (Fig. 7.5). The bands noted in alphabetic order and their corresponding assignments, are listed in table 7.2. According to the table, there is no evident shift in the band position of all spectra so the strength of Fe-O bond in FeO_6 octahedra is invariable with respect to the variation of the calcination temperature [26]. While as the temperature rises up (and consequently the size increases) the band related to E_u mode gets narrower, a signature of increasing lattice disorder in smaller particles. Moreover, in order to refine the interpretation, we have calculated the relative area of band k in each spectrum using the following equation:

$$R_{Area(k)} = \text{Area of band k/Total area of the spectrum} \quad (7.1)$$

The values of $R_{Area(k)}$ were determined and given in table 7.2. As seen, the relative area decreases with increase in the crystallite size. It was pointed out that 2 magnons scattering takes place by means of excited exchange interaction. So in the sample with a bigger size (Pechini1200), the possibility of the exchange interaction is diminished.

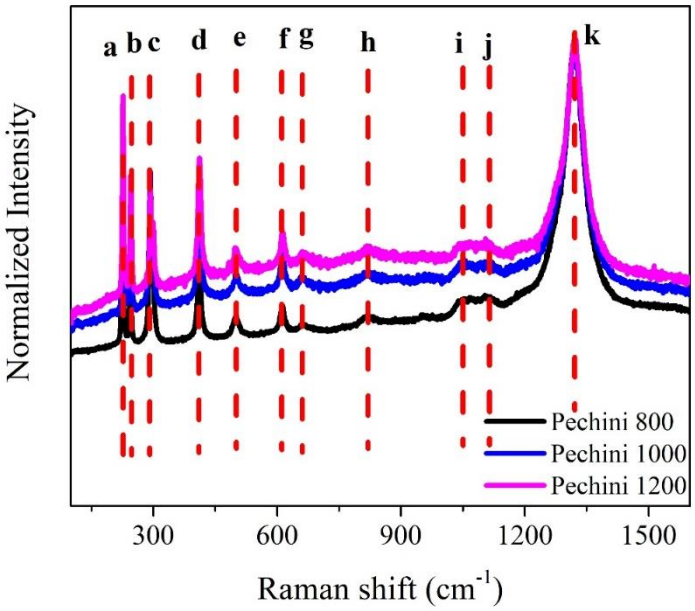

Fig. 7.4) Raman spectra of α-Fe_2O_3 samples calcined at the secondary heat treatment.

Table 7.2) Raman band assignment of the Pechini samples [21-26].

Pechini800	**Pechini1000**	**Pechini1200**	**Band´s notation**	**Assignment**
Band position (cm^{-1})				
226	226	227	a	A_{1g}
245	245	245	b	E_g
293	293	293	c	E_g
410	410	412	d	E_g
500	502	500	e	A_{1g}
611	613	613	f	E_g
663	661	661	g	E_u
818	820	822	h	1st order magnon scattering
1051	1053	1053	i	Disorder bands
1107	-	1101	j	
1319 [73.06]	1319 [64.36]	1319 [57.90]	k [$R_{Area(k)}$] in%	2nd order magnon scattering

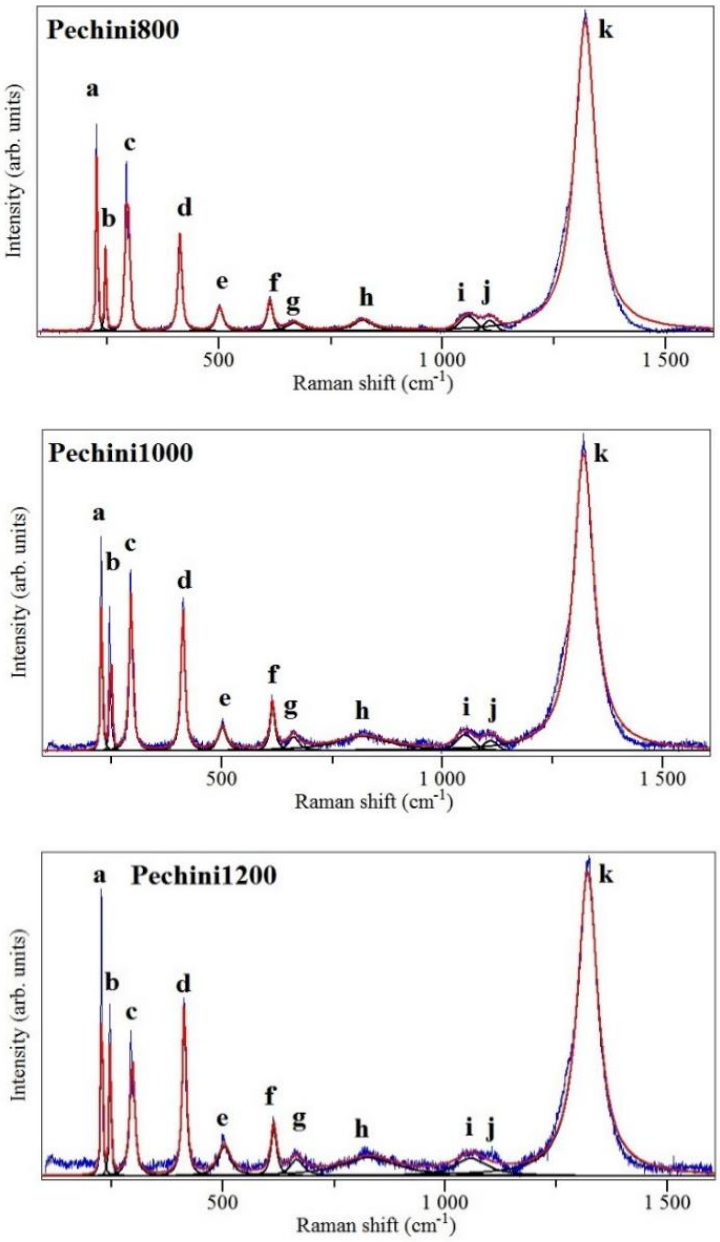

Fig. 7.5) Raman spectra deconvolution of the Pechini samples.

7.3.4) Morphology investigation

Fig. 7.6 gives an overview of the impact of heat treatment on the Pechini samples morphology. The SEM image of the as-prepared sample shows an agglomerated mesoporous polymorph structure. With increasing in the heat treatment temperature, the size of the nanocrystals increases and nanocrystals with mainly bitruncated dodecahedron shape are obtained. To calculate the average size of each sample, the size of at least 50 particles, diagonally, were

measured using ImageJ software and then the histogram of the size distribution was the plotted and shown in Fig. 7.7. The size distribution histogram was fitted to the lognormal function and the derived average sizes were listed in table 7.1. According to table 7.1, the size values obtained from SEM investigation are in consistent with the ones obtained from XRD analysis.

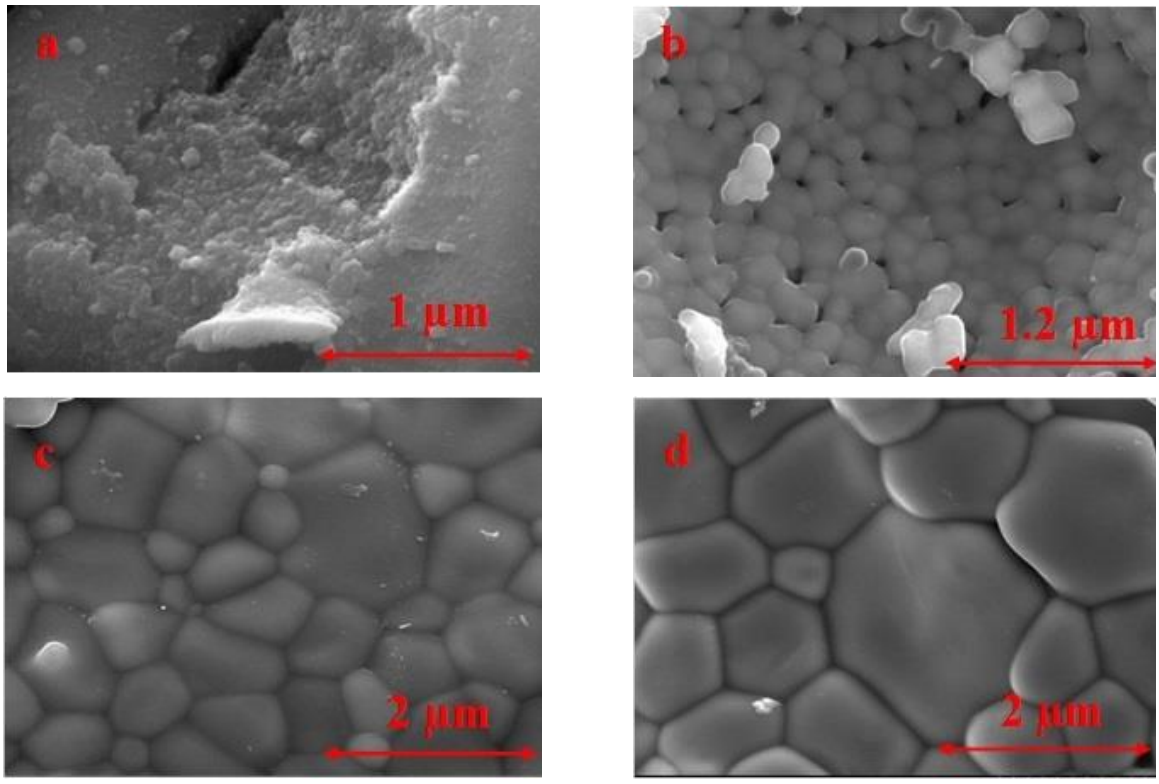

Fig. 7.6) SEM image of a) As-prepared sample b) Pechini800 c) Pechini1000 and d) Pechini1200.

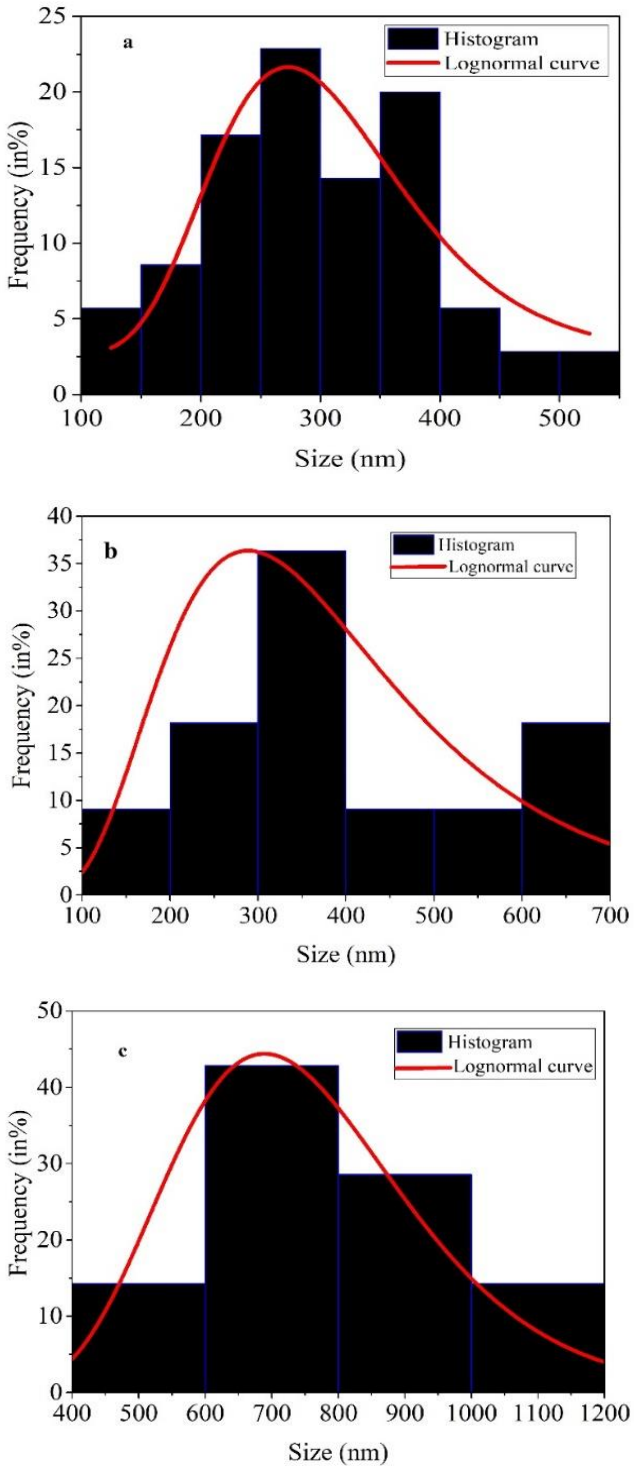

Fig. 7.7) The particle size distribution histogram a) Pechini800 b) Pechini1000 and c) Pechini1200.

7.3.5) Electrical measurements

7.3.5.i) Pechini800

The frequency dependence of the real part (ε′), imaginary part (ε′′) of the dielectric constant and loss tan (tan(δ)) of Pechini800 are shown in Fig. 7.8 (a-c), respectively. It is remarkable that ε′ decreases with the increase of frequency. The high ε′ value at the low-frequency region is associated with the ionic, space charge and interface polarization contributions [27]. Also, the dielectric constant values in lower frequencies get bigger as the temperature rises up confirming the relaxation process is thermally activated [27]. At higher frequencies, dielectric constant becomes independent of frequency. These results from the fact that the electric dipoles are unable to follow the rapid alternation of the applied field [28]. Moreover, Fig. 7.8 b shows the frequency dependence of ε′′ measured at several temperatures exhibits the relaxation steps which shift towards lower frequencies with decreasing temperature.

The relaxation process dynamics can be studied through the temperature dependence of relaxation time, $\tau_{\varepsilon''}$, expressed by Arrhenius law as:

$$\tau_{\varepsilon''} = \tau_o.\exp(\Delta E_{\varepsilon''}/k_B T) \qquad (7.2)$$

where τ_o is a pre-exponential factor, $\Delta E_{\varepsilon''}$ stands for the activation energy of relaxation and k_B is the Boltzmann constant. As illustrated in Fig. 7.8 d, the plot of $Ln(\tau_{\varepsilon''})$ vs. 1000/T perfectly obeys the Arrhenius law (eq. 7.2) and the determined value of $\Delta E_{\varepsilon''}$ is presented in table 7.2. Analogous to the ε′′ behavior, the tan loss plots vs. the frequency at the selected temperature present the relaxation peak (Fig. 7.8 c). In polycrystalline semiconductors, the dielectric loss is associated with lag in polarization with respect to the applied field due to the grain boundaries, impurities, and imperfections in the crystal lattice. As the frequency of the external ac field is synchronized with the hopping frequency of the charge carriers, the maximum electrical energy is transferred to the oscillating ions and a relaxation peak appears [29]. Similar to the ε′′ counterpart, we define $\tau_{\tan(\delta)}$ stated as:

$$\tau_{\tan(\delta)} = \tau_o.\exp(\Delta E_{\tan(\delta)}/k_B T) \qquad (7.3)$$

where $\Delta E_{\tan(\delta)}$ is the activation energy of relaxation. The experimental data along with the linear fitting to Eq. 7.3 are drawn in Fig. 7.8 d. the value of $\Delta E_{\tan(\delta)}$ listed in table 7.3, is the same as one for $\Delta E_{\varepsilon''}$.

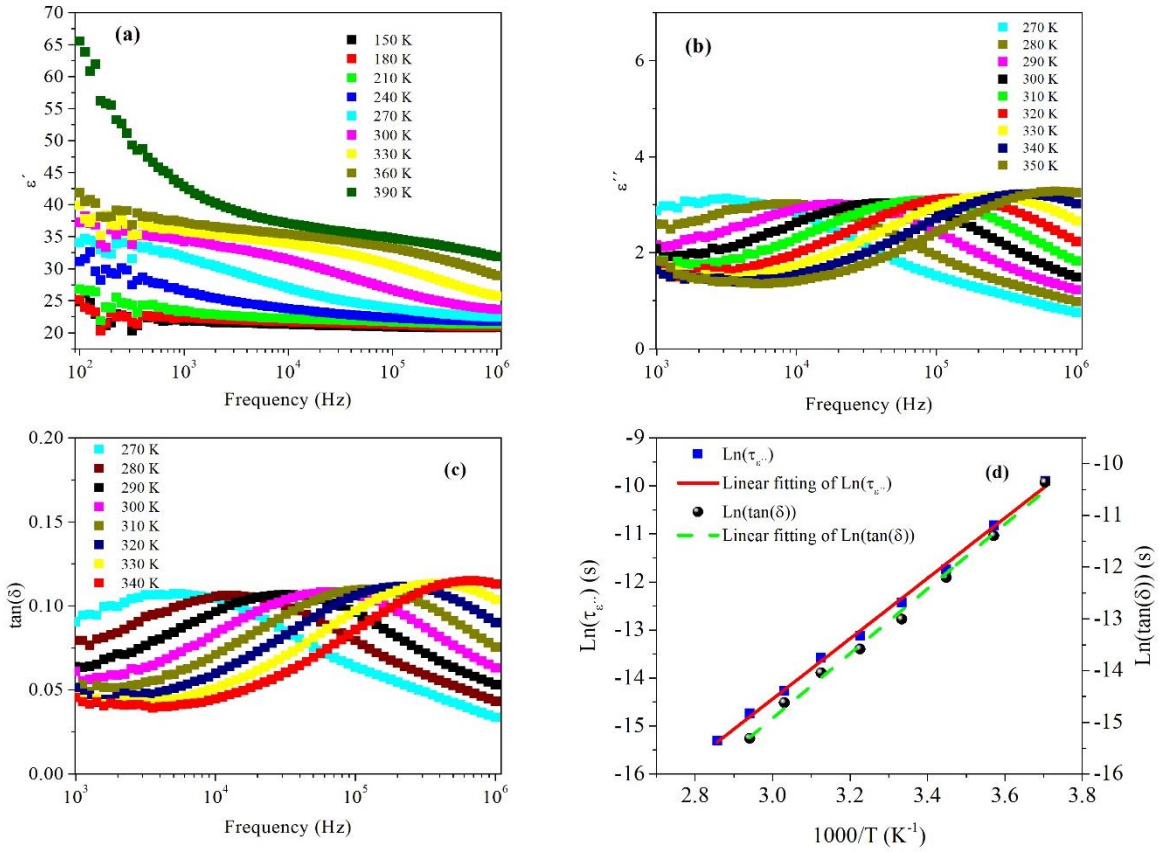

Fig. 7. 8) Temperature-dependent variation of a) real (ε´), b) imaginary (ε´´) dielectric, c) loss tangent (tan(δ)) and d) the plot of relaxation times, $\tau_{\varepsilon''}$ and $\tau_{\tan(\delta)}$, vs 1000/T all for Pechini800. The Solid red and dashed green lines are the best fit to the data according to Eq. (7.2) and Eq. (7.3), respectively.

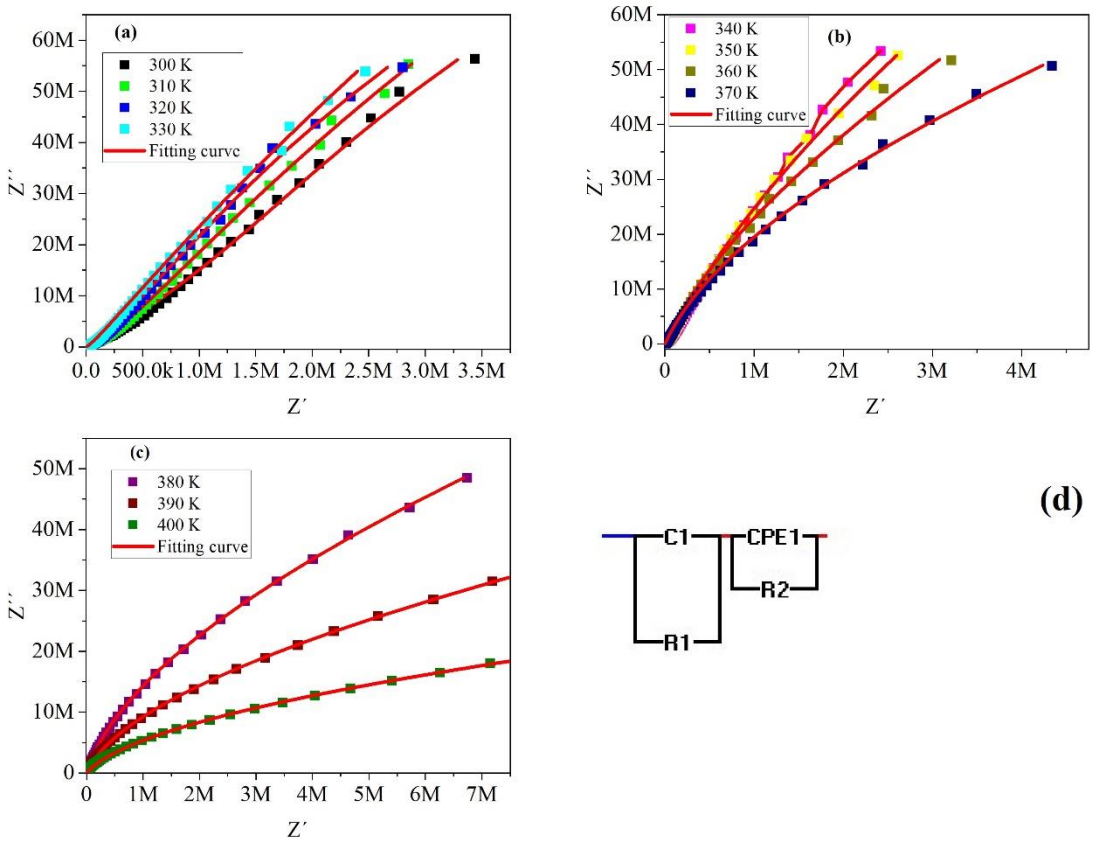

Fig. 7.9) (a-c) Complex impedance plane plots of Pechini800 at selected temperatures; (d) equivalent circuit model used for fitting.

Table 7.3) AC electrical properties of Pechini800, Pechini1000, and Pechini1200 samples measured at 300 K and 1 kHz*.

Sample	ε'	σ_{ac} (S/m)	tan(δ)	$\Delta E_{\varepsilon'}$ (eV)	$\Delta E_{tan\delta}$ (eV)	$\Delta E_{M''}$ (eV)	ΔE_g (eV)	ΔE_{gb} (eV)
Pechini 800	34.23	1.16e-7	0.061	0.54	0.54	0.51	-	-
Pechini 1000	54.20	2.41e-7	0.079	-	-	0.85	0.65	0.81
Pechini 1200	69.44	2.57e-6	0.66	-	0.77	0.76	0.69	0.73

*All values have an error less than 1%.

In order to correlate the electrical properties of the Pechini samples with their microstructures, the impedance spectra were studied in the wide frequency range from 100 Hz to 1 MHz at

several temperatures. Fig. 7.9 (a-c) show the complex (Cole-Cole) impedance plots at various temperatures. It is assumed that hematite nanocrystalline consists of the parallel conducting grains separated by the resistive grain boundaries. The arc corresponded to the grain boundaries lies in the low-frequency zone while the arc representing the grain contribution takes place at higher frequencies [30]. An equivalent circuit model can be employed to determine the grain (g) and the grain boundary contributions in the impedance data. The shape of the impedance plane plot suggests components of the equivalent circuit. The best fitting to the experimental data could be obtained by means of the equivalent circuit model ($R_{gb}C_{gb}$) (R_gCPE_g) shown in Fig. 7.9 d. the fitting data are listed in table 7.4. It is obvious to see that the grain boundary has a more resistive nature compared with the bulk grain of the sample. It has been observed that C_{gb} tends to increase with temperature inferring the accumulation of charges at the grain boundaries.

Table 7.4) The derived data from the fitting of the proposed equivalent circuit for Pechini800*.

Temperature	R_g (MΩ)	P_g ($\times10^{-10}$)	ng	C_g (pF)	R_{gb} (GΩ)	C_{gb} (pF)
300	0.657	1.61	0.792	14.6	0.412	2.70
310	0.537	2.90	0.756	17.1	0.448	2.75
320	0.468	5.73	0.716	21.8	0.535	2.81
330	0.491	11.7	0.676	32.7	0.617	2.90
340	0.411	17.3	0.660	41.5	0.607	2.90
350	0.649	25.8	0.630	60.1	0.786	2.92
360	13.2	0.897	0.877	34.7	3.14	3.32
370	16.1	0.616	0.896	27.6	1.46	3.47
380	15.4	0.452	0.901	20.3	0.688	3.70
390	20.8	0.197	0.923	10.3	0.307	4.76
400	17.3	0.166	0.905	7.06	0.0908	7.15

* Error less than 2%.

The frequency dependence of ac conductivity measured at several temperatures are plotted as illustrated in Fig. 7.10 a.

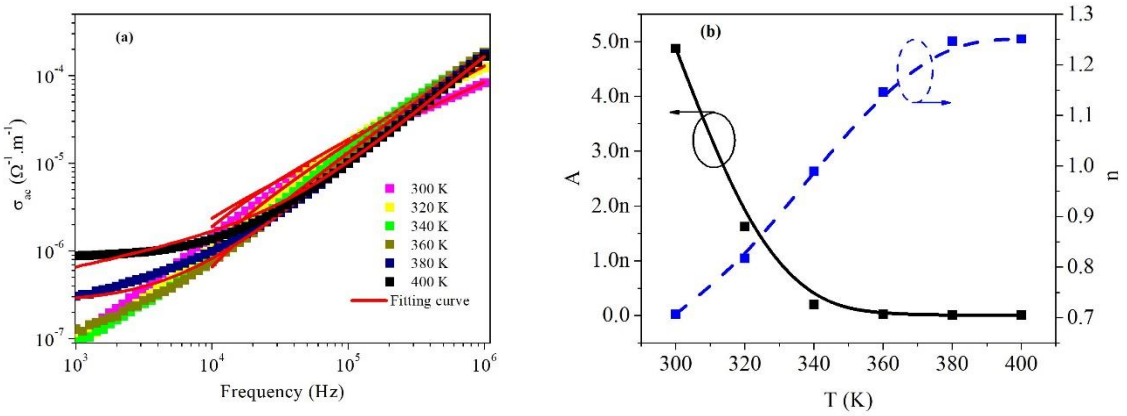

Fig. 7.10) a) Variation of ac conductivity with frequency at different temperatures of Pechini800 b) Variation of exponent 'n' and A with temperature.

As seen, the ac conductivity drastically increases with increasing frequency showing a change in the conduction mechanism from low-frequency grain boundary conduction to high-frequency bulk conduction. This increasing trend is associated with charge transport through the thermal-activated hopping of three-dimensional electrons via oxygen vacancies within the hematite grains [28]. The frequency dependence of ac conductivity follows Jonscher power law, expressed as [31]:

$$\sigma_{ac}(\omega) = \sigma_{dc}(T) + A\omega^{n} \qquad (7.4)$$

where σ_{dc} is the frequency independent (dc) conductivity, being temperature dependent constant and n is power law exponent. In Fig. 7.10 a, the symbols denote the experimental data and the red solid line represents the fitting to Eq. 7.4. It is observed that eq. 7.4 perfectly can be adjusted to the experimental data in the high-frequency region (>10^4 Hz). In the low-frequency zone, below 10^4 Hz, the deviation from the plateau region value in the conductivity spectrum is due to the electrode polarization effect [31]. The variations of fitted parameters A and n with temperature are given in Fig. 7.10 b. As depicted, the exponent n increases with the increasing temperature.

The n value is found to be between 0.6 and 1 for temperatures lower to 350 K which is attributed to the hopping conduction of mobile charge carriers over the barrier between two sites in this temperature range [32]. However, for temperatures above 350 K, n takes values

larger than one meaning that the motion involves localized hopping without the species leaving the neighborhood [33].

Besides that, the A value is reduced sharply as temperature increases indicating the weakening of the polarizability which results from the non-diffusive motion of charge carriers in the sample [34].

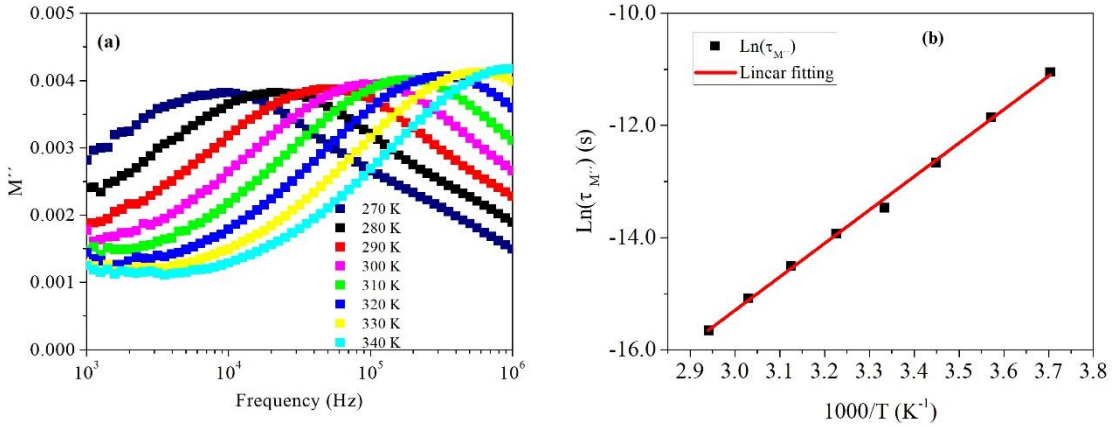

Fig. 7.11) Frequency dependence of a) imaginary electric modulus (M″) at different temperatures. b) the plot of $\tau_{M''}$ vs 1000/T for Pechini800. The Solid red line is the best fit to the data according to Eq. (7.5).

Fig. 7.11 (a) reveals an imaginary component of the electrical modulus (M″) response at several temperatures. It is noticeable that the variation of M″ spectra with frequency at each temperature shows an asymmetric broad peak. The M″ spectra shift toward the high-frequency region with temperature increasing. In resembling with the ε′′ spectra, the relaxation time τ related to the frequency maximum in the modulus spectra can be stated by:

$$\tau_{M''} = \tau_o.\exp(\Delta E_{M''}/k_B T) \qquad (7.5)$$

where $\Delta E_{M''}$ is the activation energy of relaxation. We fitted the experimental data to the eq. 7.5 and the $\Delta E_{M''}$ value was extracted and represented in table 7.3. The $\Delta E_{M''}$ value was found being nearly similar to the $\Delta E_{\varepsilon''}$ one.

7.3.5-ii) Pechini1000

The dielectric constant spectra of Pechini1000 measured at various temperatures showed similar nature as that of Pechini800 (compare Fig. 7.12 (a) with Fig. 7-8 a)). According to Fig. 7.12 (b) and (c), the variation of ε´´ with frequency for Pechini1000 follows the similar behavior of variation as that of ε´. In contrary to ε´´ and ε´ spectra, tan(δ) spectra showed a thermally activated relaxation characteristic.

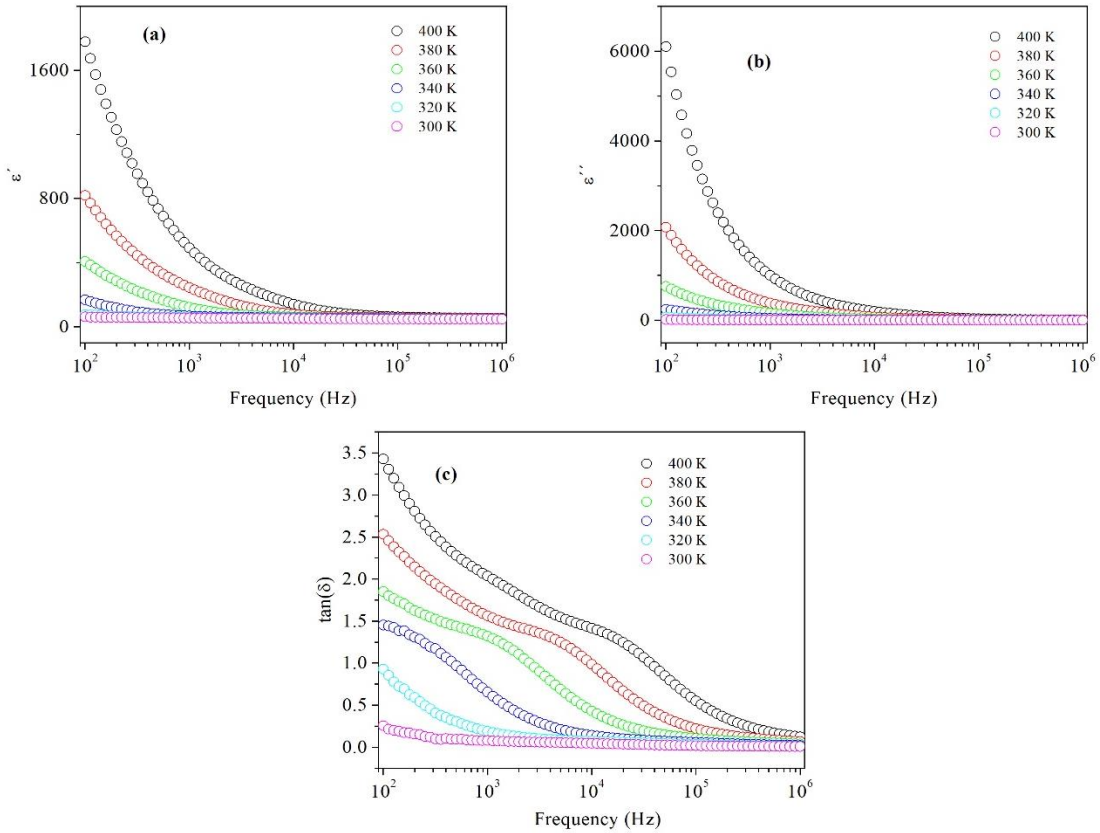

Fig. 7.12) Frequency-dependent curves of a) ε´, b) ε´´ and c) loss tangent for Pechini1000 at measured selected temperatures.

In Fig. 7.13 (a-c) complex impedance spectra (Nyquist plot) of Pechini1000 obtained at different temperatures are depicted. At lower temperatures (300 K-320 K), the impedance spectrum represents a depressed semicircular which can be deconvoluted to two overlapping semicircular arcs attributing to the bulk (grain) and the grain boundary properties of the sample. With increasing temperature, the appearance of two semicircles is clarified. Also, the

magnitude of both contributions decreases with temperature confirming the semiconducting nature of the sample. In order to quantify each contribution in the impedance spectra, an equivalent circuit model (R_gCPE_g)($R_{gb}CPE_{gb}$) connected in series is proposed (Fig. 7.13 d). As shown in Fig. 7.13 (a-c) the model successfully is fitted to the experimental data. The obtained parameters characterizing to the grain boundary and grain interior contributions are enlisted in table 7.5.

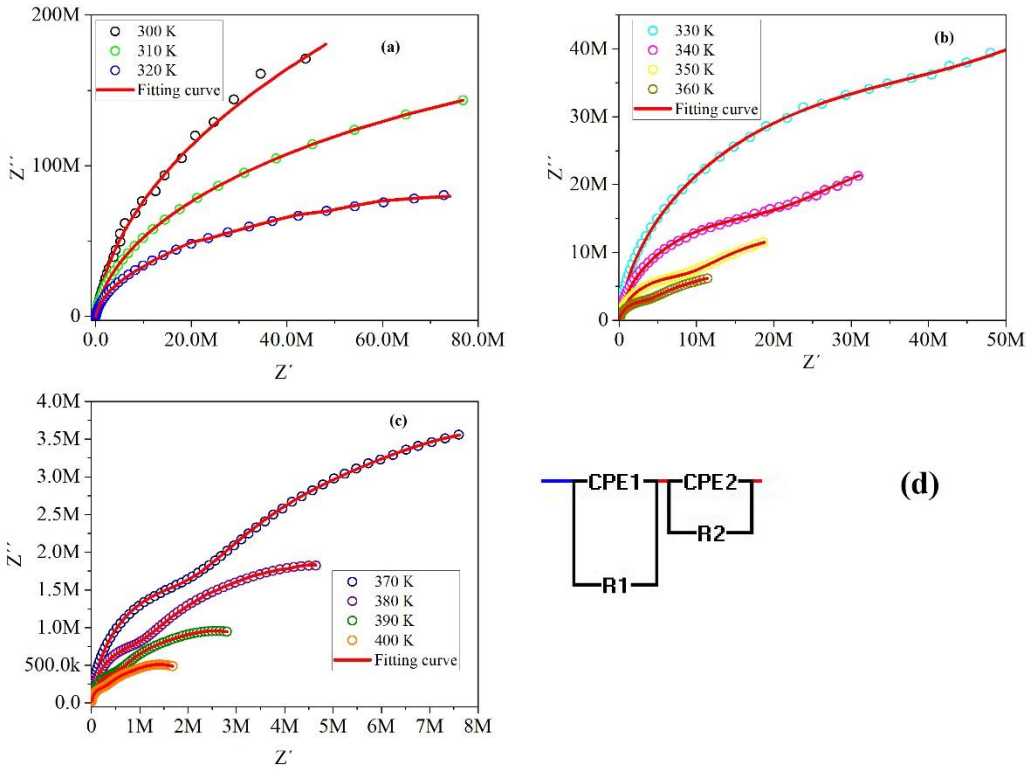

Fig. 7.13) (a-c) Complex impedance spectra (Nyquist plots) for Pechini1000 at different temperatures along with (d) the electrical equivalent circuit.

Table 7.5) The attained data from the fitting of the proposed equivalent circuit for Pechini1000 (Error less than 2%).

Temperature	R_{gb} (MΩ)	P_{gb} ($\times10^{-10}$)	n_{gb}	C_{gb} (pF)	R_g (MΩ)	P_g ($\times10^{-10}$)	n_g	C_g (pF)
300	2930	0.089	1	8.91	8.71	1.4	0.87	54.5
310	264	0.081	1	8.16	1.12	3.64	0.84	83.8
320	197	0.488	0.97	42.8	97.8	0.148	0.96	11.5
330	95.8	0.686	0.97	60.0	50.0	0.189	0.92	11.2
340	63.8	1.81	0.82	70.6	18.6	0.206	0.94	12.7
350	35.9	3.66	0.75	87.9	7.28	0.223	0.95	14.0
360	21.1	8.06	0.67	11.5	3.03	0.240	0.96	16.5
370	12.8	13.7	0.63	13.2	1.48	0.230	0.98	19.0
380	7.05	24.4	0.59	16.0	0.71	0.298	0.97	22.0
390	3.92	43.0	0.57	20.7	0.41	0.624	0.92	24.3
400	2.16	73.4	0.56	28.4	0.27	1.44	0.85	24.7

According to table 7.5, R_{gb} is larger than R_g over the measured temperature range (similar to Pechini800.). We can calculate the activation energies of conduction for grain (ΔE_g) and grain boundaries (ΔE_{gb}), based SPH model using:

$$\sigma_{g,gb} = \sigma_o.\exp(\Delta E_{g,gb}/k_BT) \qquad (7.6)$$

where σ_o is a pre-exponential factor. We obtained the ΔE_{gb} and ΔE_g values, being 0.81 and 0.65 eV, respectively.

The $\sigma_{ac}(\omega)$ of Pechini1000 was fitted to Jonscher's power law (Eq. (7.4)) as revealed in Fig. 7.14 a. It was found the best fit could be achieved for frequencies higher than 10^4 Hz. The extracted parameters of A and n as a function of temperature were demonstrated in Fig. 7.14 b. As displayed in Fig. 7.14 b, the value of n drops with temperature after reaching to a minimal point at 330 K, increase smoothly with more increasing temperature up to 360 K. Therefore it can be suggested in the temperature range of 300-360 K overlapping large polaron tunneling (OLPT) is the predominant conduction mechanism for Pechini1000 [35]. However, beyond 360 K, when the temperature further increases, n decreases abruptly so the correlated barrier hopping (CBH) mechanism is proposed as the conduction mechanism for temperatures higher

than 360 K. Moreover, it should be pointed out that the A values increase with temperature thus the polarizability is strengthened with temperature and charge carriers move diffusively in Pechini1000 [36].

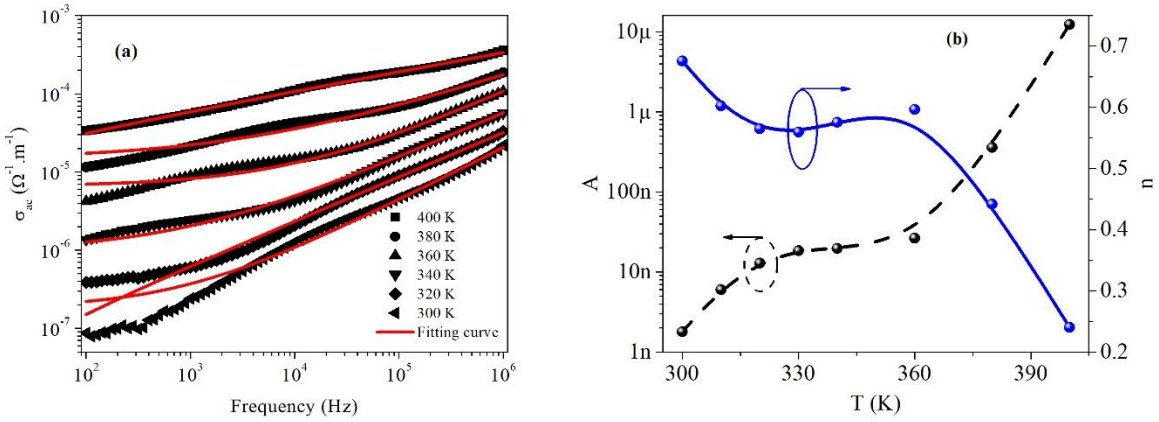

Fig. 7.14) a) Variation of ac conductivity with frequency from 300 to 400 K with a temperature step of 20 K, b) Variation of exponent 'n' and A with temperature for Pechini1000.

The obtained modulus spectra, M´´(ω), of Pechini1000 measured at various temperatures, is depicted in Fig. 7.15 a. The plots of M´´ exhibit the relaxation behavior peaks shifting towards higher frequencies with increasing temperature. The occurrence of relaxation peak suggests a transition from long range to short-range mobility of charge carriers [37]. As illustrated in Fig. 7.15 b the experimental data thoroughly is modeled to Equation 7.5 and the computed value of activation energy ($\Delta E_{M''}$) is found to be 0.85 eV (table 7.3).

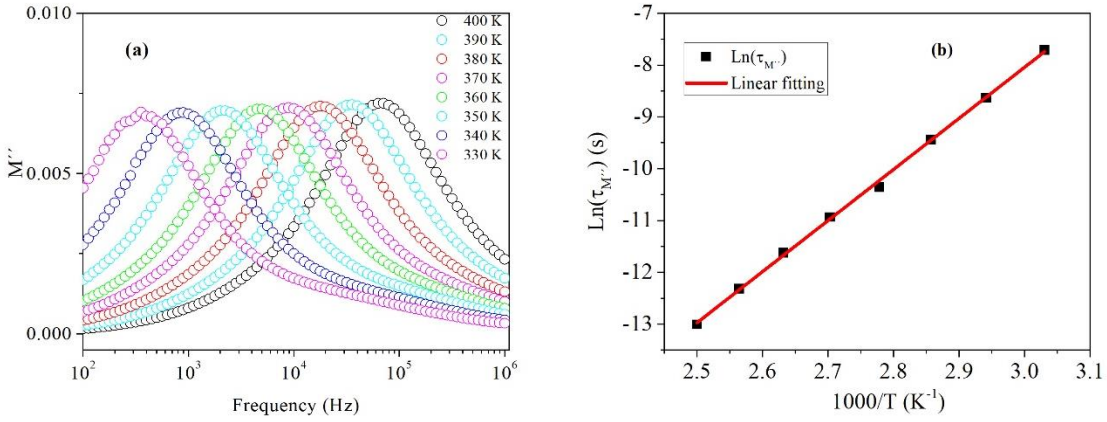

Fig. 7.15) a) Frequency dependence of the imaginary part of the electric modulus (M″) at various temperatures for Pechini1000. b) Arrhenius plot of relaxation time along with the linear fitting line based on Eq. 7.5.

7.3.5-ii) Pechini1200

Comparing Fig. 7.16 (a-b) and Fig. 7.12 (a-b) notifies us that Pechini 1200 and Pechini1000 are alike in the ε′(ω) and ε″(ω) behaviors. However, the tan(δ) response of Pechini1200 behaves in the same manner that for Pechini1000 and is characteristic of a relaxation phenomenon. In accordance with eq. 7.3, Ln($\tau_{\tan(\delta)}$) vs. 1000/T plot was modeled and the corresponding activation energy was determined and given in table 7.3.

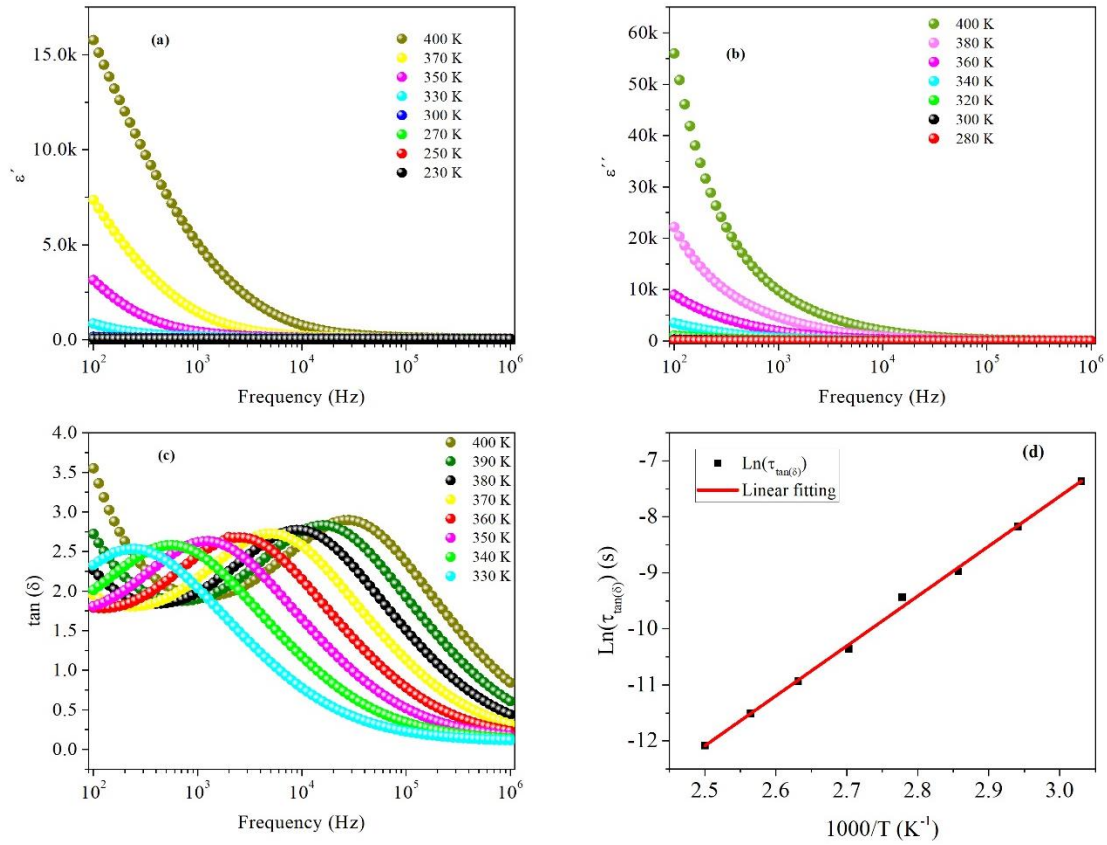

Fig. 7.16) Frequency dependence of a) the real part of dielectric permittivity (ε′) b) the imaginary part of dielectric permittivity (ε´´) and c) loss tangent (tan(δ)) measured at various temperatures for Pechini1200. c) Arrhenius plot of tan(δ) relaxation time along with the linear fitting line based on Eq. 7.3.

The Nyquist plots of Pechini1200 at several temperatures are drawn in Fig. 7.17 (a-c). Due to similarity with the impedance spectra of Pechini1000, we can suggest that the same model can conduct the Nyquist plots of Pechini1200. Fig. 7-17 (a-c) approve that the speculated model (Fig. 7.17 (d)) are well-fitted to the experimental spectra. The parameters related to each component (interior grain and grain boundary) are given in table 7.6.

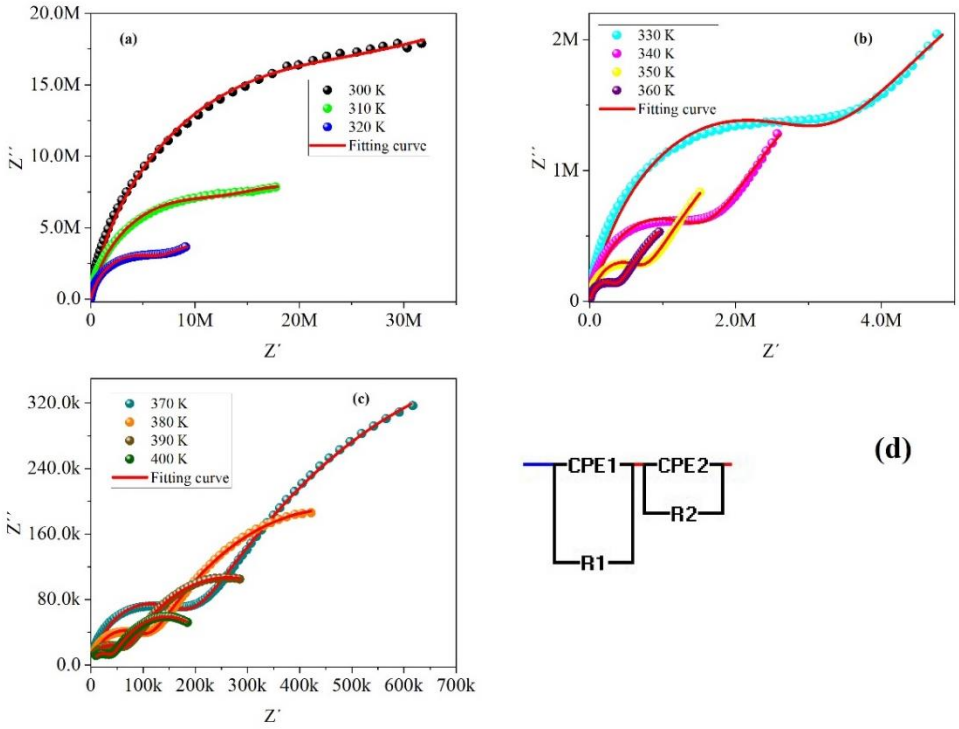

Fig. 7.17) (a-c) Complex impedance spectra (Nyquist plot) for Pechini1200 at different temperatures along with (d) the electrical equivalent circuit.

Table 7.6) The parameters extracted from the fitting to the assumed equivalent circuit for Pechini1200 (Error less than 2%).

Temperature	**R_{gb} (MΩ)**	**P_{gb} ($\times10^{-10}$)**	**n_{gb}**	**C_{gb} (nF)**	**R_g (MΩ)**	**P_g ($\times10^{-10}$)**	**n_g**	**C_g (nF)**
300	38.8	2.35	0.87	0.118	28.5	43.4	0.850	13.3
310	19.7	5.57	0.77	0.144	11.7	53.1	0.848	14.1
320	12.7	20.3	0.68	0.363	5.93	82.1	0.817	14.9
330	11.0	58.1	0.62	1.05	2.93	1.20	0.795	15.5
340	11.2	127	0.57	2.99	1.37	1.53	0.787	15.6
350	7.68	209	0.55	4.86	0.648	1.68	0.791	15.2
360	3.70	288	0.55	4.79	0.323	1.89	0.791	14.6
370	1.47	305	0.59	3.47	0.173	2.41	0.778	13.8
380	0.074	339	0.61	3.06	0.102	3.12	0.766	13.2
390	0.040	393	0.62	3.04	0.0613	4.62	0.745	13.0
400	0.021	425	0.64	3.00	0.0384	8.72	0.709	13.0

It was clarified that $R_{gb} > R_g$ in the temperature range of 300-370 K while above 370 K the R_{gb} becomes smaller than R_g. Furthermore, using equation 7.5, the ΔE_{gb} and ΔE_g were attained and brought in table 7.3.

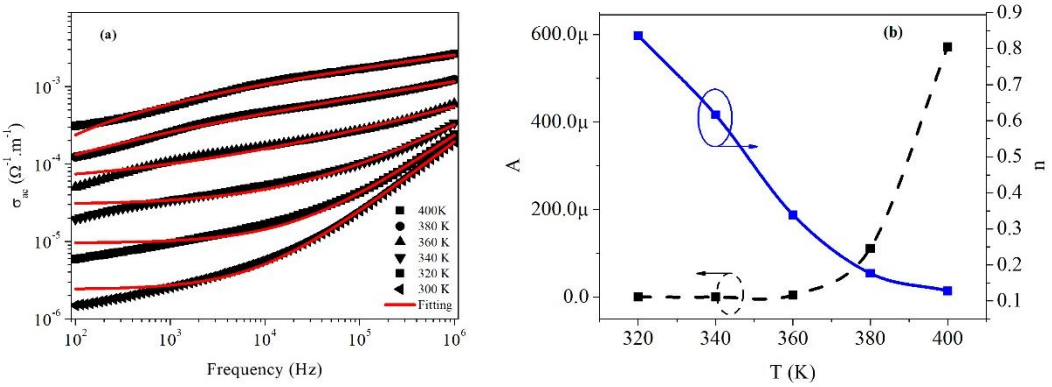

Fig. 7.18) a) $\sigma_{ac}(\omega)$ plots measured at different temperatures combine with the fitted curves according to Jonscher power law, b) Variation of exponent 'n' and A with temperature.

Our attempt to fit the $\sigma_{ac}(\omega)$ plots to Jonscher power law (eq. 7.4) was successful only for frequencies above 10^3 due to the electrode interface effect (Fig. 7.18 a). The parameter taken from the fitting were drawn in Fig. 7.18 (b). It is confirmed that the conduction mechanism in Pechini1200 follows CBH model. In addition, the A parameter has a trend as like as that for Pechini1000.

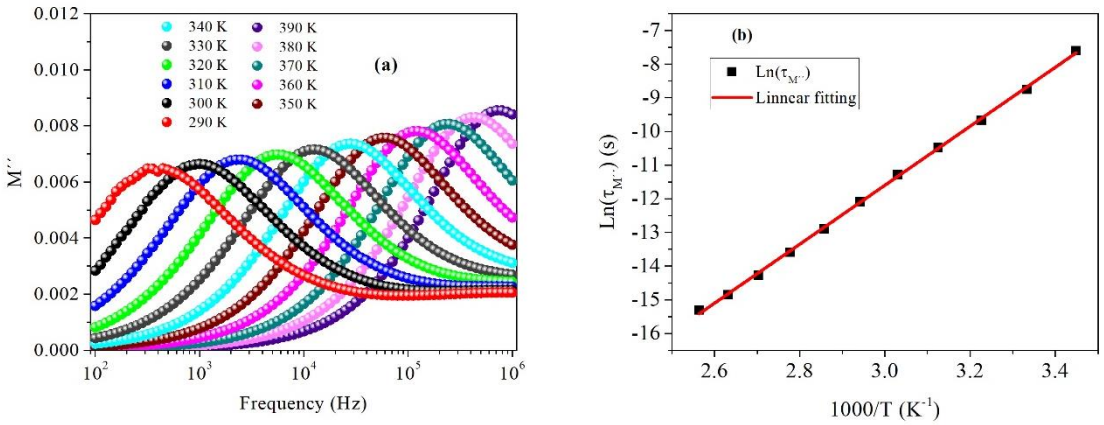

Fig. 7.19) a) M´´(ω) plots of Pechini1200 measured at different temperatures b) Arrhenius plot of M´´ relaxation time with the linear fitting line based on Eq. 7.5.

Fig. 7.19 a) shows the modulus spectroscopic plot versus frequency at temperatures from 290 K to 390 K. Peak in modulus spectra of Pechini1200 suggests the temperature dependent hopping mechanism. The temperature dependency of peak frequency observed in Pechini1200 is similar to other samples. So Eq.7.5 can be employed easily to calculate $\Delta E_{M''}$ as revealed in Fig. 7.19 (b) and the obtained value is given in table 7.3.

7.3.6) Magnetic characterizations

7.3.6-i) Pechini800

Fig. 7.20 a shows the zero field cooled (ZFC) and field cooled (FC) curves of Pechini800 which characterize the Morin transition resulting in a change from pure antiferromagnetic behavior to a weak ferromagnetic (canted antiferromagnetic) feature. To determine the Morin transition temperature, T_M, during both cooling and heating processes, the derivate of the ZFC and ZFC curves were measured as represented in Fig. 7.20 (b-c). The value of $T_{M(FC)}$ and $T_{M(ZFC)}$, the Morin transition temperature derived from FC and ZFC curves, respectively, and also $\Delta T_M=|T_{M(ZFC)}-T_{M(FC)}|$ are listed in table 7.7.

Magnetic hysteresis curves recorded at 150 K and 300 K are typical of weakly ferromagnetic components (Fig. 7.20 d). It is remarkable that the magnetization does not saturate even for our highest field (B) (10 T) being similar to previously obtained results. We consider the maximum magnetization at 10 T as the saturation magnetization and the values of M_S and also coercivity at 300 K are given in table 7.7. Moreover, it is well-known for a uniaxial antiferromagnet the spin-flop reorientation transition takes place when a large enough magnetic field is applied along the preferred axis [40]. The spin-flop, β_{sf}, is expressed as [40]:

$$\beta_{sf}=B \text{ at } (dM(B)/dB)_{max} \qquad (7.7)$$

The derivative of magnetization was plotted (inset of Fig. 7.20 d) and the taken value of β_{sf}. (Table 7.7).

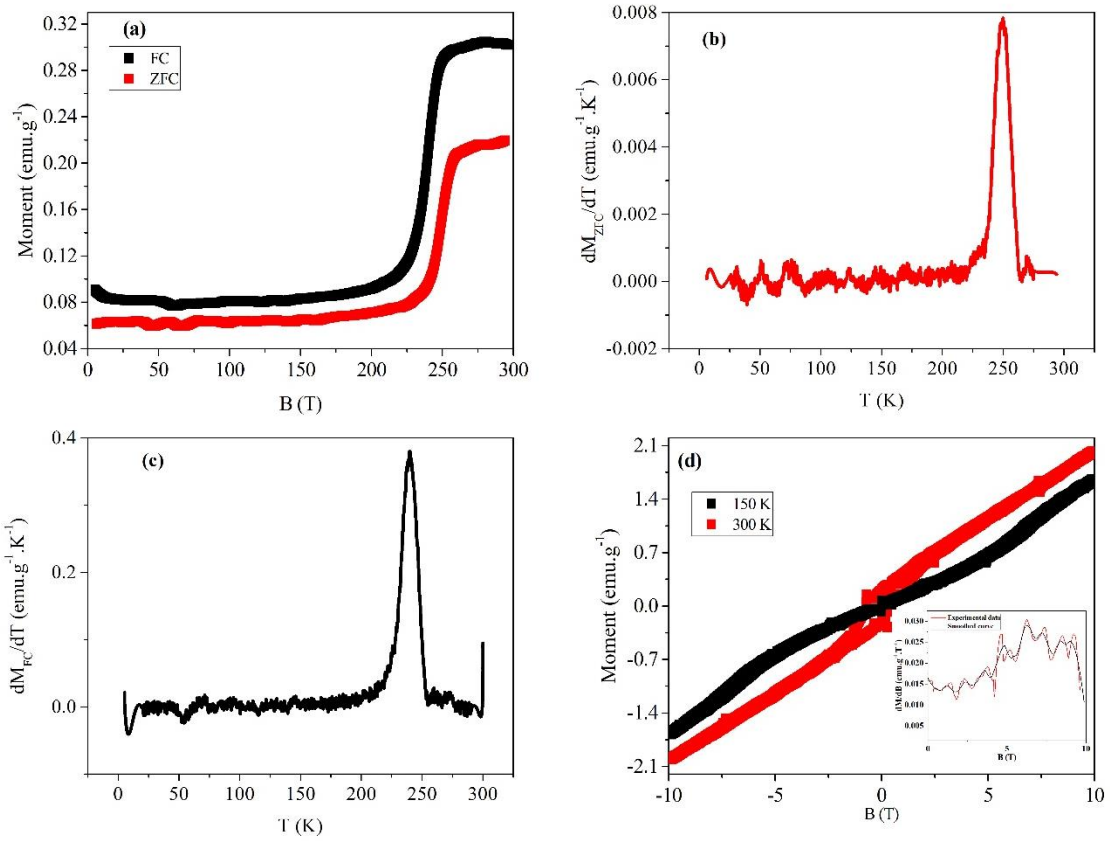

Fig. 7. 20) a) The ZFC-FC curves, b) dM_{ZFC}/dT vs. T plot, c) dM_{FC}/dT vs. T plot d) M-B curves measured at 150 K and 300 K, all for Pechini800. (the inset shows dM/dB at T=150 K, the red solid line is smoothing to the data.)

Table 7. 7) The magnetic properties of Pechini800, Pechini1000, and Pechini1200*.

Sample	$T_{M(ZFC)}$ (K)	$T_{M\ (FC)}$ (K)	ΔT (K)	β_{sf} (T)	B_c (T)	M_S ($emu.g^{-1}$)
Pechini800	249.6	239.3	10.3	6.2	0.53	2.0
Pechini1000	246.1	243.1	3	6.8	0.46	1.7
Pechini1200	247.2	245.8	1.7	6.9	0.32	1.8

*Error less than 2%.

7.3.6-ii) Pechini1000

Fig. 7.21 (a-d) shows the magnetic characteristics of Pechini1000. The values $T_{M(ZFC)}$, $T_{M(FC)}$, ΔT, β_{sf}, Bc, and M_S were obtained and given in table 7.7.

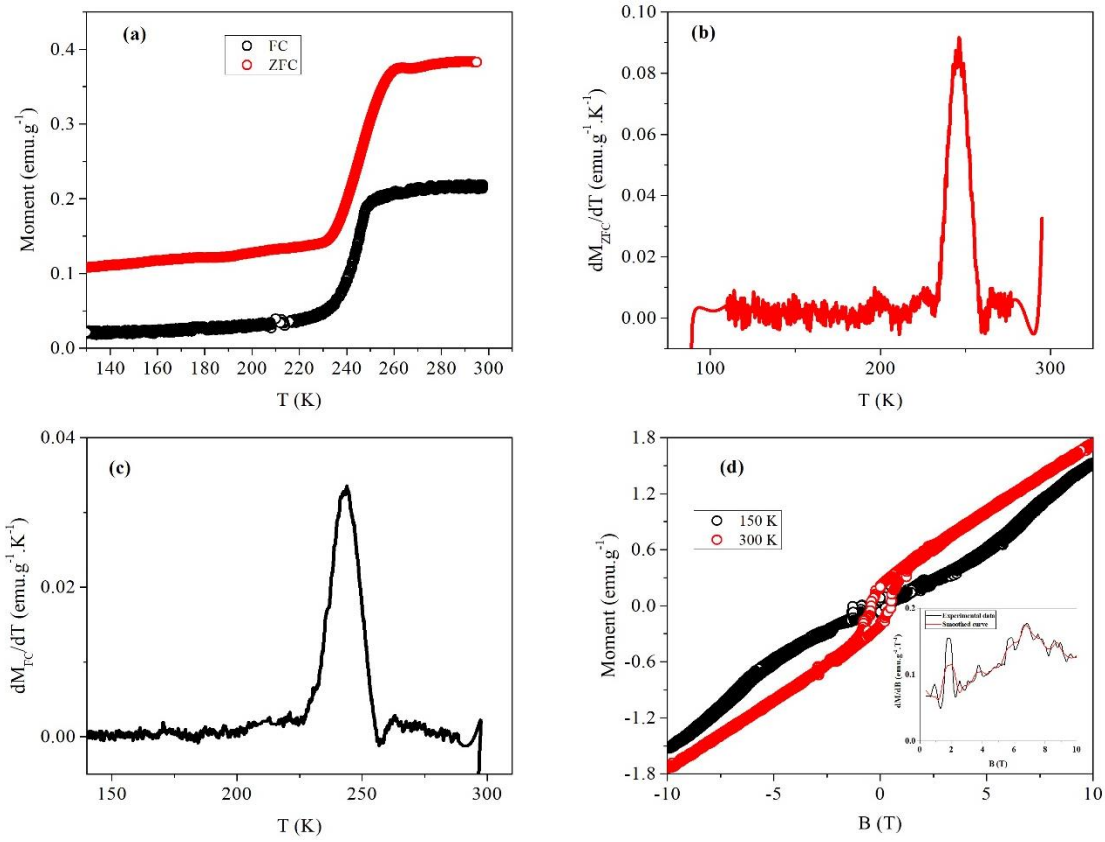

Fig. 7.21) a) The ZFC-FC curves, b) dM_{ZFC}/dT vs. T plot, c) dM_{FC}/dT vs. T plot d) M-B curves measured at 150 K and 300 K, all for Pechini1000. (the inset shows dM/dB at T=150 K, the red solid line is smoothing to the data.)

7.3.6-iii) Pechini1200

In accordance with other samples, the data regarding Pechini1200 were collected as one can see in Fig. 7.22 (a-d) and table 7.7. The data collected from the samples are used to study the influence of the thermal treatment on physical features the Pechini samples, as we discuss in the next section.

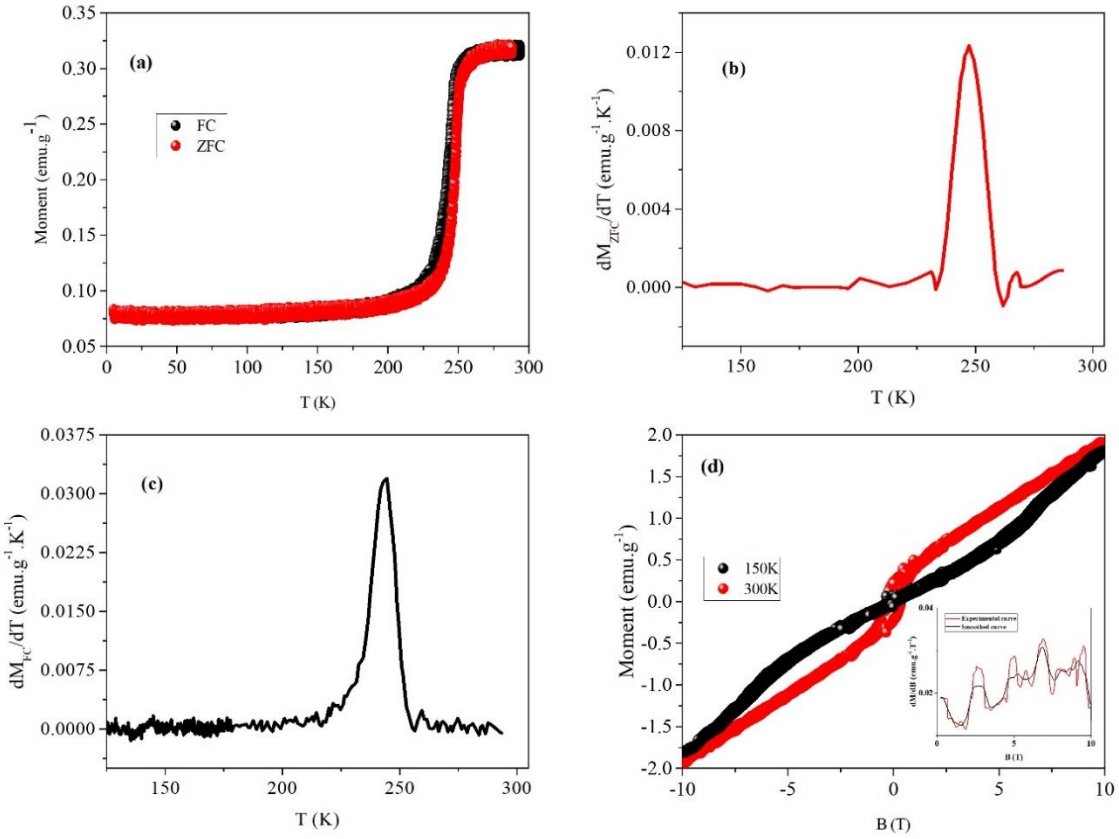

Fig. 7.22) a) The ZFC-FC curves, b) dMZFC/dT vs. T plot, c) dMFC/dT vs. T plot d) M-B curves measured at 150 K and 300 K, all for Pechini1200. (the inset shows dM/dH at T=150 K, the red solid line is smoothing to the data.

7.3.7) Thermal treatment impact on physical properties of Pechini samples

Both SEM micrographs and XRD patterns confirm that increase of the thermal treatment temperature causes the particle size growth in the Pechini samples, as expected. The high temperature has a significant effect on the conductivity vis-a-vis impedance behavior of hematite according to the following defect reactions:

$$O_O \rightarrow V^{\times}_O + 1/2O_2 \uparrow \quad (7.8)$$

$$V^{\times}_O \rightarrow V^{\bullet}_O + e^- \quad (7.9)$$

$$V^{\bullet}_O \rightarrow V^{\bullet\bullet}_O + e- \quad (7.10)$$

In Pechini800 as a consequence of the presence of some electronic trap center (like oxygen vacancies (Eq.7.8 to 7.10) and disorientation of surface/core spins, the electrostatic interaction through superexchange path of Fe^{3+}-O-Fe^{3+} is lowered and Fe^{3+}-Fe^{3+} direct interaction

becomes dominant mechanism. Moreover, with the superexchange interaction diminishing the two-magnon scattering is intensified. The energy of the two-magnon excitation is reduced when the magnons are created on neighboring anti-parallel spin sites [25]. This explanation is in agreement with Raman analysis in which $R_{Area(k)}$ has the highest value in Pechini800 as provided in table 5-2. when temperature increases, the direct cation-cation interaction decreases and simultaneously the superexchange interaction will rise $R_{Area(k)}$. Oppositely, the superexchange interaction will result in a reduction of ΔT, Bc, and M_S but increase B_{sf} because the superexchange interaction between pairs may not contribute to the flip energy and more energy (field) is necessary for spin-flop (see table 7.7.). It is also commented that consistent with dielectric data provided in table 7.3, arising in antiferromagnetic superexchange interaction boosts the polarization as already reported in other works [25].

7.4) Final remarks

The nano/microstructured hematite crystallines successfully have been synthesized using the Pechini route. XRD patterns, further supported by SEM images, confirmed high crystallinity of the samples. Based on DTA results, the secondary high-temperature heat treatment process was carried out in order to improve the size of particles. Raman, impedance spectroscopy, and VSM techniques were employed to investigate the physical properties of the sample. It was found an increase in heat treatment results in increasing the superexchange interactions within the α-Fe_2O_3 particles. Accordingly, well correlation could be made between the magneto-electrical and Raman characteristics of the samples.

7.5) References

[1] Y. Wu, X. Wang, **Materials Letters**, 2011, 65, 2062-2065.

[2] X. G. Wen, S. H. Wang, Y. Ding, Z. I. wang, S. H. Yang, **The Journal of Physical Chemistry B**, 2005, 109, 215-220.

[3] C. Wu, P. Yin, C. Ouyang, Y. Xie, **The Journal of Physical Chemistry B**, 2006, 110, 36, 17806-17812.

[4] S. Chakraborty, T. K. Jana, K. De, S. Das, K. Dey and K Chatterjee, **Materials Research Express**, 2014, 1, 046104.

[5] X. Liu, J. Zhang, X. Guo, S. Wu, S. Wang, **Nanotechnology**, 2010, 21, 095501.

[6] C. Feldmann, **Advanced Materials**, 2001, 13, 1301-1303.

[7] I. Cesar, A. Kay, J. A. G. Martinez and M. Gratzel, **Journal of the American Chemical Society**, 2006, 128, 4582–4583.

[8] T. Ohmori, H. Takahashi, H. Mametsuka, and E. Suzuki, **Physical Chemistry Chemical Physics**, 2000, 2, 3519–3522.

[9] C. Wu, P. Yin, X. Zhu, C. Ou-Yang, and Y. Xie, **The Journal of Physical Chemistry B**, 2006, 110, 17806–17812.

[10] K. J. Widder, A. E. Senyei and D. G. Scarpelli, **Proceedings of the Society for Experimental Biology and Medicine**, 1978, 158, 141-146.

[11] G. Garcon, S. Garry, P. Gosset, F. Zerimech, A. Martin, M-H. Hannothiaux and P. Shirali, **Cancer Letters**, 2001, 167 7–15.

[12] V. R. Elias, M. I. Oliva, E. G. Vaschetto, S. E. Urreta, G. A. Eimer, and S. P. Silvetti, **Journal of Magnetism and Magnetic Materials**, 2010, 322, 3438–3442.

[13] M. Busch, M. Gruyters, and H. Winter, 2006, **Surface Science**, 600, 4166–4169.

[14] X. Q. Liu, S. W. Tao, Y. S. Shen, **Sensors and Actuators B: Chemical**, 1997, 40, 161-165.

[15] A. B. Chin, I. I. Yaacob, **Journal of Materials Processing Technology**, 2007, 191, 235-237.

[16] S. U. Sonavane, M. B. Gawande, S. S. Deshpande, A. Venkatraman, R. V. Jayaram, Catalysis Communications, 2007, 8, 1803-1806.

[17] C. Q. Hu, Z. H. Gao, X. R. Yang, **Materials Chemistry and Physics**, 2007, 104, 429-433.

[18] F. Gulshan, S. Yanagida, Y. Kameshima, T. Isobe, A. Nakajima, K. Okada, **Water Research**, 2010, 44, 2876-2884.

[19] A. Valentini, N. L. V. Carreno, E. R. Leite, E. Longo, **Applied Catalysis A: General**, 2003, 255, 2, 211-220.

[20] S. Vivekanandhan, M. Venkateswarlu, N. Satyanarayana, P. Suresh, D. H. Nagaraju, N. Munichandraiah, **Material Letters**, 2006, 60, 3212-3216.

[21] I. Cesar, K. Sivula, A. Kay, R. Zboril and M. Gratzel, **The Journal of Physical Chemistry C**, 2006, 113, 772–782.

[22] I. V. Chernyshova, M. F. Hochella Jr and A. S. Madden, **Physical Chemistry Chemical Physics**, 2007, 9, 1736–1750.

[23] D. Bersani, P. P. Lottici and A. Montenero, **Journal of Raman Spectroscopy**, 1999, 30, 355-360.

[24] A. M. Jubb and H. C. Allen, **ASC Applied Materials & Interfaces**, 2010, 2, 10, 2804–2812.

[25] T. P. Martin, R. Merlin, D. R. Huffman, M. Cardona, **Solid State Communications**, 1977, 22, 565-567.

[26] L. Lu, L. Li, X. Wang and G. Li, J. **The Journal of Physical Chemistry B**, 2005, 109, 17151-17156.

[27] S. Mukherjee, R. Gupta, and A. Garg, **AIP Advances**, 2013, 3, 052115-052118.

[28] N. Guskos, G. J. Papadopoulos, V. Likodimos, S. Patapis, D. Yarmis, A. Przepiera, K. Przepiera, J. Majszczyk, J. Typek, M. Wabia, K. Aidinis, Z. Drazek, **Materials Research Bulletin**, 2002, 37, 6, 1051-1061.

[29] N. Sivakumar, A. Narayanasamy, B. Jeyadevan, R. Justin Joseyphus, and C. Venkateswaran, **Journal of Physics D: Applied Physics**, 2008, 41, 245001-245006.

[30] J.R. Macdonald, **Impedance Spectroscopy, Emphasizing Solid Materials and Systems**, 1987, John Willey & Sons, New York.

[31] D. K. Pradhan, R. N. P. Choudhary, B. K. Samantaray, **International Journal of Electrochemical Science**, 2008, 3, 597 – 608.

[32] A. Dhahri, E. Dhahri, and E. K. Hlil, **RSC Advances**, 2018, 8, 9103-9111.

[33] K. Funke, **Progress in Solid State Chemistry**, 1993, 22, 111–195.

[34] Z. Lu, J.P. Bonnet, J. Ravez and P. HagenmuUer, **Solid State Ionics**, 1992, 57, 235-244.

[35] K. S. Aneeshkumar and R. N. Bhowmik, **AIP Conference Proceedings**, 2016, 1731, 110015- 110018.

[36] M. J. Akhtar, M. Younas, **Solid State Sciences**, 2012, 14, 10, 1536-1542.

[37] V. Thakur, A. Singh, A. M. Awasthi and L. Singh, **AIP Advances**, 2015, 5, 087110-087121.

[38] L. Suber, P. Imperatori, A. Mari, G. Marchegiani, M. Vasquez- Mansilla, D. Fiorani, W. R. Plunkett, D. Rinaldi, C. Cannas, G. Ennas, and D. Peddis, **Physical Chemistry Chemical Physics**, 2010, 12, 6984-6989.

[40] R. D. Zysler, D. Fiorani, A. M. Testa, L. Suber, E. Agostinelli, M. Godinho, **Physical Review B**, 2003, 68, 212408.

[41] B. Baruwati, R.K. Rana, S.V. Manorama, **Journal of Applied Physics**, 2007, 101, 014302.

[42] A. Gaffar Lone, and R. N. Bhowmik, **AIP Advances**, 2015, 5, 047117.

Chapter 8 - Conclusions and future works

This Ph.D. work was conducted to construct magnetic nanoparticles and coating of those with inorganic (and/or organic) matrixes as a core-shell structure for both biomedical and microwave applications. By skimming through the results presented in the previous chapters it can be finalized that the goals of these plans are fairly well-achieved. Although, due to lack of time and inadequate technical and facility supports, there are some works still under process and they were not given in this dissertation. Moreover, by knowledge of the fact that the research has a dynamic nature, further efforts can be rewarded to modify and develop the obtained finding. Besides that, based on the obtained characteristics from the prepared compositions and regarding the industrial application, for both biomedical and microwave applications and also of other possible amplifications various tasks can be considered.

According to the chapter 4 results, the role of the Fe/Si ratio ranged from 0.5/99.5 to 20/80, the heat treatment conditions (rate and temperature) on the morphology, electrical and magnetic features of iron oxide NPs coated in silica obtained by the sol-gel method were found to be crucial. It was concluded that due to the presence of a large amount of non-magnetic SiO_2 matrix the samples containing 0.5 % of iron oxide, regardless to the heat treatment conditions, present paramagnetic behavior with high crystallization of silica (being in cristobalite and quartz) [1, 2]. But, silica glasses doped by 1% iron oxide after high-temperature calcination, 1400 ^{o}C, present superparamagnetic behavior with a blocking temperature at around 15 K due to the formation of ultrafine iron oxides particles, supposedly less 4 nm [3]. Although the glasses containing 1% iron oxide heat-treated at moderate temperature (from 600 up to 1000 ^{o}C) show only paramagnetic behavior [1, 2]. The big challenge is the formation of crystalline silica which is undesirable for our purpose, i.e. the iron oxide particles coating into the amorphous silica. However, the silica in crystalline form (quartz) has a bit higher dielectric constant rather than the amorphous one [4] leading to a slight enhancement in the permittivity of the prepared glass ceramics. To overcome this disadvantage a range of compositions containing a higher content of iron oxide, 2, 3, 10, and 20 %, were chosen. It has been shown that these series of glass ceramics have the capability of iron hydroxide chelating. The iron hydroxide chelation is stabilized and tends to nucleation and growth the particles with bigger size during the heat treatment. However, the troublesome task, the formation of quartz

crystallites, still persists [1-3, chapter 4]. For example, in agreement with XRD result HRTEM image of $2Fe_2O_3$-$98SiO_2$ glass ceramic heat treated with the rate of 5 ^oC/min up to 1000 ^oC for 4 h confirmed the formation of quartz crystallite, having a size of 30 nm, as shown in Fig. 8.1.

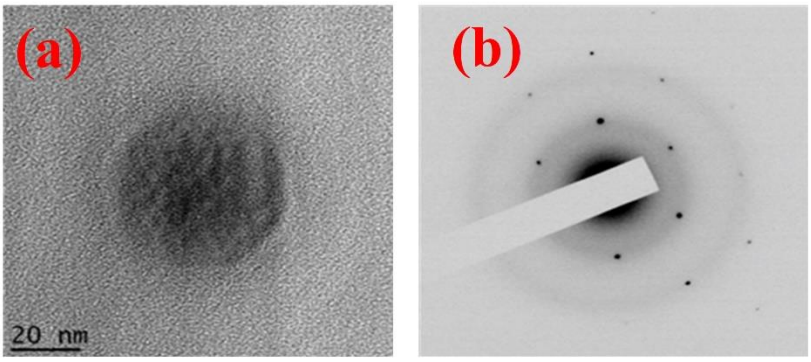

Fig. 8.1) HR TEM image of quartz crystallite formed in the silica glass doped with 2% iron oxide heat treated with the rate of 5 ^oC/min up to 1000 ^oC for 4 h, and b) the SAED pattern

Moreover, it is observed in Fig. 8.2 that the change in heat treatment time can only result in enlargement of silica and iron oxide crystallites. An overview of the morphology of the prepared compositions demonstrates that the dispersion of iron oxide nanoparticles in an amorphous silica matrix is satisfied. Though the exact phase type of iron oxide formed in these series of glass ceramics is an interesting question. The best way to answer this question is the employment of Mossbauer spectroscopy [5]. This measurement is a very sensitive technique in terms of energy resolution and capable of detecting any type of magnetic phase precisely [5].

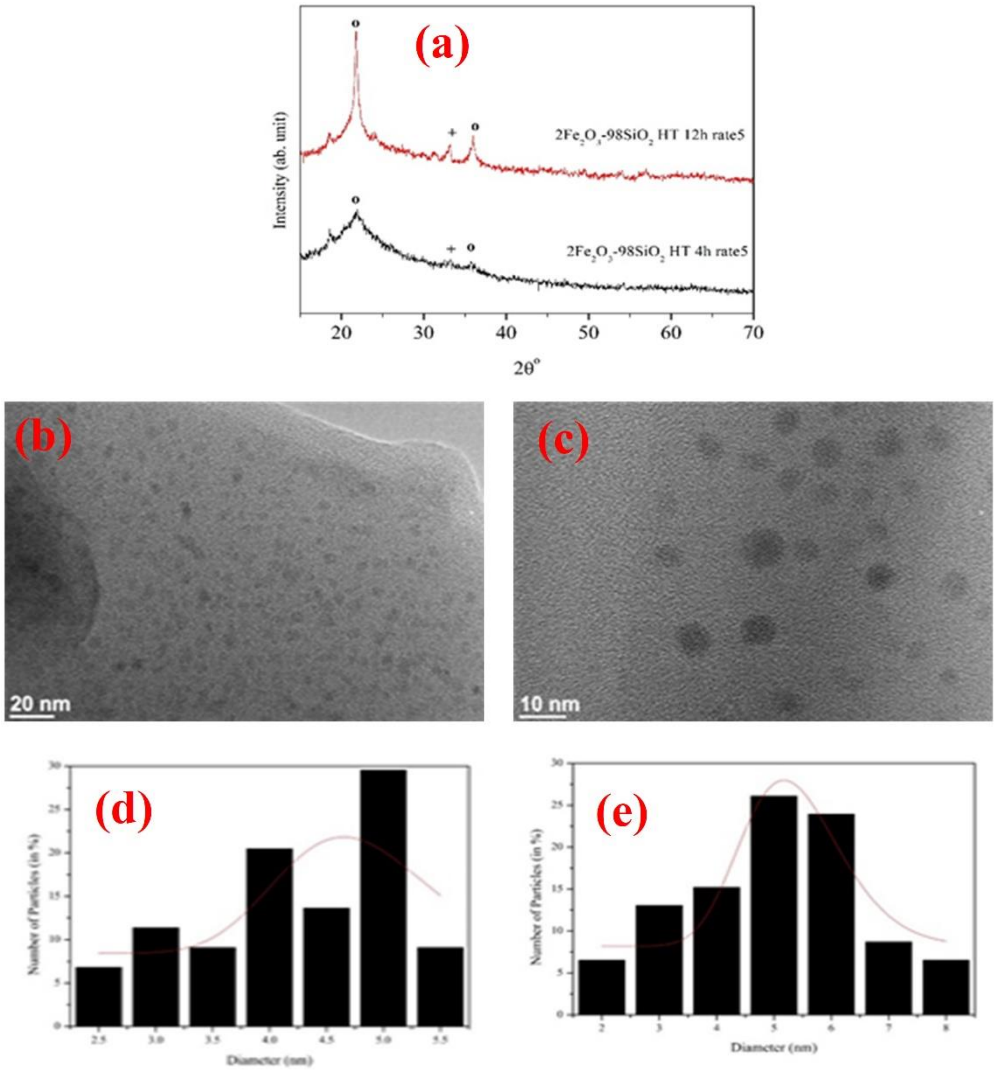

Fig. 8.2) a) XRD patterns of silica glasses doped with 2% iron oxide heat treated up to 1000 ^{o}C with the rate 5 ^{o}C/min at 4 and 12 h (o: quartz and +: hematite). A TEM image of the annealed sample at b) 4 h, c) 12 h. the size distribution of calcinated sample at d) 4 h, and, e) 12 h.

As a typical example, Fig. 8.3 depicts ZFC-FC curves of $3Fe_2O_3$-$97SiO_2$ glass ceramic annealed up to 1000 ^{o}C at 12 h. The ZFC curve shows three obvious transitions at ~ 25 K, vicinity of 100-140 K and also 150 K. one can suppose the transition in the temperature interval of 100 to 150 K is due to the formation of magnetite nanocrystallites but the iron oxide phase of ε-Fe_2O_3 also shows the similar feature [6]. So a more accurate characterization should be settled to recognize the correct phase formed in the glass ceramic.

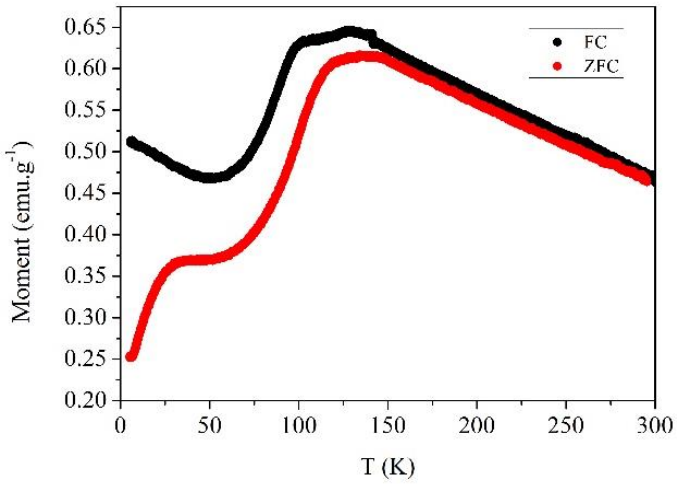

Fig. 8.3) The ZFC-FC plots of $3Fe_2O_3$-$97SiO_2$ glass heat treated up to 1000 ^oC with the rate of 5 ^oC/min for 12 h.

It is worth noting that other characterization techniques such as Raman, XRD, are unable to distinguish between different iron oxide components perfectly, hematite, magnetite, maghemite, wustite, ε-Fe_2O_3 and so on; as the features of these phases detected by the means of the usual methods are in close resemblance. Thus, Mossbauer spectroscopy studies on the prepared glass-ceramics can be considered as future work to well identify the iron oxide phases. Furthermore, as previously discussed, magnetite possesses more promising properties among other iron oxides. It was established that the formation of magnetite can actually be achieved by tuning the Fe content and the calcination environmental conditions (temperature and inert atmosphere) [7]. However, the crystallization magnetite resulting from thermal treatment at very high temperature will be unlikely compromised by the quartz crystallites. Therefore, the establishment of a specific thermal treatment under inert atmosphere (Ar or H) at moderate temperature (lower than 1000 ^oC) can be a part of the further investigation.

In the next chapter, the glass ceramic fibers with the composition of $10Fe_2O_3$-$90SiO_2$ were grown at the pulling rate ranged from 100 to 400 mm/h using the LFZ technique. The exclusive investigation on Raman spectra recorded from the powders of glass ceramics gave this conclusion to us that $Fe^{+2}/\sum Fe_{total}$ ratio increases with the pulling rate. The elemental mapping taken from SEM micrographs depicted the phase separation in the samples resulting from pulling rates. However, by a reduction in the pulling rate, the spherical crystallites gradually nucleate as observed from SEM micrographs. It could be suggested that depolymerization

increases when the pulling rate decreases. The AC conductivity of the fibers is influenced by the pulling rate.The ZFC-FC curves of the fibers are characteristics of a superparamagnetic-like behavior with a broad peak on the ZFC plot (T_P), near the Verwey transition and T_{irr} ranged from 200 to 250 K. However, the appearance of some anomalies on the fibers ZFC curves was thought to be due to the presence of the secondary phases of wustite and fayalites. Moreover, the enhancement in magnetization with the pulling rate attributed to the sharp increase of the Fe^{2+}/Fetotal ratio. The temperature-dependence of saturation magnetization and coercivity were successfully adopted to a modified Bloch law and the modified Kneller´s laws, respectively. It was shown that the pulling rate has a key impact role in the reduction-oxidation behavior and their clustering into silica glassy network of the fibers.

Fig. 8.4 (a-d) compares the magnetic behaviors observed in $10Fe_2O_3$-$90SiO_2$ glass ceramic prepared by two different: LFZ method and the sol-gel route. It can be said that the LFZ sample processing, regardless of the pulling rate, results in a superparamagnetic-like feature. While the magnetic properties of the glass-ceramic prepared by the sol-gel route with the same composition are representative of behavior consisting of the antiferromagnetic and ferromagnetic characteristics. Therefore, it seems that single-domain clustering of iron oxide particles with unignorable magnetic interactions could be achieved in the LFZ glass fibers unlike to the glass-ceramics synthesized by the sol-gel route.

It was found that incorporation of low content iron (less than 8%) into the silica-based glasses prepared by LFZ method does not provide any significant magnetic properties [8,9] and only presents paramagnetic attribute at room temperature. So due to poor clustering of iron species and huge directional crystallization of non-magnetic components, low doping of iron into the LFZ glass fibers is unappealing for our work plan goals and was not considered. Seemingly, in an excellent, agreement our results, with only after 10% iron oxide loading into the glass matrix iron ions nucleation starts to grow and clustering occurs.

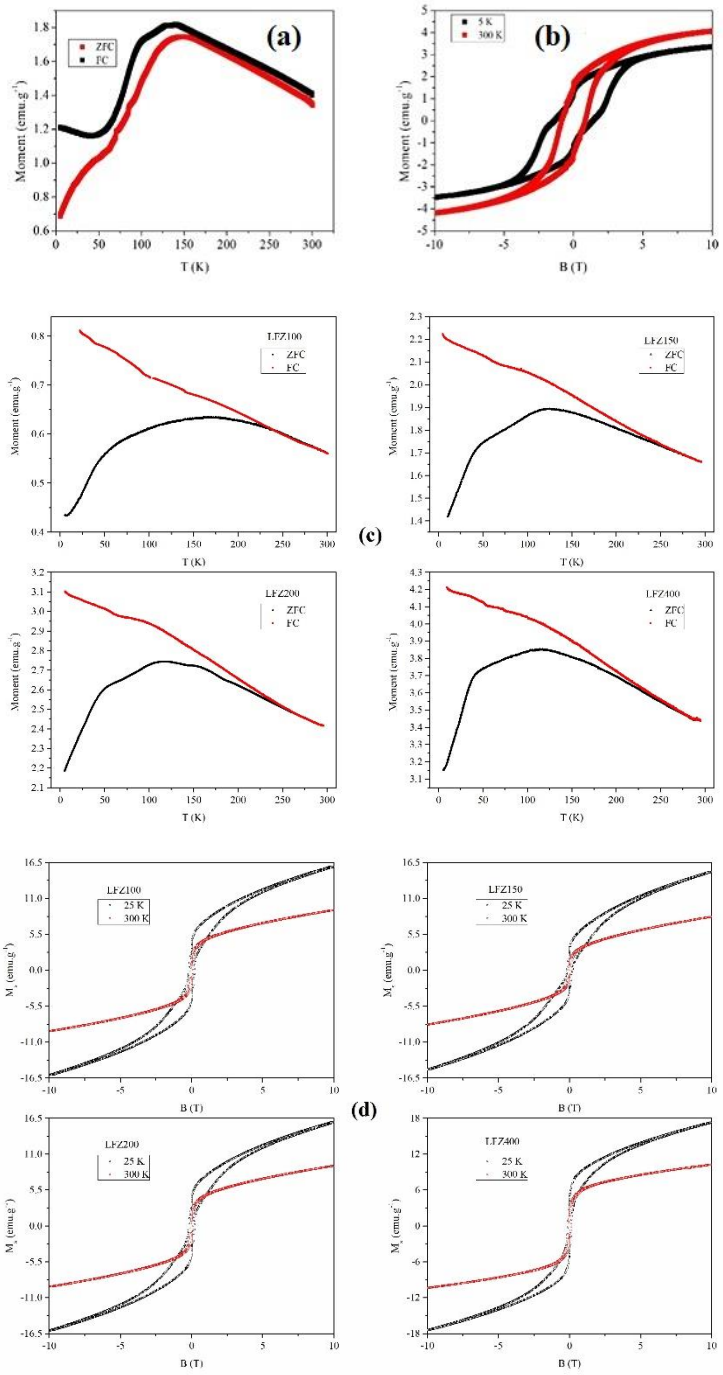

Fig. 8.4) The ZFC-FC curves and the M-H plots regarding the composition of $10Fe_2O_3$-$90SiO_2$ glass ceramics derived from two different synthesis methods; a and b) the sol-gel processed after a heat treatment up to 1000 ^oC with the rate 5 ^oC/min for 12 h; c and d) prepared by LFZ method at various pulling rates, respectively.

Nevertheless, a consequence of extensive compositional heterogeneous and irregular morphology and structure in LFZ samples, it is inferred that this method is an inappropriate approach for homogeneous dispersion of iron oxide particle into the glassy silica matrix.
Our attempts to grow fiber containing a slightly higher quantity of iron oxide, $15Fe_2O_3$-$85SiO_2$, and $20Fe_2O_3$-$80SiO_2$ starting compositions, were not successful. The reason for this failure is still open to question. But, we could successfully grow the fibers with the compositions of, $50Fe_2O_3$-$50SiO_2$ and $90Fe_2O_3$-$10SiO_2$, in spite of the fact that their supposed implications are far away from our work plan.

The $xMnFe_2O_4$-$(100-x)SiO_2$ x=10, 15, 20, and 100, were synthesized via an one-pot auto-combustion route. The size of the particles in the nanocomposites was found to be less than 100 nm. Additionally, according to the TEM images of $15MnFe_2O_4$-$(85)SiO_2$ and $10MnFe_2O_4$-$90SiO_2$, the manganese ferrite nanoparticles are homogeneously distributed into the silica matrix. The manganese ferrite-silica nanocomposites have a great advantage over the iron oxide-silica composites prepared by sol-gel and LFZ methods; any type of crystalline silica phase is not incorporated into the matrix. Thus the $MnFe_2O_4$-SiO_2 nanocomposites satisfactorily merit of being a core (Manganese ferrite nanoparticles)-shell (silica amorphous matrix) structure. According to these images, the nanoparticles formed during the self-ignition process are bigger and well-shaped than the ones processed by the sol-gel route followed by the high-temperature thermal calcination.

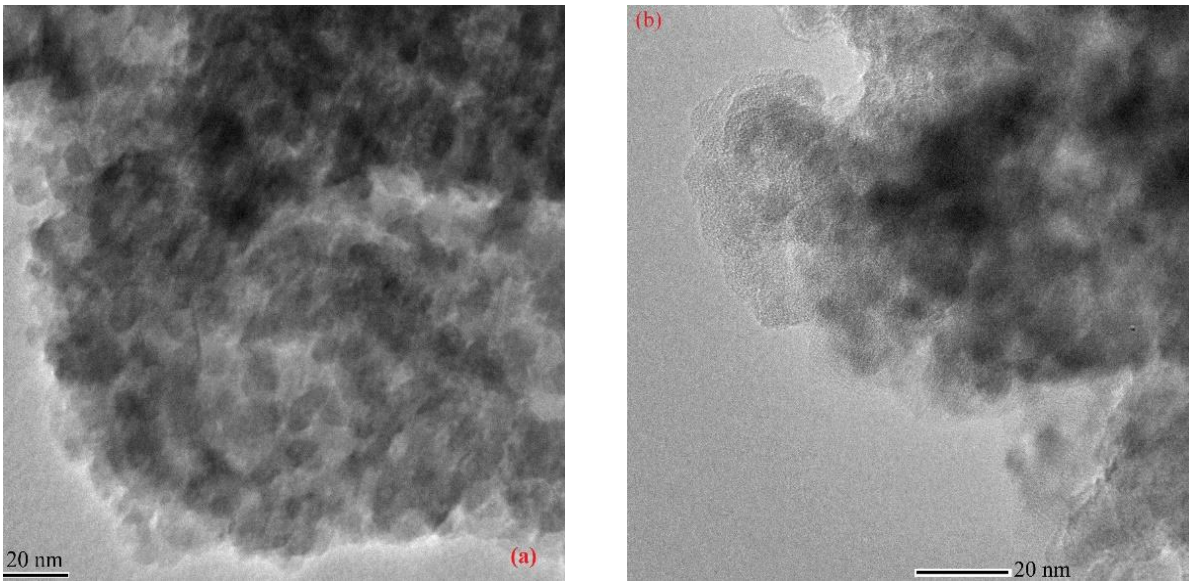

Fig. 8.5) a) the TEM image of a) $15MnFe_2O_4$-$85SiO_2$ b) $10MnFe_2O_4$-$90SiO_2$ synthesized by the auto-combustion route.

Thus, our findings reveal that the energy released during the auto-combustion process is large enough to nucleate the ferrite nanoparticles likely without suffering from the formation of silica crystallites. Off course, still more works can be accomplished on the manganese ferrite-silica nanocomposites. As a consequence of the spontaneous combustion, some structural (so compositional) defects can be created. As a result, the final product may suffer from the deficiency of the oxygen ion and the stichometry of the nano composition is not completely satisfied and it can be expressed by $MnFe_2O_{4-\varepsilon}$. The earlier studied on other ferrites [10-13] tell us that the structural-compositional defects can cause the Jahn-Teller distortion. Several techniques including X-ray absorption near edge structure (XANES), Mossbauer spectroscopy and complement Rietveld XRD refinement can be carried out to investigate in detail the structural changes and distortions formed in the nanocomposites.

One of the goals of this work plan was the production of the magnetic nanocomposites with a promising microwave absorbing characters. It is well known that the microwave absorbing properties of materials corresponds a parameter so-called eddy current loss; A large eddy current cancels or dominates the external magnetic field, leading to low permeability and poor microwave absorption properties [14]. The eddy current loss is correlated to the diameter of the nanoparticles d and the electric conductivity σ via the following equation [15]:

$$\mu_r^{''} \approx \frac{2\pi\mu_0(\mu_r^{'})^2\sigma d^2 f}{3} \quad (8\text{-}1)$$

Where μ'_r and μ''_r are the real part and imaginary part of permeability, respectively, also f is the frequency, μ_0 is the permeability of vacuum. So resistive materials decrease the reflection on the surface of absorbers and can have a better absorption feature. However, the increasing of conductance and complex permittivity should change the impedance match of the free space and the composites and enhance the reflection coefficient [16]. The nanoparticles with sizes less than a skin depth usually exhibit a relatively lower eddy current loss than the bigger particles [17].

Along with the aspects mentioned in previous, two more impact factors contributing to the absorption properties of magnetic nanoparticles are domain wall resonance and natural ferromagnetic resonance [18].

For magnetic nanomaterials, the superparamagnetic/ferromagnetic relaxation frequency is expressed using [18]:

$$f_b = f_0 \exp(\frac{-KV_p}{k_B T}) \quad (8\text{-}2)$$

Where KV_p is the magnetic anisotropy energy of a single magnetic nanoparticle and k_BT is the thermal energy. Thus, with decreasing in the nanoparticle size the effective anisotropy (K_{eff}) of the magnetic nanoparticles enhances leading to a great improvement in the frequency of natural resonance [19].

Moreover, the domain-wall resonance occurs only in multi-domain materials and MHz frequency range [20].

According to the results presented in chapter 6, samples 100MnFe/Si and 10MnFe/Si showed lower conductivity while the 15MnFe/Si was found to be the most conducting nano composition among the samples prepared by means of the auto-combustion route. Furthermore, the nanoparticles formed in 15MnFe/Si and 10MnFe/Si have a size of less than 15 nm, smaller compared with one in 100MnFe/Si. In contrary, as told previously, the K_{eff} of 15MnFe/Si and 10MnFe/Si are remarkably larger than 100MnFe/Si. While the nanoparticles in 100MnFe/Si showed an ideal single domain superparamagnetic feature. According to earlier

reports [21], 9 nm Fe_3O_4 nanoparticles encapsulated in the SiO_2 shell were presented as a good microwave absorber with a cutting-off frequency of 6.9 GHz, despite having a low permeability.

Therefore, as a future plan, it is a good idea to construct an apparatus operating in the microwave region and explore an efficient and facile method to improve the cut-off frequency of the magnetic nanocomposites without any drawback of poor permeability.

In this perspective work plan, therefore, 100MnFe/Si, 15MnFe/ Si, and 10MnFe/Si acquiring tremendous potentials as the microwave absorptive materials can be considered for extra studies.

It is worthy to note that 20MnFe/Si contains an absurd secondary phase of hematite nanocrystallites with low permeability and conductivity. So this sample with weak microwave properties can be excluded for further investigation.

Moreover, these three samples with very interesting morphology and the magnetic properties, are showing thoroughly the ability for being employed in the biomedical applications. To test the potential applications, several measurements, like in Vivo or Virto cytotoxicity measurements and magnetic targeting and MR imaging can be proposed in future. of course, these kinds of measurements are out of the scope of the presenting work plan.

We have also modified the physical characteristics of the promising nanocomposites, 100MnFe/Si, 15 MnFe/Si, and 10MnFe/Si, and functionalized them in accordance with the proposed applications. To do that an easy and fast chemistry route was used for secondary encapsulation of the nanocomposites with CTAB and polyaniline polymers. The primary results were gripping, however, the work is not totally done and requires more investigation. That is the reason we did not present this part of work in the current thesis.

In chapter 7, the construction of iron oxide nanoparticles by means the Pechini method was approached. It was finalized that the secondary thermal calcination at a temperature higher than 700 ^oC results in the hematite particles with the size > 500 nm signifying a weak ferromagnetic feature at the room temperature. Such big particles are not suitable for the biomedical application, thus the prepared nano/microparticles were not coated with any silica or inorganic matrix. Although, they can be considered to use in other technological applications for instance; lithium-iron batteries [22, 23] gas sensors [24], magnetic storage devices [25] and photoelectron chemical splitting of water [26].

8.1) References

[1] S. A. Salehizadeh, M. P. F. Graça, and M. A. Valente, **10th International Conference on Nanosciences & Nanotechnologies (NN13)**, 9-12 July 2013, Thessaloniki, Greece.

[2] S. A. Salehizadeh, M. P. F. Graça, and M. A. Valente, **E-MRS 2012 Fall Meeting**, 17-21 September 2013, Warsaw University of Technology.

[3] S. A. Salehizadeh, M. P. F. Graça, and M. A. Valente, **Physica Status Solidi C**, 11, 9-10, 1455-1458.

[4] R. D. Shannon, J. E. Dickinson, and G. R. Rossman, **Physics Chemistry of Minerals**, 1992, 19, 148-156.

[5] P. Gütlich, B. Eckhard, A. X. Trautwein, **Mössbauer Spectroscopy, and Transition Metal Chemistry: Fundamentals and Applications**, 2011, Springer-Verlag Berlin Heidelberg

[6] J. Tuček, R. Zbořil, A. Namai, and S-I. Ohkoshi, **Chemistry of Materials**, 2010, 22 (24), 6483–6505.

[7] F. Baino, E. Fiume, M. Miola, F. Leone, B. Onida, F. Laviano, R. Gerbaldo, and E. Verné, **Materials**, 2018, 11, 173-188.

[8] N. M. Ferreira, A.V. Kovalevsky, M. A. Valente, N. A. Sobolev, J. C. Waerenborgh, F. M. Costa, J. R. Frade, **Ceramics International**, 2016, 42, 2, Part A, 2693-2698.

[9] N. M. Ferreira, A.V. Kovalevsky, M. A. Valente, J. C. Waerenborgh, J. R. Frade, F. M. Costa, **Journal of Crystal Growth**, 2017, 457, 19-23.

[10] E. Veena Gopalan, I. A. Al-Omari, K. A. Malini, P. A. Joy, D. Sakthi Kumar, Y. Yoshida, M. R. Anantharaman, **Journal of Magnetism and Magnetic Materials**, 2009, 321, 8, 1092-1099.

[11] K. J. Kim, J. Han Lee, S. H. Lee, **Journal of Magnetism and Magnetic Materials**, 2004, 279, 2–3, 173-177.

[12] S. S. Ata-Allah, A. Hashhash, **Journal of Magnetism and Magnetic Materials**, 2006, 307, 2, 191-197.

[13] R. P. Mahajan, K. K. Patankar, M. B. Kothale, and S. A. Patil, **Bulletin of Materials Science**, 2000, 23, 4, 273–279.

[14] Z. Wang, H. Bi, P. Wang, M. Wang, Z. Liu, L. Shen, and X. Liu, **Physical Chemistry Chemical Physics**, 2015, 17, 3796-3801.

[15] Y. Yang, C. Xu, Y. Xia, T. Wang, F. Li, **Journal of Alloys and Compounds**, 2010, 493, 1–2, 549-552.

[16] S. Bi, X. Su, G. Hou, C. Liu, W-L. Song, M-Sh. Cao, **Ceramics International**, 2013, 39, 5, 5979-5983.

[17] M. Wu, Y. D. Zhang, S. Hui, T. D. Xiao, S. Ge, W. A. Hines, J. I. Budnick, and G. W. Taylor, **Applied Physics Letters**, 2002, 80, 4404-4408.

[18] N. Song, Sh. Gu, J. Zhou, W. Xia, P. Zhang, Q. Gul, W. Wang, H. Yang, and Zh. Cheng, **Applied Physics Letters**, 2017, 111, 133108-133113.

[19] B. Lu, X.L. Dong, H. Huang, X.F. Zhang, X.G. Zhu, J.P. Lei, J.P. Sun, **Journal of Magnetism and Magnetic Materials**, 2008, 320, 1106–1111.

[20] J. Shen, K. Chen, L. Li, W. Wang, Y. Jin**, Journal of Alloys and Compounds**, 2014, 615, 488–495.

[21] X. Zhang, Y. Liu, and G. Qin, **Applied Physics Letter**, 2015, 106, 033105.

[22] X. Zhang, and Q. Li, **Materials Letters**, 2008, 62, 988–990.

[23] Z.H. Jing, and S.H. Wu, **Materials Chemistry and Physics**, 2005, 92, 600–603.

[24] K. Sivula, F. Le Formal, and M. Grotzel, **ChemSusChem**, 2011, 4, 432-449.

[25] S. Cabanas-Polo, M. Distaso, W. Peukert, and A. R. Boccaccini, **Journal of Nanoscience and Nanotechnology**, 2015, 15, 10149-10155

[26] S. Piramana, S. Sundar, R. Mariappana, Y. Y. Kima and K. Min, Sens. **Actuators B**, 2016, 234, 386–394.